ω-photoproduction off Protons and Neutrons with CBELSA-TAPS

Inaugural-Dissertation zur Erlangung des Doktorgrades der Naturwissenschaften der Justus-Liebig-Universität Fachbereich 07

vorgelegt von

Frida Dietz

II. Physikalisches Institut der
Justus-Liebig-Universität Giessen

Februar 2013

Dekan: Prof. Dr. Christian Diller
1. Berichterstatter: Prof. Dr. Volker Metag
2. Berichterstatter: Prof. Dr. Kai-Thomas Brinkmann

Summary

The main goal of this work was to determine the cross-section for photoproduction of ω mesons off neutrons. This cross-section had so far not been measured. It is, however, important for a quantitative understanding of the ω meson-nucleon interaction and for the in-medium properties of ω mesons in nuclei. Up to the time of this thesis all information on this interaction had come from studying the production off protons. Measurements of the photoproduction of other mesons like η and η' off neutrons have shown that the cross-sections for production off neutrons and protons are different.

In this work, the ω photoproduction off hydrogen and deuterium targets was studied with the tagged photon beam of the ELSA accelerator in Bonn for incident photon energies up to 2.0 GeV. The ω meson was identified via the $\omega \to \pi^0\gamma \to \gamma\gamma\gamma$ decay mode, using the combined setup of the Crystal Barrel/TAPS detector systems, which allowed photon detection over almost the full solid angle. Charged particles were registered by a scintillating fiber detector in the CB angular region and by plastic veto detectors in front of TAPS in the forward region. A missing mass analysis enabled identification of protons and neutrons. Correction factors, determined from the data and simulations, were used to correct for the mis-identification of protons as neutrons and vice versa.

The following reactions were studied:

- The production off the free proton: $\gamma p \to \omega p$
- The quasi-free production off the bound proton: $\gamma d \to \omega p(n)$
- The quasi-free production off the bound neutron: $\gamma d \to \omega n(p)$
- The quasi-free inclusive production: $\gamma d \to \omega(np)$

Both exclusive (the recoil nucleon was detected) and inclusive (detection of the recoil nucleon was not required) analyses have been carried out. The differential and total cross-sections were determined for each reaction channel. For all reaction channels, a strong

forward rise of the differential cross-section, indicative of t-channel production processes, is observed. For larger momentum transfers the excitation and decay of nucleon resonances play a dominant role.

The differential cross-section obtained from the exclusive and the inclusive analysis generally agree quite well. For the inclusive analysis the cross-section rises more steeply in the region where the ω meson goes forward in the c.m. system for incident photon energies $E_\gamma > 1.5$ GeV. In this region, the exclusive differential cross-section had to be extrapolated due to an acceptance hole for the protons for $0.9 \leq \cos(\theta^{\omega}_{c.m.}) \leq 1.0$. The total cross-sections obtained from the inclusive analysis is therefore $\approx$10% higher than that obtained from the exclusive analysis. This discrepancy is taken into account by the systematic errors.

Comparison to data by SAPHIR [18] and CLAS [19] on the ω photoproduction off the free proton shows a slight disagreement in the small momentum transfer region, where the differential cross-sections from this work lie above the previously published data. For incident beam energies < 1.3 GeV the total cross-section agree with the SAPHIR data, within the systematic errors. However, at higher incident beam energies the total cross-sections from the exclusive analysis lies generally 1-2 μb above the data published by SAPHIR.

The cross-section off the bound proton is found to be smaller than the one off the free proton. In the resonance peak region of $\approx$1.3 GeV incident beam energy the cross-section off the bound proton is $\approx$6.5 μb which is $\approx$30% smaller than the cross-section off the free proton. This difference cannot be attributed to a mere smearing due to the Fermi motion, showing that at energies close to the production threshold the interaction with the neutron plays a role. Only at higher energies the ω meson production cross-section off the bound proton comes close to that off the free proton.

The cross-section for ω production off the bound neutron was determined in two different ways; directly by the exclusive analysis and indirectly by subtracting the cross-section off the bound proton from the inclusive quasi-free cross-section off deuterium,

$$\sigma_n^{indirect} = \sigma_{incl} - \sigma_p \, .$$

In the indirect determination the neutron acceptance does not enter. Both determinations yield a cross-section off the bound neutron which is larger than that off the bound proton. For incident photon energies 1.2-1.6 GeV the ratio is $< \sigma_n/\sigma_p > \approx 1.3$. A stronger resonance contribution to the cross-section for ω production off the bound neutron compared to that off the bound proton is observed. At higher energies $E_\gamma > 1.7$ GeV the

cross-sections come close to each other, indicating production mechanisms independent of isospin.

The average cross-sections off the bound proton and the bound neutron from the exclusive determination are 6.6±0.1 μb and 8.4±0.2 μb, respectively, in the incident photon energy range 1.2-2.0 GeV. The systematic error was estimated to ≈15-20% in the cross-section determination off protons and to ≈20-35% in that off neutrons.

The cross-sections of this work were compared to coupled-channel calculations of the ω production off the free proton and off the free neutron. The calculated cross-section off neutrons is larger than the calculated cross-section off the proton. However, by an even larger factor of $< \sigma_n/\sigma_p > \approx 2.3$ in the range from threshold up to 1.8 GeV. The calculation of the ω production off the free neutron is crude, since it did not take any of the available neutron data into account, but it shows that there exist theoretical models that predict a larger cross-section for ω mesons produced off neutrons compared to off protons, as observed experimentally in this thesis.

Zusammenfassung

Das Hauptziel der vorgelegten Arbeit ist die Bestimmung des Photoproduktionsquerschnitts von ω Mesonen am Neutron. Dieser Wirkungsquerschnitt ist bisher nicht gemessen worden; er ist jedoch wichtig für ein quantitatives Verständnis der ω-Nukleon Wechselwirkung und der in-Medium Eigenschaften des ω Mesons in Kernen. Bis zu dieser Doktorarbeit beruhten alle Informationen zur ω-N Wechselwirkung auf der ω Produktion am Proton. Messungen der Photoproduktion anderer Mesonen wie η oder η' haben gezeigt, dass die Wirkungsquerschnitte an Proton und Neutron durchaus verschieden sein können.

In dieser Arbeit wurde die ω Photoproduktion am Wasserstoff und Deuterium untersucht mit energiemarkierten Photonenstrahlen am ELSA Beschleuniger in Bonn mit Photoneneinschussenergien bis zu 2.0 GeV. Das ω Meson wurde identifiziert über den $\omega \to \pi^0\gamma \to \gamma\gamma\gamma$ Zerfallskanal. Dazu diente der gemeinsame Detektoraufbau von Crystal Barrel und TAPS, der einen Photonennachweis über fast den gesamten Raumwinkel ermöglichte. Geladene Teilchen wurden im Winkelbereich des Crystal Barrel in einem Detektor aus szintillierenden Fasern und im Vorwärtswinkelbereich durch Plastik-Veto-Detektoren vor TAPS nachgewiesen. Eine "missing mass" Analyse erlaubte die Identifikation von Protonen und Neutronen. Korrekturfaktoren für die Mis-identifikation von Protonen als Neutronen und umgekehrt wurden aus den Daten und Simulationen ermittelt und bei der Bestimmung der Wirkungsqerschnitte angewendet.

Folgende Reaktionen wurden untersucht:

- Die Produktion am freien Proton: $\gamma p \to \omega p$
- Die quasi-freie Produktion am gebundenen Proton: $\gamma d \to \omega p(n)$
- Die quasi-freie Produktion am gebundenen Neutron: $\gamma d \to \omega n(p)$
- Die quasi-freie inklusive Produktion: $\gamma d \to \omega(np)$

Sowohl exklusive (das Rückstoß-nukleon wird nachgewiesen) wie inklusive (Nachweis des Rückstoß-nukleons nicht verlangt) Analysen wurden durchgeführt. Differentielle und totale Querschnitte wurden für jeden Reaktionskanal bestimmt. Der differentielle Wirkungsquerschnitt weist für jeden Reaktionskanal einen exponentiellen Anstieg für kleine Impulsüberträge an das Nukleon auf, was charakteristisch ist für einen t-Kanal Austauschprozess. Bei größeren Impulsüberträgen spielt die Anregung und der Zerfall von Nukleonresonanzen eine dominante Rolle.

Die differentiellen Querschnitte am freien Proton aus der exklusiven bzw. inklusiven Analyse stimmen recht gut überein. Für Photoneneinschussenergien $E_\gamma > 1.5$ GeV, ergibt die inklusive Analyse einen etwas steileren exponentiellen Anstieg. In diesem Bereich muss der exklusive Querschnitt durch Extrapolation bestimmt werden wegen eines Akzeptanzlochs bei den Protonen für $0.9 \leq \cos(\theta^{\omega}_{c.m.}) \leq 1.0$. Der totale Querschnitt aus der inklusiven Analyse ist daher um ≈10% höher als in der exklusiven Analyse. Diese Diskrepanz ist im systematischen Fehler berücksichtigt.

Ein Vergleich mit publizierten Daten der SAPHIR und CLAS Kollaborationen zur ω Photoproduktion am freien Proton zeigt leichte Abweichungen. Für Photoneneinschussenergien < 1.3 GeV stimmt der totale Querschnitt mit dem von SAPHIR publizierte Querschnitt, im Rahmen der systematischen Fehler, überein. Bei größeren Photoneinschussenergien liegt der Querschnitt aus der exklusiven Analyse in dieser Arbeit 1-2 μb höher als der von SAPHIR publizierte Querschnitt.

Im Vergleich zur Produktion am freien Proton ist der am gebundenen Proton gemessene Querschnitt niedriger. Im Bereich des Resonanzmaximums um ≈ 1.3 GeV Photonenenergie beträgt der Querschnitt am gebundenen Proton nur ca. 6.5 μb, ≈30% niedriger als der Querschnitt am freien Proton. Dieser Unterschied lässt sich nicht durch eine Faltung des Querschnitts am freien Proton mit der Fermibewegung der Nukleonen im Deuterium erklären. Im Energiebereich nahe der Produktionsschwelle ist die Wechelwirkung mit dem Neutron bedeutend. Nur im höheren Energiebereich nähert sich der Querschnitt am gebundenen Proton dem am freien Proton an.

Der Querschnitt am gebundenen Neutron wurde über zwei verschiedene Methoden bestimmt: einerseits direkt in einer exklusiven Analyse und andererseits indirekt durch Abzug des Querschnitts am gebundenen Proton vom inklusiven quasi-freien Querschnitt:

$$\sigma_n^{indirekt} = \sigma_{inkl.} - \sigma_p \,.$$

Die indirekte Bestimmung ist unabhängig von der Neutronen-Akzeptanz. Beide Bestimmungen geben einen größeren Querschnitt am gebundenen Neutron im Vergleich zum Querschnitt am gebundenen Proton. Für Photonenergien von 1.2-1.6 GeV ist der Wirkungsquerschnitt am gebundenen Neutron ein Faktor 1.3 größer als der Wirkungsquerschnitt am gebundenen Proton. Am gebundenen Neutron wurde ein stärkerer Anteil von Resonanzanregungen zum Querschnitt beobachtet im Vergleich zum Querschnitt am gebundenen Proton. Für Photoneneinschussenergien größer als 1.7 GeV wird beinahe eine Übereinstimmung von beiden Querschnitten gefunden. Dies weist auf einen Produktionsmechanismus unabhängig vom Isospin hin.

Der durchschnittliche Querschnitt am gebundenen Proton ist 6.6±0.1 μb und am gebundenen Neutron 8.4±0.2 μb für den Photoneneinschussenergiebereich von 1.2-2.0 GeV. Der systematische Fehler für den Querschnitt am gebundenen Proton ist ≈15-20% und ≈20-35% für den Querschnitt am gebundenen Neutron.

Die in dieser Arbeit bestimmten Querschnitte wurden mit gekoppelten Kanal Rechnungen für die ω Photoproduktion am freien Proton und freien Neutron verglichen. Der berechnete Querschnitt am Neutron ist größer als der am Proton, sogar um einen Faktor $< \sigma_n/\sigma_p > \approx 2.3$ im Bereich von der Produktionsschwelle bis zu 1.8 GeV. Die Berechnung der ω Produktion am freien Neutron ist jedoch recht grob, zeigt aber dass theoretische Modelle existieren, die größere Querschnitte für die ω Photoproduktion am Neutron als am Proton vorhersagen, so wie es in dieser Arbeit experimentell gefunden wurde.

Contents

1. Introduction

1.1. Motivation

Most of the information about the meson nucleon interaction comes from data of the mesons produced off free protons, for the simple reason that there exists no free neutron target. However, for a quantitative understanding of the meson production off nuclei, it is crucial to also study the meson production off neutrons. The target used for this purpose is deuterium, which complicates the analysis by the presence of the spectator proton in the nucleus. In addition, the motion of the nucleons inside the nucleus has to be taken into account. The photoproduction of ω mesons produced off the neutron had not been studied before and thus the cross-section was unknown. The determination of this cross-section was the main goal of this work.

Cross-sections for other mesons off protons and off neutrons

Studies of the production of other mesons such as the η and η' mesons have shown that there indeed is a difference in the cross-section for the mesons produced off protons compared to off neutrons. Figure 1.1 shows that the cross-section of η mesons produced off protons (blue triangles) is different from the cross-section off neutrons (red circles) [5]. The cross-section off the neutron was scaled with a factor 3/2. After this scaling there is good agreement to the cross-section off the proton close to threshold. However, at an incident photon beam energy of 1 GeV there is a peak structure seen in the cross-section off the neutron that is not observed in the cross-section off the proton. It becomes even more apparent when looking at the ratio of the cross-sections, σ_n/σ_p, which is shown in the inset of fig. 1.1. This peak structure could be due to *resonances*[1] that couple weakly to the proton and strongly to the neutron. Different model calculations have tried to explain this structure with different resonant contributions, but so far no conclusion has been drawn as to its origin.

[1] A resonance is an intermediate state of higher energy formed in the production process. The resonances decay via the strong interaction (see sect. 2.1.2) and are thus very short-lived with a life-time of 10^{-24} s. Therefore, they can not be observed directly, but have to be reconstructed from the decay products (*i.e.* the meson and the nucleon, in this case).

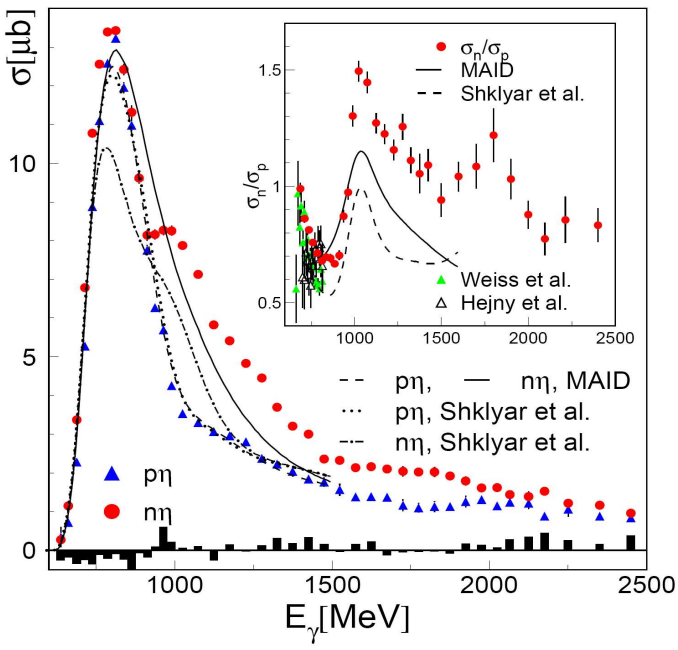

Figure 1.1: Quasi-free total cross-sections for η mesons produced off the proton (blue triangles) and off the neutron (red circles). The curves are model predictions [1, 2] folded with Fermi motion. Neutron data and calculations have been scaled up by a factor 3/2. Insert: neutron/proton cross-section ratio. Low energy data from for σ_n/σ_p from earlier experiments [3, 4]. The figure was taken from [5].

The η' production cross-sections off neutrons and off protons have also been studied. It was also found to be different for the two different nucleons, however, in a completely different way than in the case of the η meson. Figure 1.2 show that the η' cross-section off neutrons (red circles) is smaller than the one off protons (blue squares) at incident energies up to 1.9 GeV. As in the case of the peak structure observed in η meson cross-section off neutrons, the reason for this difference could be different resonance contributions. Other explanations might be interference effects between different resonances or between resonances and non-resonant background [6]. At incident photon energies higher than 2 GeV the cross-section off neutrons agree well with the cross-section off protons.

These discoveries of the different behavior of the cross-section off protons compared to that off neutrons of course raises the question of what this looks like for the ω meson production off nucleons.

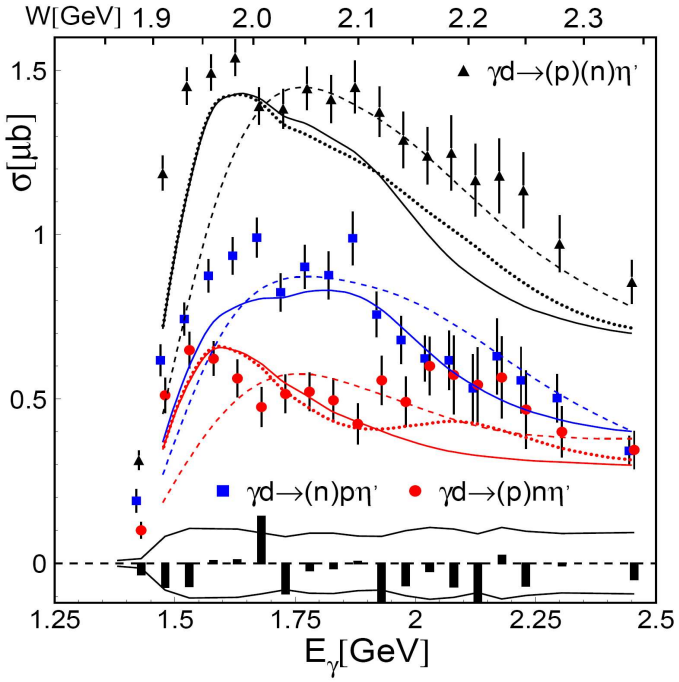

Figure 1.2: Total cross-sections for η' mesons produced off the proton (blue squares), off the neutron (red circles) and quasi-free inclusively (black triangles). The curves are fits to different model calculations. The figure was taken from [6].

Search for "missing resonances"

As discussed above, structures in the excitation functions could indicate resonance contributions. This leads to another important area of hadron physics, namely, the so-called search for missing resonances. All present theoretical models predict more resonance states than have been seen experimentally, hence the name *missing* resonances. Different models of the hadron structure predict different resonances, so pinning down these missing resonances can help in selecting the most accurate model description. Looking at structures in the total cross-sections is a first step for observing resonances. However, for a clear picture of which resonances contribute, generally polarization observables are needed [7].

In-medium modifications

One of the hot topics in modern hadron physics, where the work of this thesis would make a contribution, is the search for in-medium modifications, *i.e.* changes of the properties of

hadrons when embedded in a medium other than vacuum (for example hot and/or dense matter). The background for this field is that for composite systems such as molecules, atoms or nuclei the mass is close to the sum of the masses of the constituents (apart from small binding energy effect). This is, however, not true for hadrons (systems made up of quarks, such as mesons). Here, the sum of the constituent quarks only makes up a very small part of the hadron mass. The remaining part of the hadron masses can be thought to be generated dynamically, *i.e.* due to the energy in the interaction among the constituents. Another aspect is that the hadron masses are connected to the spontaneous breaking of chiral symmetry which, in the limit of vanishing quark masses, is a fundamental symmetry of QCD. If chiral symmetry were to hold also in the hadronic sector one were to expect masses of chiral partners (states with the same spin but opposite parity) to be mass degenerate. Instead mass splittings are observed which are almost of the same order of magnitude as the masses themselves [8]: there is a mass difference of 600 MeV between the nucleon ground state with $J^\pi = \frac{1}{2}^+$ and the first excited $\frac{1}{2}^-$ state of the nucleon at 1535 MeV. The mass splitting between $\frac{3}{2}^+$ $\Delta(1232)$ state and the $\frac{3}{2}^-$ $D_{13}(1520)$ state amounts to 300 MeV. Similar mass splits are also observed in the meson sector, *e.g.* ρ (1^-; 775 MeV) and a_1 (1^+; 1230 MeV). Chiral symmetry is, however, predicted to be at least partially restored when entering into a dense matter and/or increased temperatures. Consequently, a modification of observable properties of hadrons in the medium, such as changes in their mass or widths would be expected. Various experiments have seen indications for such modifications and a lot of theoretical work has been invested for understanding these changes. For an overview of the experimental and theoretical efforts made in this field see [9].

The experimental observable for extracting the in-medium width of mesons is the so-called nuclear transparency ratio, which is defined as

$$T_A = \frac{\sigma_{\gamma A \to VX}}{A \cdot \sigma_{\gamma N \to VX}}\,, \tag{1.1}$$

where $\sigma_{\gamma A \to VX}$ is the inclusive cross-section per nucleon for producing the meson off a nucleus with mass number A divided by the inclusive cross-section for producing the meson off a free nucleon multiplied by A. The transparency ratio describes the probability that a meson escapes the nucleus. If the nucleus were transparent to the ω meson the transparency ratio would be $T_A = 1$. The loss of flux of mesons is related to the absorptive part of the meson-nucleus potential and to the width of the meson in the nuclear medium. The method to use the transparency ratio in order to extract the ω meson width has been motivated in [10] and [11]. However, since the cross-section for ω photoproduction off the neutron has been unknown up to the time of this thesis the transparency ratio has instead

been normalized to the cross-section off carbon, *i.e.*

$$T_A = \frac{12 \cdot \sigma_{\gamma A \to VX}}{A \cdot \sigma_{\gamma C_{12} \to VX}} . \tag{1.2}$$

Normalizing to carbon avoids systematic errors due to the possibly different cross-sections for production off neutrons compared to off protons and enables comparisons to theoretical calculations [12]. If both the cross-section off protons and neutrons were to be known the transparency ratio could be calculated from the measured ω production cross-section on a nucleus with mass number A. This cross-section is an important input information for model calculations and thus gives a quantitative understanding of the production off nuclei.

1.2. Other experiments on ω production

1.2.1. SAPHIR

The photoproduction of ω mesons off the free proton has been studied with the SAPHIR detector at the ELSA facility in Bonn. The SAPHIR detector was a multi-purpose magnetic spectrometer which covered the full polar angular range. The solid angle, however, was limited to $0.6 \times 4\pi$ sr. The ω mesons were identified via the decay mode $\omega \to \pi^+\pi^-\pi^0$. The differential and total cross-sections were measured for the threshold energy up to $E_\gamma = 2.6$ GeV. For very small momentum transfers to the nucleon, $|t - t_{min}|$, the acceptance approaches zero, due to too low momenta of the proton. Therefore, in the region $|t - t_{min}| < 0.01$ GeV the differential cross-sections could not be determined, but had to be extracted from an exponential extrapolation. The total cross-sections were obtained by integration of the exponential fit and adding the values of the bins with larger $|t - t_{min}|$. The result can be seen in fig. 1.3 together with previous measurements and partial wave decomposition. The differential and total cross-sections indicate that there are strong resonance contributions close to threshold. A coupled-channel analysis performed by G. Penner and U. Mosel taking the SAPHIR data into account showed that the dominating resonance is the $P_{11}(1710)$ [13]. Apart from that, there is a non-negligible contribution from the π^0 t-channel exchange process. For a comparison of the data of this work to the SAPHIR data see fig. 6.3 for the differential cross-sections and fig. 6.14 for the total cross-section. The slope parameters of the exponential fits are compared in fig. 6.4.

1.2.2. JLab

High-statistics differential cross-sections and spin-density matrix elements for ω mesons produced off the free proton ($\gamma p \to \omega p$) have been measured by the CEBAF large acceptance spectrometer (CLAS) at the Thomas Jefferson National Accelerator Facility [19].

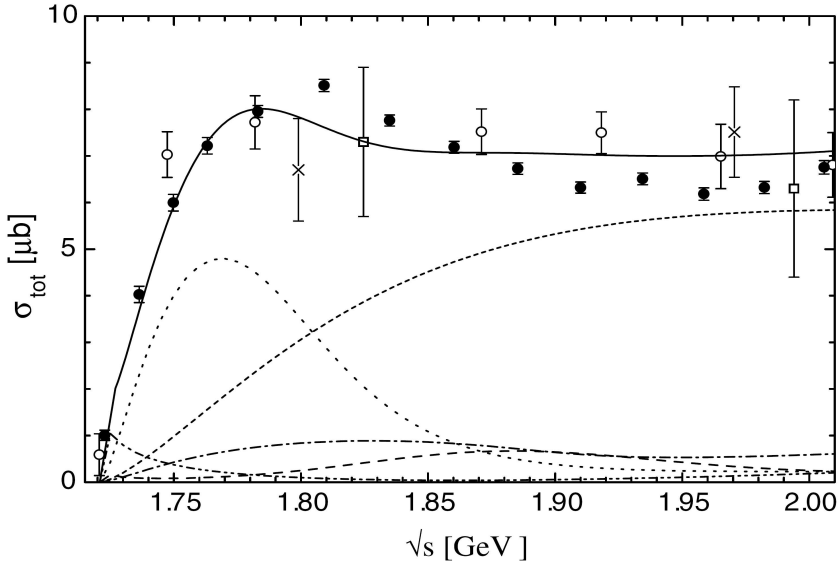

Figure 1.3: Total cross-sections for $\gamma p \to \omega p$. Data from SAPHIR (full circles), from [14] (open circles), from [15] (crosses) and from [16] (open squares). Partial-wave decomposition [13, 17]: $J^P = \frac{1}{2}^+$ (dotted line), $J^P \geq \frac{5}{2}^+$ from π^0 exchange (short dashed line), $J^P = \frac{1}{2}^-$ (dashed line), $J^P = \frac{3}{2}^+$ (dashed-dotted line), $J^P = \frac{3}{2}^-$ (dashed-double-dotted line). The figure was taken from [18].

The ω meson was identified through its decay $\omega \to \pi^+\pi^-\pi^0$. The charged particles were detected (and their momenta calculated) by drift chambers placed in a magnetic field. The π^0 meson was treated as a missing particle. The differential cross-sections were computed for 10 MeV wide bins for incident beam energies from threshold up to 2.84 GeV. Each energy bin was divided into 20 bins of $\cos(\theta^{\omega}_{c.m.})$ of 0.1. Due to limitations of detector acceptance, however, computation in all angular bins were not possible. Figure 1.4 shows the differential cross-sections from CLAS data (blue circles) together with the SAPHIR data (open squares). It shows that although the CLAS data have higher statistics, the acceptance is worse than what SAPHIR had. In general there is a good agreement between the data of the two experiments. For moderate angles $\cos(\theta^{\omega}_{c.m.}) < 0.5$ the agreement is very good for incident beam energies up to W = 2.0 GeV but for higher incident beam energies the data from CLAS tend to be higher than the data from SAPHIR. For larger angles the agreement is good for the full energy range. Due to the limited acceptance, no total cross-sections were determined from the CLAS data. None of the theoretical models

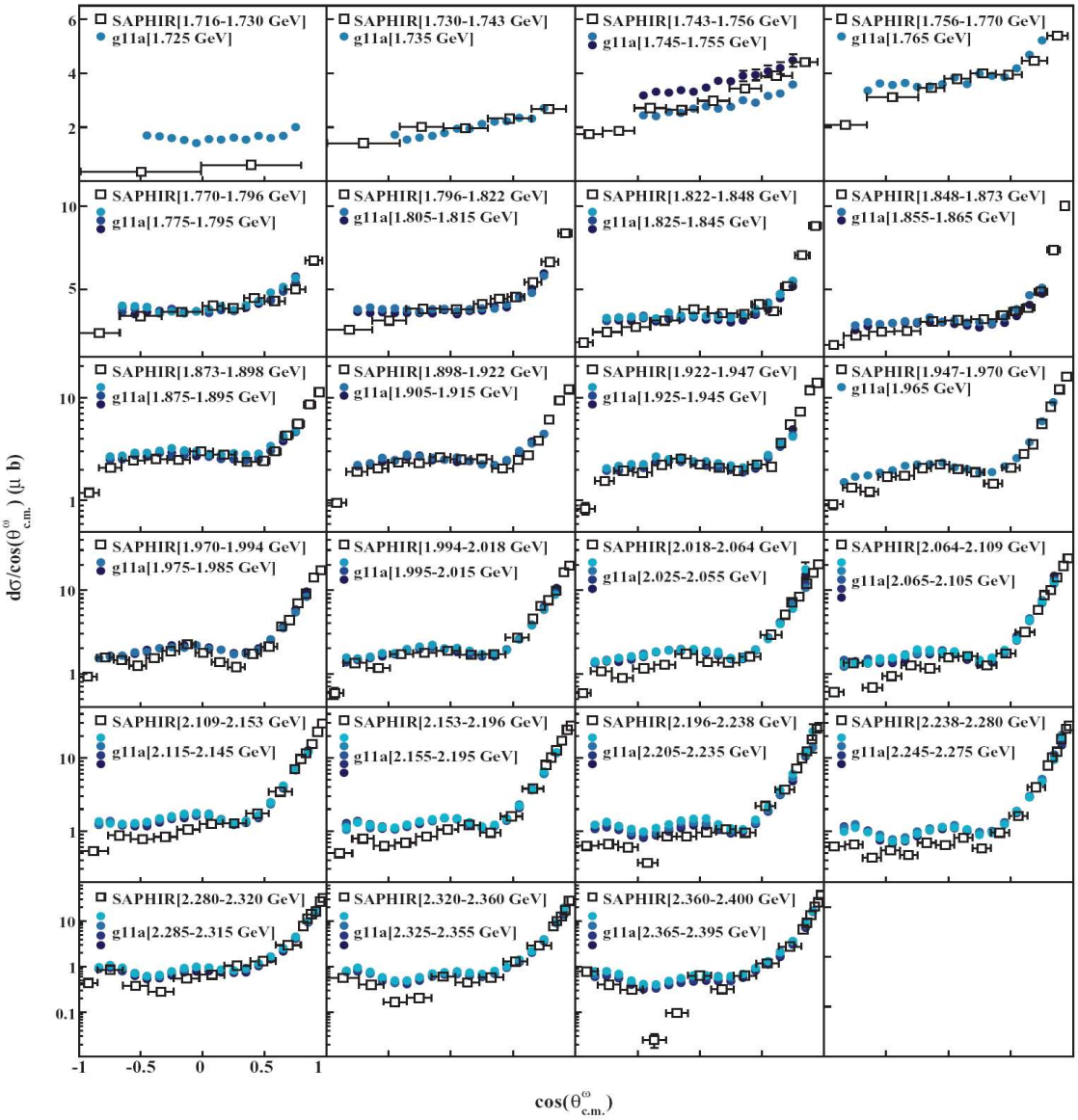

Figure 1.4: Differential cross-section from SAPHIR (open squares) and CLAS (blue circles) [19].

available at the time were able to describe the behavior of the spin density matrix elements calculated, which implies that the experiment is valuable for further development of theoretical models describing vector-meson photoproduction.

1.2.3. GRAAL

The photoproduction of ω mesons off protons and off neutrons (bound in a deuterium target) has been studied at the GRAAL (Grenoble Anneau Accelerateur Laser) experiment which is located at the ESRF (European Synchrotron Radiation Facility) in Grenoble. A linearly polarized photon beam, enabling both a study of cross-sections and of polarization variables, with tagged photon energies going up to 1.5 GeV was used on both liquid hydrogen and liquid deuterium targets. The decay channels studied were $\omega \to \pi^0\pi^+\pi^-$ for the $\gamma p \to \omega p$ reaction channel and $\omega \to \pi^0\gamma$ for the $\gamma n \to \omega n$ reaction channel. For detection of the decay products a barrel of plastic scintillators and a ball of BGO crystals were used in the central region and two walls of plastic scintillators plus a sampling calorimeter in the forward region for photon-neutron discrimination. In addition, there were wire chambers for tracking of charged particles in both the central and the forward regions.

The GRAAL experiment claims to get beam asymmetries consistent with the ones obtained by SAPHIR for ω mesons produced off the free proton. For ω mesons produced off the neutron higher statistics are needed for a clear interpretation of the results and only a preliminary cross-section of 4μb close to threshold was stated [20].

1.3. Outline of this thesis

The next chapter discusses the basics of elementary particle physics as it is described in the Standard Model. The properties of the mesons relevant for this work are listed in table 2.4 and explained in the text. The photoproduction process is described and the definitions of differential and total cross-sections are given. The chapter ends with a short description of the theoretical model used for calculations to which the data of this thesis is compared.

Chapter 3 gives an overview of the experimental setup at the ELSA accelerator in Bonn which was used to obtain the data analysed. The different components of the detector system and their properties are described as well as the targets used. The relevant beam times are listed in a table at the end of this chapter.

Chapter 4 explains the calibration procedure used in order to transform the recorded raw-data into physical quantities.

Chapter 5 explains the particle reconstruction and the analysis steps done for each reaction channel studied. The acceptances obtained from simulations are shown and the photon flux determination is described.

In Chapter 6 the results of this work are shown and compared to previous results from other experiments when possible. Furthermore, a comparison to theoretical calculations is given.

Chapter 7 discusses the conclusions of this work as well as the uncertainty of the results.

1.4. Units used

In particle physics the usual unit of energy is electron volt (eV). 1 eV is defined as the energy that a particle with 1 elementary charge (such as an electron) gains when falling through a potential of 1 V. For convenience the so-called natural system is often used. This implies setting the natural units $\hbar = c = 1$, where $\hbar$ is the reduced Planck constant and c is the speed of light in vacuum. The formulas $E = mc^2$ and $p = E/c$ show that both energy and momentum are measured in eV. This notation is also used in this thesis.

2. Theory

2.1. The Standard Model of particle physics

2.1.1. The fundamental particles

The Standard Model combines all the knowledge we have so far about the structure and interactions of matter into a consistent picture, with the exception of gravity. It states that all matter is composed out of a small number of fundamental spin-$\frac{1}{2}$ particles, so-called $fermions$. These fundamental constituents are six types (or $flavors$) of $quarks$ and six $leptons$, listed in table 2.1 together with their charges. The pairs are ordered in the table according to increasing masses from left to right. Each particle also has a corresponding anti-particle with the same properties but opposite charge and magnetic moment.

The **quarks** carry fractional charges $+\frac{2}{3}e$ or $-\frac{1}{3}e$. The flavors are denoted by u for *up*, d for *down*, c for *charm*, s for *strange*, t for *top* and b for *bottom*. In addition, each quark carries a property called color (red, green or blue) giving a total of $6 \cdot 3 \cdot 2 = 36$ different quarks (anti-particles included). In table 2.2 the six flavors of quarks are grouped into three pairs (or three generations). Their masses are also listed in addition to two quantum numbers (isospin and strangeness) that is explained in sect. 2.2.1.

The **leptons** are colorless particles with integer electric charges. The *electron* e^-, *muon* μ^- and *tauon* τ^- each have unit negative charge. The μ^- and τ^- are much heavier than the electron ($m_\mu = 105$ MeV and $m_\tau = 1784$ MeV compared to $m_e = 511$ keV) and thus very unstable and quickly decay into electrons and other lighter particles. The mean life time of the muon is $2.2 \cdot 10^{-6}$ s and that of the tauon $2.9 \cdot 10^{-13}$ s. The neutral leptons, called *neutrinos*, exist in three flavors corresponding to the three charged leptons, ν_e, ν_μ and ν_τ. The neutrinos are extremely light particles and only upper limits of their masses have been determined. As a consequence of the observation of neutrino oscillations, at least two of the neutrinos are known to have non-zero masses.

Fundamental Particles				
Particle	Flavor			Charge
Quarks	u	c	t	$+\frac{2}{3}e$
	d	s	b	$-\frac{1}{3}e$
Leptons	e^-	μ^-	τ^-	$-e$
	ν_e	ν_μ	ν_τ	0

Table 2.1: According to the Standard Model all matter is built from these twelve fundamental particles. The charge is given in the quantity e, elementary charge.

Generation	Name	Mass [MeV]	Isospin I_3	Strangeness S
1	up (u)	1.7–3.3	1/2	0
	down (d)	4.1–5.8	-1/2	0
2	charm (c)	1270+70-90	0	0
	strange (s)	101+29-21	0	-1
3	top (t)	$(172 \pm 0.9 \pm 1.3) \cdot 10^3$	0	0
	bottom (b)	4190+180-60	0	0

Table 2.2: The quark families and their properties [21].

2.1.2. The fundamental interactions

It has been found that nature is governed by four forces: gravitation, the electromagnetic force, the strong and the weak force. Gravitation affects all particles and even though it is the oldest known force it is also the least understood and the force carrier, the *graviton*, has not been experimentally detected. Thus it has not yet been successfully implemented into the Standard Model and this is one of the major reasons why this model is not the final word and physicists are looking for physics beyond the Standard Model. However, in the sub-atomic region the gravitational force becomes so weak that it can be neglected and the Standard Model works well to describe processes in this region. The three interactions (listed in table 2.3) that are included in the Standard Model are:

- **The Electromagnetic Interaction** which acts between all particles with electric charges. It is attractive for particles with electric charges of opposite sign and repulsive for charges of the same sign. The force carrier of this interaction are photons, γ, which are neutral and massless particles, hence the range of the electromagnetic force is infinite. QED (Quantum Electro Dynamics) is the well established and extremely precise theory describing the electromagnetic interaction.

- **The Weak Interaction** which affects all particles, but is so weak that it only plays a role in interactions between particles which do not interact via the electromagnetic and strong force. The only particles which fulfill these conditions of neither electric charge nor color are the neutrinos. The force carriers that mediate the weak force are W^+, W^- and Z^0. They are all very massive which implies that the weak force is very short ranged. The electromagnetic and weak interaction have been successfully unified into the electroweak force.

- **The Strong Interaction** which works between particles that carry color. As the name implies this force is stronger than both the electromagnetic and weak interactions. It is the force responsible for binding quarks into protons and neutrons and between protons and neutrons inside nuclei. This implies that it is strong enough to overcome the electromagnetic repulsion between protons inside the nucleus. The force carriers mediating this force are called *gluons*. The gluons themselves also carry color charge and thus interact with each other via the strong force. This is the major difference to the QED (describing the electromagnetic interaction) where the photons are charge-less and it implies that the strong interaction is short-ranged (roughly the diameter of a nucleon) even though the gluons are massless.

Interactions					
Force	Strong	Electromagnetic	Weak		
Force Carrier	8 gluons	photon	W^+	W^-	Z^0
Mass [GeV]	0	0	≈ 80	≈ 80	≈ 90
Range [m]	$\approx 10^{-15}$	∞	10^{-18}		

Table 2.3: Properties of the fundamental forces of the Standard Model. The gravitational force is not included in the Standard Model. The force carriers are so-called Gauge Bosons.

2.2. Hadrons

So far only colorless particles have been observed experimentally and thus single quarks and other colored object are thought to be forbidden. The colorless composite particles consisting of quarks are called *hadrons*. The discovered hadrons are divided into two types, *baryons* and *mesons*. Baryons are three quark states (qqq) where each quark has a different color so that the composite state is colorless. The mesons are a combinations of a quark and an anti-quark ($q\bar{q}$) where the anti-quark carries the anti-color of the quark so it fulfills the requirement to be colorless.

There is no apparent reason why other combinations of more than three quarks (*e.g.* $qqqq\bar{q}$ called pentaquarks), quark-gluon combinations (e.g. $q\bar{q}g$ called *hybrids*) or particles composed only out of gluons (*e.g.* gg-states called glueballs) should not exist, as long as they are colorless, but so far there is no clear experimental evidence of such *exotic states*. So, although these exotic stated are predicted by theories their existence is still under debate and there are several experiments dedicated for this search.

2.2.1. Hadron quantum numbers

Any quantum system, such as hadrons, is characterized by its mass and certain *quantum numbers*. These quantum numbers are discrete values that usually are conserved quantities under symmetry operations. There are also so-called *internal quantum numbers* which are not associated with space-time symmetries. They include the electric charge Q and baryon number B, which are conserved in all known interactions, and quantum numbers related to the flavor of the constituent quarks such as strangeness S, charm C,

beauty $\tilde{B}$ and truth T (T is zero for all known hadrons since the top quark is too unstable to form observable hadrons). These flavor related quantum numbers are conserved in the strong and electromagnetic interaction but not in the weak interaction.

The internal quantum numbers are so-called *additive quantum numbers* which means that the sum of the numbers for the constituent quarks will give the quantum number of the hadron and the sum of the quantum numbers of the particles in an interaction is the conserved quantity. For *multiplicative quantum numbers* on the other hand the product of the quantum numbers of the interacting particles is preserved, rather than the sum. Here follows a short description of the main quantum numbers used to characterize hadrons:

- **Spin S** is the intrinsic angular momentum of sub-atomic particles. It was originally thought to be the rotation of a particle around its own axis with a certain magnitude and orientation of the rotational axis. However, contrary to ordinary orbital angular momentum, spin can have half-integer values and is truly a fundamental property, such as charge, of a particle. As mentioned in sect. 2.1.1 all fermions carry half-integer spin whereas bosons carry integer spin. Quarks have spin 1/2 and they can thus exist in the two different states, +1/2 or -1/2.

- **Orbital angular momentum L** results from the motion of a particle, as opposed to spin. It describes the relative orbital angular momentum with which two particles couple. The lightest states of any combination of qqq or $q\bar{q}$ are assumed to have L = 0, whereas more massive states may have higher orbital angular momenta.

- **Total angular momentum J** is a combination of spin and orbital angular momentum. For mesons the allowed states are $|L - S_{q\bar{q}}| \leq J \leq |L + S_{q\bar{q}}|$.

- **Parity P** is the eigenvalue of a state under a parity transformation, which implies a simultaneous change of sign for all space coordinates. There exist only two possible values for this quantum number, P = +1 or P = -1. Parity is a multiplicative quantum number and it is given by the product of the intrinsic parities of the constituent quarks and a factor $(-1)^L$ from the coupling.

- **C-parity C** is the eigenvalue of *charge conjugation*, which is an operation which replaces all particles by their antiparticles. Like parity, C-parity is multiplicative and can obtain the values, C = +1 or C = -1. C-parity is only defined for particles that are their own antiparticle, *i.e.* neutral mesons.

- **Isospin I** was introduced to simplify the interpretation of hadron physics. Based on the fact of the similar masses of u and d quarks they were assumed to be two states of the same particle, only distinguishable by their opposite direction of isospin. Thus the third component of the isospin I_3 is the important quantity. Obviously, u and d quarks have opposite electrical charges so this formalism does not hold for electromagnetic interactions, but since the electromagnetic force is weak compared to the strong force, isospin symmetry is still a good approximation. The isospin formalism also holds for composite particles and implies that *e.g.* protons and neutrons can be treated as the same type of particle, the nucleon. Such families of particles are called *isospin multiplets*.

- **G-parity G** was introduced to be able to characterize also charged systems where the C-parity cannot be applied. The G-parity is the eigenvalue of a charge conjugation operation combined with an isospin rotation. The G-parity is calculated by $G = (-1)^{S+L+I}$.

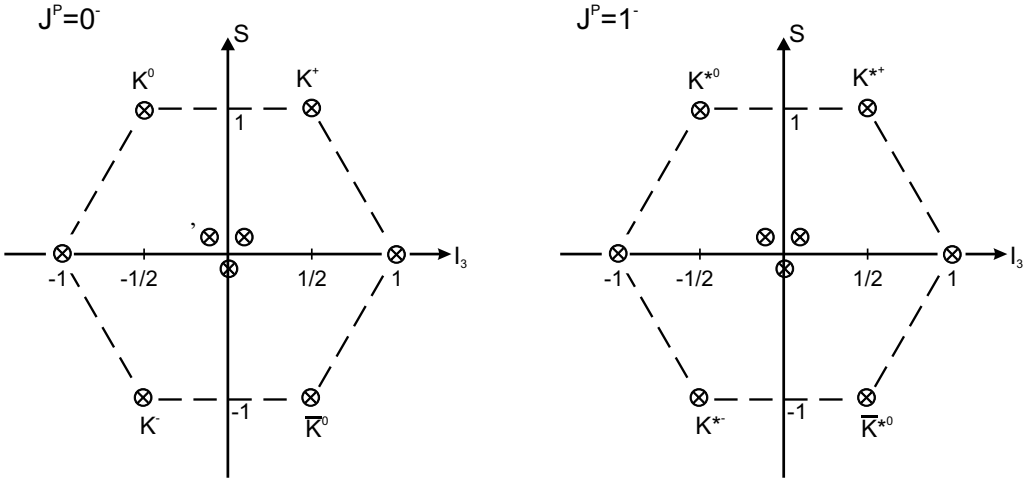

Figure 2.1: The nonets of pseudo-scalar (left) and vector mesons (right)

	I^G	J^{PC}	mass	life time τ	$c\tau$	decay modes Γ_{br}	
π^0	1^-	0^{-+}	134.98 MeV	$8.4{\cdot}10^{-17}$ s	$\approx$ 24 nm	$\gamma\gamma$	98.798%
						$e^+e^-\gamma$	1.198%
ω	0^-	1^{--}	782.59 MeV	$8.3{\cdot}10^{-23}$ s	$\approx$23 fm	$\pi^0\pi^+\pi^-$	89.1%
						$\pi^0\gamma$	8.28%

Table 2.4: Fundamental properties of the π^0 and ω mesons in vacuum [21]. Γ_{br} is the branching ratio for the given decay channel.

2.2.2. Mesons

As previously mentioned, mesons are particles consisting of a quark-antiquark pair, $q\bar{q}$. They are ordered in groups according to their quantum numbers described above. A quark and an anti-quark can couple to form mesons with spin $S_{q\bar{q}} = |S_q + S_{\bar{q}}|$ and $S_{q\bar{q}} = |S_q - S_{\bar{q}}|$, which means that the total spin of a meson is either 0 or 1 (thus they are bosons). The lightest mesons have J^P=0^- (S = 0 and L = 0), they are the so-called $pseudo-scalar$ mesons, and $J^P = 1^-$ (S = 1 and L = 0), so-called *vector* mesons. Focusing only on the three lightest quarks, u, d and s, 9 $q\bar{q}$ states can be formed and they are divided into one octet and one singlet. Figure 2.1 shows the nonets of pseudo-scaler mesons and vector mesons ordered according to their third component of the isospin and strangeness (S = -1 for strange quarks and S = 1 for strange antiquarks). Due to the similar masses of these quarks there will be a mixing of states. The two mesons of interest in this thesis can be expressed by their quark content as

$$\begin{aligned} |\pi^0\rangle &= \frac{1}{\sqrt{2}}(|u^\uparrow \bar{u}^\downarrow\rangle - |d^\uparrow \bar{d}^\downarrow\rangle) \\ |\omega\rangle &= \frac{1}{\sqrt{2}}(|u^\uparrow \bar{u}^\uparrow\rangle + |d^\uparrow \bar{d}^\uparrow\rangle)\,, \end{aligned} \tag{2.1}$$

where the arrows denote the direction of the spin of the quarks. The main properties characterizing these mesons are listed in table 2.4.

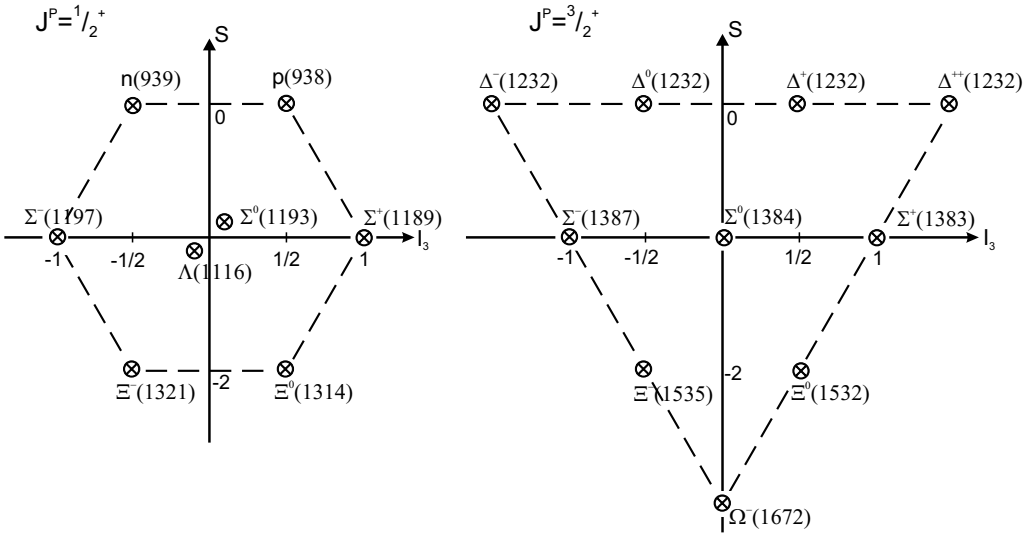

Figure 2.2: The lightest baryon octet (left) and decuplet (right).

	quark content	I	I_3	J^P	mass	life time τ
proton	uud	1/2	1/2	$1/2^+$	938.27 MeV	$> 2.1 \cdot 10^{29}$ years
neutron	udd	1/2	-1/2	$1/2^+$	939.57 MeV	885.7 s

Table 2.5: Fundamental properties of the two lightest baryons in vacuum [21].

2.2.3. Baryons

Baryons consist of three quarks, qqq, which implies that they are fermions, *i.e.* they carry half-integer spin. Because of the increase of degrees of freedom (three quarks instead of two, as is the case of the mesons) the number of possible states is highly increased and the wave functions are more complex. However, they are ordered in a similar fashion as the mesons according to their quantum numbers. As in the case of the mesons, the lightest baryons will couple to a total angular momentum L = 0. Together with the possible spin orientations this gives $J^P = 1/2^+$ and $J^P = 3/2^+$. These lightest baryon multiplets are shown in fig. 2.2 ordered according to their strangeness and third component of the isospin. Table 2.5 lists some important properties of the proton and the neutron since they are the baryons of interest in this thesis.

2.3. ω-photoproduction

The two main processes contributing to the ω-photoproduction are:

- **resonance contribution** The photon couples electromagnetically to the nucleon and creates an excited state of the nucleon, called resonance. Because of its short life time (typically $\tau \approx 6{\cdot}10^{-24}$ s; $\Gamma \approx 100$ MeV) this resonance decays predominantly into a nucleon and one or several mesons via the strong interaction. The Feynman diagram for this process is shown in fig. 2.3(a).

- **t-channel exchange** The photon transforms into an ω meson by emitting an intermediate meson (most likely a π^0 meson because of its low mass) which is absorbed by the nucleon, see fig. 2.3(b). This process becomes important for small momentum transfers to the nucleon which means that both the ω meson and the nucleon is moving in forward direction in the laboratory system.

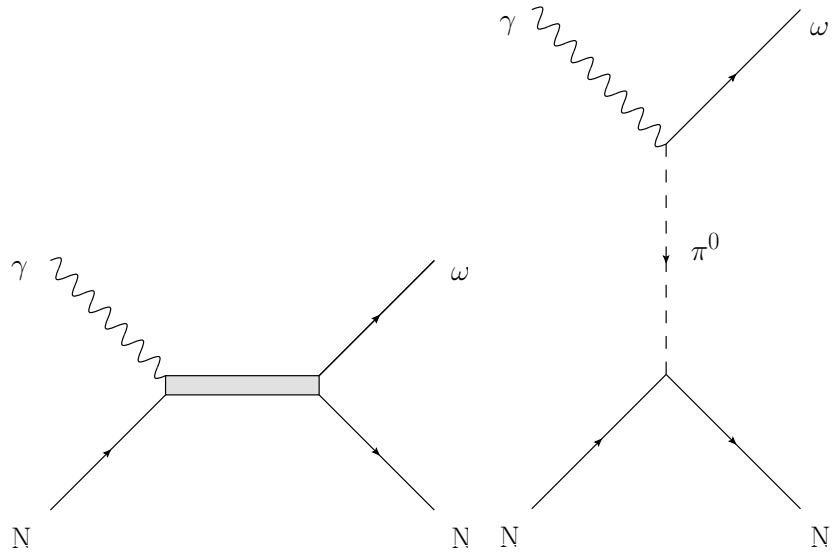

(a) resonance (b) t-channel

Figure 2.3: Feynman diagrams of the ω meson photoproduction through a resonance (a) and through t-channel exchange (b).

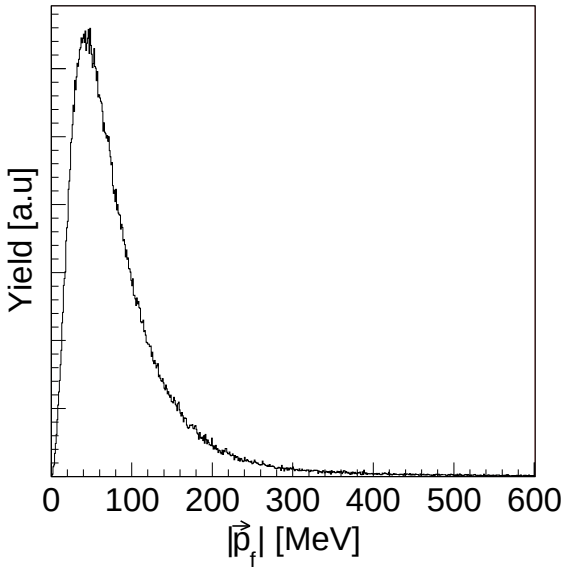

Figure 2.4: The Fermi momentum $|\vec{p}_f|$ distribution for a nucleon in the deuteron calculated from the Paris potential wave function [22]. The most probable momentum is ≈40 MeV.

2.4. Impulse Approximation

The Impulse Approximation (IA) was used in the event generators for the Monte-Carlo simulations for the reactions off the bound target nucleons as a way of taking the the momentum distribution of the nucleons (Fermi motion) into account. In addition, it was also used for folding the Fermi motion on the ω cross-section off the free proton for a comparison to the cross-section off the bound proton. One way of describing the momentum distribution of nucleons bound in deuterium is with the Paris wave function [22] which is depicted in fig. 2.4. For the reaction off the bound proton, the proton is the participant nucleon and the neutron the spectator nucleon, of course the opposite holds for the reaction off the bound neutron. The participant nucleon has a momentum $P_P = \vec{p}_f$ according to the Fermi distribution and the spectator nucleon has momentum $P_S = -\vec{p}_f$. According to energy and momentum conservation

$$E_P = m_d - \sqrt{m_S^2 + P_P^2} \tag{2.2}$$

$$E_S = \sqrt{m_S^2 + P_S^2}\,, \tag{2.3}$$

where E_P and E_S is the energy of the participant and spectator nucleon, respectively, and m_d=1875.6 MeV is the mass of the deuteron. The Fermi momentum vector components

are

$$p_{f,x} = |p_f| \sin(\theta) \cos(\phi) \tag{2.4}$$
$$p_{f,y} = |p_f| \sin(\theta) \sin(\phi) \tag{2.5}$$
$$p_{f,z} = |p_f| \cos(\theta) \,, \tag{2.6}$$

where p_f was generated randomly from the distribution in fig. 2.4. The initial state is then

$$P_{tot,x} = p_{f,x} \tag{2.7}$$
$$P_{tot,y} = p_{f,y} \tag{2.8}$$
$$P_{tot,z} = E_\gamma + p_{f,z} \tag{2.9}$$
$$E_{tot}^{on} = E_\gamma + E_S \tag{2.10}$$
$$E_{tot}^{off} = E_\gamma + E_P \,, \tag{2.11}$$

where E_{tot}^{on} and E_{tot}^{off} was calculated either on-shell or off-shell, respectively. The on-shell and off-shell invariant mass squared were calculated by

$$s^{on} = (E_{tot}^{on})^2 - ||P_{tot}||^2 = 2E_\gamma(E_S - P_{S,z}) + E_S^2 - P_S^2 \tag{2.12}$$
$$s^{off} = (E_{tot}^{off})^2 - ||P_{tot}||^2 = 2E_\gamma(E_P - P_{P,z}) + E_P^2 - P_P^2 \,. \tag{2.13}$$

In this work the off-shell calculation was used. The produced ω meson in the c.m.-system could now be calculated by

$$E_{\omega,cm} = \frac{s^{off} - m_P^2 + m_\omega^2}{2\sqrt{s_{off}}} \tag{2.14}$$
$$|P_{\omega,cm}| = \sqrt{E_{\omega,cm}^2 - m_\omega^2} \tag{2.15}$$
$$P_{\omega,cm,x} = |P_{\omega,cm}| \sin(\theta_{cm}) \cos(\phi_{cm}) \tag{2.16}$$
$$P_{\omega,cm,y} = |P_{\omega,cm}| \sin(\theta_{cm}) \sin(\phi_{cm}) \tag{2.17}$$
$$P_{\omega,cm,z} = |P_{\omega,cm}| \cos(\theta_{cm}) \,. \tag{2.18}$$

The participant nucleon in the c.m.-system

$$E_{P,cm} = \frac{s^{off} - m_\omega^2 + m_P^2}{2\sqrt{s_{off}}} \tag{2.19}$$
$$|P_{P,cm}| = \sqrt{E_{P,cm}^2 - m_P^2} \tag{2.20}$$
$$(P_{P,cm})_x = -P_{\omega,cm,x} \tag{2.21}$$
$$(P_{P,cm})_y = -P_{\omega,cm,y} \tag{2.22}$$
$$P_{P,cm,z} = -P_{\omega,cm,z} \,. \tag{2.23}$$

In the laboratory frame

$$E_{\omega,lab} = \gamma(E_{\omega,cm} + \beta_z \cdot P_{\omega,cm,z}) \tag{2.24}$$
$$P_{\omega,lab,x} = P_{\omega,cm,x} \tag{2.25}$$
$$P_{\omega,lab,y} = P_{\omega,cm,y} \tag{2.26}$$
$$P_{\omega,lab,z} = \gamma(P_{\omega,cm,z} + \beta_z \cdot E_{\omega,cm})\,, \tag{2.27}$$

where

$$\gamma = \frac{E_\omega}{m_\omega} = \sqrt{\frac{P^2_{\omega,lab,x} + P^2_{\omega,lab,y} + P^2_{\omega,lab,z}}{m^2_\omega} + 1} \tag{2.28}$$

and

$$\beta_x = -P_{\omega,lab,x}/(\gamma \cdot m_\omega) \tag{2.29}$$
$$\beta_y = -P_{\omega,lab,x}/(\gamma \cdot m_\omega) \tag{2.30}$$
$$\beta_z = -P_{\omega,lab,x}/(\gamma \cdot m_\omega)\,. \tag{2.31}$$

Each of the decays $\omega \to \pi^0\gamma \to \gamma\gamma\gamma$ were performed in the c.m.-system of the decaying particle and then the four-vectors of the decay products were calculated in the laboratory system according to the Lorentz transformations described above.

2.5. Theoretical calculations

The study of pion- and photon induced reactions on nucleons is an important part of modern hadron physics. It provides information on meson-baryon interactions which is crucial for the investigation of in-medium effects in nuclear media. In addition, the information on the baryon resonance spectrum will increase the understanding of the hadron structure and the strong interaction. Some quark models predict more resonant states than have been confirmed by experiments so far. It is thought that these so-called "missing" resonances couple weakly to the πN channel which has for many years been the predominant experimental approach to study the excitation energy spectrum of the nucleon. For this reason it is important to study data from other reactions as well as to have a theoretical model that involves other final states.

The results of this thesis have been compared to coupled-channel effective Lagrangian calculations. The idea of such calculations is to include as many channels and partial waves as possible and to allow for much experimental information as constraints. The

model used by V. Shklyar includes the γN, πN, $2\pi N$, ηN, ωN, $K\Lambda$ and $K\Sigma$ final states (with resonance spins J = 1/2, 3/2 and 5/2) for the energy region $\sqrt{s}$ ≤2 GeV [23]. Data measured by SAPHIR off the free proton has been incorporated, but no data off neutrons have been used. In order to give reliable results on cross-sections off neutrons, that would have to be included. Till now the calculations are just crude but can still give some indications, so a comparison is still interesting. A through explanation of nucleon resonance analysis in a coupled-channel approach is given in [17].

2.6. Cross-section

The cross-section is a measure of the probability of a certain reaction to take place. The rate W_r at which a specific reaction occurs in a scattering experiment with a beam hitting a stationary target is proportional to the number N of particles in the target and the rate per unit area at which the beam particles cross the target. The later rate is the so-called $flux$

$$J = n_b v_i \,, \tag{2.32}$$

where n_b is the density of particles in the beam and v_i is their velocity with respect to the target. Thus the rate W_r can be written as

$$W_r = JN\sigma_r \,, \tag{2.33}$$

where σ_r is the *cross-section* for the reaction r. The *luminosity* is then defined as

$$L \equiv JN \tag{2.34}$$

and it absorbs the dependence on the densities and geometry of the target and the beam, while the cross-section is independent of these factors. It is clear from eq. 2.33 that the cross-section has the unit of area and since it is typically a very small quantity it is usually expressed in *barns*, b, where 1 b = 10^{-28} m^2.

Written in a slightly different way the cross-section is

$$\sigma(E_\gamma) = \frac{N_{events}(E_\gamma)}{\varepsilon(E_\gamma) \cdot \xi \cdot N_\gamma(E_\gamma) \cdot \Gamma_{br}} \,. \tag{2.35}$$

In the case of ω photoproduction, $\mathrm{N}_{events}(E_\gamma)$ is the total number of ω events in the channel of interest in a certain window of incident beam energy of the photons, ε is the detection efficiency obtained from simulation, ξ is the target density (number of target nuclei/cm^2), $N_\gamma(E_\gamma)$ is the number of incident beam photons in the selected energy window and Γ_{br} is

the branching ratio of the chosen channel. The branching ratio is defined as the fraction of all decays leading to the selected final state. The relevant branching ratios are listed in table 2.4. The target density is calculated by

$$\xi = \frac{N_{av} \cdot \rho \cdot L}{A}\,, \tag{2.36}$$

where $N_{av} = 6.022{\cdot}10^{23} mol^{-1}$, ρ is the density of the target ([g/cm^3]), L is the length of the target and A is the atomic weight. The properties of the target used in this experiment are listed in table 3.1.

2.7. Differential cross-section

If the produced particles in the reaction are not isotropically distributed and the true angular distribution is unknown, the total cross-section has to be calculated from the integral of the differential cross-section, *i.e.*

$$\sigma = \int \frac{\mathrm{d}\sigma}{\mathrm{d}\Omega}\mathrm{d}\Omega\,. \tag{2.37}$$

The differential cross-section is proportional to the probability of the particle being produced in a certain solid angle $\mathrm{d}\Omega = \mathrm{d}\cos\theta\mathrm{d}\phi$ in the direction (θ,ϕ). The differential cross-section depends not only on the energy and the angle but also on the spin states of the particles involved. However, in most experiments the beam and target are unpolarized and the spin of the final state particles are not measured. In such cases there exists a perfect cylindrical symmetry around the beam axis and the *unpolarized cross-section* is independent of the ϕ angle. This is the case for the cross-sections discussed in this thesis and thus the total cross-section can be calculated from

$$\sigma = \int_{-1}^{1} \mathrm{d}\cos\theta \frac{\mathrm{d}\sigma}{\mathrm{d}\cos\theta}\,. \tag{2.38}$$

3. Experimental Setup

The experiment was performed in 2002-2003 at the ELectron-Stretcher-Anlage (ELSA) in Bonn, Germany. This chapter describes the production of the photon beam, the target and the detector system which detected the final decay products from the hadronic reactions produced in the target. The two major parts of the detector system were the Crystal Barrel (CB) and the Two Arm Photon Spectrometer (TAPS) and together they formed a near 4π solid angle coverage.

3.1. The accelerator

The ELSA facility delivered a beam of polarized or unpolarized electrons with an energy of up to 3.5 GeV. The electrons were produced by an ionic generator, the electron gun, at energies between 1 eV and 1 keV. They were subsequently accelerated by the LINAC (LINear ACcelerator) up to 20 MeV and then injected into the booster synchrotron for further acceleration up to 1.2 GeV. After that they were injected into the stretcher ring for the final acceleration up to 3.5 GeV. Figure 3.1 shows an overview of the accelerator. In the stretcher ring the electron bunches were also stretched out into a continuous beam. The maximum energy possible was 3.5 GeV, but for the data sets analysed in this work the electron energy was set to 2.6 GeV and 3.2 GeV. More details about the ELSA facility can be found in [24].

3.2. The beam line

The beam extracted from ELSA entered the experimental hall, hit a radiator (copper foil) and created Bremsstrahlung photons. The electrons that did not undergo Bremsstrahlung in the radiator were deflected out of the photon beam by a magnetic field and directed into the so-called beam dump. The beam dump was made out of lead, iron, boron carbide and polyethylene and had the purpose to absorb the electrons and shield the detectors from its reaction products. The electrons that did scatter in the radiator were even more deflected by the magnetic field (since they had lost some of their energy in the Bremsstrahlung process) and were detected by the tagging system where their position

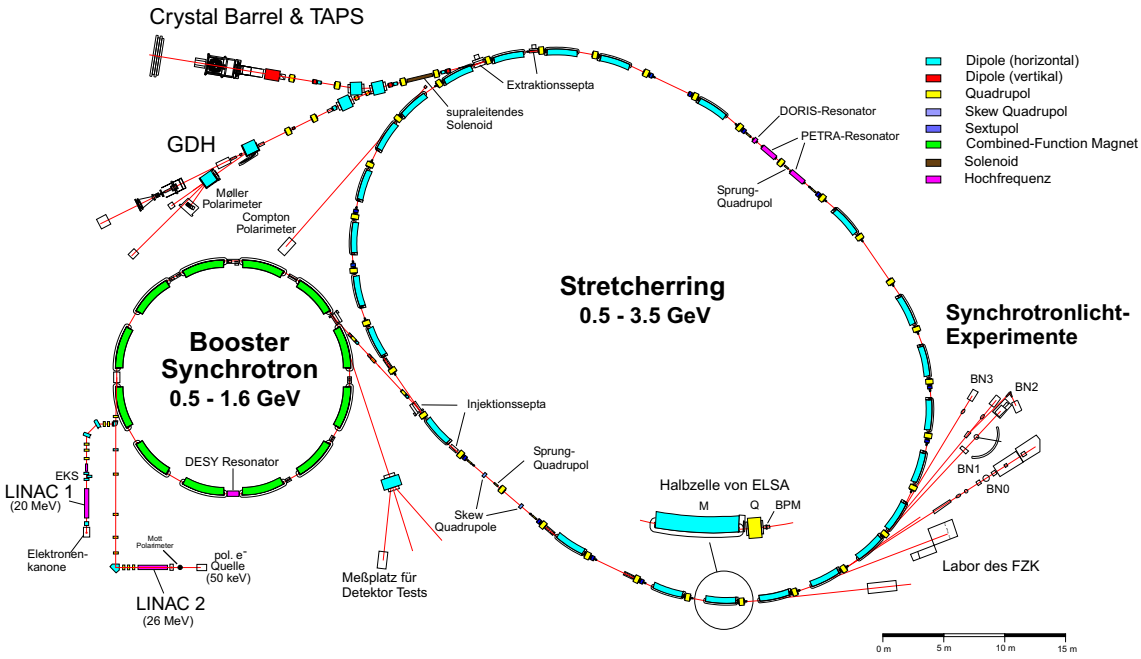

Figure 3.1: A schematic view of the ELSA electron accelerator in Bonn.

and time were measured. The Bremsstrahlung photons went in forward direction and hit the target, which was surrounded by the inner detector at the center of the CB, where possible interactions took place. Short-lived particles produced in the target decayed on their way to the detector where their decay products were registered. The photons that did not interact with the target were counted by the gamma veto at the end of the beam line and their number was used to estimate the flux. The gamma veto was also used for monitoring the position of the beam. A schematic layout of the beam line can be seen in fig. 3.2.

3.3. The tagging system

The photon beam produced by Bremsstrahlung processes in the radiator has an energy spectrum that was, in first approximation, given by $\Phi \propto 1/E_\gamma$. The time and energy information of the recoil electrons, E'_e, was extracted by the tagging system, placed in the focal plane (see fig. 3.3). Combined with the information of the energy of the electron beam when extracted from the stretcher ring, E_e, the energy of the photons, E_γ, could be

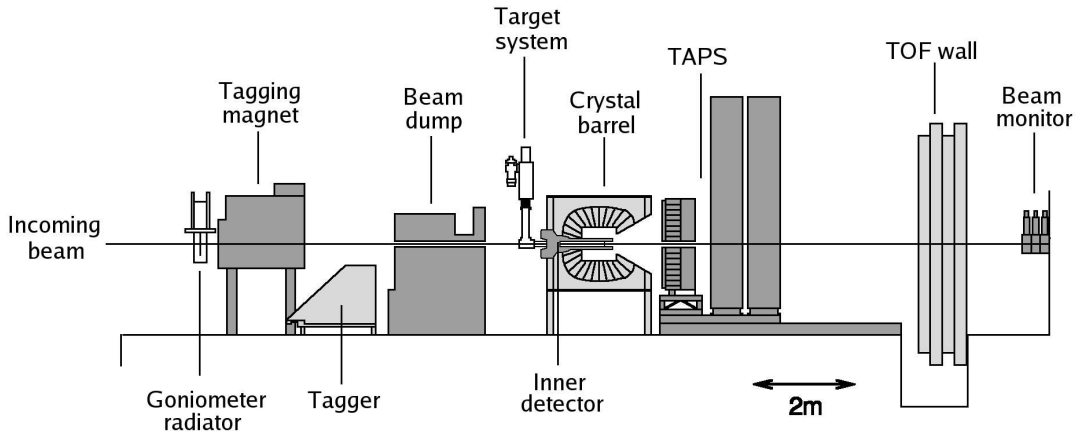

Figure 3.2: The setup of the CB/TAPS experiment. The beam was coming from the left. The different detector components are described in the text.

calculated on an event-by-event basis according to

$$E_\gamma = E_e - E'_e \,. \tag{3.1}$$

The tagging system consisted of 14 overlapping plastic scintillator bars read out by photomultipliers on both ends of each bar. To improve the energy resolution a scintillating fiber detector was added in front of the bars in the region where the energy of the deflected electrons was highest. The scintillating fiber detector consisted of two layers of 240 fibers each. The two layers were positioned in an offset manner so that each fiber partly overlapped with two fibers in the other layer. The bars covered an electron energy region of 22% to 92% of the incoming electron energy. For the scintillator fiber detector the covered region was 18% to 80%. A proportional wire chamber was also installed at the lower electron energy side, but this was not in use for obtaining the data analysed in this work, since the energy region covered was outside the region of interest. For a detailed description of the tagging system see [25].

3.4. The target

The target was of cylindrical shape with a length of 5.275 cm and a radius of 1.5 cm and made out of a kapton foil with a thickness of 0.625 mm. For this work the target was

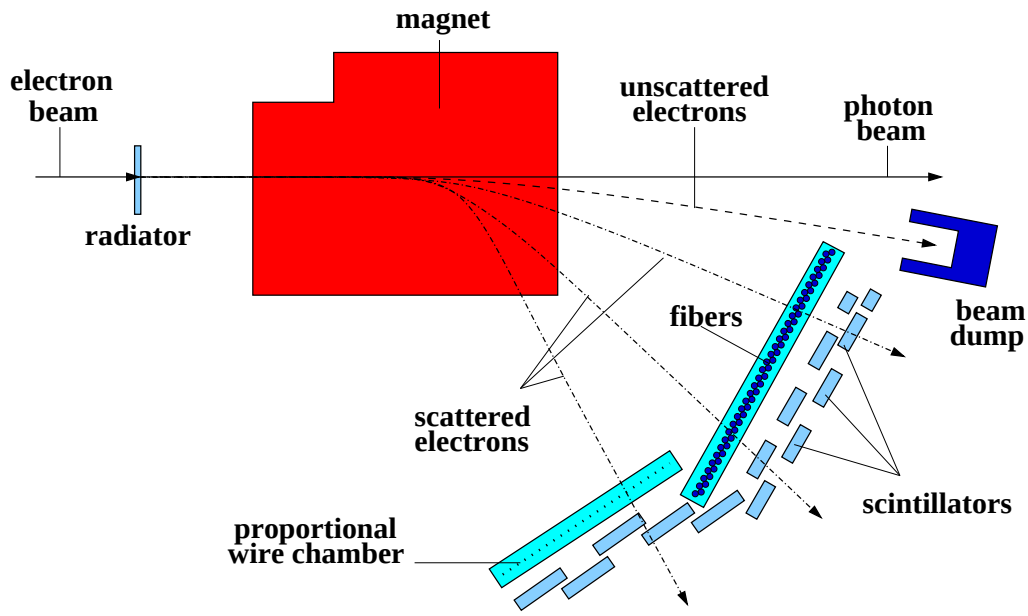

Figure 3.3: The Tagging system. The e^--beam generated photons through the Bremsstrahlung process in the radiator. The scattered electrons were bent by the magnetic field and registered by the tagger consisting of a proportional wire chamber, scintillating bars and fibers. More details are given in the text.

filled with either liquid hydrogen (LH_2) or liquid deuterium (LD_2). The properties of both targets are listed in table 3.1. The target was situated inside the aluminum beam pipe surrounded by the Crystal Barrel and it was cooled by a heat exchanger. More details about the target can be found in [26].

Target	Length [cm]	Density ρ [g/cm^3]	Density ξ [cm $^{-2}$]	Atomic weight [u]
LH_2	5.275	0.071	2.24×10^{-23}	1.008
LD_2	5.275	0.169	2.67×10^{-23}	2.014

Table 3.1: Target properties. The target density ξ has been calculated according to eq. 2.36.

3.5. The CB/TAPS detectors

The CB/TAPS detector system collected information about the decay particles, originating from the reaction of the Bremsstrahlung photons with the target, and the recoil nucleons/nuclei. The parameters that were directly measured by the detectors were time, position and energy. From these values the reaction in the target could be identified and the original meson could be reconstructed and its momentum and energy calculated.

Material		BaF_2 (TAPS)	CsI(Tl) (CB)
Density [g/cm^3]		4.89	4.53
Radiation length X_0 [cm]		2.05	1.86
Crystal length [cm]		$25 \approx 12X_0$	$30 \approx 16X_0$
Molière radius [cm]		4.3	3.8
Fast component	decay time [ns]	0.6	0.9 and 7000
Light Yield [photons/MeV]		1430	51800
Maximum emission:	wavelength [nm]	195 and 220	550
Slow component	decay time [ns]	620	
Light Yield [photons/MeV]		9950	
Maximum emission:	wavelength [nm]	320	

Table 3.2: Properties of the scintillating materials BaF_2 and CsI(Tl). While BaF_2 has two scintillating light components with different decay times, CsI(Tl) only has one. The radiation length X_0 corresponds to the length in which the energy of an electron is reduced by a factor 1/e due to radiation losses. Two Molière radii (in the transverse direction) contain more than 90% of the shower energy.

3.5.1. Crystal Barrel (CB)

The Crystal Barrel is an electromagnetic calorimeter consisting of 1290 CsI crystals, doped with thallium in order to increase the light yield (the number of generated photons per MeV deposited energy in a scintillating material). The properties of CsI(Tl) as a scintillator are listed in table 3.2 (as well as the properties for BaF_2 which was the material used in TAPS). Its main purpose was to detect photons in an energy range from 20 MeV to 2 GeV with good energy and spacial resolution. The energy resolution was given by

$$\frac{\sigma_E}{E} = \frac{2-3\%}{\sqrt[4]{E/GeV}} \tag{3.2}$$

and the spacial resolution was 20 mrad (40 mrad for the backward rings). The crystals were arranged in a barrel shape covering polar angles from 30° to 168°, with all crystal modules facing the vertex with a mean distance to the target of 300 mm. They were ordered in 23 rings of 60 crystals and each crystal module (see fig. 3.4) was surrounded by a kapton foil for electrical isolation and mounted in a titanium case for mechanical stability. The crystals were approximately 30 cm long and were read-out by photodiodes attached to the end surface with a 3 mm plexiglas sandwiched in-between, to improve the light transfer from the crystal to the somewhat smaller sensitive area of the photodiode. A light pulser system was connected to each crystal in order to monitor the stability of the gain of the crystal. The cross-section and a photo of the CB detector can be seen in fig. 3.5. For more details about the crystal barrel read [27].

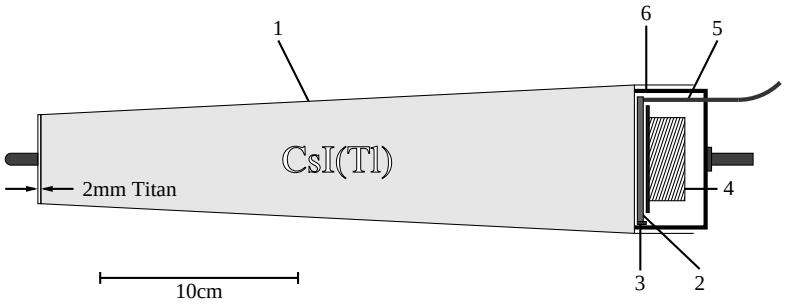

Figure 3.4: cross-section of a CsI(Tl) module of the Crystal Barrel: (1) titanium housing, (2) wavelength shifter, (3) photodiode, (4) preamplifier, (5) optic light fiber, (6) case cover.

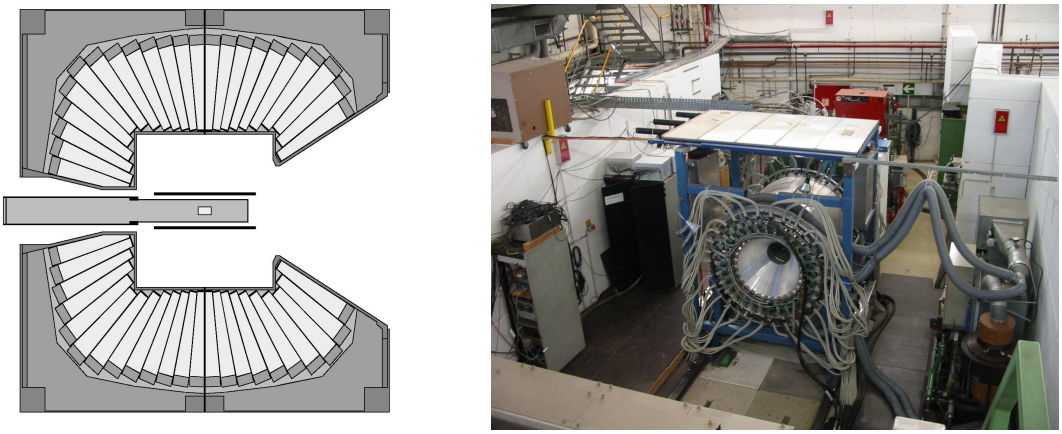

(a) cross-section (b) photograph

Figure 3.5: The Crystal Barrel (CB) detector. The target was situated at the center of the detector surrounded by the inner detector (used for charged particle identification).

3.5.2. The inner detector

The inner detector (depicted in fig. 3.6) was placed between CB and the target and it was used for identification of charged particles [28]. It consisted of three layers of scintillating fibers with a thickness of 2 mm. Each layer was oriented at an angle to the others in such a way that it was possible to obtain all three spatial coordinates of a charged particle crossing the detector. The outer layer had a diameter of 128 mm and consisted of 191 fibers. The middle layer contained 165 fibers oriented at an angle of +25° with respect to the outer layer. The innermost layer had a diameter of 116 mm and consisted of 157 fibers oriented at an angle of -25°. The three layers were mounted in an epoxy composite cylinder of 0.8 mm thickness for support. The inner detector covered a region of polar angles from 28° to 172°. The energy deposition was not measured with this detector, only the position and time information of charged hits were registered.

3.5.3. The Two Arm Photon Spectrometer (TAPS)

The TAPS detector is an electromagnetic calorimeter made out of 528 BaF_2 crystals. It was designed to detect photons over a wide range of energies, from a few MeV up to a few GeV. But it is also capable of detecting charged mesons and recoil nucleons. The crystals are of hexagonal shape with a length of 250 mm (12 radiation lengths) and a cone

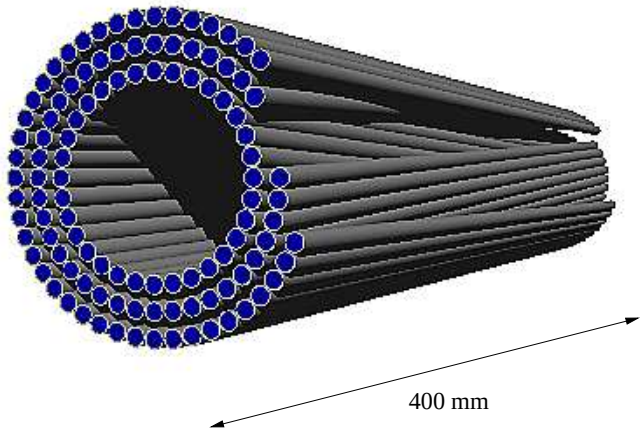

Figure 3.6: The inner detector for charged particle identification, consisting of three layers of scintillating fibers.

diameter of 59 mm (the last 25 mm have a cylindrical shape in order to facilitate the connection to the photomultiplier) and they were assembled in a hexagonal wall according to fig. 3.7. This arrangement made it possible to obtain a better spacial resolution than what was given by the width of the crystals, because the energy of the particles were deposited in several crystals in a so-called *cluster*[1] and through weighting, the true (within the resolution) position could be calculated. The position resolution was found to be 20 mm for 790 GeV photons and the energy resolution was given by $\sigma_E/E = 3\%/\sqrt{E/GeV}$ [29]. TAPS was positioned at 1.18 m distance from the target in forward direction in order to fill the hole of the Crystal Barrel. It covered a region of polar angles from 5° to 30°.

Each crystal was wrapped in 8 layers of 38 μm PTFE and one layer of aluminum foil as a reflector and coupled optically to a photomultiplier (Hamamatsu R2059-01). The photomultiplier converted the light generated in the crystal into charge and multiplied it. In order to get the required mechanical support, the crystal and the base of the photomultiplier was covered by a 0.2 mm thick light-tight PVC tube. A schematic view of a TAPS module is shown in fig. 3.8 and the scintillating properties of BaF_2 are listed in table 3.2. For more details see [30].

[1] The largest possible group of adjacent crystals with a registered energy above the CFD threshold.

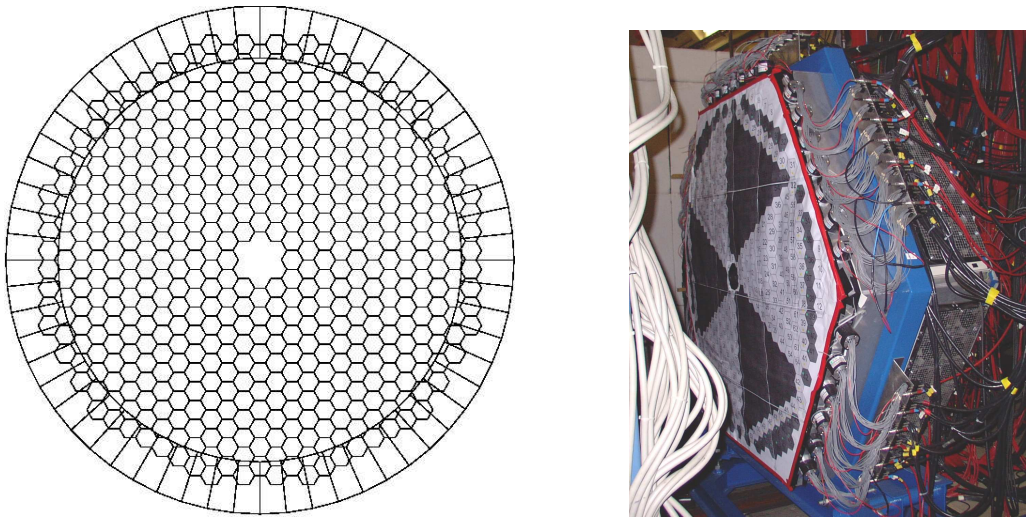

(a) schematic view (b) photograph

Figure 3.7: The TAPS detector.

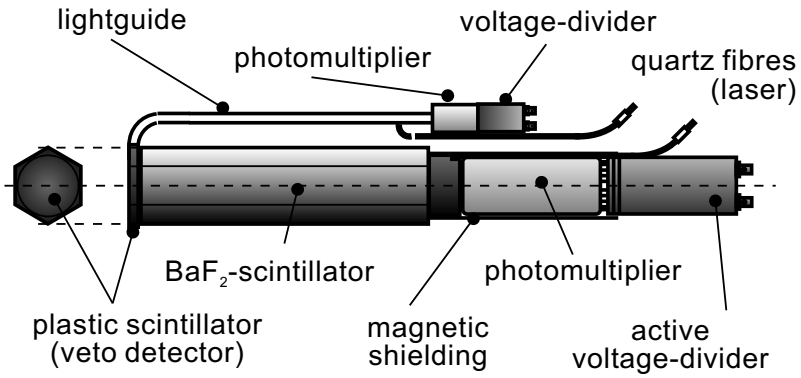

Figure 3.8: Schematic view of a TAPS module, which consists of a BaF_2 crystal with a plastic scintillator in front, both being read-out by photomultiplier tubes. The crystal has a length of 25 cm with a diameter of 5.9 cm

3.5.4. The veto wall

Placed in front of each crystal in TAPS was a plastic scintillator (NE 120A) of hexagonal shape, with the same diameter as the crystals and a thickness of 0.5 cm [31]. The plastic scintillators were sensitive only to charged particles and could therefore be used as a veto on those. To each veto detector a light fiber guide was attached to transport the generated light to the photomultipliers mounted at the side of TAPS. See fig. 3.9 for a photo of one veto plastic scintillator with attached optical fiber.

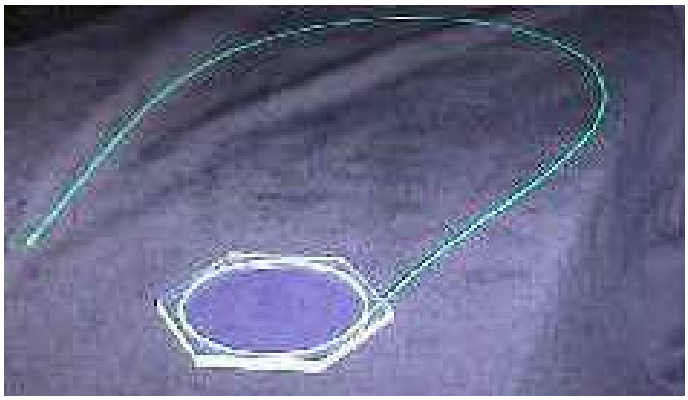

Figure 3.9: Photo of one Veto detector element, a 5 mm thick hexagonal plastic scintillator with the attached fiber which collected the light and transported it to the photomultiplier.

3.5.5. Beam monitor

In order to determine the total cross-sections, information about the flux of photons hitting the target is needed. This number was not equal to the number of electron hits in the tagger, since there could also be accidental hits plus the fact that only the photons passing the collimator would reach the target. For this reason a gamma veto detector was installed at the end of the beam line (see fig. 3.2) consisting of 9 lead glass crystals. The gamma veto registered those photons that did not undergo any reaction with the target. Since rates of a hadronic reaction in the target are extremely small the gamma veto rate could be taken to be the flux. The gamma veto was also used to monitor the position of the beam in order to check the alignment.

3.6. Particle interactions with detector material

The decay particles entering the detector loose energy in the detector material in different reactions depending on the type of particle. Here follows a list of the main processes occurring when particles pass through matter.

- **Charged hadrons** (protons): Loose their energy primarily through ionization. However, elastic scattering and nuclear reactions also contribute.
- **Neutral hadrons** (neutrons): Since there is no electric charge present, there is no Coulomb interaction, therefore they loose their energy through strong interactions with the target nuclei. There are various different nuclear processes possible depending on the energy of the neutrons. For low energy neutrons (below 1 MeV) the main processes are elastic scattering, radiative neutron capture and absorption. At higher energies nuclear reactions creating charged particles occur and at energies above 100 MeV hadronic showers can be formed.
- **Photons (and electrons):** High energy photons entering the detector material create electron-positron pairs (pair-production) which in turn generate photons by the Bremsstrahlung process. These photons generate new electron-positron pairs which produce further Bremsstrahlung photons. These two processes alternate and result in a cascade in the material called *electro-magnetic shower* which continues until the electrons/positrons are not energetic enough to further produce Bremsstrahlung photons, but instead loose their energy through atomic collisions.

A more detailed account of the passages of particles through matter and the processes governing their energy losses can be found in [32].

3.7. Data acquisition

This section describes the handling of the electronic signals from the different detector parts and the decision-making of which data will be stored on disc, the so-called *triggering*.

3.7.1. The tagging system

Each of the 480 wires in the tagging system were connected to Constant-Fraction Discriminators (CFDs) positioned close to the tagger. The resulting logic signals were taken outside of the experimental hall through delay cables and passed through a passive splitter. Then the signals were fed into a multi-hit Time to Digital Converter (TDC), with a

resolution of 64 ps/ch, and into a scaler. A coincidence between an electron in the tagger and a hit in the CB/TAPS detector system signals that a photo reaction in the target took place. The TDCs were operated in common stop mode and a signal from the CB/TAPS was used as a stop. The TDCs were read out only when this coincidence condition was fulfilled. Scalers were read out without this coincidence requirement. The TDCs and scalers were mounted on top of CATCH (COMPASS Accumulate Transfer and Control Hardware) boards that were readout via a VME interface [33]. The signals from the bars (two from each bar) were fed through delay cables and read by standard TDCs, QDCs (Charge to Digital Converters) and scalers. A logic AND was constructed to count the hits in the overlapping region between two bars.

3.7.2. Crystal Barrel electronics

The CB electronics recorded the deposited energy in all modules for each event. The signals from the CB photodiodes were passed through shapers and were integrated by QDCs in two different energy ranges. The QDCs contain two capacitors and the incoming signal was split between them in a ratio of 1 to 8. The internal logic then decided which charge would be digitized. If the signal was small the charge on the capacitor with the largest charge was used and if the signal was large the smaller charge on the other capacitor was integrated. In this way, the two capacitors cover two different energy ranges, up to 200 MeV and up to 2 GeV, respectively. The selected range was digitized in 12 bits and an additional bit was set to specify which range was selected. The QDCs were read out by VMCI compatible boards running Linux. The interface VME backplane was accomplished via a Tundra Universe PCI-VME interface. There were two such modules, one for the upstream half of CB and one for the downstream part. The two VMCI computers each build their sub-event that was then sent via TCP/IP to a central event builder. More details can be found in [34]

3.7.3. The inner detector electronics

The inner detector recorded the time and position of charged particles. The signals from the photomultipliers were sent to trigger electronics inside the experimental hall where the number of layers hit were used to trigger on charged events. The signals were then taken out of the experimental hall and fed into TDCs.

3.7.4. TAPS electronics

The TAPS electronics recorded the deposited energy and the time in all modules for each event. A diagram of the TAPS electronics can be seen in fig. 3.10. The signals from the BaF_2 modules were split 4-fold by active splitters close to the TAPS wall. Two of these signals were used to generate the TAPS pre-trigger and were fed to two Leading-Edge Discriminators (LED low and LED high). The LED low and high were set differently according to the position of the BaF_2, *i.e.* in which ring it was positioned. The calibration of the LEDs were done by checking for each ring where the discriminators cut off the calibrated energy spectrum. The third signal was used for timing purposes and was fed into a CFD. The CFD thresholds were set to 20 mV which corresponds to an energy of 15 MeV. Only detectors with a registered energy above this threshold were read out.

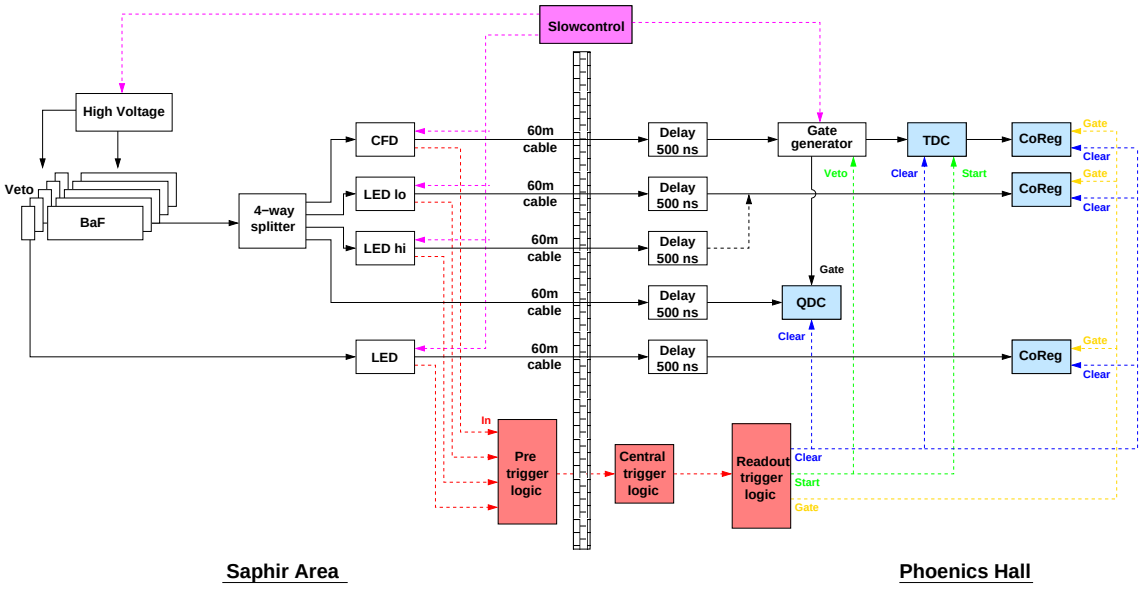

Figure 3.10: Schematic drawing of the TAPS read-out electronics.

The forth signal was the analogue signal with the energy information. It was delayed with 60 m of cable and a 500 ns delay box (to allow enough time for the trigger to be formed) and was then fed into a QDC. There, it was integrated over a short gate (50 ns) and a long gate (2 μs) which made it possible to distinguish between different types of par-

ticles that give different pulse shapes. The time gates for the integrations were generated by a gate-generator (RDV) which was started by a signal from the CFDs. The voltage on the photomultipliers were set so that the dynamic range was 2400 MeV, which gave 0.6 MeV/channel.

The time was measured by TDCs which were started by the trigger and stopped by the CFDs. In this way the time of flight of the particles was measured and the resolution was such that it was possible to distinguish between photons and nucleons, which have a difference in flight time of 3 ns to 10 ns, respectively. For more details see [35].

3.7.5. The veto wall electronics

The signals from the Veto photomultipliers were fed to LEDs and a Veto was said to have fired when the logic signal was above the LED threshold. This was recorded by a pattern unit.

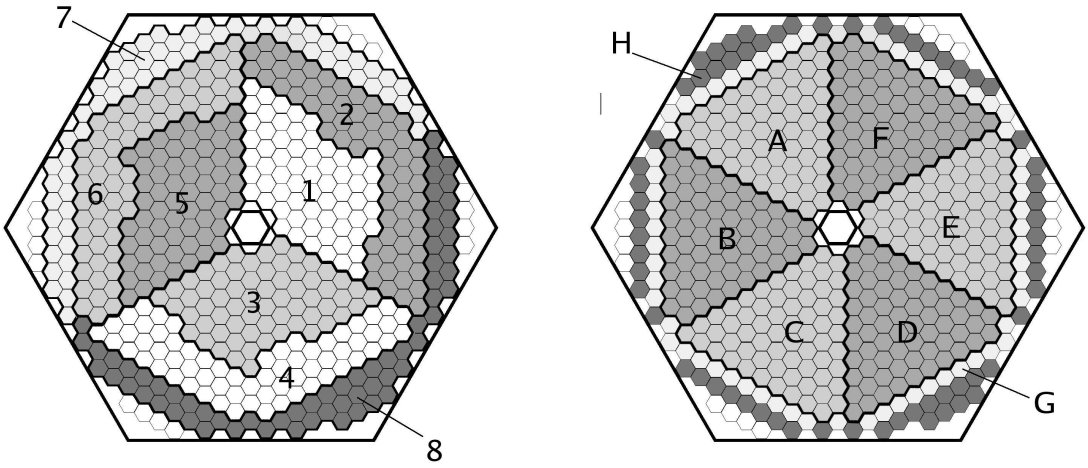

(a) LED low multiplicity 2 pre-trigger

(b) LED high multiplicity 1 pre-trigger

Figure 3.11: Segmentation of the TAPS detector for the first-level triggers (or *pre-triggers*) [35].

3.8. Trigger

Since the data acquisition system was not fast enough to record everything that was seen by the detectors and because many processes that took place in the target were not of interest to this particular experiment, there had to be a way of selecting interesting events on-line. This was done by the trigger system. For this experiment it was built in two stages, the first-level trigger that has to be very fast (less than 300 ns) and the second-level trigger that could take a bit longer time and thus be more complex. The first-level trigger decided whether an event was interesting enough to start the digitization of the measured data. Because of the speed requirement, only TAPS, which was read out by fast photomultipliers, was used for the first-level trigger, the photodiodes of the CB had a too long rise time (2 μs) for this purpose. The second-level trigger was formed during the digitization time and could thus also include information from the CB. It decided whether an event should be read out and stored.

3.8.1. First-level trigger

The first-level trigger was based solely on the information coming from TAPS, which was divided into segments and three different triggers were defined according to the number of hits (above LED-low and/or above LED-high) in these segments.

- `LED-low mult 2:` At least two hits above the LED-low threshold in different sectors shown in fig. 3.11(a). The logic for this trigger can be seen in the lower branch in the diagram in fig. 3.12.
- `LED-low OR:` At least one hit above the LED-low threshold (see the upper branch in the diagram in fig. 3.12. This trigger was down-scaled.
- `LED-high OR:` At least one hit above the LED-high threshold. The segmentation for LED-high was different than for LED-low and can be seen in fig. 3.11(b). Due to a lack of LED modules some detectors did not have a LED-high module. For these detectors the information from the LED-low had to be used. The detectors with only LED-low modules were the outer crystals corresponding to segments 7 and 8 in fig. 3.11(b). The logic of this pre-trigger is drawn in fig. 3.13.

If any of these three requirements were fulfilled the digitization of the event was started.

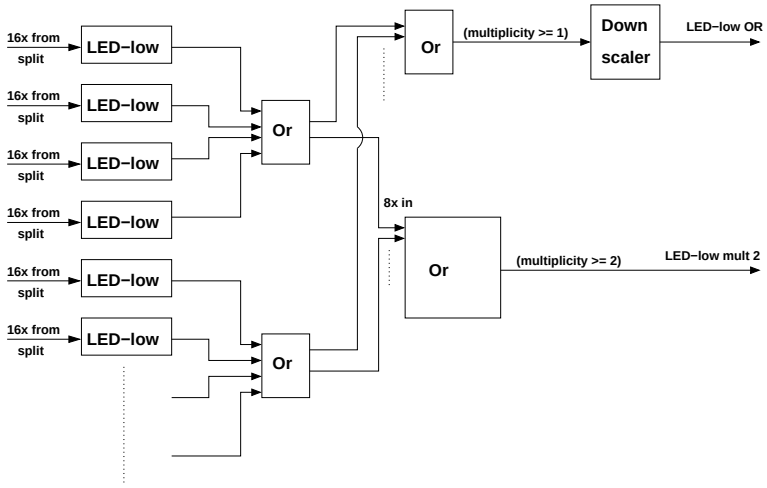

Figure 3.12: Diagram of the LED-low pre-trigger [35]. Each LED module was connected to 16 detectors. An OR was built in between 4 LEDs according to the eight segments shown in fig. 3.11(b). The multiplicity of hits in different segments were used to form the pre-triggers.

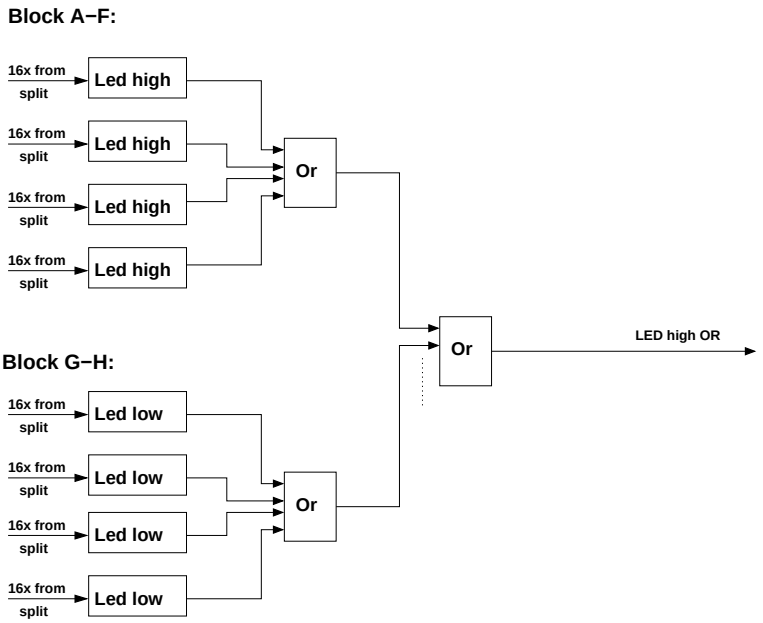

Figure 3.13: Diagram of the LED-high OR pre-trigger [35]. Multiplicities of 1 or higher were selected.

3.8.2. Second-level trigger

In the second-level trigger the information from the CB could also be used. This was done by the FAst Cluster Encoder (FACE) which counted the number of clusters in CB. The trigger requirements for the different second-level triggers used were:

- `facetest2new:` At least two clusters in CB and one LED-high hit OR two LED-low hits (without any further requirement on hits in the CB).
- `t2onosifi:` At least one cluster in CB and one LED-high hit OR two LED-low hits (without any further requirement on hits in the CB).

If either of these conditions corresponding to the selected trigger were fulfilled the data was read out and stored for further processing. Table 3.3 lists the selected triggers with the corresponding runs.

It should be noted that two other types of triggers were also used during the beam time. Firstly, `taggeror` which had the only requirement that at least one electron has to have fired the tagger. This trigger was used in order to calculate the tagging efficiency and consequently the incoming photon flux. Secondly, there was a trigger used when measuring cosmic radiation for debugging and calibration purposes. For this trigger the requirement was set to be at least one hit above the CFD threshold for any detector module in TAPS.

3.9. Beam time overview

Table 3.3 lists important information, such as running time, beam energy, collected number of events and which trigger was used, for the beam times with LH_2 and LD_2 targets, which were the beam times analysed for this thesis.

Target	Date	$E_{e^-}[GeV]$	Hours	No. of events	trigger
LH_2	2002/10-31 – 2002/11/15	3.2	200	326.094.892	t2onosifi
LD_2	2003/07/18 – 2003/08/18	2.6 pol.	340	561.948.781	facetest2new

Table 3.3: Overview of the analysed beam times with LH_2 and LD_2 targets. The term "pol." refers to a linearly polarized beam.

4. Calibration

The data acquisition provided raw-data which have to be calibrated in order to get the information in physical units, energy in MeV and time in ns. Due to unstable temperature in the experimental hall (which for example affects the light yield of the crystals) and aging of the electronics, a new calibration had to be done each day.

4.1. The tagging system

The tagging system was used to determine the energy of the incident photon beam reaching the target. In order to do that, both energy and time had to be calibrated for the tagging system.

4.1.1. Energy calibration

The energy calibration was necessary in order to find the relation between fiber number in the tagging system and the energy in MeV of the Bremsstrahlung photons. The energy of the recoil electron E_{e^-} is related to its hit position in the tagger which in turn depends on the momentum of the electron (p) according to

$$E_{e^-} = pc = q_{e^-} B\rho c\,, \tag{4.1}$$

where B is the magnetic field and ρ is the radius of the trajectory. Since B and ρ are known, the energy of the electron can be calculated and thus the energy of the photon through

$$E_\gamma = E^0_{e^-} - E_{e^-}\,, \tag{4.2}$$

where $E^0_{e^-}$ is known from the accelerator.

The calibration was done by inserting a low-intensity electron beam with known energy and scan over the tagging fibers by adjusting the magnetic field of the tagging magnet. A more detailed account of this calibration method can be found in [36]. As a check, a second calibration method was used which implied inserting a beam with different energies directly into the tagging system. This was done for four different energy settings and a

calibration function of fourth order was determined [9]. A discrepancy between the two calibration methods of up to 30 MeV for the lowest photon energies was observed. Therefor, a third calibration procedure had to be carried out. It made use of the fact that for a linearly polarized beam, where the angle of the crystalline radiator is known, it is possible to calculate the exact energy of the coherent peak [37]. The later two methods agreed within errors, thus they gave a second order polynomial which was used as correction to the fourth order polynomial obtained from the first method. For more detail see [38].

In this experiment two different beam energies $E^0_{e^-}$ were used, 2.6 GeV for the LD_2 beam time and 3.2 GeV for the LH_2 beam time. The magnetic field was adjusted in such a way that when no Bremsstrahlung process took place the electron trajectory was the same for the two different beam energies. Thus

$$E_\gamma^{2.6GeV} = \frac{E_{e^-}^{2.6GeV} E_\gamma^{3.2GeV}}{E_{e^-}^{3.2GeV}} . \tag{4.3}$$

Figure 4.1 shows the relationship between the beam energy [MeV] and the tagger fiber hit after calibration for the LD_2 beam time and the LH_2 beam time.

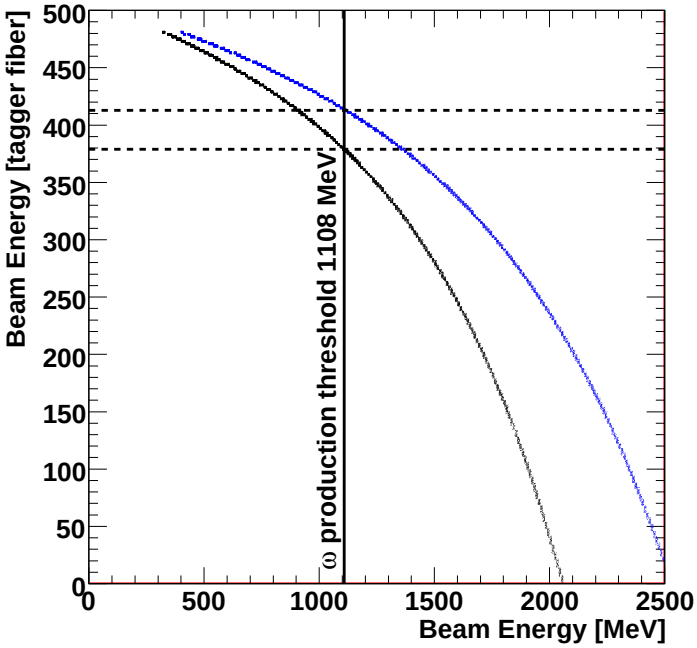

Figure 4.1: Relationship between the photon beam energy [MeV] and the tagger fiber hit for the LD_2 beam time (black), where $E_{e^-} = 2.6$ GeV, and LH_2 beam time (blue), where $E_{e^-} = 3.2$ GeV.

4.1.2. Time calibration

The time calibration of the tagger was performed after the TDC calibration of TAPS was done and the time difference between each tagger fiber and TAPS was set to be zero. The tagger TDCs were started by the detection of an electron and stopped by the trigger

$$TaggerTDC = trigger - electron \tag{4.4}$$

The TAPS TDC was started by the trigger and stopped by the TAPS CFD

$$TAPS\ TDC = photon - trigger \tag{4.5}$$

These two equations together give

$$TaggerTDC + TAPS\ TDC = photon - electron \tag{4.6}$$

Figure 4.2 (left) shows the time difference between detecting a photon in TAPS and an electron in the tagging system versus tagging fiber number after alignment. Figure 4.2 (right) shows the same time difference summed over all tagging fibers. The prompt peak in this time spectrum defines a true reaction in the target and selects the electron that created the photon that induced it, in order to get the correct value of the incident beam energy. The time resolution of the fibers was found to be 2 ns (FWHM), which is worse than the TAPS resolution.

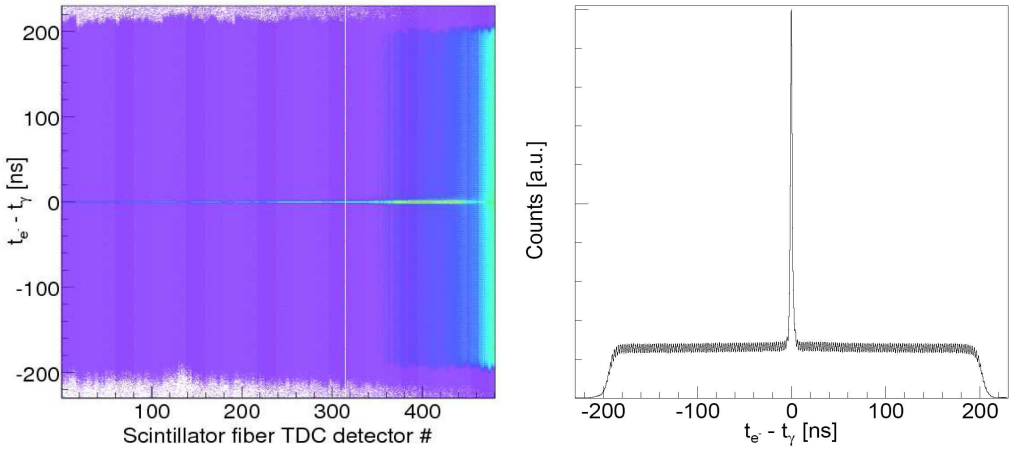

Figure 4.2: Left: The time difference between a photon in TAPS and an electron registered in the tagging system as a function of tagger fiber number. Right: The same time difference summed over all tagging fibers.

4.2. Crystal Barrel

For the CB, only the energy needed to be calibrated. No time information is taken from the CB because of the slow read out of the photodiodes, as discussed in sect. 3.8.

4.2.1. Energy calibration

It has been shown that the response of the crystal modules is linear to the deposited energy according to:

$$energy = gain * (channel - pedestal) \tag{4.7}$$

The gain factor was calculated in the low energy regime by π^0 invariant mass and in the higher energy range the calibration was done by injecting laser light with different known energies into the crystals. The pedestal is the channel with zero energy which can be seen as a sharp peak (originating from noise) at the very beginning of the spectrum.

Figure 4.3 shows the invariant mass of two photons detected in the Crystal barrel after calibration. The π^0 and η peak can be seen at 135.9 MeV and 545.6 MeV, respectively, with an accuracy of $\pm 1\%$. A more detailed description of the energy calibration can be found in [39].

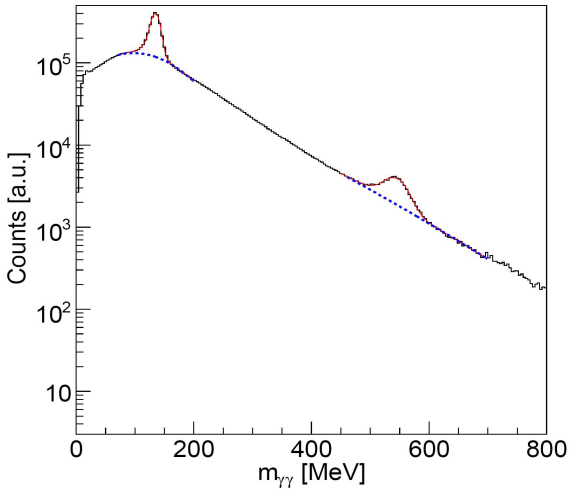

Figure 4.3: The invariant mass spectrum of two photons detected in CB after calibration. The π^0 and η peak can be seen at 135.9 MeV and 545.6 MeV, respectively.

4.3. The inner detector

For the inner detector only time had to be calibrated. The TDC signals were aligned to each other online. In the offline analysis a gate was placed around the peak in the TDC spectra to identify that a fiber was hit.

4.4. TAPS

For the TAPS detector both energy and time had to be calibrated.

4.4.1. Energy calibration

The energy calibration of TAPS was done in three stages. First with cosmic muons for a rough calibration, during the experiment the position of the pion peak was monitored to improve the calibration and as a last check the η peak position was checked in order to get the energy dependence (which was non-linear due to shower leakage) of the calibration to be able to extend it to higher energies.

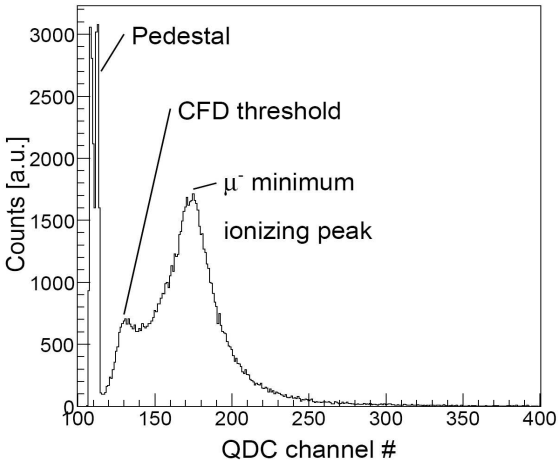

Figure 4.4: A cosmic ray energy spectrum in TAPS showing the pedestal (0 MeV energy peak) and the cosmic muon peak corresponding to 38.5 MeV.

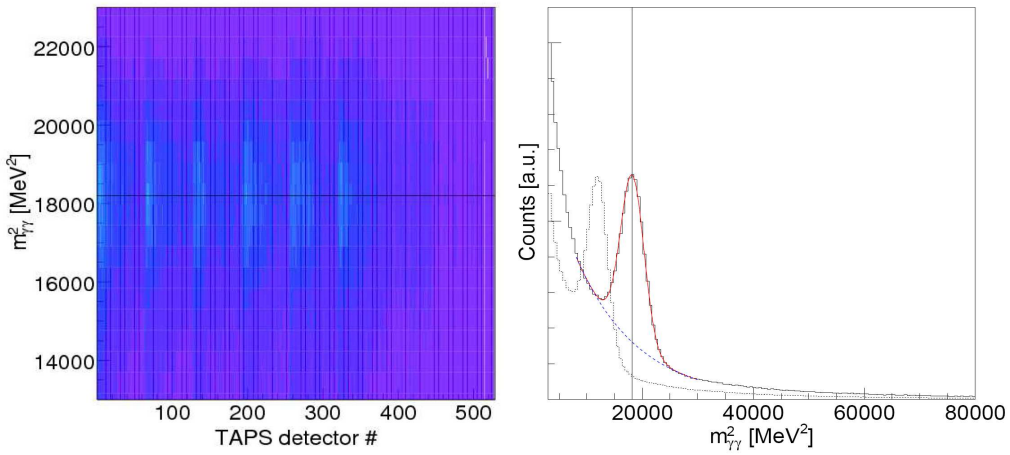

Figure 4.5: Left: The invariant mass squared spectrum of two photons detected in TAPS versus the detector number. Right: The same invariant mass squared summed over all TAPS modules before (dotted line) and after (solid line) the second stage correction.

Cosmic muon calibration

Cosmic data were taken at the beginning of each data taking period. Since the dimensions and orientation was the same for all TAPS crystals and since the cosmic muons are minimum ionizing, their energy loss in the crystal only depends on the length of the track through the crystal, the energy deposition was on average 38.5 MeV for all crystals [40]. This peak position with corresponding energy and pedestal position together with eq. 4.7 gave the relation between channel and energy for the calibration. In fig. 4.4 an example of a cosmic ray energy spectrum can be seen. The cosmic muon calibration is, however, only valid for cosmic rays and not for photons since there is a difference in the efficiency to create scintillation light in the BaF_2 between the two. Therefore, a second calibration stage was needed.

π^0 invariant mass calibration

With the π^0 invariant mass calibration a correction factor was calculated and used to put the π^0-peak in the correct position. The channel used was $\pi^0 \rightarrow \gamma\gamma$. Hence, at least two neutral hits in TAPS were required and the invariant mass of all possible combinations was formed. The invariant mass is given by

$$m_{\gamma 1 \gamma 2} = \sqrt{E_{\gamma 1} E_{\gamma 2} (1 - cos\theta_{1,2})}\,, \tag{4.8}$$

where $E_{\gamma 1}$ and $E_{\gamma 2}$ are the measured photon energies (central detector added with neighboring detectors) and $\theta_{1,2}$ is the opening angle between the two photons. This calibration procedure is iterative and had to be repeated with the latest calculated gain until the $\gamma\gamma$ invariant mass converged to the π^0 mass for all modules. Figure 4.5 shows the invariant mass squared of two photons in TAPS before (dotted line) and after (solid line) the second stage correction. For more details see [41].

η invariant mass calibration

The purpose of the $\eta \rightarrow \gamma\gamma$ invariant calibration was to correct for any possible non-linearity that could occur at higher energies. Indeed, when the $\gamma\gamma$ invariant mass spectrum was extended beyond the η mass region is was seen that while the π^0 peak was sitting at the correct position the η peak was shifted by $\approx$10 MeV. This can be explained by shower leakage below the CFD threshold to neighboring detectors which depends on the energy of the photon [42]. Both the η-peak and the π^0-peak was checked and the new corrected energy of the photons was calculated according to

$$E_{new} = a + bE_{old} + cE_{old}^2\,, \tag{4.9}$$

where a is the peak position of the pedestal a = 0 MeV, and

$$c = (1 - m_{\pi 0}/M_\eta)/(m_{\pi 0} - m_\eta) \tag{4.10}$$

and

$$b = 1 - (m_{\pi^0} * c)\,. \tag{4.11}$$

M_η is the measured position of the η-peak, m_{π^0} = 134.98 MeV and m_η = 547.75 MeV. The correction factors were determined for each data taking period.

As for the π^0 invariant mass calibration, also this calibration stage was iterative and several iterations had to be made before the peaks were at a position of $\pm$1% from the correct one. Figure 4.6 shows the invariant mass of two photons in TAPS before (dotted line) and after (solid line) the energy dependence correction. The π^0 and η peak can be seen at 134.7 MeV and 566 MeV before correction and at 134.75 MeV and 553 MeV after correction, respectively. As expected, the π^0 peak was hardly affected by this third calibration procedure, for the η peak, on the other hand, a clear shift can be seen.

4.4.2. Pulse-shape calibration

The scintillation mechanism in BaF_2 works in such a way that there are two different components (one fast and one slow) of the light produced with different intensities depending

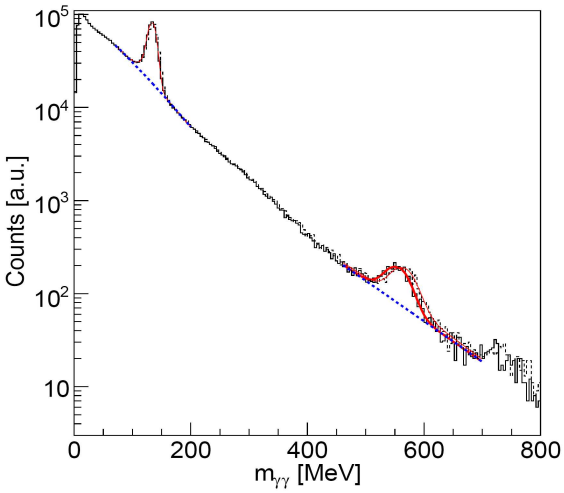

Figure 4.6: The invariant mass spectrum of two photons detected in TAPS before (dotted line) and after (solid line) the energy dependence correction. The π^0 and η peak can be seen at 134.7 MeV and 566 MeV before correction and at 134.75 MeV and 553 MeV after correction, respectively.

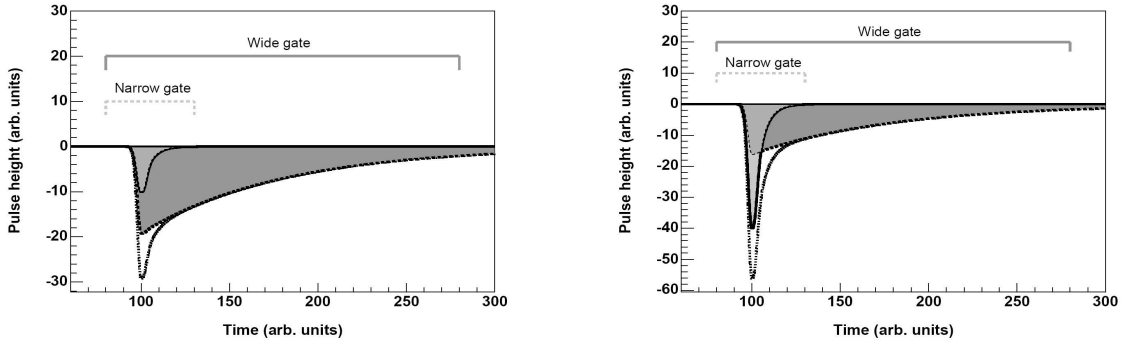

Figure 4.7: Schematic picture of the pulse-shape of protons (left) and of photons (right) in TAPS.

on the type of particle creating it. This makes it possible to distinguish between types of particles due to their pulse shape. Electronically, this is done by integrating the charge on the BaF_2 anode with two different time gates, 50 ns and 2 μs giving E_{narrow} and E_{wide}, respectively. Figure 4.7 shows a schematic figure of the pulse shape for protons (left) and photons (right) in TAPS.

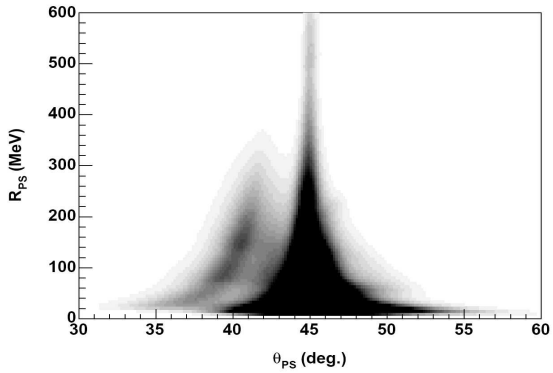

Figure 4.8: The pulse-shape spectrum in polar coordinates after calibration. The band at 45 ° are photons and the band to the left are protons.

Each event can be described by polar coordinates

$$\theta_{PS} = arctan\Big(\frac{E_{narrow}}{E_{wide}}\Big) \tag{4.12}$$

$$R_{PS} = \sqrt{E_{narrow}^2 + E_{wide}^2}\,. \tag{4.13}$$

Figure 4.8 shows a pulse shape spectrum in polar coordinates after calibration. The photons can be seen in the band at 45 ° and the protons in the band to the left. However, due to electronics problems the pulse-shape calibration was only possible for ≈ 75 % of the BaF_2 modules, thus it was not used in this experiment.

4.4.3. Time calibration

To obtain the gain for the time calibration pulses with known frequencies were sent to the TDCs. This resulted in spectra with sharp peaks from which the gain could be calculated (see fig. 4.9)

$$time = gain * (channel - offset)\,. \tag{4.14}$$

The offsets were calculated by using the two photons originating from the pion detected in TAPS. These photons were identified by requiring no hit in the veto detectors in front of the BaF_2 and a cut was placed around the π^0 mass in the invariant mass spectrum. Then the time difference was checked between these two photons and it was set to 0, indicating that the two photons arrived simultaneously. There was also a correction made because of the so-called time-walk. This effect comes about when two signals from the same event have different amplitudes that make them cross the thresholds at different times. See [43] for a description of how this correction is done.

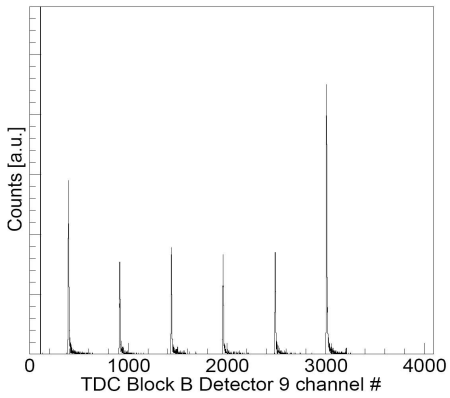

Figure 4.9: 20 ns pulse pattern for a TAPS module used for the time calibration.

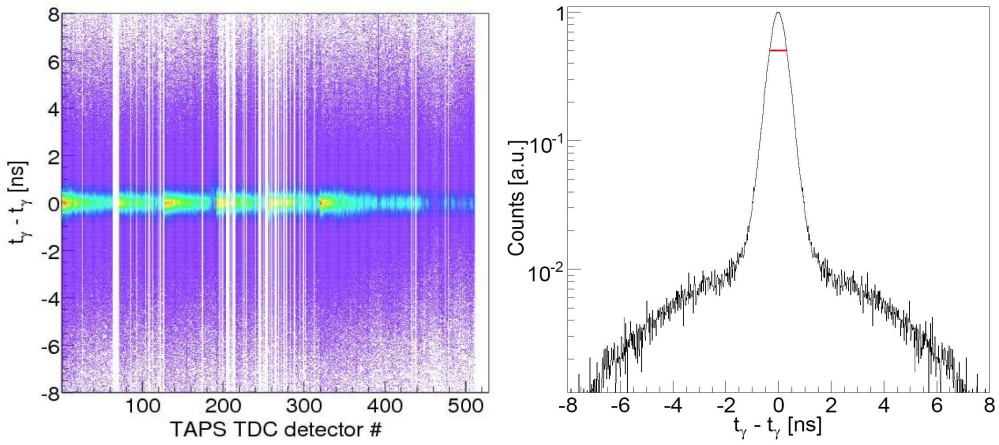

Figure 4.10: Left: The time difference of two photons detected in TAPS versus the detector number. Right: The same time difference summed over all TAPS modules.

Figure 4.10 (left) shows the time difference after the calibration as a function of TAPS detector number. The sum over all detectors can be seen in 4.10 (right). The FWHM of the peak was determined to be 0.65 ns. This time calibration corrects both for length differences of the cables and for differences in flight path of the photons.

About 10% of the TDCs could not be used for timing (seen as empty channels in fig. 4.10 (left)), either the peak was too wide or there were two peaks in the spectra. These detectors were listed in a table and if one of these were the central detector of a cluster, the time information were instead taken from a neighboring crystal in the cluster.

4.4.4. LED threshold calibration

The purpose of the LEDs was to discriminate hits that deposit an energy below the specified threshold so they will not be recorded, *i.e.* it was used by the hardware trigger. The correct setting needed to be known before the real data taking started, so it was done with cosmics data before the beam time. The threshold was set in mV but, since each LED behaved differently, an energy calibration was needed in order to get the correct setting for the desired threshold in MeV. This was done by determining the resulting threshold in MeV for three different mV-settings and finding the (linear) correlation. The edge was seen clearly when dividing the LED spectra with the energy spectra, both had to be calibrated into MeV first. The threshold was defined to be at the point where the ratio was 0.5. Because of different pulse shapes, different types of particles yield different energy threshold settings. During the offline analysis threshold values were found for each type of particle which were allowed to trigger. For the analysis in this work, however, a comparison between reactions off protons and off neutrons is desired, therefore only photons were allowed to trigger (in the software trigger). Figure 4.11 shows the LED-high and LED-low threshold for one ring in TAPS for photons. A more detailed account of the LED threshold calibration in given in [35].

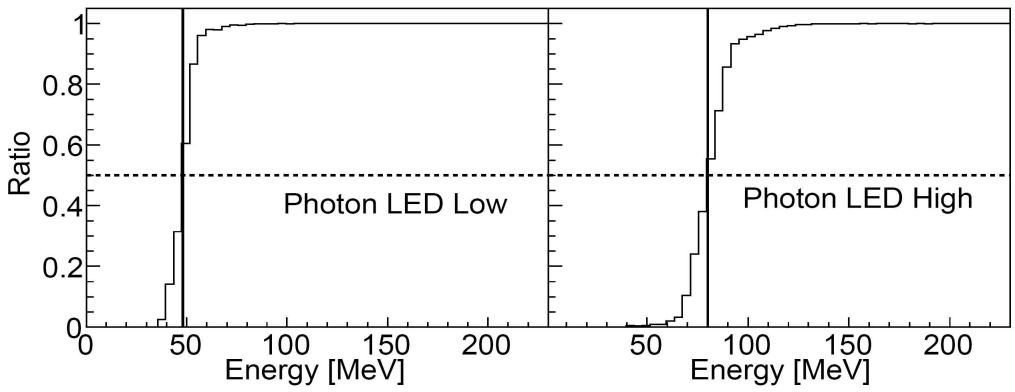

Figure 4.11: Left: The fraction of photons firing with the LED-low threshold setting. Right: The fraction of photons firing with the LED-high threshold setting. For detector modules in ring 7 of TAPS.

4.5. The veto wall

The Vetos did not require any calibration since they only give the information if a charged particle has passed or not. All LEDs were set with a threshold at 20 mV, which corresponded to 0.15 MeV in average (see sect. 5.5.2).

5. Particle Reconstruction and Analysis

This chapter describes the reconstruction of particles from the information registered by the detectors. Since mesons are short-lived it is not possible to directly observe the ω mesons, but they had to be reconstructed from their decay particles entering the detector. The channel studied in this thesis was $\gamma N \to \omega N \to \pi^0 \gamma N \to \gamma\gamma\gamma N$, where N was either a proton or a neutron (or deuteron, in the case of coherent production). The analysis steps for each reaction studied will be explained in this chapter.

5.1. Reconstruction of particles

The four-vectors of particles, $\vec{P} = (E, p_x, p_y, p_z)$, were calculated by measuring their deposited energy in the detectors and their position, together with kinematic constraints (energy and momentum conservation) and the known information of the initial state (beam and target).

5.1.1. Energy reconstruction (clustering)

A particle entering a detector generally do not deposit all its energy in a single crystal, instead it is spread out over several neighboring crystals in a so-called cluster. A cluster-finding algorithm scanned over all modules to identify clusters. The total deposited energy of the particle was the integral over all the modules in the cluster, provided that the energy in each module was larger than the CFD-threshold (10 MeV for TAPS and 1 MeV for CB). The module with the maximum registered energy in the cluster was taken to be the central crystal of the cluster.

Due to the higher granularity of the CB detector a second step in the cluster routine was required in order to separate overlapping clusters. This second step looked for local energy maxima of the cluster. These local maxima, required that the energy was above 13 MeV, were then taken as the centers of two separate sub-clusters, so-called PEDs (Particle Energy Deposits). The energy and position of the particle were then given by the PEDs and not the cluster.

Figure 5.1 shows schematically a scenario where there were two local maxima (A and B) within a cluster. These modules were considered to be central modules of two PEDs. The remaining modules of the cluster were assigned to the PED with the closest maximum. The energy deposited in modules with equal distance to both maxima (C, D and E) were divided between the two PEDs with a weight factor depending on the ratio between the energy in the central module of the PED and this energy plus the energy deposited in its eight neighbors. The total energy of the PEDs was the weighted energy of the shared modules plus the energy deposited in the remaining modules of the respective PED.

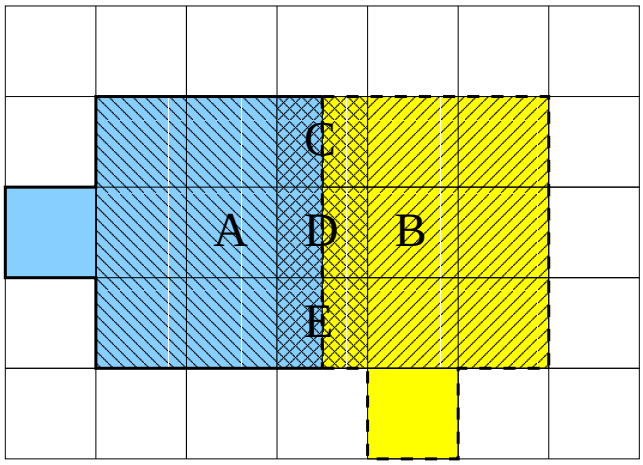

Figure 5.1: Schematic figure of a cluster in CB (each square represents a crystal) with two local maxima (A and B) divided into two sub-clusters (blue and yellow) by the cluster routine.

5.1.2. Position reconstruction

The position of a particle, $\vec{r}$, was calculated by taking the average distance of all modules in the cluster weighted with the logarithm of their energies.

$$\vec{r} = \frac{\Sigma_i W_i \vec{r}_i}{\Sigma_i W_i} \,, \tag{5.1}$$

where

$$W_i = MAX\left\{0, \left[W_0 + \ln \frac{E_i}{\Sigma_i E_i}\right]\right\} . \tag{5.2}$$

It was found through GEANT simulations that $W_0 = 4$ for TAPS and $W_0 = 4.25$ for CB [35].

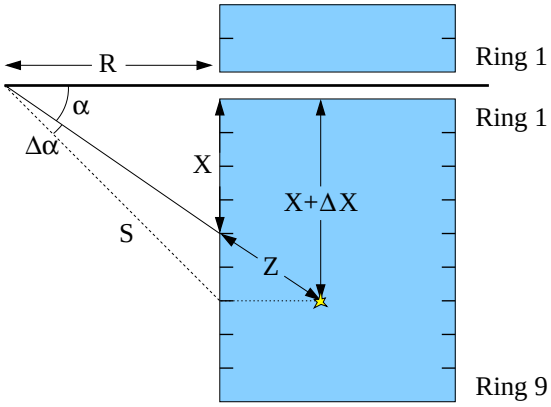

Figure 5.2: Schematic drawing of the TAPS forward wall located a distance R behind the target. Due to the non-vertex-pointing geometry of TAPS a systematic error of the position is introduced by particles entering TAPS askew. The distance between the entry point and the beam axis appears to be $X + \Delta X$, while the true distance is X. This effect is corrected for by calculating the distance traveled by the particle inside the detector before generating the shower maximum (Z).

For TAPS an extra correction was needed to account for the fact that the crystals were not vertex-pointing, which meant that a shower started at some distance after the particle entered the crystal (Z in fig. 5.2) would give the wrong position ($X + \Delta X$ instead of X). This effect was corrected for by calculating the distance that a particle traveled inside the crystal before generating the shower maximum. This distance depends on the energy of the particle and the detector material so that

$$Z = X_0 \left(\ln \left(\frac{E}{E_c} \right) + 1.2 \right), \tag{5.3}$$

where X_0 is the radiation length and E_c is the critical energy of the detector material (X_0 = 2.05 cm and E_c = 12.78 MeV for BaF_2) and E is the energy of the particle [40]. The corrections to the position (ΔX and ΔY) was calculated by

$$\frac{\Delta X}{X} = \frac{\Delta Y}{Y} = \left(\frac{S}{Z} + 1 \right)^{-1}. \tag{5.4}$$

The final polar angle position resolution obtained for photons in TAPS was 1.3° [41]. For CB (where this last step was not needed since the modules in CB were vertex-pointing) the polar angle resolution was 1°. In the case that all the energy of a particle was deposited in a single crystal the resolution was 6° (or 12° for the most backward ring), limited by the size of the crystal.

5.2. The software trigger

To enable a direct comparison of the free proton and bound proton acceptances, a software trigger mimicking the stricter conditions of the hardware trigger used for the LD_2 beam time (discussed in sect. 3.8.2), was implemented. In addition, the aim for a comparison of the reaction off the proton and off the neutron required a software trigger that only allowed for photons to trigger. The software trigger was thus; at least one photon in TAPS over the high energy threshold and two photons in CB OR two photons in TAPS over the low energy threshold. The LED-low and LED-high thresholds for the software trigger are listed in table 5.1.

Ring number	1	2	3	4	5	6	7	8	9	10	11	12
LED-low [MeV]	2000	300	150	90	60	60	60	60	60	60	60	60
LED-high [MeV]	2000	400	210	150	140	120	80	80	80	80	80	80

Table 5.1: LED-high and LED-low threshold values for the different rings in TAPS which were used in the software trigger. The innermost ring had such high threshold values in order to reduce e^+e^--pairs created by the beam.

5.3. Time coincidence analysis

The electron beam impinging on the radiator produces a large amount of photons and an equally large number of hits in the tagger. In order to get the correct energy information of the photon that produced a reaction in the target, the time between the hits of the decay products in TAPS and the hit of the electrons in the tagger is used. This made it possible to distinguish between the true coincidence photon that produced a reaction in the target and accidental coincidences. Figure 5.3 (right) shows the time spectrum and the random hits show up as a flat distribution under the coincidence peak. Their contribution was determined by making cuts in this spectrum around the peak (-4 ns to 6 ns) and in two bands on either side of the peak (-80 ns to -10 ns and 10 ns to 80 ns), see fig. 5.3. Events from the sidebands were subtracted with a weight factor (10/140) due to the width of the bands in order to remove the accidental coincidences under the prompt peak according to

$$S = (S + SBG) - \frac{\Delta S}{\Delta BG} \cdot BG\,, \tag{5.5}$$

where ΔS and ΔBG are the width of the coincidence and the background windows, respectively. S and BG is the number of events in the corresponding time windows and SBG is the background under the signal.

Figure 5.3 (right) shows the multiplicity of hits in the tagging system after a cut was placed around the coincidence peak. It shows that in many cases the multiplicity was larger than one so that an event would be entered several times in the analysis with different incident beam energies. After additional cuts, however, the multiplicity was reduced to be mainly one or two. When the multiplicity was two, neighboring tagger fibers were hit. Since these multiple entries also occur in the flux measurement, this double-counting did not cause problems in the cross-section determinations. The flux determination is explained in sect. 5.14.

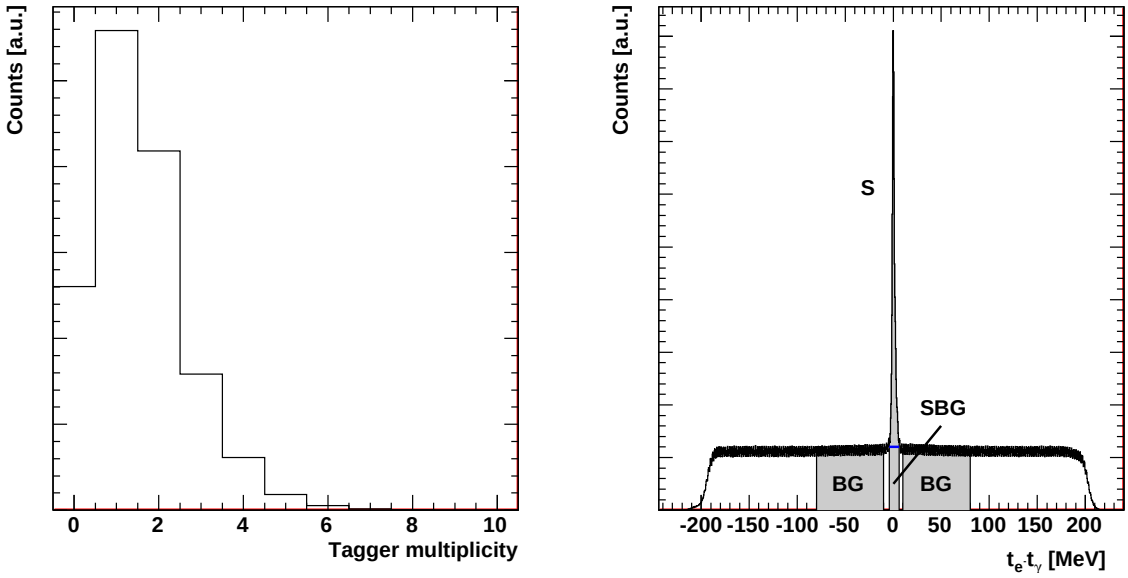

Figure 5.3: Left: The multiplicity of hits in the tagger inside the coincidence window. Right: The relative time for photons detected in TAPS to the electrons detected in the tagging system. The area under the peak labeled SBG is due to accidental coincidences and needs to be subtracted from the signal S.

5.4. Simulations

In order to calculate cross-sections it is crucial to know the detector efficiency for registering the decay particles. The detection efficiencies were obtained from simulation using the GEANT3 package [44], which has the dimensions and materials of the detector implemented giving a realistic response of the detector to the generated particles. In order to describe low energy neutron interactions, the GCALOR package was used for the simulations [45]. The decay channel of interest was specified by letting the particle decay according to kinematics but not taking any cross-sections or branching ratios into account. The simulations also made it possible to check the behavior of background channels and obtain cuts in order to improve the signal-to-background ratio. The channels simulated for this work were:

- **The production off the free proton:** $\gamma p \rightarrow \omega p \rightarrow \pi^0 \gamma p \rightarrow \gamma\gamma\gamma p$
- **The quasi-free production off the bound proton:** $\gamma d \rightarrow \omega p(n) \rightarrow \pi^0 \gamma p(n) \rightarrow \gamma\gamma\gamma p(n)$. The spectator neutron was not registered in the reaction.
- **The quasi-free production off the bound neutron:** $\gamma d \rightarrow \omega n(p) \rightarrow \pi^0 \gamma n(p) \rightarrow \gamma\gamma\gamma n(p)$. The spectator proton was not registered in the reaction.
- **Isotropically distributed ω mesons** in $(E^{\omega}_{kin}, E^{\omega}_{\theta})$: $\omega \rightarrow \pi^0\gamma \rightarrow \gamma\gamma\gamma$. This simulation gave the efficiency used in the grid method for the inclusive analysis.
- **Background channel:** $\gamma p \rightarrow \pi^0\pi^0 p \rightarrow \gamma\gamma\gamma\gamma p$
- **Background channel:** $\gamma p \rightarrow \pi^0 p \rightarrow \gamma\gamma p$
- **Coherent production:** $\gamma d \rightarrow \omega d \rightarrow \pi^0\gamma d \rightarrow \gamma\gamma\gamma d$

The protons and neutrons bound in deuterium are simulated as having a momentum distribution corresponding to their Fermi motion in the nucleus. In this work the Paris wave function was used to obtain the momentum distribution [22]. For deuterium the distribution has the shape illustrated in fig. 2.4 which is peaking at a momentum around 40 MeV.

The output of the simulation was treated in the analysis in exactly the same way as the data. By knowing the start distribution (the number of particles that were generated and their momentum distribution) and seeing how many were reconstructed, allowed to calculate the detection efficiency.

5.5. Charged and neutral hit separation

Charged and neutral hits were separated by using the response from the inner detector in the CB-region and the veto-detectors in front of TAPS.

5.5.1. in CB

The condition for a charged hit in CB was that two or three of the fibers in the inner detector had fired within a 10° angle to the CsI module which registered energy in CB, see fig. 5.4. The neutral hits were identified as hits when no fiber in the inner detector fired in coincidence with one of the detectors in CB within an angle of 10°. Events where only one fiber fired in the inner detector were discarded.

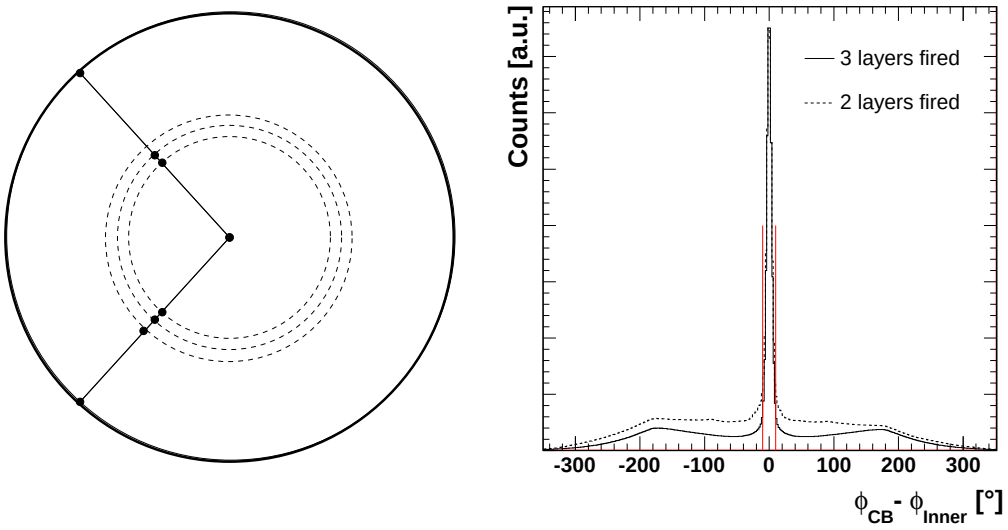

Figure 5.4: Left: Schematic figure of the CB and inner detector seen along the beam line. Right: The difference in azimuthal angle between a hit in CB and two or three layers firing (dashed and solid line, respectively) in the inner detector. Events within $|\phi_{CB} - \phi_{Inner}| < 10°$ were identified as charged hits in CB.

5.5.2. in TAPS

For a charged hit in TAPS the veto must have fired in front of the central BaF_2 detector of the cluster or in front of one of the BaF_2 modules in the ring surrounding the central detector of the cluster. For a veto to fire, the deposited energy in the veto detector had to be higher than the veto threshold. Unfortunately, there was no read-out of the veto threshold available for the experiment, hence the threshold setting was unknown and had to be determined afterwards by using a simulation. This was done by checking how many π^0 signals were lost in TAPS requiring two hits in TAPS (and no further hits) which were either charged or neutral (*i.e.* no veto used) or with the specific requirement that they were both identified as neutral (*i.e.* veto did not fire). The amount lost from the pion signal is a measure of how many photons were mis-identified as charged particles due to a backscattering of the electromagnetic shower in the BaF_2 detector firing the veto in front. For the data this number was determined to be 11 % loss of pion signals by the requirement that the two photons were registered as neutral. Different threshold settings were tested for the simulation until the same behavior of the loss was observed as in the data, see fig. 5.5 and table 5.2. It was found that a veto threshold of 0.15 MeV corresponded to a loss of 11 % of the pion signal, thus that value was assumed to be the threshold that was set for the experiment and thus had to be used in the simulations.

For neutral hits in TAPS the condition was that no veto had fired in front of the central detector of a cluster or in the ring around the central detector of the cluster.

Veto threshold	0.025 MeV	0.15 MeV	0.3 MeV
Loss of π^0 in DATA 11%			
Loss of π^0 in MC [%]	16	11	6

Table 5.2: Fraction of π^0 lost when requiring that no veto fired for different threshold settings for the simulation compared to the data with unknown threshold. The table indicates that a threshold of 0.15 MeV was the one set during data taking.

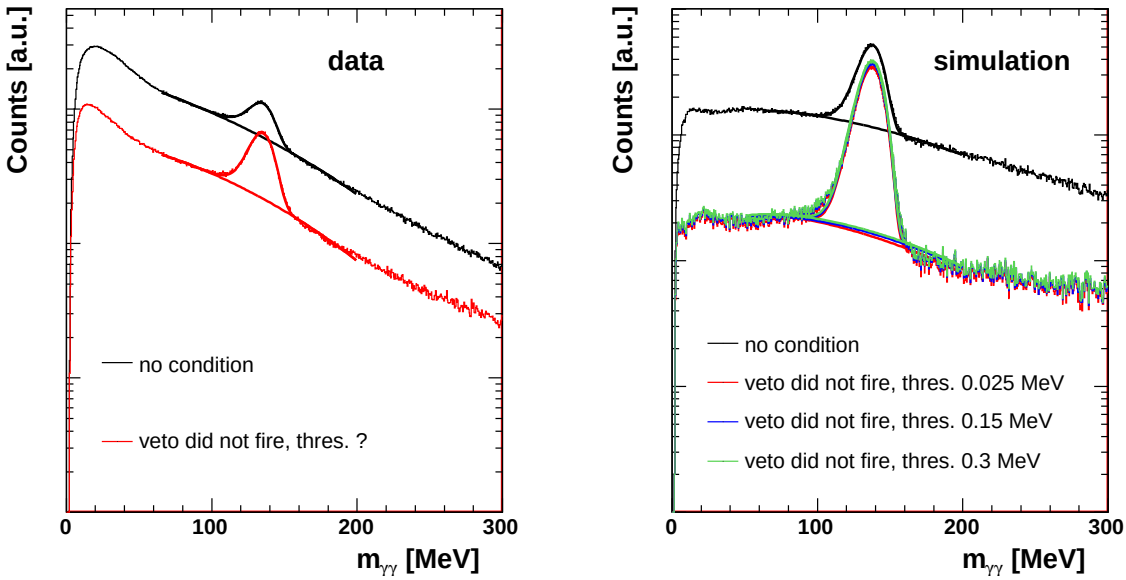

Figure 5.5: The loss of pion signals in TAPS requiring two hits in TAPS (and no further hits) which were either charged or neutral (*i.e.* no veto used) or with the specific requirement that they were both identified as neutral (*i.e.* veto did not fire) for data (left) and simulation (right).

5.6. Inner detector and veto detection efficiencies

The inner detector and veto detection efficiencies show the probability that a charged particle was mis-identified as a neutral particle and vice versa. For the LD_2 target data it was important to remove the events coming from the competing channel, where the recoil nucleon was mis-identified, before determining the cross-sections. This was not corrected for by the detector acceptance, but the magnitude of this effect could be estimated and the mis-identifed events were removed by correction factors.

Figure 5.6 shows the percentage of events where the recoil nucleon was mis-identified determined from simulations. It is shown as a function of azimuthal angle for the case when the recoil nucleon was going into the inner detector/CB (the left column in the figure) and as a function of veto number for recoil nucleons going into TAPS (right column). The figures in the upper row are for a simulation of the ω meson produced off a bound proton and the lower row figures are for a simulation of the ω meson produced off a bound neutron. The largest effect of mis-identification was observed when recoil neutrons were

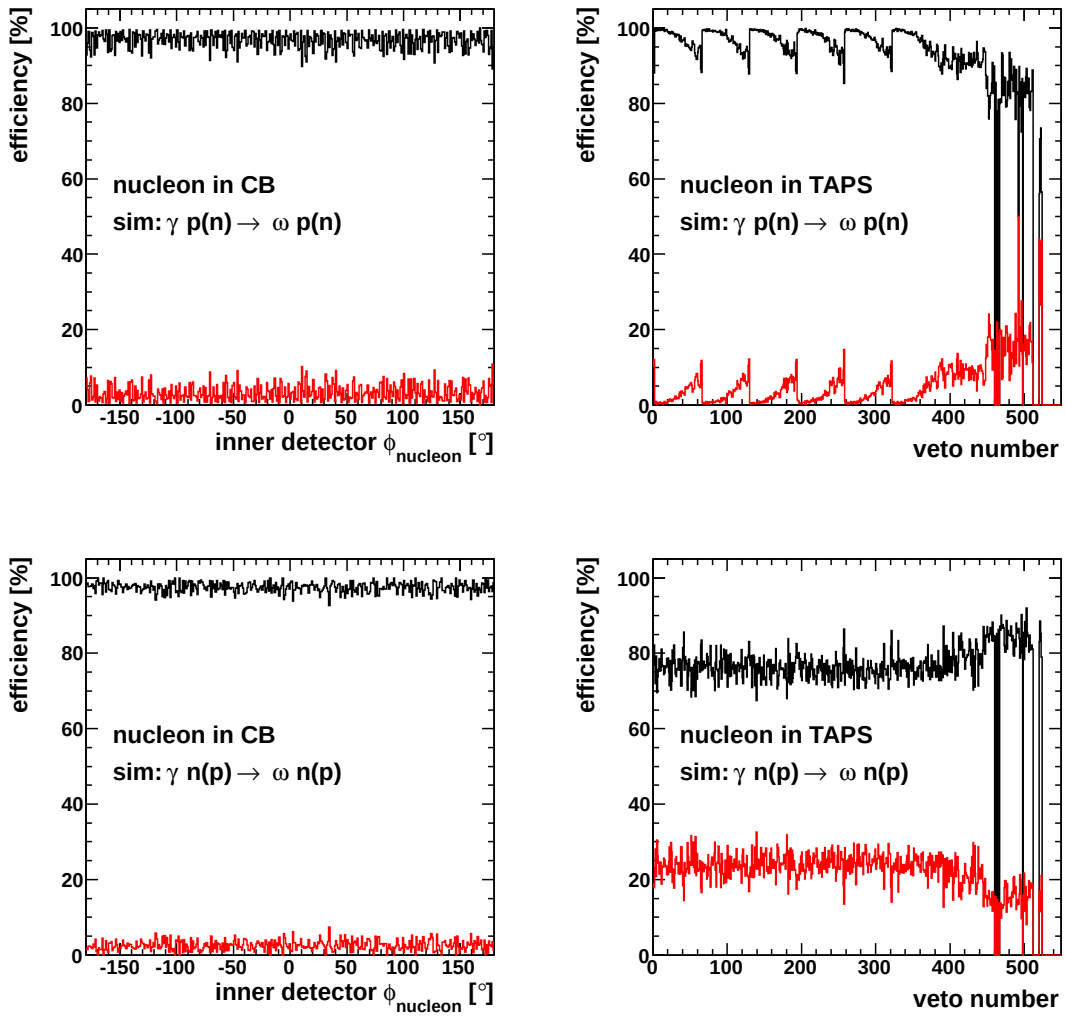

Figure 5.6: Contamination in CB (left) and in TAPS (right) for simulation of $\gamma d \to \omega p(n)$ (top row) and $\gamma d \to \omega n(p)$ (bottom row). The fraction of registered events where the recoil nucleon was correctly identified (black) and mis-identified (red).

going into TAPS (lower right in fig. 5.6). For this case, in ≈ 20-25 % of the events the neutrons was mis-identified as charged. The ω mesons for these events were thought to have been produced off a proton and had to be subtracted from the events seen in the charged channel. The correction factors as a function of $\cos(\theta^{\omega}_{c.m.})$ used to correct for this effect are shown in fig. 5.24. For the opposite case (protons being mis-identified as neutrons) a larger effect of mis-identification was observed in the LH_2 data than for the simulation. These correction factors as a function of $\cos(\theta^{\omega}_{c.m.})$ are shown in fig. 5.22 for both data and simulation. The factors obtained from the LH_2 data were used for correcting the ω yield in the cross-section determinations.

5.7. Invariant mass calculation

The invariant mass of a particle, M, decaying into N particles was calculated according to

$$M^2 = \left(\sum_{i=1}^{N} E_i\right)^2 - \left(\sum_{i=1}^{N} \vec{p}_i\right)^2, \tag{5.6}$$

where E_i and $\vec{p}_i$ are the energy and momentum of the decay particles. In case of a two-body decay the invariant mass was

$$M = \sqrt{(m_1^2 + m_2^2 + 2 \cdot (E_1 \cdot E_2 - (\vec{p}_1 \cdot \vec{p}_2))}\,. \tag{5.7}$$

If the two decay products were photons, this expression simplified further into

$$M = \sqrt{(2E_1E_2(1 - \cos\psi_{12}))}\,, \tag{5.8}$$

where ψ_{12} is the angle between the two decay photons.

The ω mesons with the decay $\omega \rightarrow \pi^0\gamma \rightarrow \gamma\gamma\gamma$ were identified through the invariant mass calculated from the three photons registered by the detector. The channel consisted of two two-body decays. First, the two photons originating from the pion were identified through an invariant mass calculation and secondly the third photon was added and the ω meson was seen as a peak in the $\pi^0\gamma$ invariant mass spectrum.

5.8. Identification of reaction channels

The reaction channels analysed in this work were identified through the following event selections.

Exclusive analyses:

- **The production off the free proton** $\gamma p \rightarrow \omega p$ (LH_2 target) was identified through events with three neutral hits and one charged hit.
- **The quasi-free production off the bound proton** $\gamma d \rightarrow \omega p(n)$ (LD_2 target) was identified through events with three neutral hits and one charged hit.
- **The quasi-free production off the bound neutron** $\gamma d \rightarrow \omega n(p)$ (LD_2 target) was identified through events with exactly four neutral hits and no charged hits.

Inclusive analyses:

- **The production off the free proton** $\gamma p \rightarrow \omega p$ (LH_2 target) was identified through events with three neutral hits and no further hits or events with at least three neutral hits and four hits in total (the fourth hit may be charged or neutral).
- **The quasi-free inclusive production** $\gamma d \rightarrow \omega(np)$ (LD_2 target) was identified through events with three neutral hits and no further hits or events with at least three neutral hits and four hits in total (the fourth hit may be charged or neutral).

In the following sections the analysis steps (listed in table 5.3 and 5.4) for these different reactions will be described. However, no distinction is made between the first two reactions, the ω meson being produced off a free proton ($\gamma p \rightarrow \omega p$) or bound proton($\gamma d \rightarrow \omega p(n)$), since the analysis was identical in these two cases.

The main difference in the analysis was introduced from the difference in identification of the proton and the neutron. Because of the neutral nature of the neutron it is difficult to distinguish it from photons and thus the reaction off the neutron required a more complicated analysis (as will be explained in sect. 5.10).

Steps for exclusive analysis	3 neutral and 1 charged hit	4 neutral hits
$\pi^0\pi^0$ subtraction		X
$\chi^2 = \frac{(m(\gamma\gamma)-m_{\pi^0})^2}{(\Delta m(\gamma\gamma))^2}$	X	X
110 MeV $< m_{\pi^0} <$ 160 MeV	X	X
$\chi^2_{miss} = (m_{miss} - m_N)^2$		X
m_{miss} cut(E_γ^{beam})	X	X
$\theta_{lab.}^{nucl}(E_\gamma^{beam})$ cut	X	X
nucleon mis-identification corr.	X	X

Table 5.3: Analysis steps for the two different groups of selected events in the exclusive analyses.

Steps for inclusive analysis	3 neutral and 1 charged hit	4 neutral hits	3 neutral hits
$\pi^0\pi^0$ subtraction		X	
$\chi^2 = \frac{(m(\gamma\gamma)-m_{\pi^0})^2}{(\Delta m(\gamma\gamma))^2}$	X	X	X
110 MeV $< m_{\pi^0} <$ 160 MeV	X	X	X
$\chi^2_{miss} = (m_{miss} - m_N)^2$		X	
m_{miss} cut(E_γ^{beam})	X	X	X
$\theta_{c.m.}^{\gamma,\pi^0}(p_{c.m.}^{\omega})$ cut	X	X	X

Table 5.4: Analysis steps for the three different groups of selected events in the inclusive analyses.

5.9. The production off the free and bound proton

The event selection for this reaction channel was the requirement that three neutral hits and one charged hit was registered. The analysis steps are listed in table 5.3 in the left column and will be described below.

The ω meson was reconstructed from the combinatorics of the three neutral particles (assumed to be three photons) as it was briefly described in the previous section. In a little more detail, the registered neutral particles were paired two by two and the combination (out of the three possible ones) with the invariant mass closest to the pion mass was selected by a χ^2-test minimizing

$$\chi^2 = \frac{(m(\gamma\gamma) - m_{\pi^0})^2}{(\Delta m(\gamma\gamma))^2}\,, \tag{5.9}$$

where the invariant mass of two photons, $m(\gamma\gamma)$, was calculated according to eq. 5.8 and the term $\Delta m(\gamma\gamma)$ handled the error arising from the detector resolution

$$\Delta m(\gamma\gamma) = \frac{1}{2} m(\gamma\gamma)\Big(\frac{\Delta E_1}{E_1} + \frac{\Delta E_2}{E_2} - \frac{\Delta\cos\psi_{12}}{1-\cos\psi_{12}}\Big)\,, \tag{5.10}$$

where

$$\begin{aligned}\Delta\cos\psi_{12} = {} & \sin\theta_1\cos\theta_2(\cos(\phi_1-\phi_2)-1)\Delta\theta_1 + \\ & \cos\theta_1\sin\theta_2(\cos(\phi_1-\phi_2)-1)\Delta\theta_2 - \\ & \sin\theta_1\sin\theta_2\sin(\phi_1-\phi_2)(\Delta\phi_1-\Delta\phi_2) - \\ & \sin(\theta_1-\theta_2)(\Delta\theta_1-\Delta\theta_2)\,.\end{aligned} \tag{5.11}$$

The χ^2 distribution is shown in fig. 5.7 (left) for the LH_2 target data and the simulation off the free proton. They are in good agreement. If the number of degrees-of-freedom is known (1 in this case) the confidence level CL can be calculated according to

$$CL = 1 - \int_0^{\chi^2} f_{st}(\chi^2)d\chi^2\,. \tag{5.12}$$

In fig. 5.7 (right) the confidence level is depicted. A flat CL distribution implies that the errors were properly taken into account. Figure 5.8 shows the χ^2 distribution (left) and the confidence level (right) for the LD_2 target data and simulation off the bound proton.

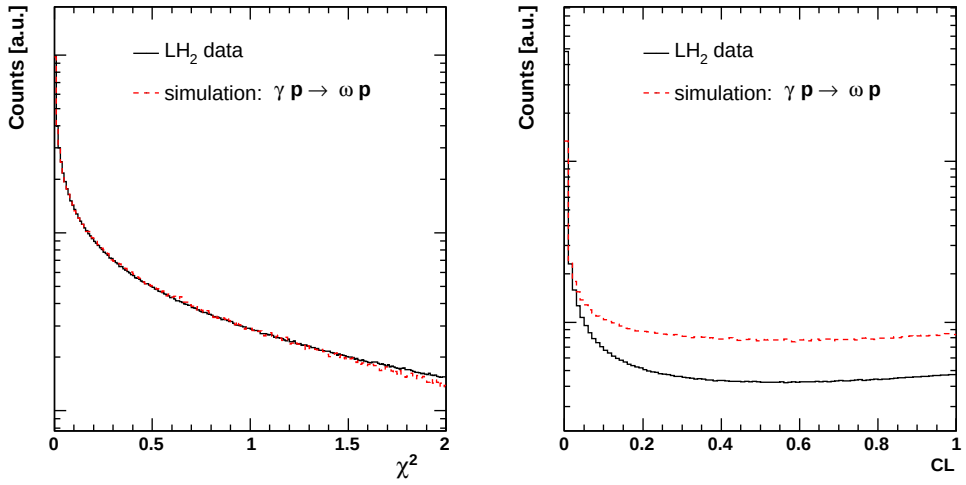

Figure 5.7: Left: χ^2 calculated by eq. 5.9 for the LH_2 data (black solid) and simulation (red dashed) for three neutral hits and one charged hit. Right: Confidence level. A flat distribution shows that the errors are under control.

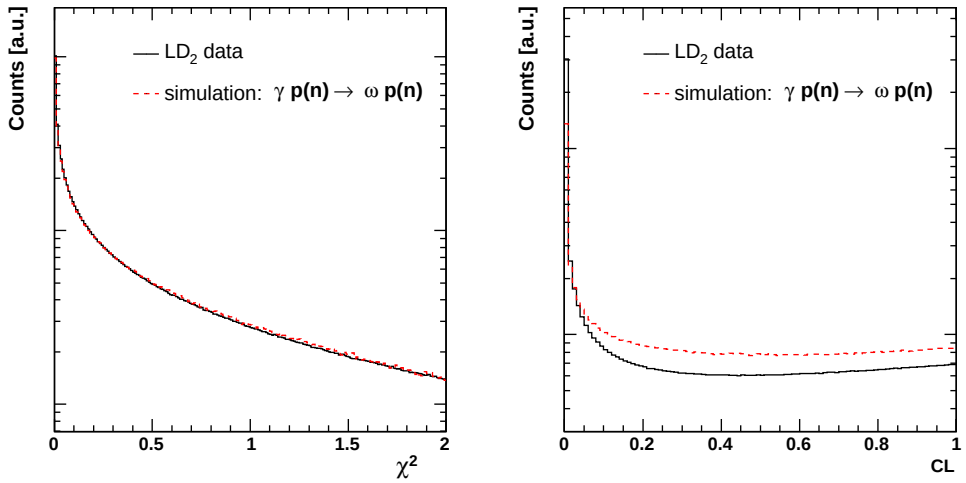

Figure 5.8: Left: χ^2 calculated by eq. 5.9 for the LD_2 data (black solid) and simulation (red dashed) for three neutral hits and one charged hit. Right: Confidence level. A flat distribution shows that the errors are under control.

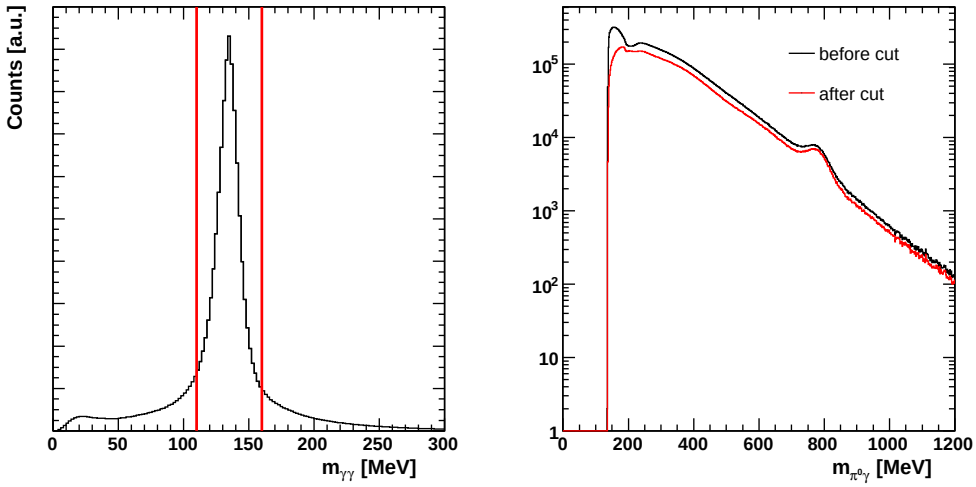

Figure 5.9: Left: The $\gamma\gamma$ invariant mass is depicted and the cut (110 MeV $< m_{\gamma\gamma} <$ 160 MeV) ensuring that the two photons originated from a π^0. Right: The effect of this cut on the $\pi^0\gamma$ invariant mass, without the cut (black) and with the cut (red). The cut is reducing the background under the ω peak.

A cut was placed in the invariant mass spectrum around the pion peak (110 MeV $< m_{\gamma\gamma} <$ 160 MeV) and the events outside of this cut were discarded. For the events that satisfied this requirement the invariant mass was adjusted to be the pion mass, m_{π^0}. The third neutral particle (photon) was then added using eq. 5.7 and the ω meson was identified from the $\pi^0\gamma$-invariant mass spectrum. In fig. 5.9 the π^0 cut is depicted to the left and the effect of this cut on reducing the background in the $\pi^0\gamma$ spectrum is shown to the right.

Since the proton did not deposit all of its energy in the detector, its mass could not be calculated directly, using the deposited energy, instead it was treated as a missing charged particle and its mass was calculated using energy balance assuming the reaction. The missing mass for this reaction was calculated by

$$m^p_{miss} = |\mathbf{P}_\gamma + \mathbf{P}_p - \mathbf{P}_{\pi^0\gamma}|, \tag{5.13}$$

where $\mathbf{P}_\gamma$, $\mathbf{P}_p$ and $\mathbf{P}_{\pi^0\gamma}$ are the four-momenta of the incident photon, the initial state proton (assumed to be at rest) and the detected $\pi^0\gamma$, respectively. A peak around the proton mass in the missing mass spectrum (see fig. 5.10 (left) for the LH_2 data and fig. 5.11 (left) for the LD_2 data) indicates that the ω meson was indeed produced off a proton and underwent the decay described above.

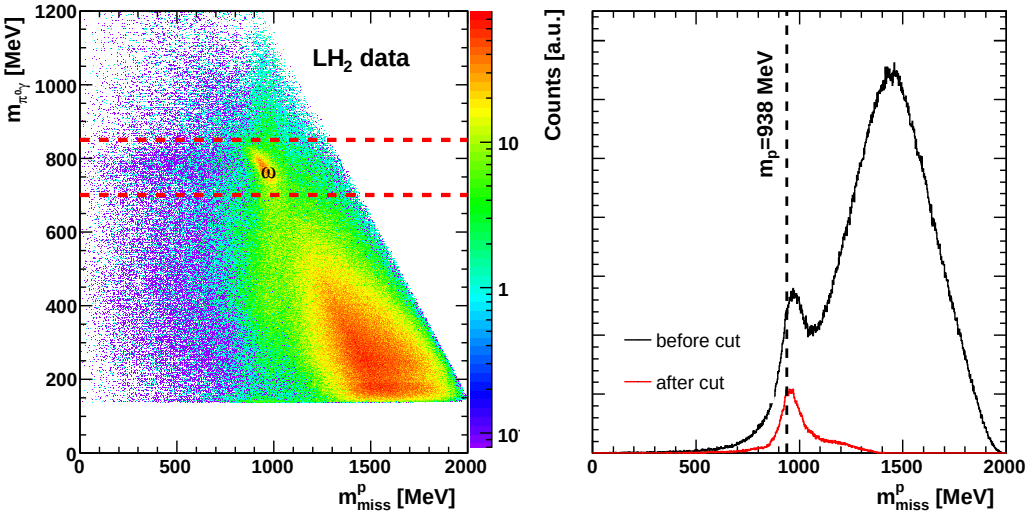

Figure 5.10: Left: The $\pi^0\gamma$ invariant mass versus the missing mass for LH_2 data for events with three neutral hits and one charged hit. The ω mesons that were produced off protons are marked in the picture together with a cut around the ω mass. Right: The missing mass before (black) and after (red) the indicated cut. After the cut a peak around the proton mass can clearly be seen.

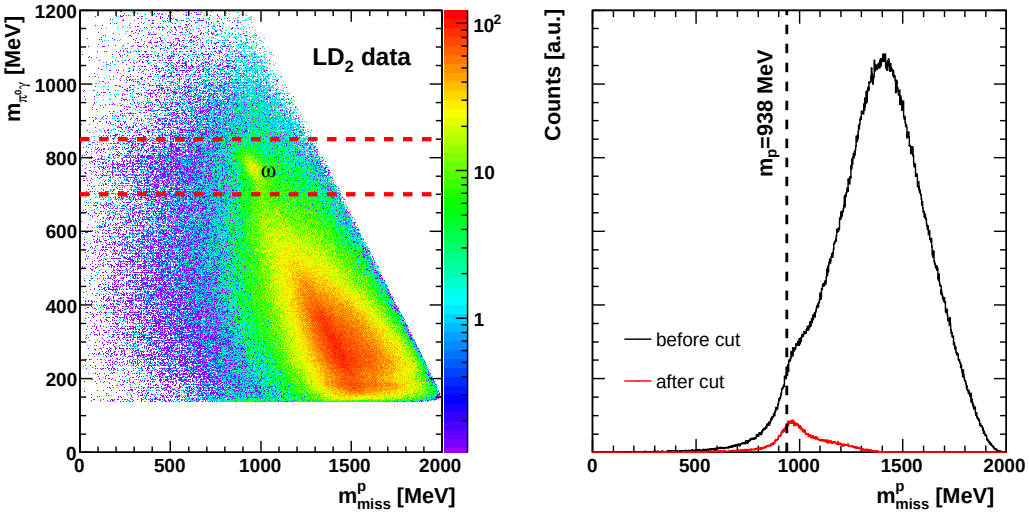

Figure 5.11: Left: The $\pi^0\gamma$ invariant mass versus the missing mass for LD_2 data for events with three neutral hits and one charged hit. The ω mesons that were produced off protons are marked in the picture together with a cut around the ω mass. Right: The missing mass before (black) and after (red) the indicated cut. After the cut a peak around the proton mass can clearly be seen.

These are the events of interest and the signal-to-background-ratio can be enhanced by cutting on the missing mass requiring it to be close to the proton mass. Figure 5.10 (right) and fig. 5.11 (right) show the full projection on the missing mass, without any requirement on the $\pi^0\gamma$ invariant mass, and the projection when cutting around the ω mass in the $\pi^0\gamma$ invariant mass spectrum. With this cut the background is reduced and the proton peak can be more clearly seen.

Simulations showed that the width of the proton peak in the missing mass spectra depended on the incident beam energy, becoming wider as the beam energy was increasing. This is shown in fig. 5.12 and 5.13 for the simulated ω productions off the LH_2 target and off the LD_2 target, respectively. The missing mass spectra for several different incident beam energies were fitted with Gaussians and the missing mass cut was chosen to be a mean-$3\sigma < m^p_{miss} <$ mean+2σ cut around the proton peak varying linearly with the incident beam energy (shown in fig. 5.12 (bottom right) and 5.13 (bottom right)).

For the LH_2 target the missing mass cut was

$$616.267 + 0.52929E^{fiber}_{\gamma} < m^p_{miss} < 1179.956 - 0.401389E^{fiber}_{\gamma}\,, \tag{5.14}$$

which implies cuts at 835 MeV $< m^p_{miss} <$ 1009 MeV at an incident beam energy $E_\gamma =$ 1108 MeV and 740 MeV $< m^p_{miss} <$ 1083 MeV at an incident beam energy $E_\gamma = 2008$ MeV. For the LD_2 target the missing mass cut was

$$686.465 + 0.329099E^{fiber}_{\gamma} < m^p_{miss} < 1179.02 - 0.401269E^{fiber}_{\gamma}\,, \tag{5.15}$$

and the corresponding cuts were 811 MeV $< m^p_{miss} <$ 1027 MeV and 699 MeV $< m^p_{miss} <$ 1164 MeV for $E_\gamma = 1108$ MeV and $E_\gamma = 2008$ MeV, respectively. The missing mass cut is broader for the LD_2 target data than for the LH_2 target data due to the smearing effect of the Fermi motion present in the LD_2 target.

The missing mass cut was then applied on the data in order to reduce background. Figure 5.14 (left) and fig. 5.15 (left) show the missing mass in the data versus the incident beam energy (in fiber numbers) for the LH_2 target and LD_2 target, respectively. The missing mass cut applied is shown in red. The effect of the missing mass cut on reducing the background in the $\pi^0\gamma$ invariant mass spectrum can be seen in fig. 5.14 (right) and fig. 5.15 (right). A clear improvement in the signal-to-background-ratio can be seen after the cut.

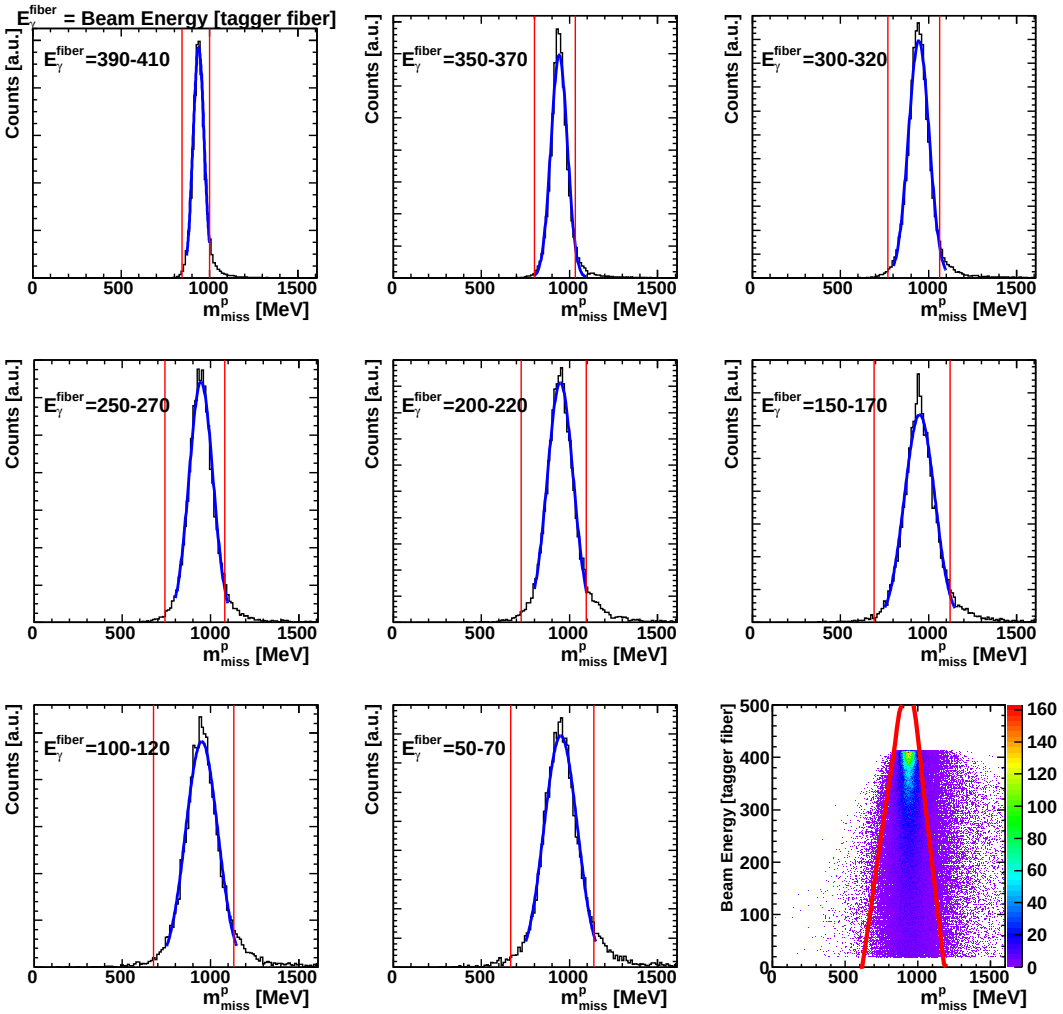

Figure 5.12: Missing mass spectra fitted with a Gaussian for different incident beam energies (in tagger fiber numbers) for a simulation of the reaction of an ω meson produced off the free proton and decaying into $\pi^0\gamma$. The beam energy is increasing with decreasing fiber number. Bottom right: The mean-$3\sigma < m^p_{miss} <$ mean+2σ missing mass cut around the proton peak which is varying linearly with the incident beam energy.

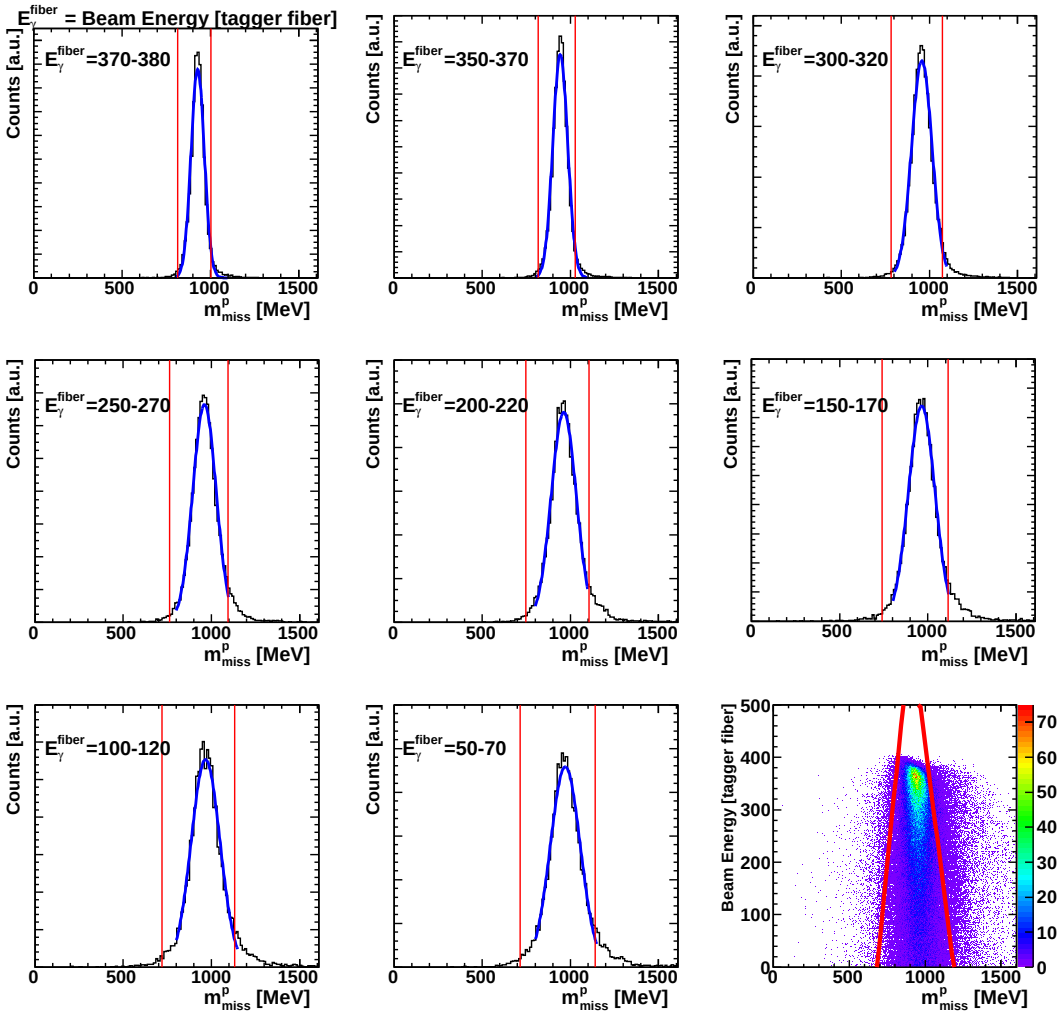

Figure 5.13: Missing mass spectra fitted with a Gaussian for different incident beam energies (in tagger fiber numbers) for a simulation of the reaction of an ω meson produced off a bound proton and decaying into $\pi^0\gamma$. The beam energy is increasing with decreasing fiber number. Bottom right: The mean-$3\sigma < m^p_{miss} <$ mean+2σ missing mass cut around the proton peak which is varying linearly with the incident beam energy.

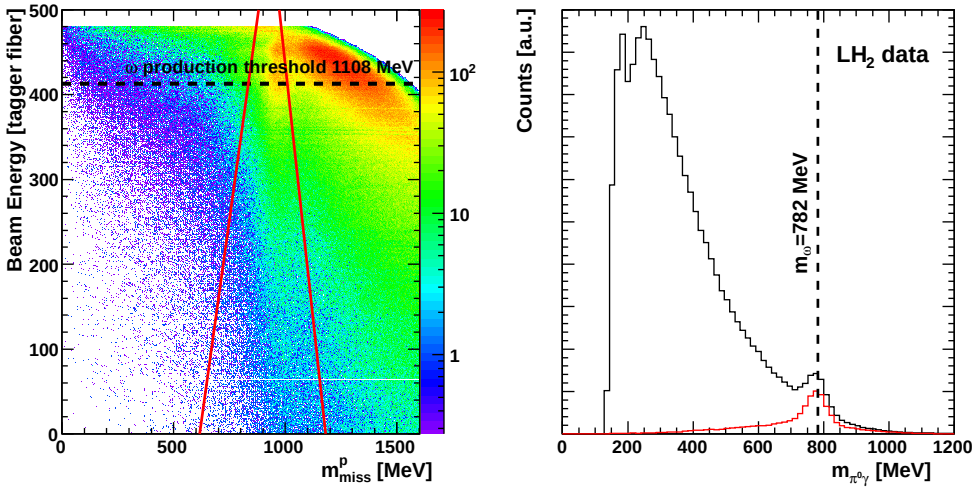

Figure 5.14: Left: The missing mass versus the incident beam energy in tagger fibers (the beam energy is increasing with decreasing fiber number) for ω mesons produced off the free proton. The missing mass cut is drawn in red. Right: The $\pi^0\gamma$ invariant mass above the production threshold of the ω meson without a missing mass cut (black) and with the missing mass cut (red).

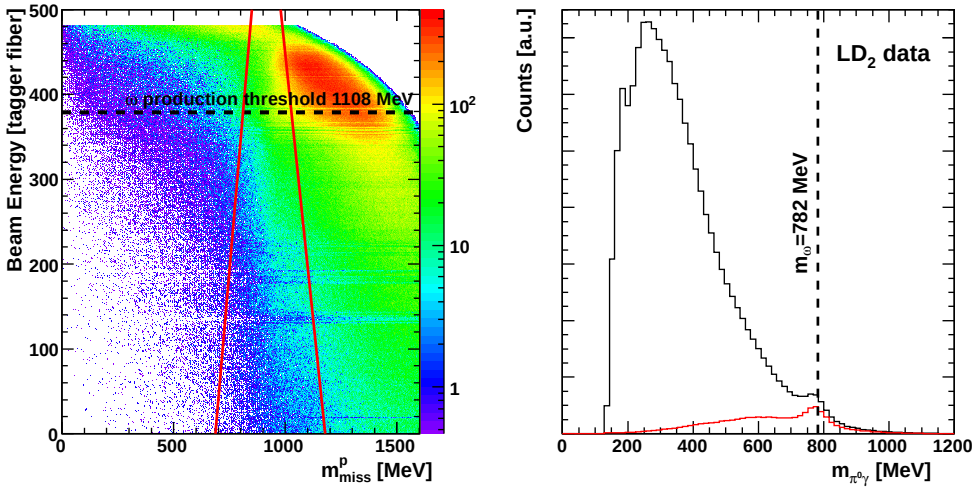

Figure 5.15: Left: The missing mass versus the incident beam energy in tagger fibers (the beam energy is increasing with decreasing fiber number) for ω mesons produced off the bound proton. The missing mass cut is drawn in red. Right: The $\pi^0\gamma$ invariant mass above the production threshold of the ω meson without a missing mass cut (black) and with the missing mass cut (red).

The next cut was a cut on the $\theta_{lab.}$-angle of the recoil nucleon in the lab-system. This cut was important in the case of the ω meson being produced off the neutron (see sect. 5.10), but for consistency it was placed also in the case of the ω meson being produced off the proton, where is was seen to reduce the background without removing the true events in the ω meson signal.

For each incident beam energy there is a maximum $\theta_{lab.}$-angle allowed for the recoil nucleon due to kinematics, the allowed angle being smaller at lower incident beam energies. This is shown in fig. 5.16 (upper left) for the simulations of ω mesons produced off a free proton and in fig. 5.17 (upper left) for the simulations of ω mesons produced off a bound proton. The cut had to be defined differently for the two targets because of the different electron beam energies (3.2 GeV for the LH_2 beam time and 2.6 GeV for the LD_2 beam time) giving different correlations between tagging fiber and energy in eV. The cuts are shown in red in the respective figure. Figures 5.16 (upper right) and 5.17 (upper right) show the situation for the data together with the cut. Figures 5.16 (lower left) and 5.17 (lower left) show the full projection onto the $\theta^p_{lab.}$-axis for simulation and data. It can be seen that some of the events in the data end up outside of the kinematically allowed region. Figures 5.16 (lower right) and 5.17 (lower right) illustrate the effect of the $\theta_{lab.}$-cut on reducing the background in the $\pi^0\gamma$ invariant mass spectra. The spectrum for events inside the cut is plotted together with the spectrum for events outside the cut. It shows that this cut successfully removed some of the background without removing anything from the signal.

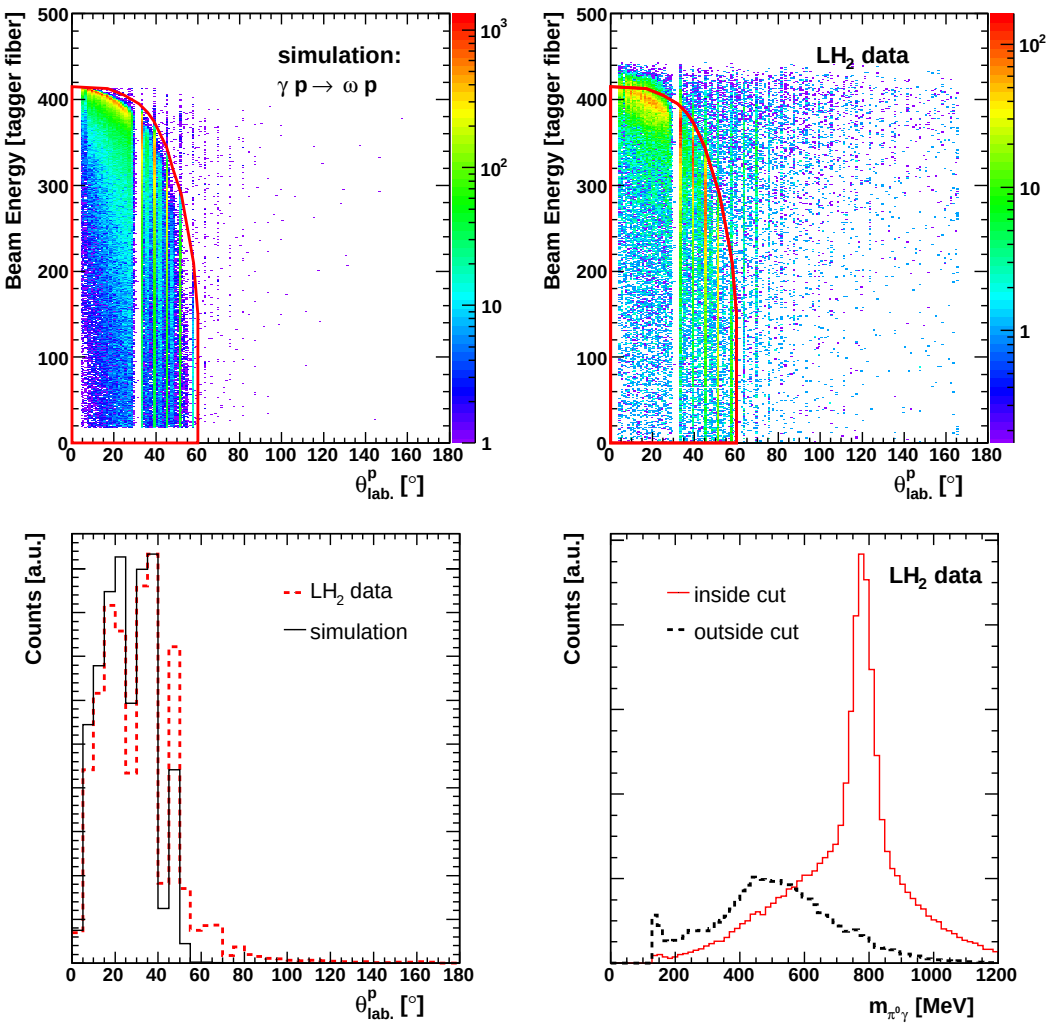

Figure 5.16: Polar angle of the proton versus incident beam energy [fiber numbers] for simulation (upper left) and for data (upper right) for the reaction off the free proton. The cut is drawn in red in both figures. Lower left: Projection onto the $\theta^p_{lab.}$-axis for simulation (black solid) and data (red dashed). Lower right: The invariant mass of $\pi^0\gamma$ for events inside the cut (red solid) and for events outside the cut (black dashed) for the LH_2 target data.

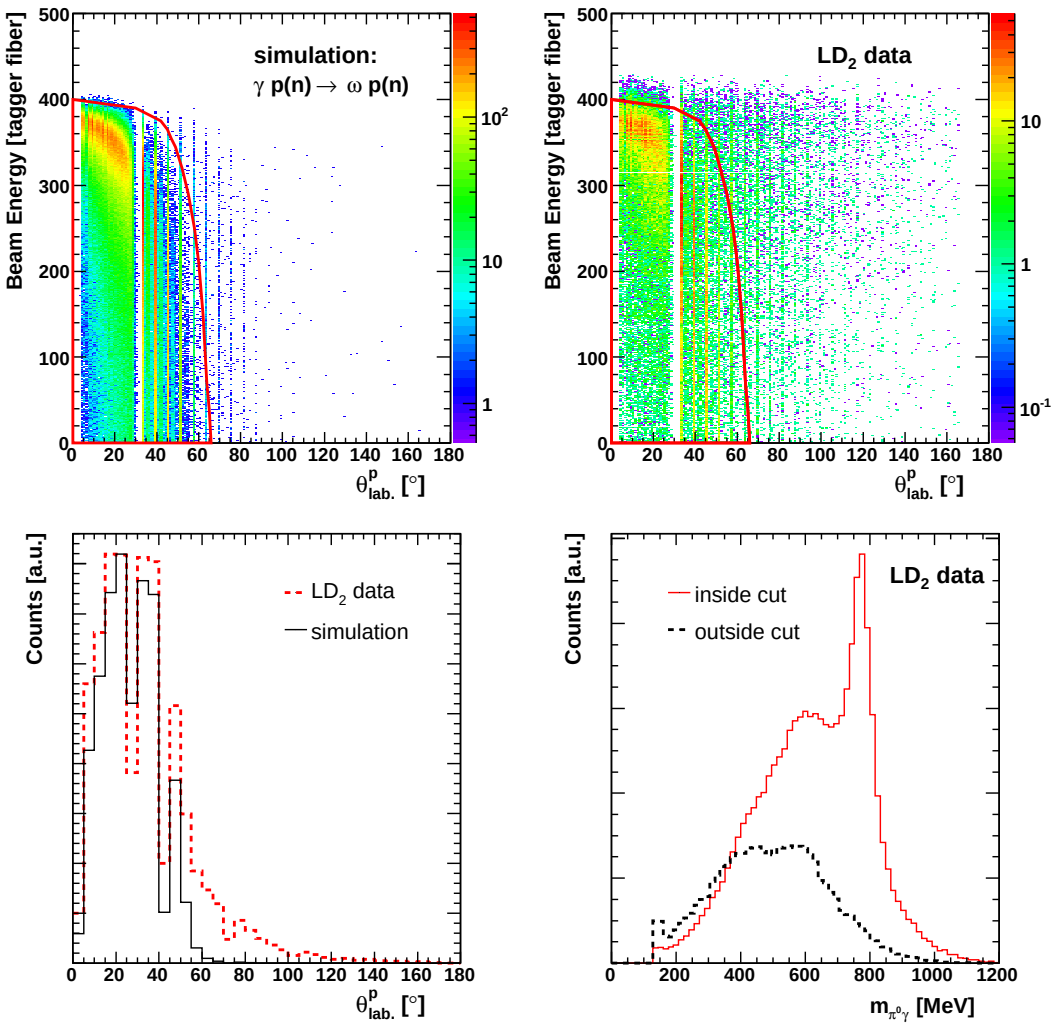

Figure 5.17: Polar angle of the proton versus incident beam energy [fiber numbers] for simulation (upper left) and for data (upper right) for the reaction off the bound proton. The cut is drawn in red in both figures. Lower left: Projection onto the $\theta^p_{lab.}$-axis for simulation (black solid) and data (red dashed). Lower right: The invariant mass of $\pi^0\gamma$ for events inside the cut (red solid) and for events outside the cut (black dashed) for the LD_2 target data.

After these cuts the $\pi^0\gamma$ invariant mass spectra were fitted and the remaining background subtracted, so that the number of ω mesons in the peak could be estimated. The fitting function used was a five parameter function for describing the background and a Gaussian function describing the signal

$$f(x) = \gamma(x - x_L)^\alpha (x - x_H)^\beta + Gaussian\,, \tag{5.16}$$

where x_L and x_H are the lower and higher crossing points of the function and the x-axis, respectively. Figures 5.18 and 5.19 show some examples of spectra for four different incident beam energies together with the fits for the LH_2 target and the LD_2 target, respectively. Close to the ω production threshold (E_γ = 1108 MeV) the fitting was difficult due to the fact that the background ended somewhere under the peak and did not extend to the higher mass side. In addition, for the LD_2 target data the signal-to-background-ratio was not that good close to threshold. For that reason, the energy bin E_γ = 1108-1158 MeV could not be used and no cross-sections were calculated for that bin. With increasing incident beam energy the signal-to-background-ratio improved and the background extended to higher masses, which made the fitting easier.

If the ω mesons were to be produced isotropically, the total cross-section could be calculated directly from the ω meson yield in each incident beam energy bin. However, since the production of ω mesons in forward direction was favored, it was necessary to look at the angular distribution of the produced ω mesons and to calculate the differential cross-sections. The total cross-sections were given by the integral of the differential cross-sections.

Figure 5.20 shows the $\pi^0\gamma$ invariant mass spectra for different bins of $\cos(\theta^\omega_{c.m.})$ for incident beam energy E_γ = 1708-1808 MeV for the LH_2 target data. The bin sizes in $\cos(\theta^\omega_{c.m.})$ vary and were chosen according to the available statistics and the ability to fit the spectra. The production of ω mesons going in forward direction was favored. However, at higher incident beam energies ($E_\gamma > 1550$ MeV), basically no ω mesons was seen in the most forward bin. The forward going ω mesons were correlated to protons going backward in the c.m.-system which meant slow protons that did not have enough energy in order to be detected (giving zero efficiency as well, see fig. 5.26). For this reason, the most forward bin could not be used for calculating cross-sections for incident beam energies $E_\gamma > 1550$ MeV. The differential cross-sections had to be extrapolated into this region with a fit. All fits to the $\pi^0\gamma$ invariant mass spectra for the exclusive analysis off the free proton are shown in appendix D.

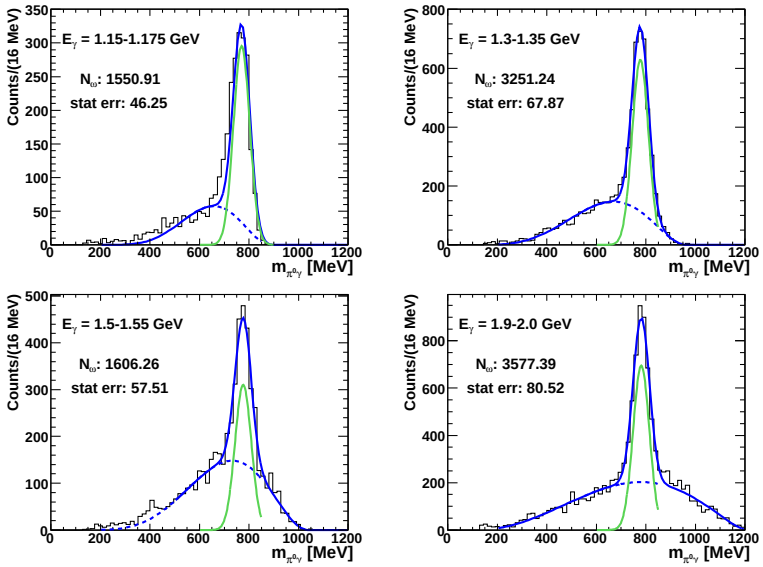

Figure 5.18: A few examples of $\pi^0\gamma$ invariant mass spectra for four different incident beam energies for the event selection three neutral hits and one charged hit for the LH_2 target data.

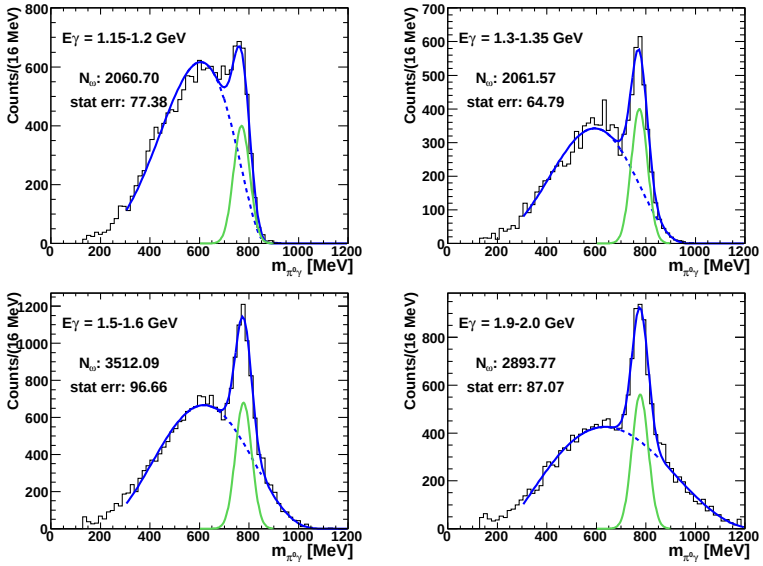

Figure 5.19: A few examples of $\pi^0\gamma$ invariant mass spectra for four different incident beam energies for the event selection three neutral hits and one charged hit for the LD_2 target data.

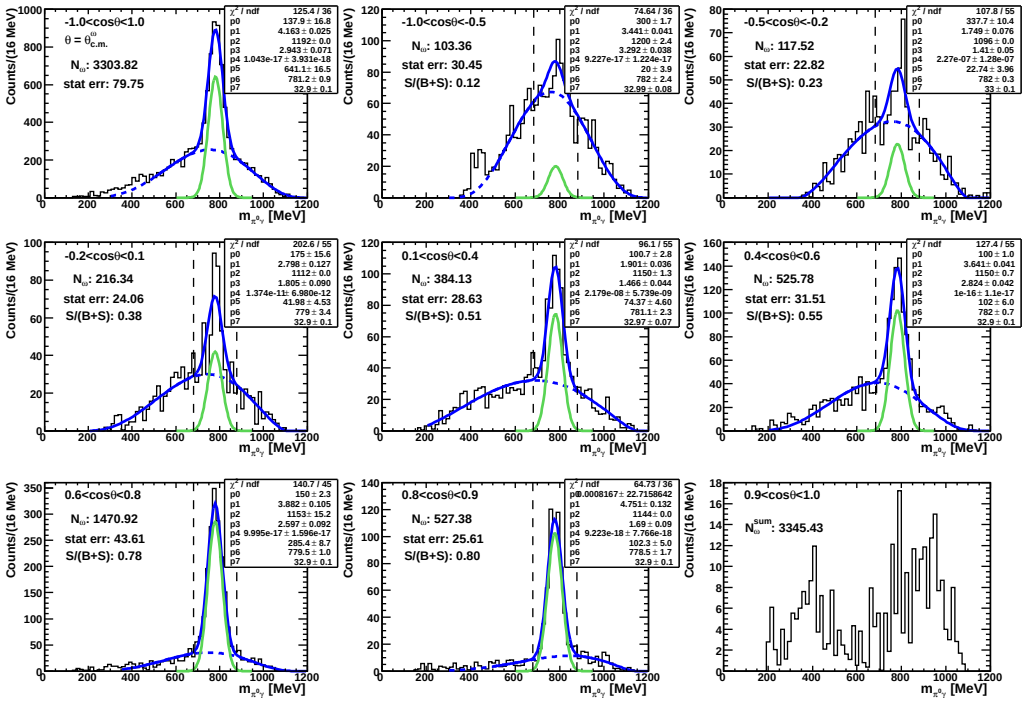

Figure 5.20: $\pi^0\gamma$ invariant mass spectra for the $\cos(\theta^{\omega}_{c.m.})$ angular bins with E_γ=1700-1800 MeV for the events with three neutral hits and one charged hit for the LH_2 target data.

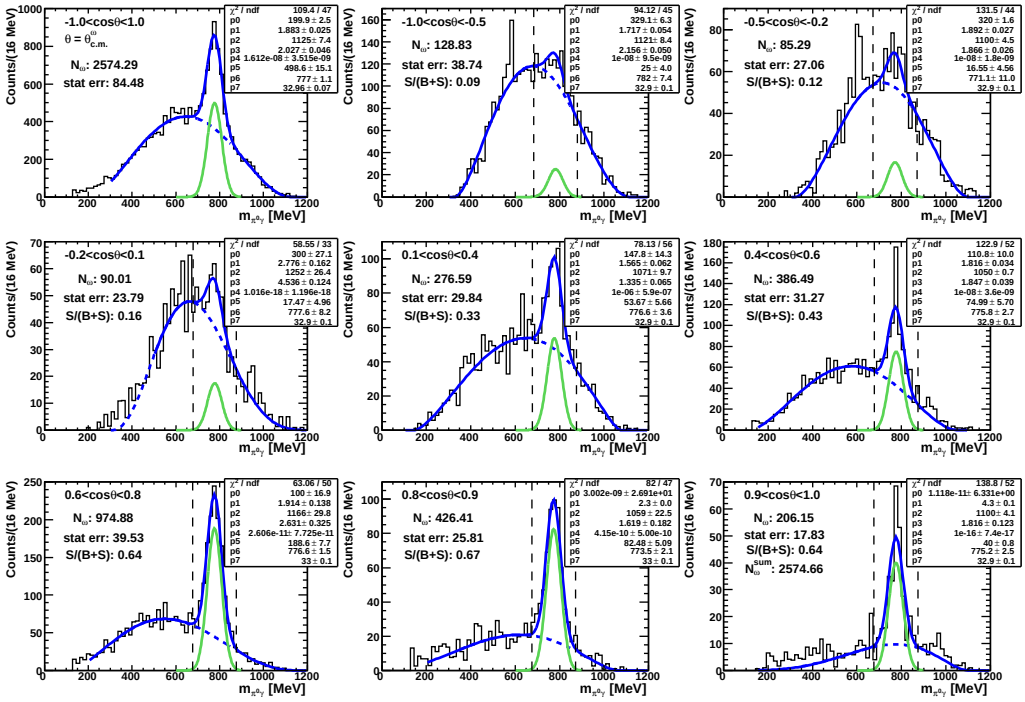

Figure 5.21: $\pi^0\gamma$ invariant mass spectra for the $\cos(\theta^{\omega}_{c.m.})$ angular bins with E_γ=1708-1808 MeV for the events with three neutral hits and one charged hit for the LD_2 target data.

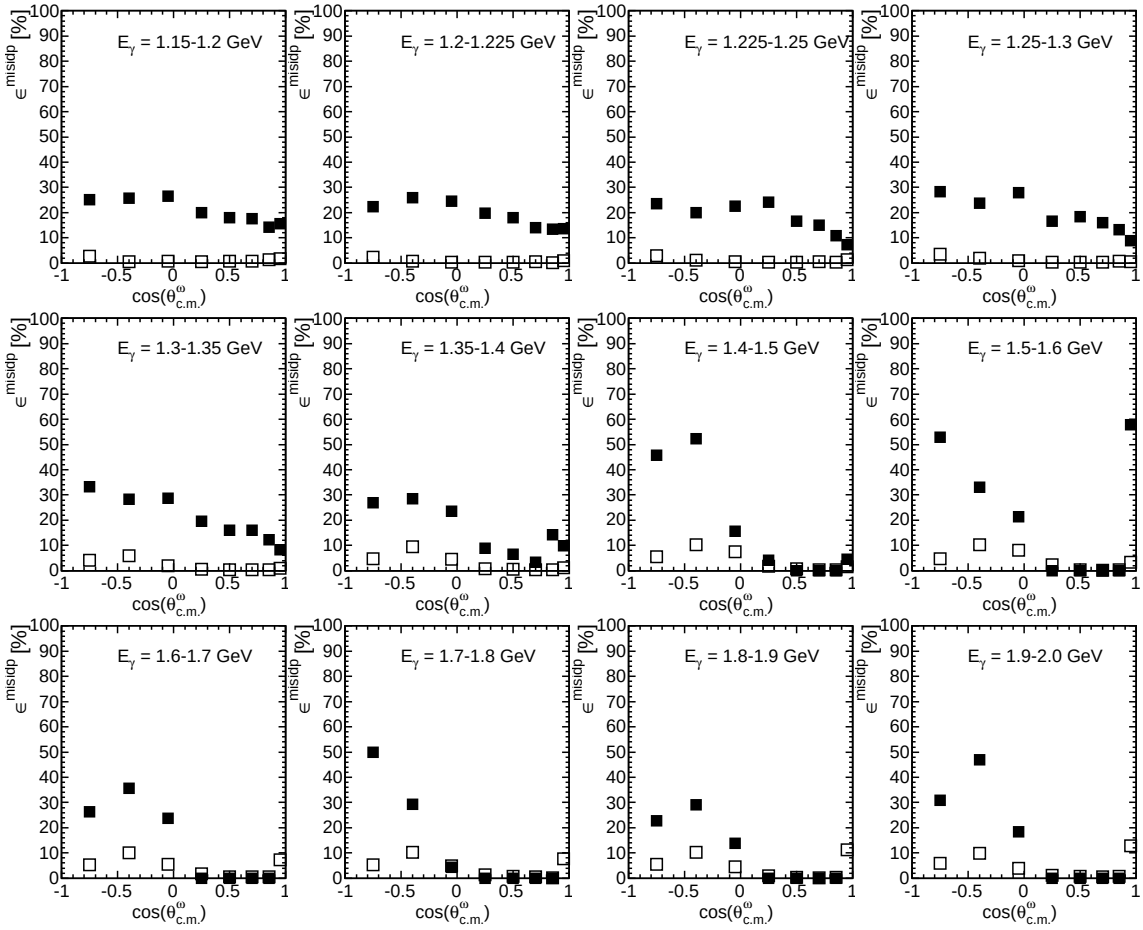

Figure 5.22: The correction factors due to mis-identification of protons as neutrons, ϵ^{misidp}, calculated from the LH_2 target data (full squares) and from the $\gamma p(n) \rightarrow \omega p(n)$ simulation (open squares).

Figure 5.21 shows the $\pi^0\gamma$ invariant mass spectra for different bins of $\cos(\theta^{\omega}_{c.m.})$ for the incident beam energy E_γ = 1708-1808 MeV together with the fits for the events with three neutral hits and one charged hit for the LD_2 target data. All $\pi^0\gamma$ invariant mass spectra together with the fits for the exclusive analysis off the bound proton are shown in appendix F.

The number of ω mesons produced off the proton determined from the fits, however, had to be corrected for the mis-identification of the recoil nucleons due to inefficiencies of the fiber and veto detectors which was not taken into account by the detector acceptances.

The probability for mis-identifying a proton as a neutron was determined from the LH_2 data by

$$\epsilon_{data}^{misidp} = \frac{N_{\omega n}^{LH_2}}{N_{\omega p}^{LH_2}}\,, \tag{5.17}$$

where $N_{\omega p}^{LH_2}$ was the number of ω mesons detected in coincidence with a proton and $N_{\omega n}^{LH_2}$ was the number of ω mesons detected in coincidence with mis-identified protons, *i.e.* events with four neutral hits treated in the analysis as described in sect. 5.10. The corresponding factors were determined for the $\gamma p(n) \rightarrow \omega p(n)$ simulation as well. Figure 5.22 shows the correction factors obtained from the data and from the simulation for each angular bin and incident beam energy. For the most forward bin $0.9 < \cos(\theta_{c.m.}^{\omega}) < 1.0$ for incident beam energies $E_\gamma < 1.5$ GeV no correction factors could be calculated for the data due to the vanishing proton acceptance in this region. The data generally gave larger correction factors than what was seen in the simulation, implying that the effect of mis-identification of protons as neutrons is not taken into account by the acceptance correction (since the acceptance is determined from simulations). Therefore, the events with protons mis-identified as neutrons seen in the LH_2 data were added to the number of events contributing to the cross-section off the proton. Figure 5.23 shows the number of ω mesons (corrected for the varying angular bin sizes) produced off the free proton before and after the addition of events where the protons were mis-identified as neutrons. For low incident beam energies $E_\gamma < 1.4$ GeV there was a contribution to the ω cross-section off the free proton from this correction.

For determining the number of ω mesons produced off the bound proton an additional correction was needed due to the mis-identification of neutrons detected as protons. This correction was only necessary for the data with LD_2 target, where there existed two possible production channels of the ω mesons (off protons or off neutrons). The correction factors were determined by running the analysis over the $\gamma n(p) \rightarrow \omega n(p)$ simulation and by counting how large a fraction of the correctly identified events, $N_{\omega n}^{sim}(\gamma n(p) \rightarrow \omega n(p))$, were mis-identified and seen as ωp events, $N_{\omega p}^{sim}(\gamma n(p) \rightarrow \omega n(p))$, (*i.e.* with the event selection of three neutral hits and one charged hit and all the cuts described above),

$$\epsilon^{misidn} = \frac{N_{\omega p}^{sim}(\gamma n(p) \rightarrow \omega n(p))}{N_{\omega n}^{sim}(\gamma n(p) \rightarrow \omega n(p))}\,. \tag{5.18}$$

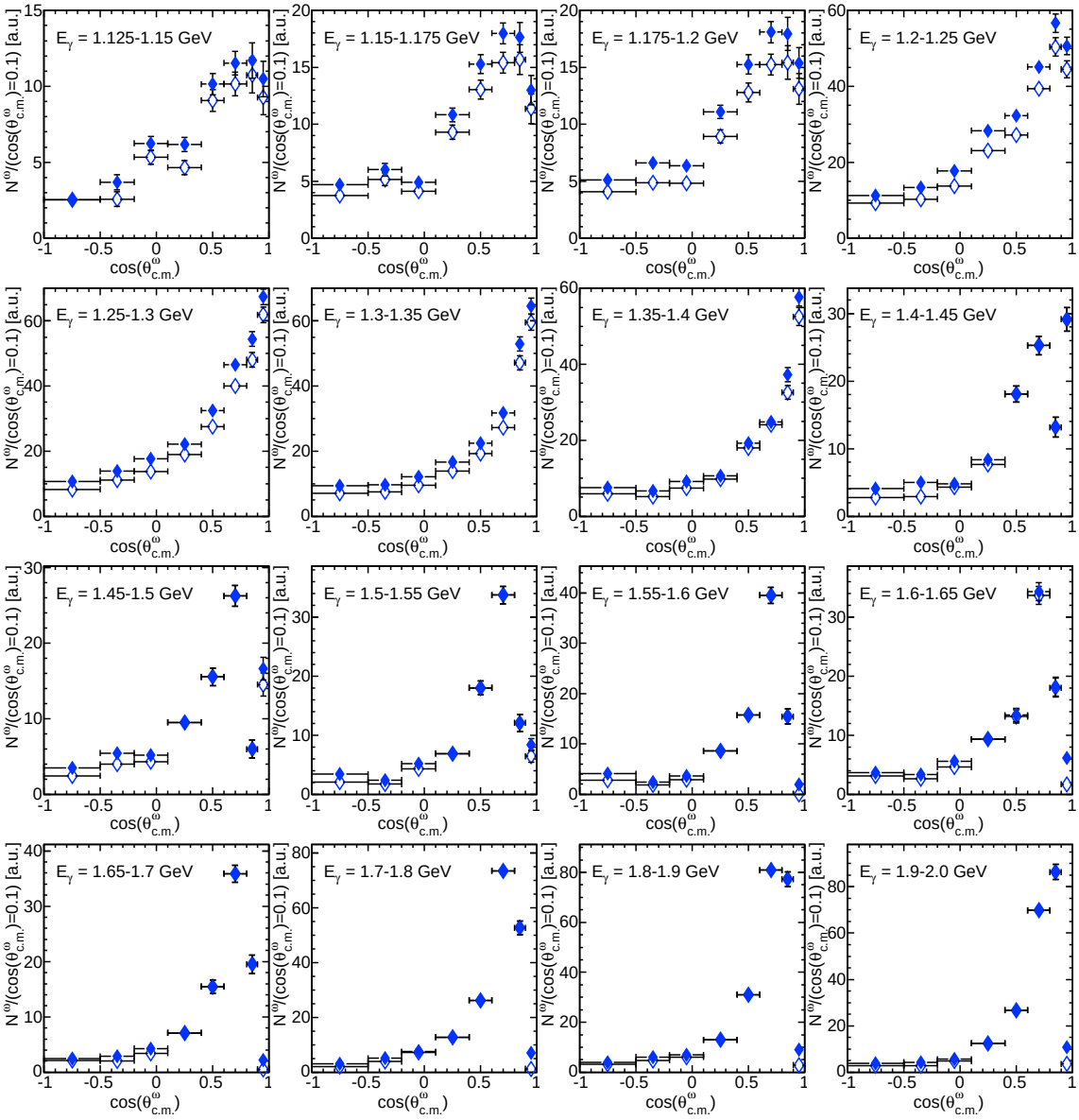

Figure 5.23: Number of ω mesons produced off the free proton as a function of $\cos(\theta^{\omega}_{c.m.})$ with the different angular bin sizes taken into account before (open symbols) and after (full symbols) addition of the events where protons were mis-identified as neutrons. Note that the numbers are not yet corrected for detection efficiencies. The statistical errors are shown.

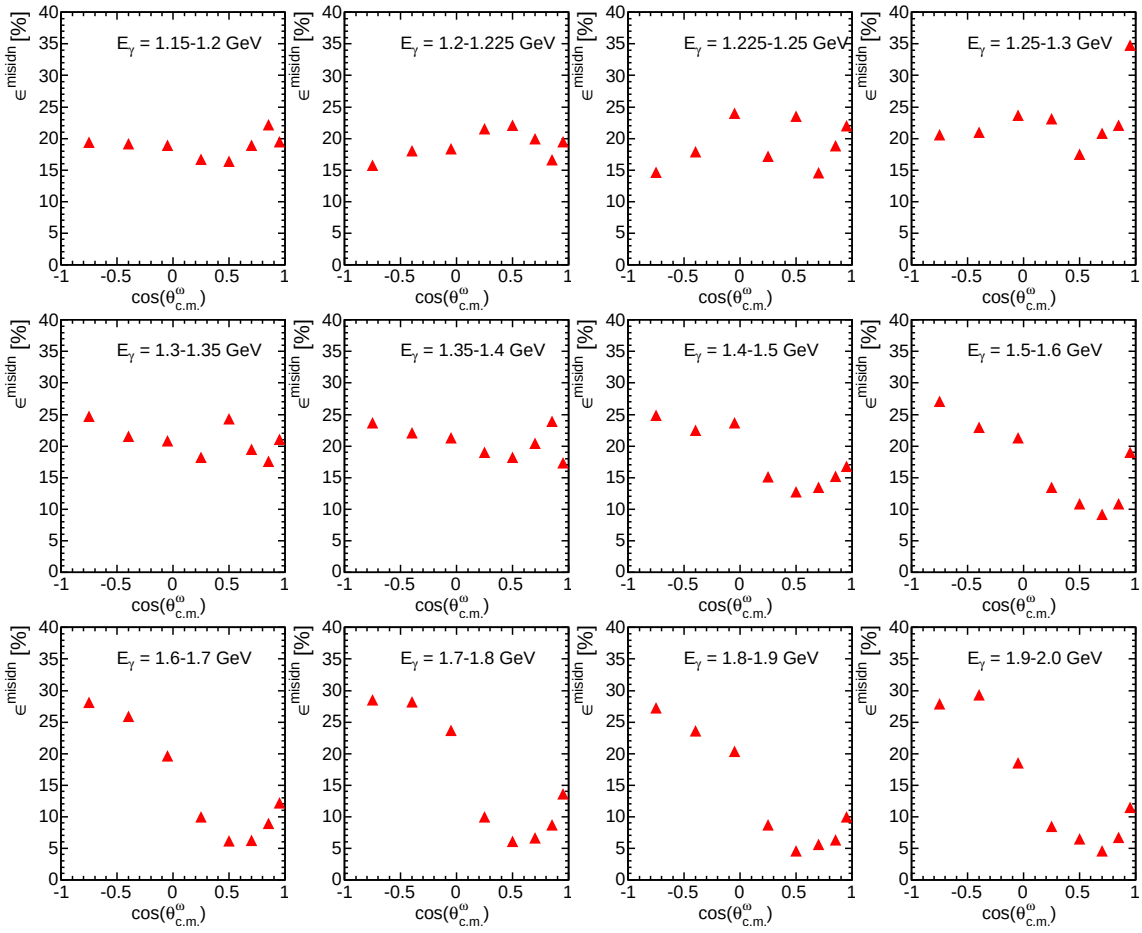

Figure 5.24: Correction factors due to mis-identification of neutrons as protons, ϵ^{misidn}, calculated from the $\gamma n(p) \rightarrow \omega n(p)$ simulation according to eq. 5.18.

The correction factors obtained for each angular bin and incident beam energy bin are shown in fig. 5.24. Note that these factors refer to the number of ω mesons that were registered in coincidence with a neutron, $N^{corr}_{\omega n}$, calculated by eq. 5.23.

The true number of ω mesons produced off a proton bound in deuterium were calculated by

$$N^{corr}_{\omega p} = N_{\omega p} + \epsilon^{misidp}_{data} \cdot N_{\omega p} - \epsilon^{misidn} \cdot N^{corr}_{\omega n} \, . \tag{5.19}$$

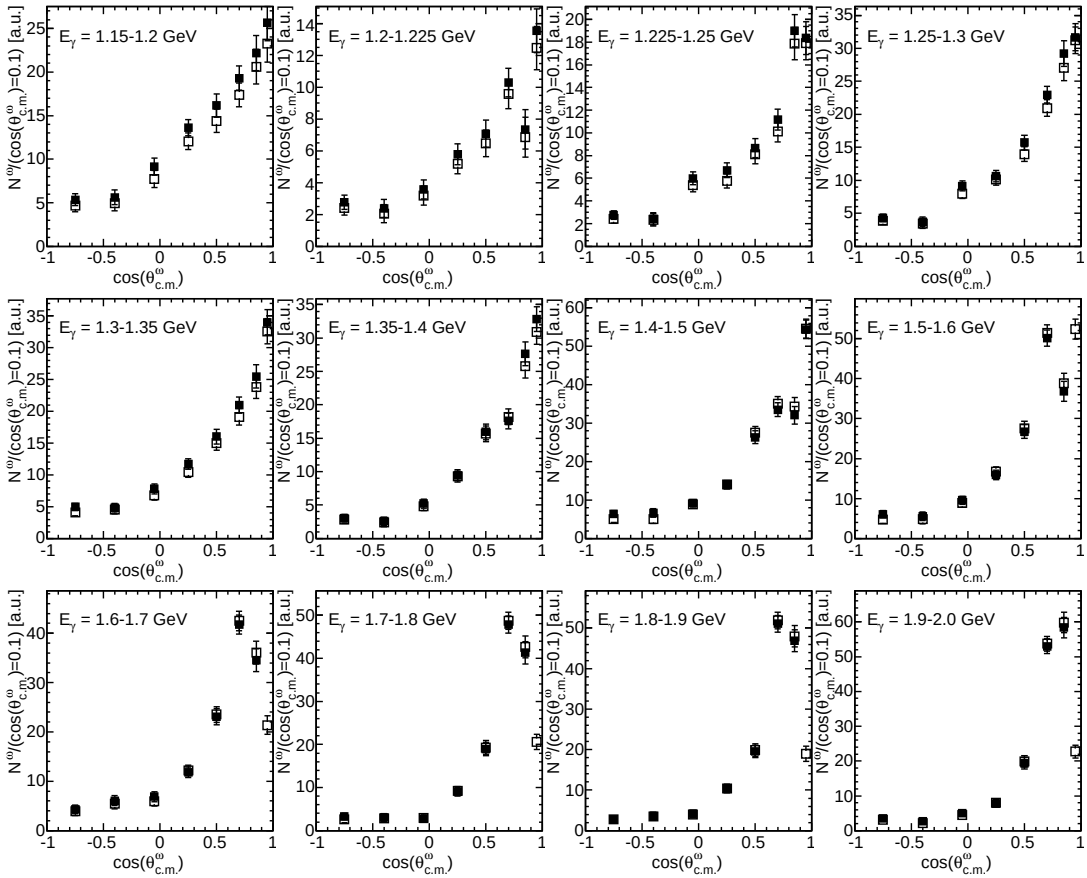

Figure 5.25: Number of ω mesons produced off the bound proton as a function of $\cos(\theta^{\omega}_{c.m.})$ normalized to $\cos(\theta^{\omega}_{c.m.}) = 0.1$ before correction $N_{\omega p}$ (open symbols) and after correction $N^{corr}_{\omega p}$ (full symbols) (see eq. 5.19). Note that the numbers are not yet corrected for detection efficiencies. The statistical errors are shown.

Since the correction factor ϵ^{misidp}_{data} enters, $N^{corr}_{\omega p}$ could not be determined for the angular bin $0.9 < \cos(\theta^{\omega}_{c.m.}) < 1.0$ for incident beam energies $E_\gamma < 1.5$ GeV. The differential cross-section off the bound proton, just as that off the free proton, had to be extrapolated into this region with a fit.

Figure 5.25 shows the number of ω mesons produced off the bound proton as a function of $\cos(\theta^{\omega}_{c.m.})$ with the different angular bin sizes taken into account before correction

$N_{\omega p}$ and after correction $N_{\omega p}^{corr}$. Even rather high values of the correction factors ϵ^{misidn}, since these correction factors are related to the relatively small number of detected neutrons, lead only to a minor correction of the number of ω mesons produced off the bound proton.

Acceptance of reaction off protons

The detection efficiency was obtained from a simulation of the reaction $\gamma p \rightarrow \omega p$ with LH_2 target and $\gamma d \rightarrow \omega p(n)$ with LD_2 target (here the effect of the Fermi motion is taken into account). In both cases the decay channel was $\omega \rightarrow \pi^0\gamma \rightarrow \gamma\gamma\gamma$. The ω mesons were isotropically generated in $\cos(\theta^{\omega}_{c.m})$. The event selection and analysis steps were exactly the same for the simulation as for the data. The angular efficiencies obtained for ω mesons produced off the free proton can be seen in fig. 5.26. The start distribution of the generated ω mesons off the free proton was flat in $\cos(\theta^{\omega}_{c.m.})$ and had a $1/E_\gamma$ behavior for the incident beam energy. The simulation of ω produced off the bound proton were done both with a flat $\cos(\theta^{\omega}_{c.m.})$ start distribution, shown in fig. 5.27 (left), and a forward peaking $\cos(\theta^{\omega}_{c.m.})$ start distribution, shown in fig. 5.27 (right). The later distribution is more realistic, due to the forward peaking behavior observed in the ω photoproduction process. The incident beam energy was in both cases a $1/E_\gamma$ distribution. The acceptance for ω mesons produced off a bound proton is shown in fig. 5.28 for both the flat start distribution and the forward peaking start distribution. They show a good agreement impying that the angular acceptance was independent of the shape of the start distribution. A flat start distribution was used to calculate the acceptance used to determine the differential cross-sections in this work.

It is important to note that the analysis was such that the recoil proton was required to be detected, so that the acceptances shown are the combined acceptances of detecting the three decay photons from the ω meson and the proton, *i.e.* $(\epsilon_{excl})^p = \epsilon_\omega \epsilon_p = \epsilon_{3\gamma}\epsilon_p$.

The angular acceptances show that the detection efficiency was decreasing as the ω meson was going in forward direction, especially for higher incident beam energies. When the ω meson was produced off the free proton the efficiency was even zero in the most forward bin, $0.9 < \cos(\theta^{\omega}_{c.m.}) < 1.0$ for $E_\gamma > 1550$ MeV. The ω mesons in this region were correlated to protons going backward in the c.m.-system, *i.e.* slow protons that did not have enough energy in the laboratory system in order to be detected. This was true also for the case when the ω meson was produced off a bound proton, but here the smearing of the Fermi motion allowed some protons to be detected so that the efficiency was small in this most forward bin, but non-zero.

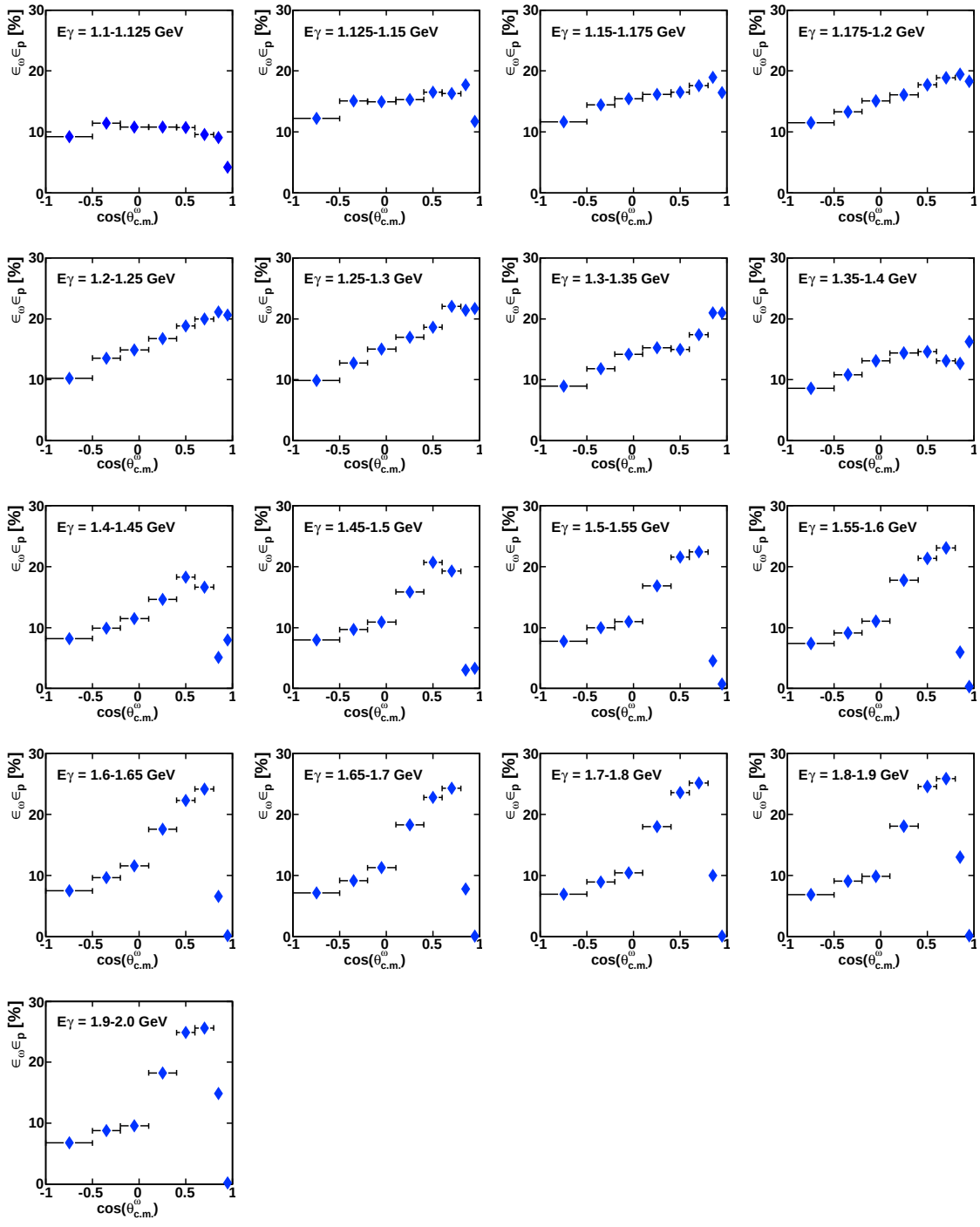

Figure 5.26: Angular efficiencies for detecting an ω meson in coincidence with a proton, $\epsilon_{3\gamma}\epsilon_p$, obtained from the simulation of the reaction $\gamma p \to \omega p \to \pi^0 \gamma p \to \gamma\gamma\gamma p$. The target was LH_2 and the proton assumed to be free.

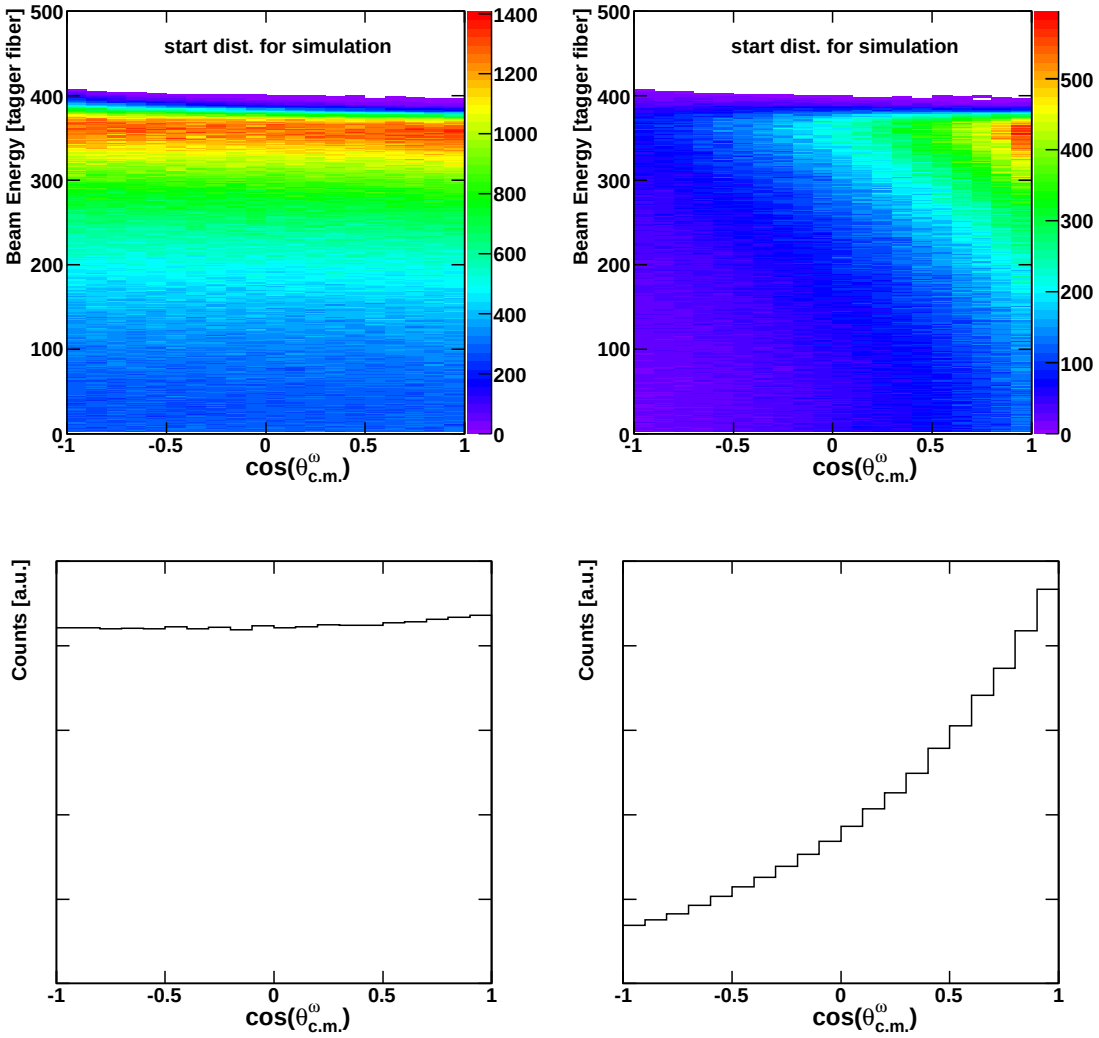

Figure 5.27: The $\cos(\theta^{\omega}_{c.m.})$ start distribution was taken to be flat (left) and forward peaking (right).

The forward peaking seen in the production of ω mesons together with the sharp decrease in efficiency in the same bin gave differential cross-sections that were steeply rising, as will be shown in sect. 6.1.1.

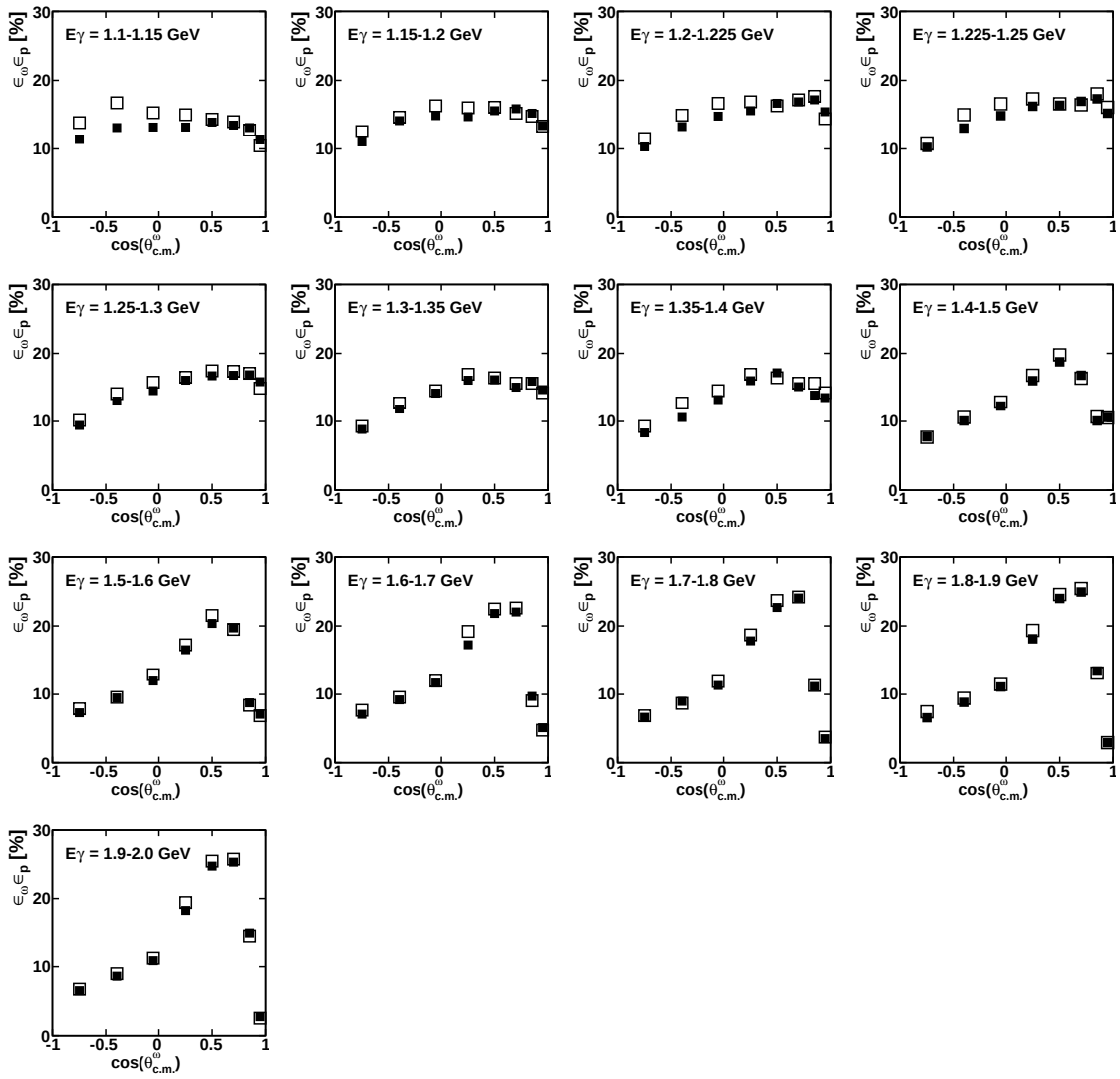

Figure 5.28: Angular efficiencies for detecting an ω meson in coincidence with a proton, $\epsilon_{3\gamma}\epsilon_p$, obtained from the simulation of the reaction $\gamma p(n) \rightarrow \omega p(n) \rightarrow \pi^0\gamma p(n) \rightarrow \gamma\gamma\gamma p(n)$. The target was LD_2 and the proton assumed to be bound with the Fermi momentum distribution shown in fig. 2.4. The $\cos(\theta^\omega_{c.m.})$ start distribution was flat (full symbols) and forward peaking (open symbols).

5.10. The quasi-free production off the bound neutron

The event selection for this reaction was that four neutral hits were registered and no further hits. Since the neutron is neutral, there was no straightforward way to distinguish it from the photons originating from the ω meson (as opposed to the case of the proton which is charged and was identified with the fiber detector or the vetos). This made the analysis a bit more complicated, requiring additional steps as can be seen in table 5.3.

Like in the proton case, the neutron did not deposit its whole energy, thus the mass cannot be determined and used as identification. Instead a missing mass analysis has to be used in order to identify the neutron from the four neutral hits ($n_1 n_2 n_3 n_4$). However, the first step was an attempt to remove the most prominent background, which in this case originated from the $\pi^0\pi^0$-channel (where the neutron was assumed not to have been detected). This was done by combining the four neutral hits two by two, plotting one combination versus the other. The events originating from the $\pi^0\pi^0$-channel showed up as a peak around the pion mass. A cut was placed around this peak (115 MeV $< m_{n_1 n_2} <$ 155 MeV and 115 MeV $< m_{n_3 n_4} <$ 155 MeV) in this two dimensional histogram (see fig. 5.29) and all events that fulfilled this condition were discarded.

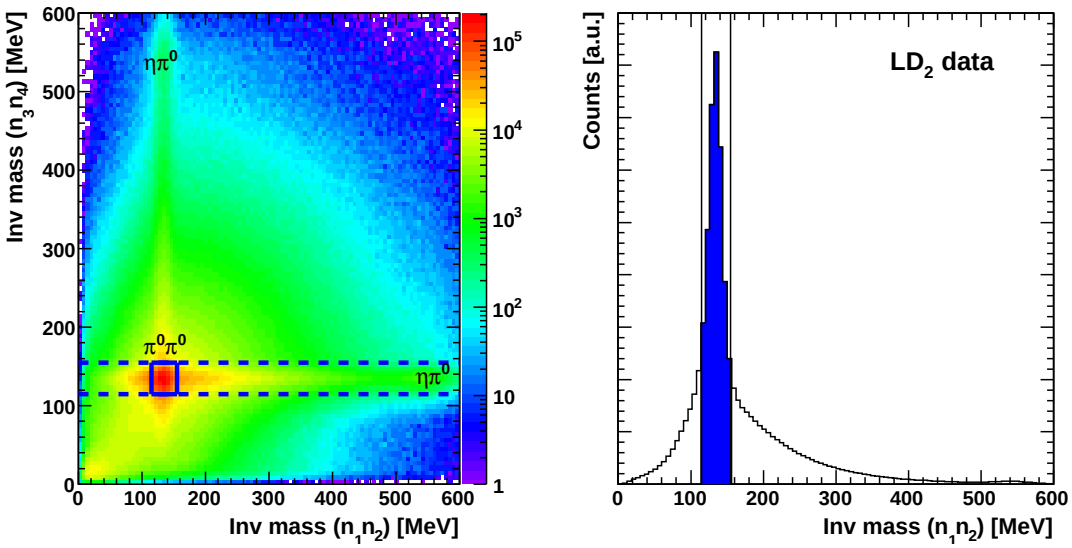

Figure 5.29: The anti-cut that was used to subtract $\pi^0\pi^0$-background in the case when the ω meson was produced off a neutron. Left: The invariant mass of two neutral hits versus the invariant mass of the other two neutral hits. The cut made around the $\pi^0\pi^0$-peak is shown in blue. All events inside this cut were eliminated. Right: The projection for 115 MeV $< m_{n_3 n_4} <$ 155 MeV. The excluded events are marked in blue. The contribution from the $\eta\pi^0$-channel is also seen, but was so small that no cut was made on that.

For the remaining events the pion was determined in the same way as in the proton-case (described in sect. 5.9) with the difference that here the combinatorics was made out of four neutral hits, giving six possible combinations. The invariant mass of all possible combinations of two photons were formed and a χ^2-test requiring the mass of a pion was used for the selection, see eq. 5.9. The χ^2 distribution and confidence level are shown in fig. 5.30. Subsequently, a cut around the pion peak (110 MeV $< m_{\gamma\gamma} <$ 160 MeV) for the selected solutions was placed. For the events where the selected solution fulfilled this cut the mass was set to the pion mass. The other events were discarded.

When the pion was successfully identified there exist two solutions for forming the ω meson with the two remaining neutral hits added to the pion. In order to select the true solution the missing mass for both solutions was calculated according to

$$m^n_{miss} = |\mathbf{P}_\gamma + \mathbf{P}_n - \mathbf{P}_{\pi^0\gamma}|, \tag{5.20}$$

where $\mathbf{P}_\gamma$, $\mathbf{P}_n$ and $\mathbf{P}_{\pi^0\gamma}$ are the four-momenta of the incident photon, the initial state neutron (assumed to be at rest) and the detected $\pi^0\gamma$. Because of the multiplicity of hits in the tagger, the correct one (corresponding to the incident photon) had to be selected. This was done by looking at the time information of the hit in TAPS (time information was only available for TAPS) compared to the time of the hits in the tagger. If at least one of the two photons originating from the pion entered TAPS, its time was used. In case both entered TAPS, their mean was used. If none of them entered TAPS, the time information from the two remaining neutral hits was used. It would have been preferable not to use the timing of the neutrons since they are slower than the photons, but since at this stage they were not separable, in some cases this was unavoidable. A cut was then placed on the calculated time difference at -3 ns to 3 ns defining the true taggerhit. This time interval could still contain several taggerhits and the missing mass and χ^2,

$$\chi^2 = (m^n_{miss} - m_n)^2\,, \tag{5.21}$$

were calculated for all these possibilities. This did not pose a problem because with the χ^2-test only one solution was chosen and, for example, hits in neighboring tagger fibers will all give the same combination. The χ^2-distribution and CL are shown in fig. 5.31. For the χ^2 calculation the nominal mass of the neutron was not used because it was found from simulation that the calculated missing mass waried with the incident energy. Therefore, m_n was corrected for by the fit in fig. 5.32 (left). Figure 5.32 (right) shows the $\pi^0\gamma$ invariant mass for the combinations selected by the χ^2-test together with the not selected combinations for the simulation. It shows that the χ^2-test successfully identified the correct combination. Only in a negligible part of the events the wrong combination was selected and the true solution discarded.

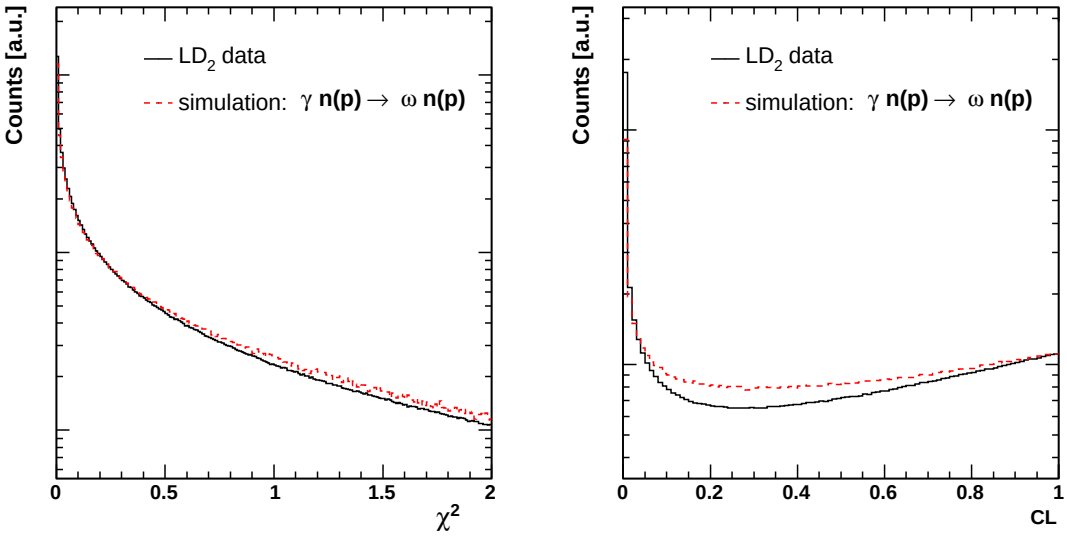

Figure 5.30: Left: χ^2 calculated by eq. 5.9 for the LD_2 data (black solid) and simulation (red dashed) for four neutral hits. Right: Confidence level. A rise in the CL distribution at higher CL values indicates that errors are underestimated.

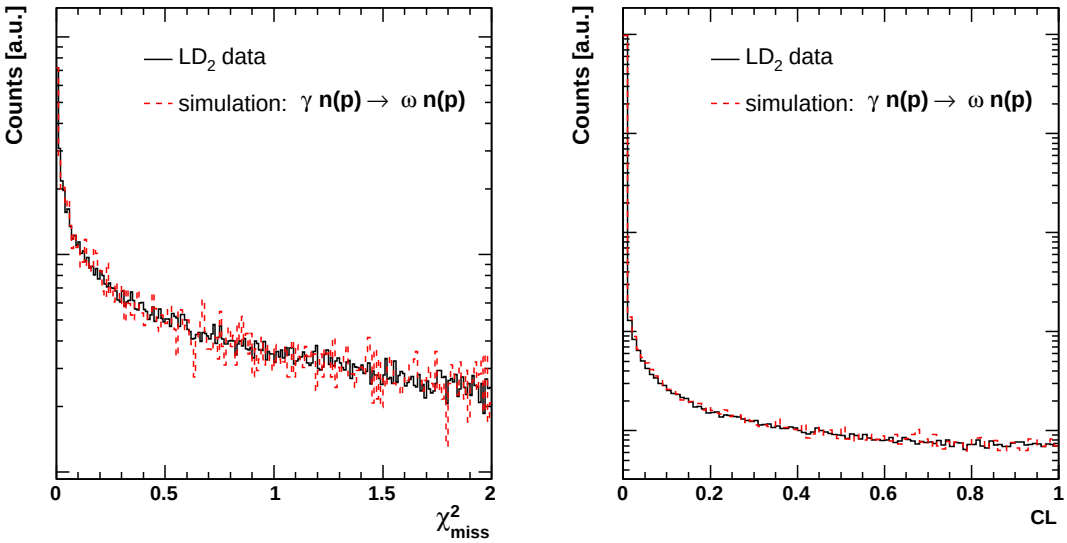

Figure 5.31: Left: χ^2_{miss} calculated by eq. 5.21 for the LD_2 data (black solid) and simulation (red dashed) for four neutral hits. Right: Confidence level. A decrease in the CL distribution at higher CL values indicates that errors are overestimated.

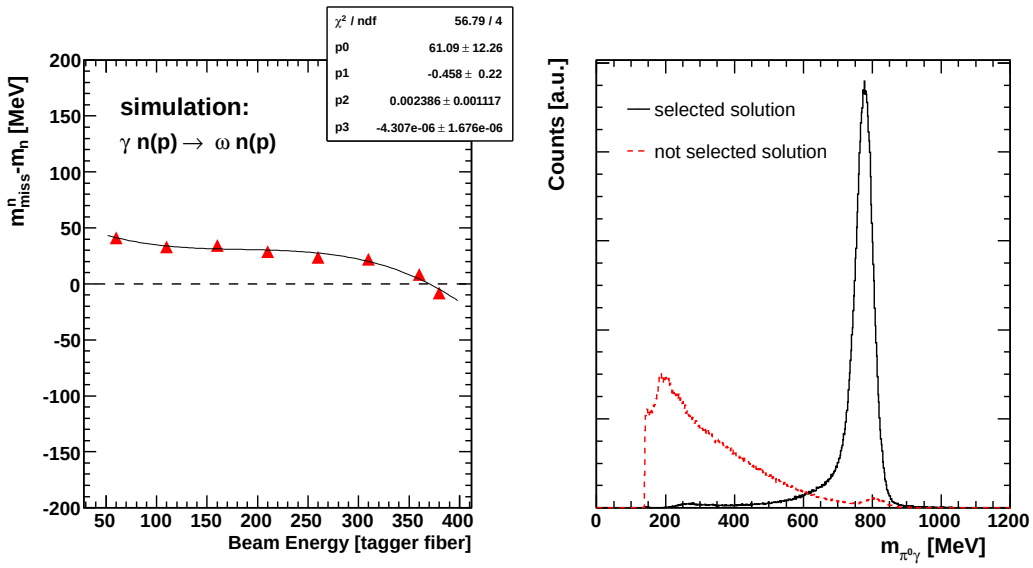

Figure 5.32: Left: Difference between the missing mass peak position and the nominal value of the neutron mass for simulation. Right: Invariant mass of $\pi^0\gamma$ for the selected solution (black) compared together with the not selected solution (red).

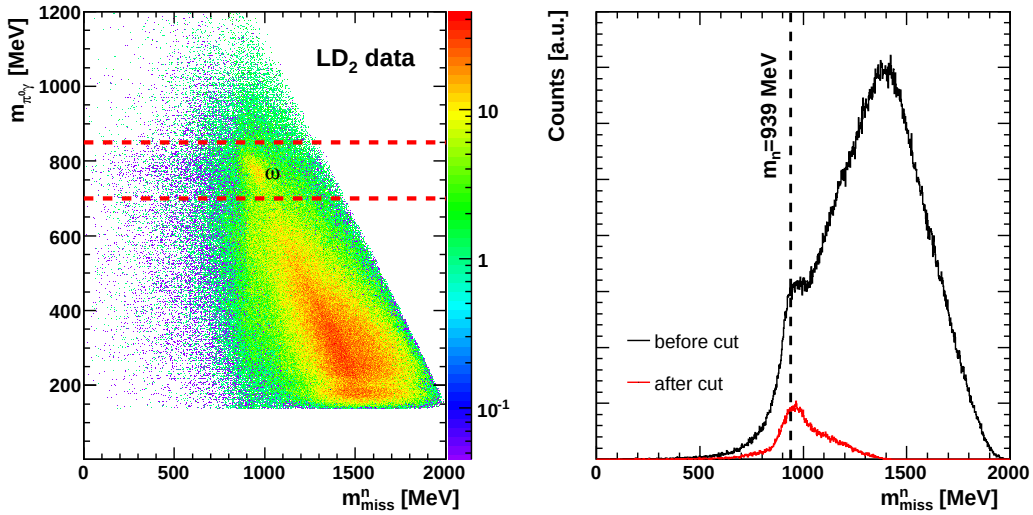

Figure 5.33: Left: The $\pi^0\gamma$ invariant mass versus the missing mass for LD_2 data for events with four neutral hits. The ω mesons that were produced off neutrons are marked in the picture together with a cut around the ω mass. Right: The missing mass before (black) and after (red) the indicated cut. After the cut a peak around the proton mass can clearly be seen.

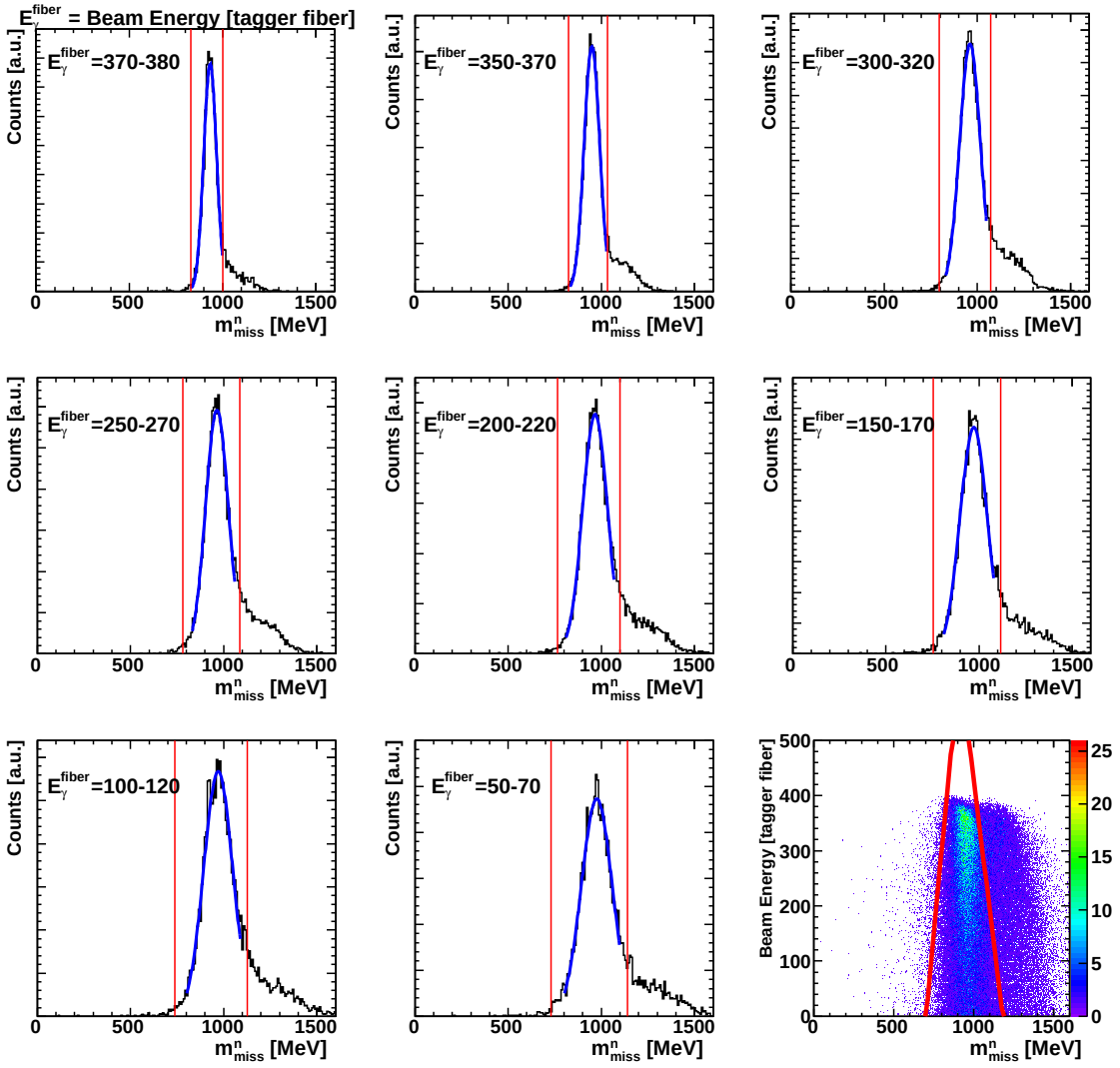

Figure 5.34: Missing mass spectra fitted with a Gaussian for different incident beam energies (in tagger fiber numbers) for a simulation of the reaction of an ω meson produced off a bound neutron and decaying into $\pi^0\gamma$. The beam energy is increasing with decreasing fiber number. Bottom right: The mean-$3\sigma < m^n_{miss} <$ mean+2σ missing mass cut around the neutron peak which is varying linearly with the incident beam energy.

Figure 5.33 (left) shows the $\pi^0\gamma$ invariant mass versus the missing mass calculated by eq. 5.20. The events of interest, the ω mesons detected in coincidence with neutrons, are marked in the figure. With a cut around the ω mass the peak in the missing mass spectrum around the neutron became more apparent, see fig. 5.33 (left).

This indicated that a missing mass cut around the neutron mass could reduce the background under the ω meson peak. The cut was obtained from the $\gamma n(p) \rightarrow \omega n(p)$ simulation. The simulation showed that the width of the proton peak in the missing mass spectra depended on the incident beam energy, becoming wider as the beam energy was increasing. This is shown in fig. 5.34 where the missing mass spectra for several different incident beam energies were fitted with Gaussians and the missing mass cut was chosen to be a mean-$3\sigma < m^n_{miss} <$ mean+2σ cut around the neutron peak varying linearly with the incident beam energy (shown in fig. 5.34 (bottom right)). The missing mass cut was

$$703.547 + 0.318076E^{fiber}_{\gamma} < m^n_{miss} < 1174.22 - 0.38852E^{fiber}_{\gamma}\,, \tag{5.22}$$

which implied a cut of 824 MeV $< m^n_{miss} <$ 1027 MeV at an incident beam energy $E_\gamma =$ 1108 MeV and 715 MeV $< m^n_{miss} <$ 1160 MeV at an incident beam energy $E_\gamma = 2008$ MeV.

Figure 5.35 (left) shows the missing mass cut together with the missing mass versus incident beam energy for the LD_2 data. To the right in the same figure the effect of the cut on reducing the background in the $\pi^0\gamma$ invariant mass spectrum is illustrated. The signal-to-background is highly improved by the cut.

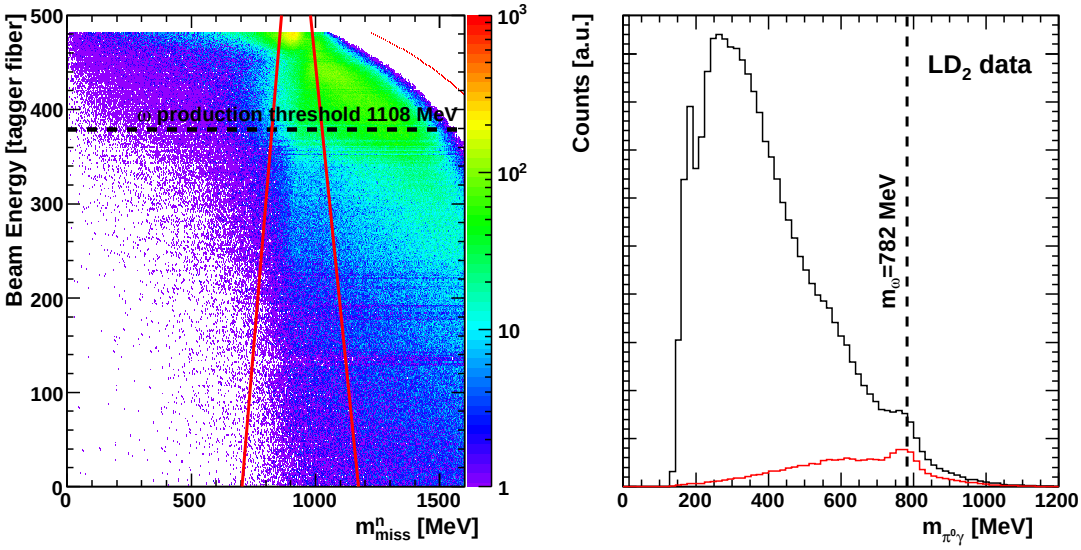

Figure 5.35: Left: The missing mass versus the incident beam energy in tagger fibers (the beam energy is increasing with decreasing fiber number) for the case when the ω meson is produced off a bound neutron. The missing mass cut is drawn in red. Right: The effect of the missing mass cut on removing background. The invariant mass of $\pi^0\gamma$ above the production threshold of the ω meson without (black) and with (red) the missing mass cut.

The next step in the analysis was a cut on the polar angle of the particle that was thought to be the neutron, $\theta^n_{lab.}$. This angle was restricted by kinematics to a certain maximum value which depended on the incident beam energy. Figure 5.36 (upper left) shows this dependence for the $\gamma n(p) \rightarrow \omega n(p)$ simulation. The maximum $\theta^n_{lab.}$ was $\approx$65° at in incident beam energy of 2.0 GeV ($E^{fiber}_{beam} = 79$). Lower incident beam energies [MeV] allowed for smaller maximum $\theta^n_{lab.}$. Figure 5.36 (upper right) shows the situation for the data. Here, events at angles that were not allowed by the kinematics of the reaction were found. These particles cannot be neutrons and therefore they were discarded by the cut shown in red. Figure 5.36 (lower left) illustrates the difference observed in the data compared to the simulation by showing the full projection onto the $\theta^n_{lab.}$-axis of the two upper figures. A considerable part of the events in the data was found at angles above the maximum allowed angle. Figure 5.36 (lower right) shows the $\pi^0\gamma$ invariant mass spectrum for events inside and outside the cut. It can be seen that some of the particles at high $\theta^n_{lab.}$ correspond to an ω signal in the $\pi^0\gamma$ invariant mass spectrum. They were removed by the $\theta^n_{lab.}$-cut, since they did not come from the sought for $\gamma n(p) \rightarrow \omega n(p)$ channel.

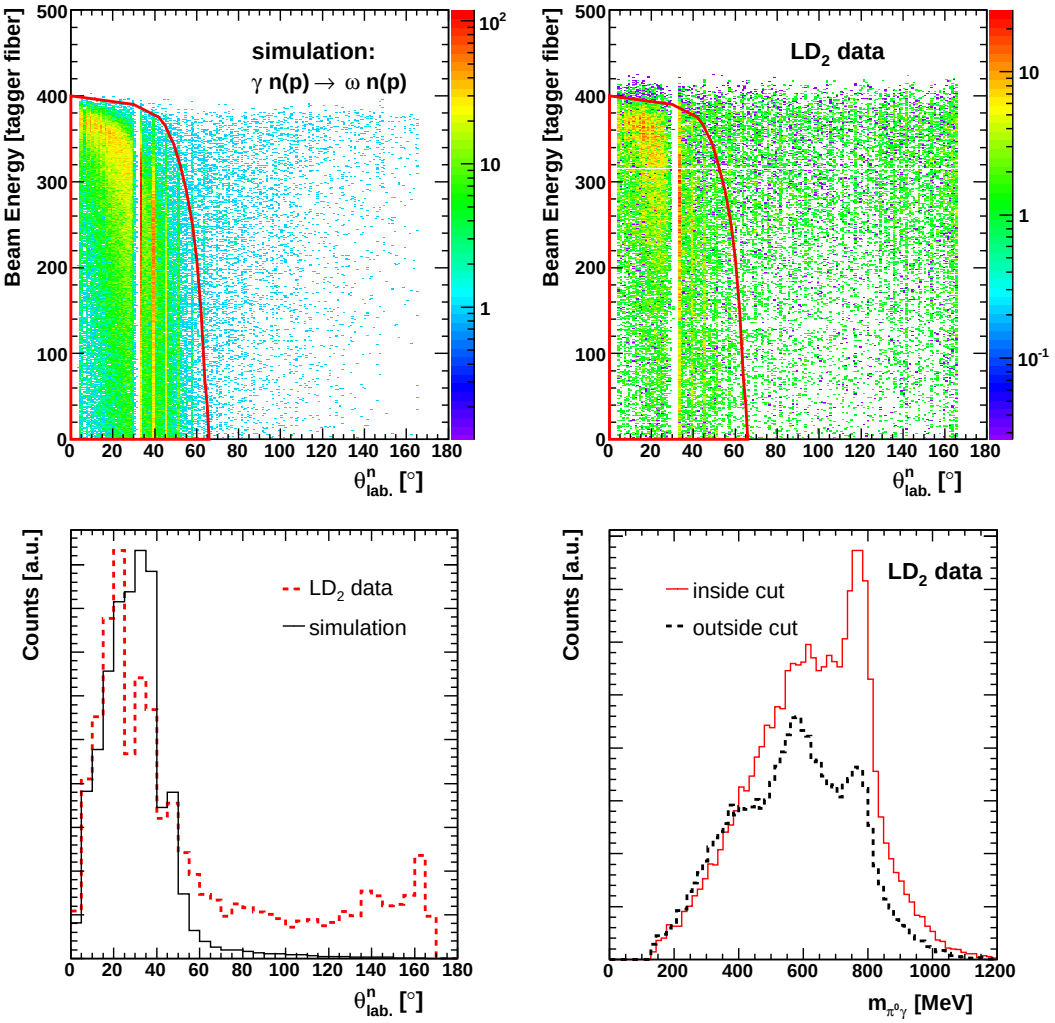

Figure 5.36: Polar angle of the neutron versus incident beam energy [fiber numbers] for simulation (upper left) and for data (upper right). The cut used is drawn in red in both figures. Lower left: Projection onto the $\theta^n_{lab.}$-axis for simulation (black solid) and data (red dashed). Lower right: The invariant mass of $\pi^0\gamma$ for events inside the cut (red solid) and for events outside the cut (black dashed) for the data.

After these cuts, the $\pi^0\gamma$ invariant mass spectra were fitted with the function 5.16, the background was subtracted and the number of ω mesons was estimated, $N_{\omega n}$. Some examples of spectra at different incident beam energies are shown in fig. 5.37, but (as in the case of the ω meson being produced off the proton) the production was not isotropic

and therefore the angular distributions had to be studied. The invariant mass spectra for different bins of $\cos(\theta^{\omega}_{c.m.})$ are shown in fig. 5.38 for the incident beam energy E_{γ} = 1708-1808 MeV. For the incident energy bin E_{γ} = 1108-1158 MeV the fitting was too difficult, hence, no cross-sections were determined for this bin. All $\pi^0\gamma$ invariant mass spectra together with the fits for the exclusive analysis off the bound neutron can be seen in appendix G.

The number of ω mesons determined from the fits did not all come from the sought after channel. They had to be corrected for protons which were mis-identified as neutrons due to inefficiencies of the fiber and veto detectors. The correction factors for this mis-identification were determined from the LH_2 data as described in sect. 5.9 and defined in eq. 5.17. The true number of ω mesons produced off a neutron was calculated by

$$N^{corr}_{\omega n} = N_{\omega n} - \epsilon^{misidp}_{data} \cdot N_{\omega p}\,. \tag{5.23}$$

Figure 5.39 shows the number of ω mesons produced off the bound neutron as a function of $\cos(\theta^{\omega}_{c.m.})$ with the different angular bin sizes taken into account before correction $N_{\omega n}$ and after correction $N^{corr}_{\omega n}$. The necessary corrections due to the mis-identification of protons as neutrons mostly affect the region where the ω meson is going in forward direction. However, even after these corrections the production off neutrons favors ω mesons in the forward region.

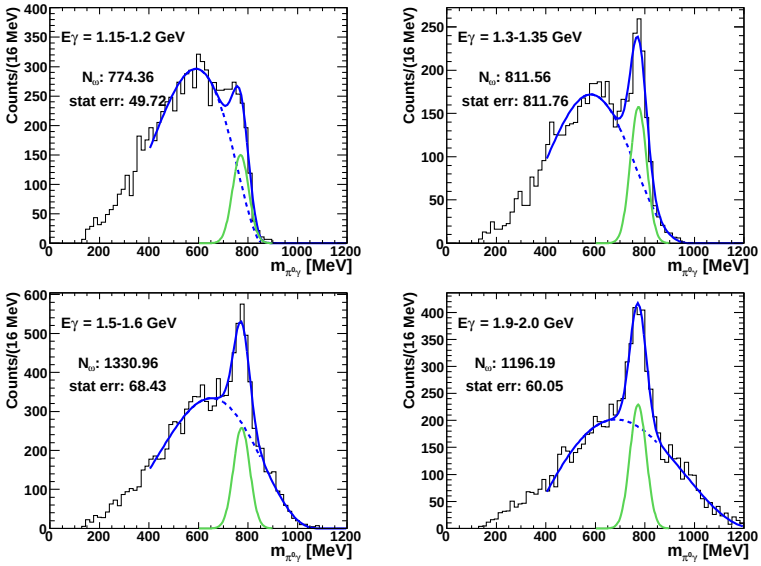

Figure 5.37: A few examples of $\pi^0\gamma$ invariant mass spectra for four different incident beam energies for the event selection four neutral hits for the LD_2 target data.

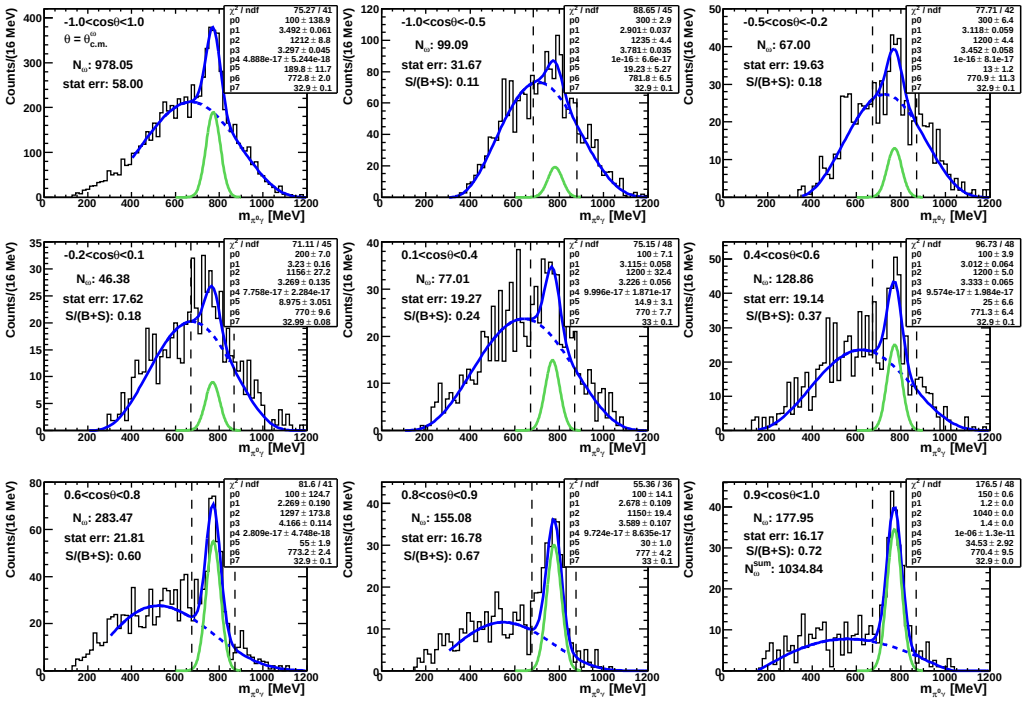

Figure 5.38: $\pi^0\gamma$ invariant mass spectra for the $\cos(\theta^{\omega}_{c.m.})$ angular bins with E_γ = 1708-1808 MeV for the events with four neutral hits for the LD_2 target data.

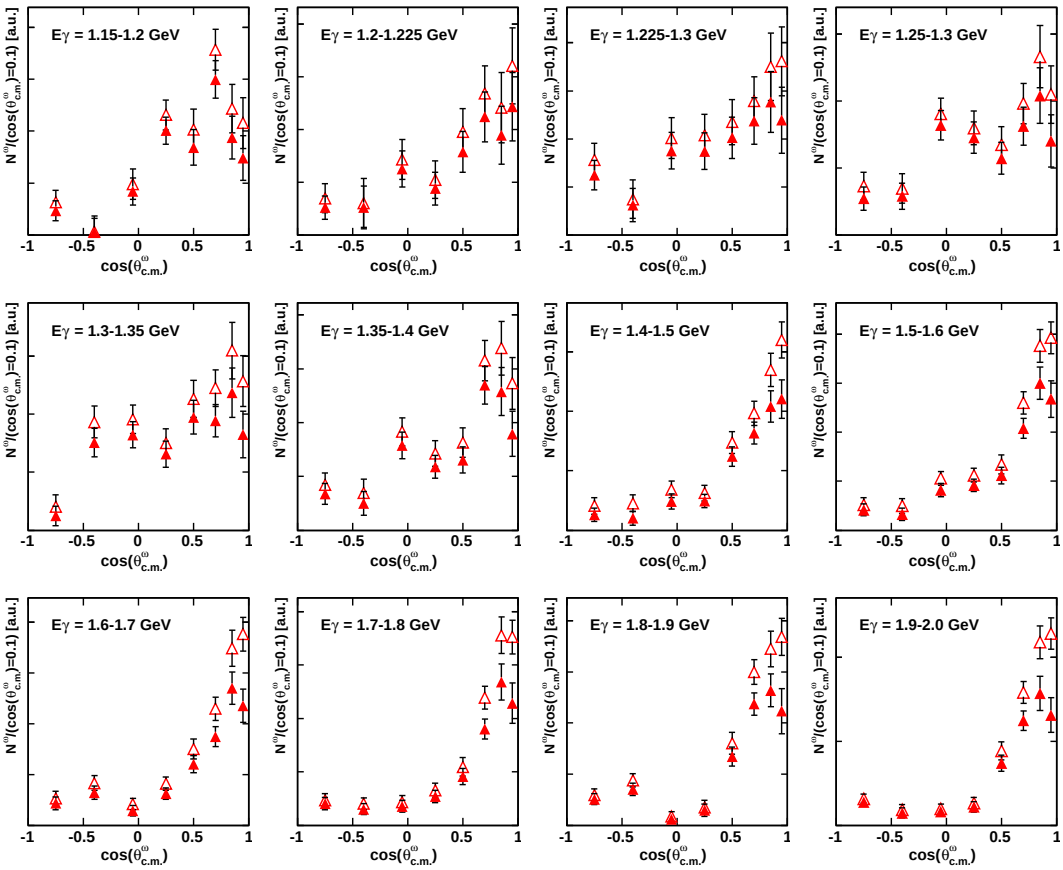

Figure 5.39: Number of ω mesons produced off the bound neutron as a function of $\cos(\theta^{\omega}_{c.m.})$ normalized to $\cos(\theta^{\omega}_{c.m.}) = 0.1$ before correction $N_{\omega n}$ (open symbols) and after correction $N^{corr}_{\omega n}$ (full symbols) (see eq. 5.23). Note that the numbers are not yet corrected for detection efficiencies.

Acceptance of reaction off neutrons

The detection acceptance was obtained from a simulation of the reaction $\gamma d \rightarrow \omega n(p) \rightarrow \pi^0 \gamma n(p) \rightarrow \gamma\gamma\gamma n(p)$ with LD_2 target (here the effect of the Fermi motion was taken into account). The simulations were done for a flat start distribution with ω mesons were isotropically generated in $\cos(\theta^{\omega}_{c.m})$ and for a forward peaking start distribution such as the ones shown in fig. 5.27. The incident beam energy had a $1/E_{\gamma}$ behavior. The event selection and analysis steps were exactly the same for the simulation as for the data. The angular acceptances for ω mesons produced off a bound neutron are shown in fig. 5.40 for both the flat and the forward peaking start distribution. The acceptances can be seen to be independent of the shape of the start distribution. A flat start distribution was used to calculate the acceptance used to determine the differential cross-sections in this work.

It is important to note that the analysis was such that the recoil neutron was required to be detected, which means that the efficiencies shown are the combined efficiency for detecting the three decay photons from the ω meson and the neutron, *i.e.* $(\epsilon_{excl})^n = \epsilon_{\omega}\epsilon_n = \epsilon_{3\gamma}\epsilon_n$.

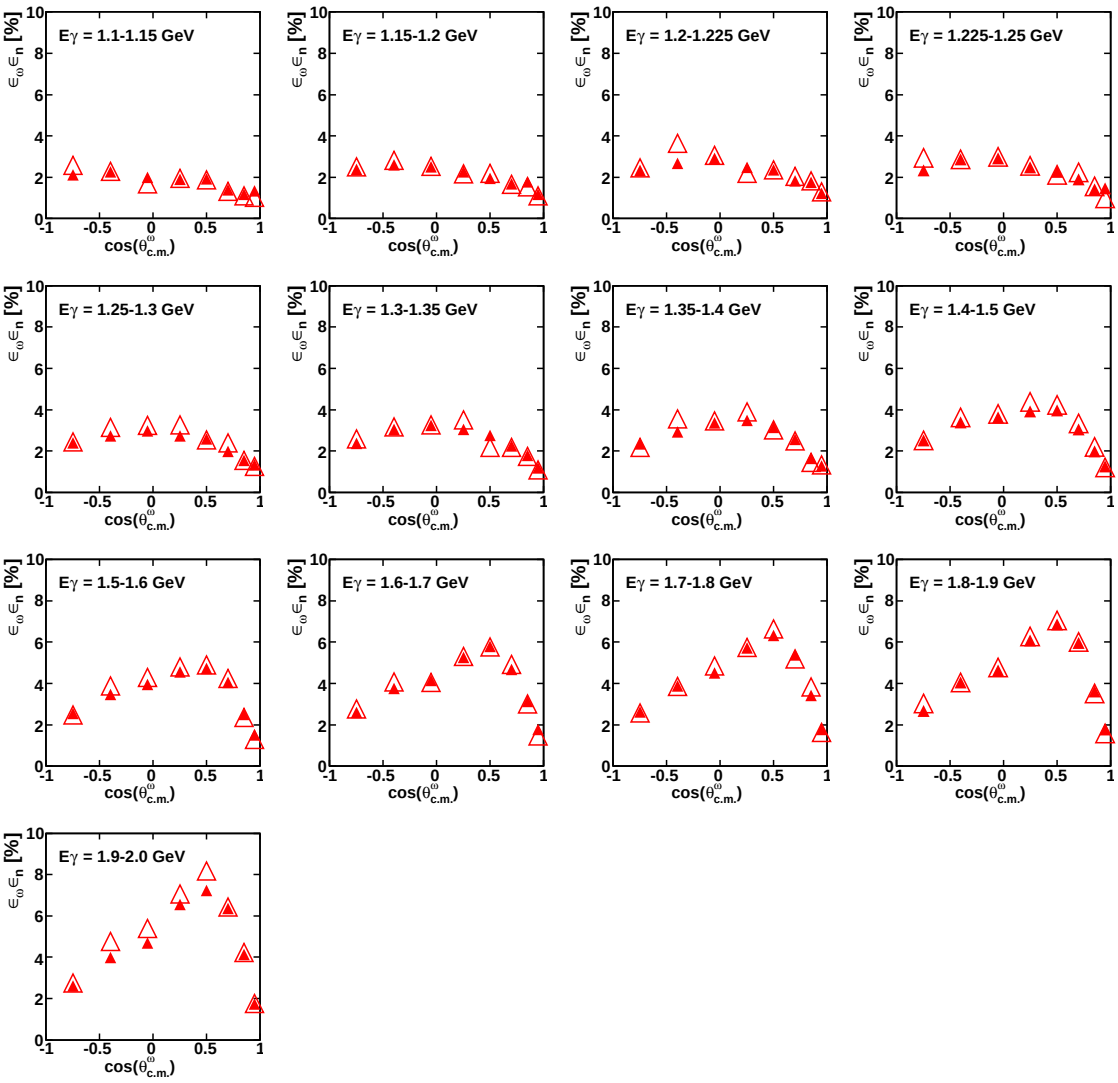

Figure 5.40: Angular efficiencies for detecting an ω meson in coincidence with a neutron, $\epsilon_{3\gamma}\epsilon_n$, obtained from the simulation of the reaction $\gamma n(p) \rightarrow \omega n(p) \rightarrow \pi^0 \gamma n(p) \rightarrow \gamma\gamma\gamma n(p)$. The target was LD_2 and the neutron was assumed to be bound with the Fermi momentum distribution shown in fig. 2.4. The $\cos(\theta^\omega_{c.m.})$ start distribution was flat (full symbols) and forward peaking (open symbols).

The angular efficiencies show that the detection efficiency decreases as the ω meson goes forward, especially for higher incident beam energies. The explanation for this is the same as in the case that the ω meson was produced off the bound proton; in this angular bin the neutrons (backward going in the c.m.-system) were so slow that they did not have enough energy in order to be detected. Due to the Fermi smearing some of them were detected, but the detection efficiency is low in this angular region.

The forward peaking that was seen in the production of ω mesons together with the sharp decrease in efficiency in the same bin made the differential cross-sections steeply rising as is shown in sect. 6.1.2.

Total detection efficiencies

The total detection efficiencies for the three different reaction channels as a function of incident beam energy are shown in fig. 5.41. They are the angle integrated efficiencies for the simulations with flat start distributions shown in figures 5.26, 5.28 and 5.40.

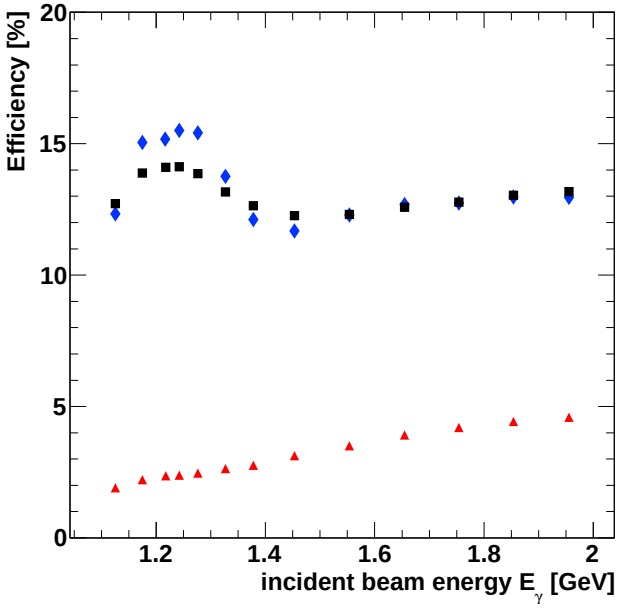

Figure 5.41: Total efficiencies for the three reaction channels: ω meson produced off the free proton (blue diamonds), off the bound proton (black squares) and off the bound neutron (red triangles).

5.11. The time-of-flight (TOF)

The time-of-flight (TOF) is generally the time it takes for a particle to travel from the target to the detector. For the setup used in this experiment time information was only available for particles entering the TAPS detector. The time was measured relative to either hits in the tagger or to photons registered in TAPS for the same event. These different time references have different resolutions (650 ps for TAPS and 1.6 ns for the tagging system). Figure 5.42 shows the deposited energy versus the time-of-flight of what is thought to be the recoil nucleon for charged particles (left) and for neutral particles (right). In the upper two figures the time information from the tagger was used and in the lower two figures the time of photons entering TAPS was used as reference time. One clearly sees the difference in time resolution between the TAPS and the tagger system. Since TAPS had the better time resolution it was preferred as reference time. Figure 5.42 also illustrates the different patterns displayed by protons, neutrons and photons. The characteristic proton band can clearly be seen (left). This band is due to the fact that protons loose their energy primarily through ionization and there is a dependence between the kinetic energy of the protons and the energy deposited in the detector. Generally, the dependence is such that the faster the protons the more energy they deposit. However, this is only true until they reach the maximum at $E_{dep} = 400$ MeV. At that point they start exiting at the back of the crystals and deposit less and less energy. There is an intensity in this plot around $E_{dep} \approx 200$ MeV at time zero, where the protons become minimum ionizing particles since they deposit exactly this amount of energy before they exit at the back of the crystals. The neutrons loose their energy through other processes (see sect. 3.6) and do not show an E_{dep}-time-dependence. The photons can be seen as a line at zero time, since they are all traveling with the same speed regardless of their energy.

Since the distance traveled by a particle from the target to TAPS varied depending on the direction of the particle, a normalization was required in order to give a meaningful comparison. The time-of-flight normalized to a distance of 1 m was calculated by

$$TOF = \frac{t - t_\gamma}{d} + t_{\gamma,1m}\,, \tag{5.24}$$

where t was the time of the particle of interest, t_γ was the mean time of the neutral particles belonging to that event which were assumed to be photons (the neutron was excluded from this group by the missing mass analysis), d is the flight path of the particle and $t_{\gamma,1m}$ is the time required for a photon to travel a distance of 1 m (*i.e.* $t_{\gamma,1m} = \frac{1 \cdot 10^9}{c} = 3.33564$ ns, c is the speed of light $c = 299792458$ m/s).

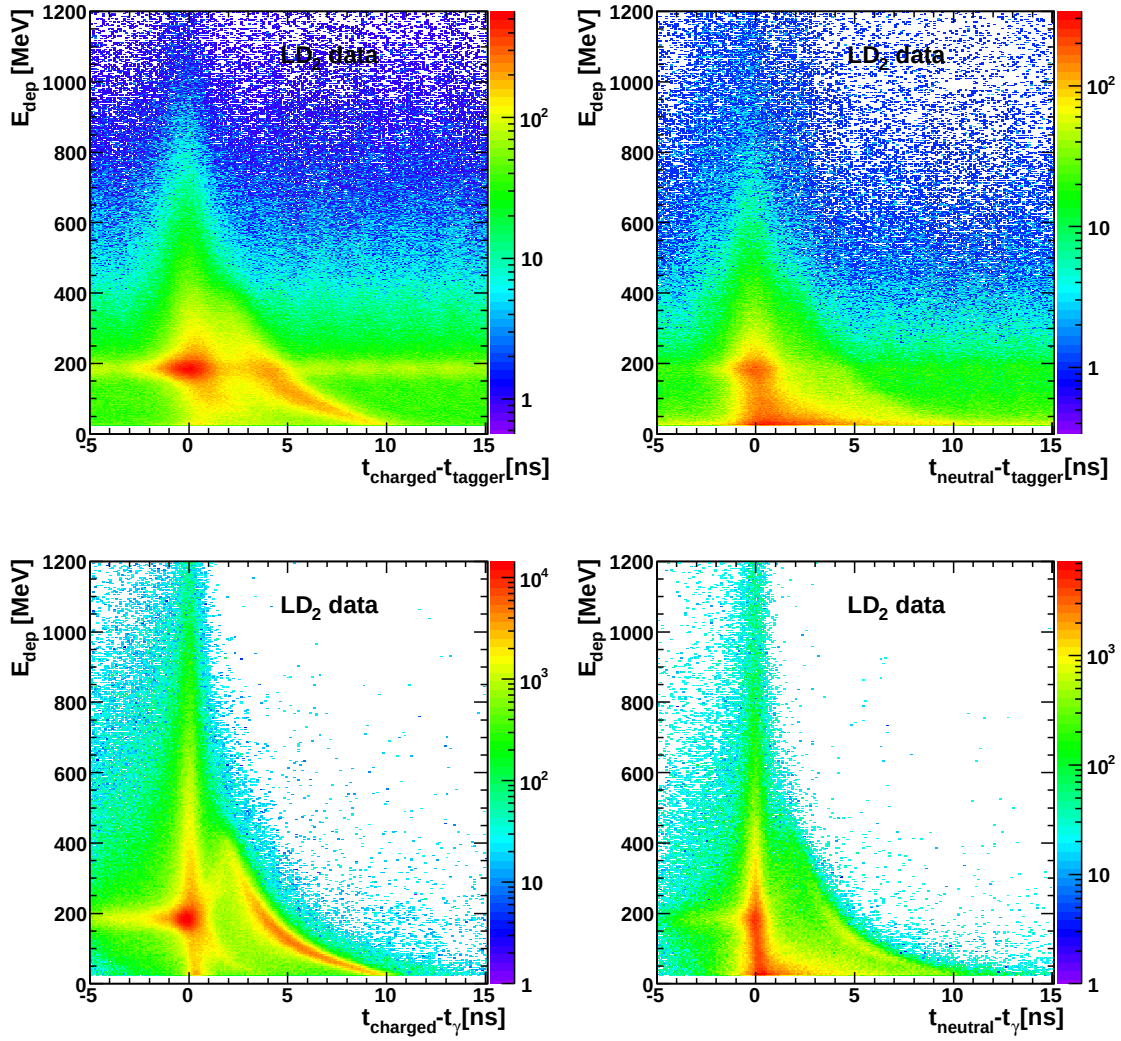

Figure 5.42: The deposited energy E_{dep} as a function of relative timing of what is believed to be the recoil nucleon using the time information of the tagger (top) and the time information of photons in TAPS (lower) for charged nucleons (left) and neutral nucleons (right). The effect of the different time resolutions can clearly be seen. The resolution (σ) was 650 ps for TAPS and 1.6 ns for the tagging system.

Placing cuts in the E_{dep}-TOF spectra according to where the protons and neutrons are expected helps in identifying the reaction of interest and reduces the background. Figure 5.43 illustrates the effect of a cut around the proton band (events outside of this cut were discarded) on reducing the background for the reaction when the ω mesons were produced off the bound proton. The upper figures show the E_{dep}-TOF spectra for simulation of the particular reaction channel (left) and for data (right). The reference time from TAPS was used and the TOF was normalized to 1 m. The cut is drawn in red. The lower left figure shows the $\pi^0\gamma$ invariant mass for all events, for events where the recoil nucleon was detected in TAPS, for events where the recoil nucleon was detected in TAPS where the time information was available, and the same events after the time cut depicted in the upper figures was applied. The lower right figure shows the invariant mass for all events and the total remaining events after the time cut was placed. Both spectra were fitted and their signal-to-background ratios were determined, yielding S/(S+B) = 0.42 without the cut and S/(S+B) = 0.45 with the time cut for the ω meson produced off the bound proton.

The same type of figures, but for the case when the ω meson was produced off a bound neutron, are shown in fig. 5.44. Here the cut was TOF $>$ 4 ns as shown in the upper two figures. Only events satisfying this cut were kept. The lower right figure shows the effect of this cut on the total events, before cut compared to after cut. For ω meson produced off the bound neutron the numbers were S/(S+B) = 0.33 before the cut and S/(S+B) = 0.37 after the cut.

Such a small gain in the signal-to-background ratios was not enough to motivate the more complicated analysis required to use time cuts. Therefore, they were not used in the analysis to obtain the results of this thesis.

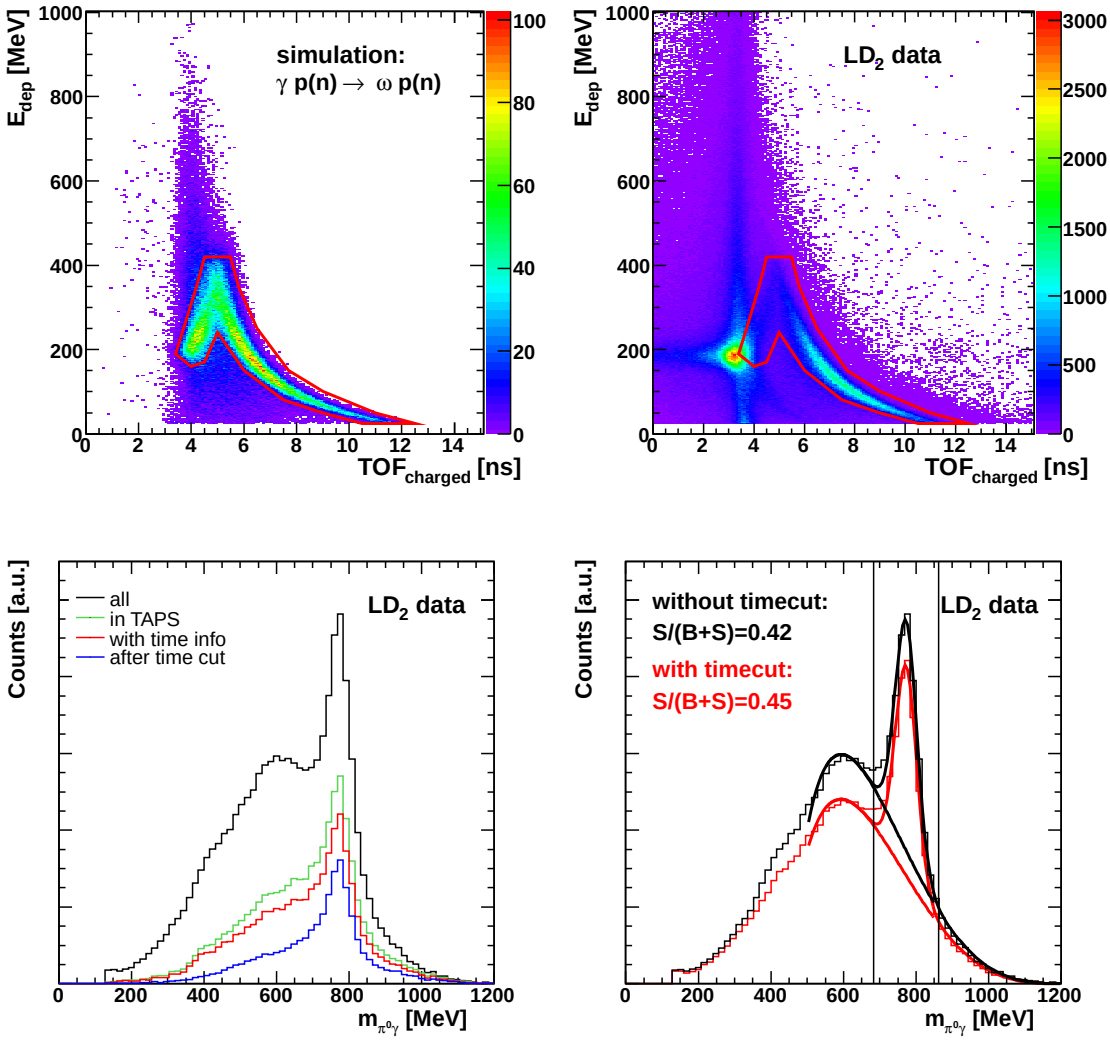

Figure 5.43: Top: The deposited energy E_{dep} as a function of the time-of-flight TOF of what is believed to be the recoil proton, for simulation (left) and for the LD_2 target data (right). The cut is drawn in red. Lower left: The $\pi^0\gamma$ invariant mass in the incident beam energy range E_γ = 1108-2008 MeV for all events (black), for events where the recoil proton is going into TAPS (green), for events where the recoil proton is going into TAPS with available time information (blue), events remaining after the cut around the proton band (red). Lower right: The effect of the time cut on the total signal-to-background ratio.

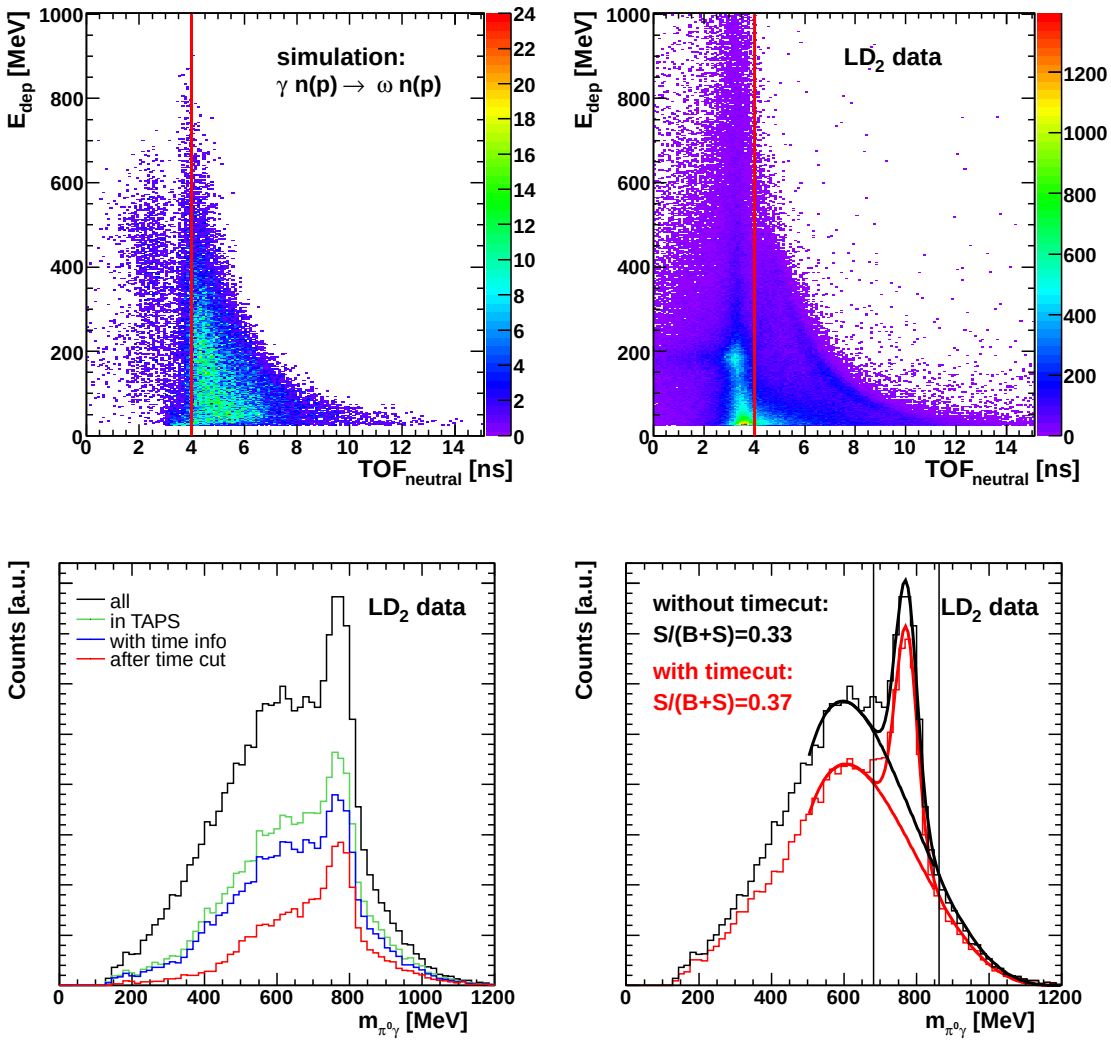

Figure 5.44: Top: The deposited energy E_{dep} as a function of the time-of-flight TOF of what is believed to be the recoil neutron, for simulation (left) and for the LD_2 target data (right). The cut is drawn in red. Lower left: The $\pi^0\gamma$ invariant mass in the incident beam energy range E_γ = 1108-2008 MeV for all events (black), for events where the recoil neutron is going into TAPS (green), for events where the recoil neutron is going into TAPS with available time information (blue), events remaining after the cut around the neutron band (red). Lower right: The effect of the time cut on the total signal-to-background ratio.

5.12. Inclusive analyses

The inclusive analyses were done as a check of the results from the exclusive analyses. In the inclusive analyses the recoil nuclei were not required to have been detected. This means that the method was independent of proton or neutron detection efficiencies, only the ω meson detection efficiency played a role. The event selection for the inclusive analyses was three neutral hits and no further hits or at least three neutral hits and four hits in total (the fourth hit may be charged or uncharged). The analysis steps for the inclusive reactions are listed in table 5.4. For the four hits events the steps were identical to the ones in the exclusive analysis up to the point of the $\theta_{lab.}^{nucl}(E_{\gamma}^{beam})$-cut that was only made in the exclusive analyses. This cut was not made in the inclusive analyses, since here the nucleon was not required to have been detected.

The three neutral hits (and no further hits) events, included in the inclusive analysis, introduced an additional cut that was not used in the exclusive analyses, namely a cut on the opening angle between the π^0 and the γ originating from the ω meson. This cut was necessary in order to reduce a strong background channel seen in the three neutral hits events, but for consistency it was also placed for the four hits events in the inclusive analysis.

The analysis steps in the inclusive analyses will be described in more detail in sect. 5.12.3 for ω mesons produced off LH_2 and in sect. 5.12.4 for ω mesons produced off LD_2. The figures illustrating the cuts in these sections are for the group of events with three neutral hits (and no further hits) since the four hits events have been shown in the exclusive analyses.

The inclusive analysis had the advantage over the exclusive analysis that the nucleon detection efficiency was irrelevant. As was shown in figure 5.26 the proton detection efficiency was dropping to zero for the reaction when the ω meson went forward in the c.m.-system for incident beam energies above 1500 MeV. In this region, the protons did not have enough kinetic energy in order to be detected. Therefore, the exclusive differential cross-sections had to be extrapolated into this region in order to determine the total cross-section. This problem was avoided in the inclusive analysis, where full differential cross-sections could be obtained, without any extrapolation needed.

Since the recoil nucleon detection efficiencies did not enter in the inclusive analyses, the detection efficiency (the one to detect the ω meson) was the same, irrespective of the

target. The ω meson detection efficiency was determined in two different ways giving two different methods for determining the inclusive cross-sections.

5.12.1. Phase Space Method

In this method the same phase space simulation as for the exclusive channels was used, but treated in an inclusive manner by the event selection described above. Figure 5.55 shows this efficiency, *i.e.* the ω detection efficiency, for the phase space simulation of ω meson produced off the free proton. Figure 5.63 shows the same angular efficiencies obtained from the simulation of the ω meson produced off the bound proton and off the bound neutron treated in an inclusive manner. They are in very good agreement, as would be expected.

5.12.2. The Grid Method

The so-called grid method is independent of any reaction kinematics and uses an event-by-event efficiency correction depending on the kinetic energy ($T^{\omega}_{lab.}$) and the polar angle ($\theta^{\omega}_{lab.}$) of the ω meson. The ω mesons were generated in GEANT with a flat ($\theta_{lab.}, T_{lab.}$)-distribution (see fig. 5.45 (upper left)) and the same two dimensional histogram was plotted for the detected ω mesons, *i.e.* the requirement 650 MeV $< m_{\pi^0\gamma} <$ 900 MeV, (see fig. 5.45 (upper right)). The ratio of these two histograms gave the efficiency (see fig. 5.45 (lower left)). This efficiency was smoothed in order to avoid irregularities and the resulting grid efficiency after smoothing is shown in fig. 5.45 (lower right). Each event was corrected event-wise with this efficiency according to the kinetic energy and polar angle of the reconstructed ω meson.

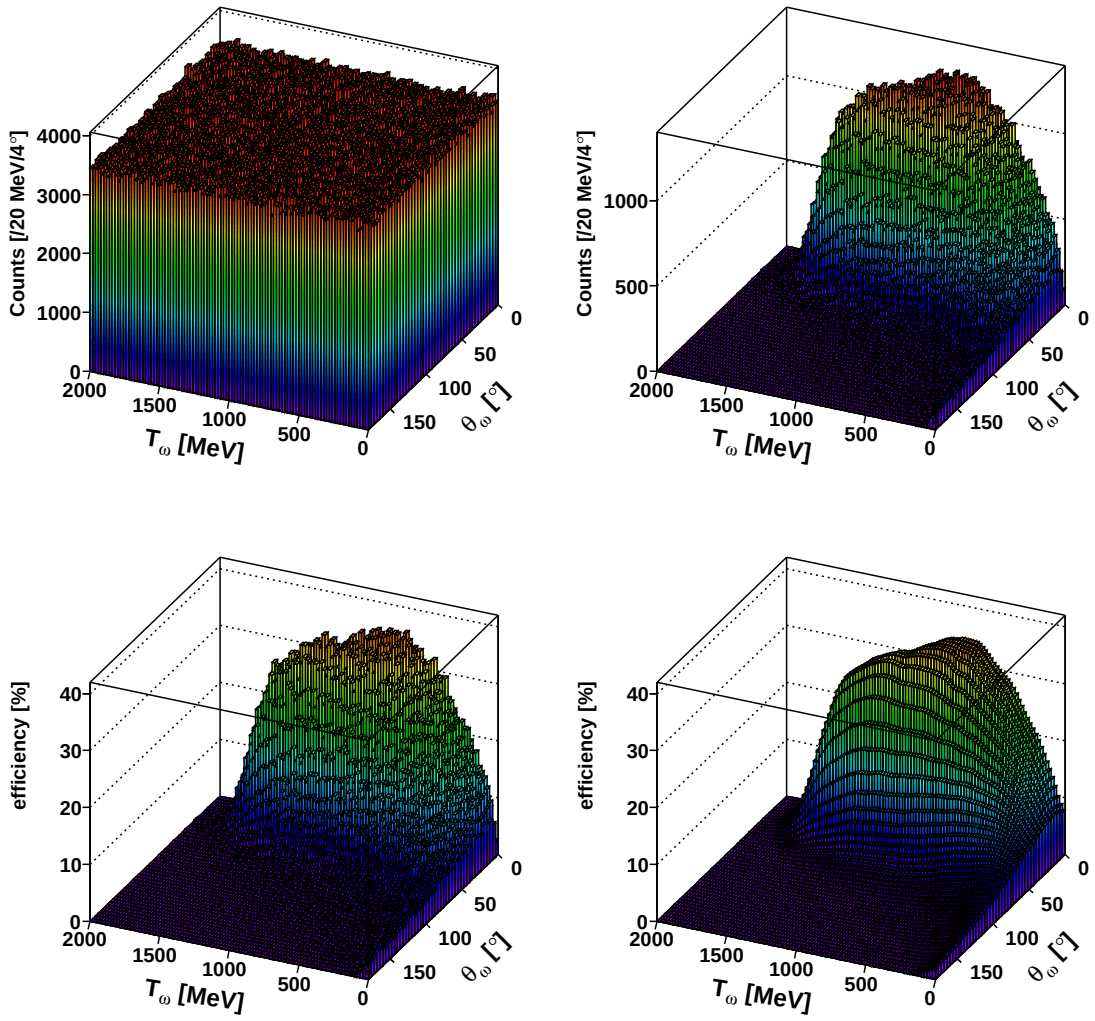

Figure 5.45: Upper left: start distribution of a simulation of isotropically distributed ω mesons as a function of kinetic energy of the ω meson T_ω and its polar angle in the laboratory system θ_ω. Upper right: reconstructed ω mesons for the simulation. Lower left: The grid efficiency obtained. Lower right: The grid efficiency after smoothing.

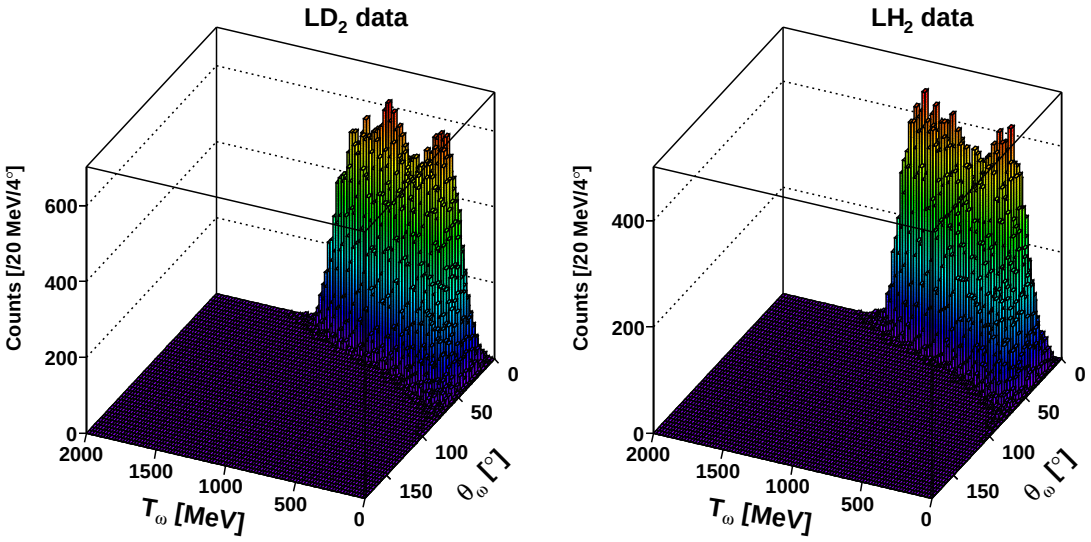

Figure 5.46: The distribution of an ω mesons as a function of kinetic energy of the ω meson T_ω and its polar angle in the laboratory system θ_ω for the LD_2 data (left) and LH_2 data (right) before acceptance correction. A missing mass cut and a cut around the ω mass in the $\pi^0\gamma$ invariant mass spectrum, 650 MeV $< m_{\pi^0\gamma} <$ 900 MeV, were placed.

Figure 5.46 shows the distribution in the ω meson region, 650 MeV $< m_{\pi^0\gamma} <$ 900 MeV, (background and signal) for the LD_2 target data (left) and LH_2 target data (right). This check was done in order to ensure that the events in this mass region were covered by an efficiency in the grid, which was the case. To avoid that too low entries create spikes in the efficiency corrected histograms, a cut was placed at an efficiency of 1.0 %. Events with a lower acceptance were discarded.

5.12.3. The inclusive production off LH_2

The inclusive analysis of the ω meson produced of LH_2 provided an independent check of the cross-section of the ω meson produced off the free proton, obtained in the exclusive analysis. Since there is no other nucleon, other than the proton, present in the target the cross-sections from the two different methods should be the same, *i.e.*

$$\sigma_{incl}^{LH_2} = \sigma_p \,, \tag{5.25}$$

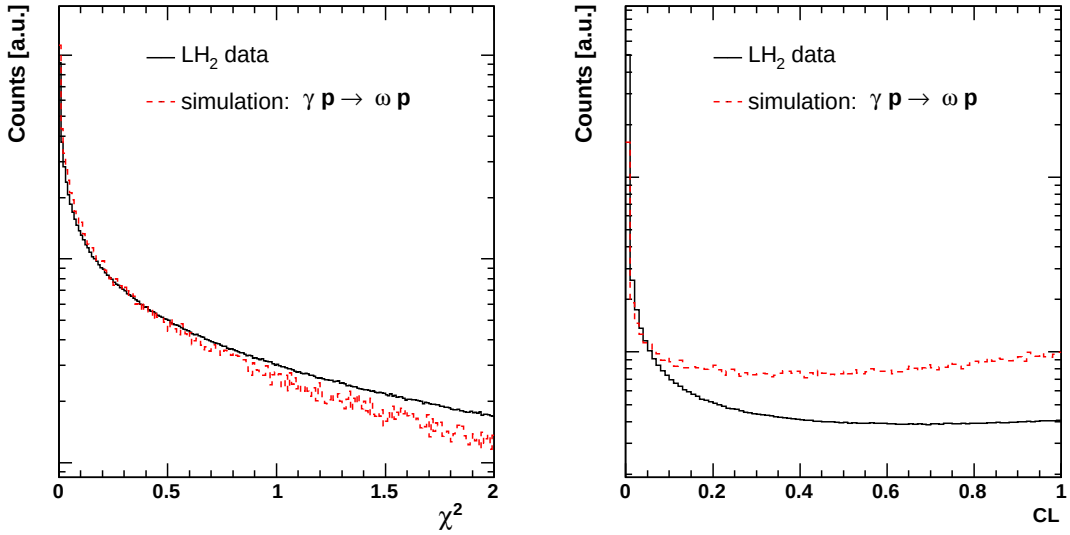

Figure 5.47: Left: The χ^2 distribution for the selection of the two photons originating from the π^0 for for events with three neutral hits and no further hits from the LH_2 data (black solid line) and $\gamma p \to \omega p \to \pi^0 \gamma p \to \gamma\gamma\gamma p$ simulation (red dashed line). Right: The confidence level.

where σ_p is the exclusive cross-section of the ω meson being produced off the free proton. At higher incident beam energies, though, other possible production channels may imply that the equality in eq. 5.25 no longer holds.

The first step in the inclusive analysis was to select the two photons originating from the pion. This was done with a χ^2 test (see eq. 5.9). Figure 5.47 shows the χ^2 (left) and the confidence level (right) for the simulation and for the data for three neutral hits events. A cut around the pion mass (110 MeV $< m_{\gamma\gamma} <$ 160 MeV) was placed and the third neutral hit was then added to the invariant mass. The missing mass was then calculated according to eq. 5.13. Figure 5.48 (left) shows the invariant mass of $\pi^0\gamma$ versus the missing mass for events with three neutral hits and no further hits. The ω mesons in connection with protons can clearly be seen in the figure. Figure 5.48 (right) shows the projection onto the missing mass axis before and after a cut around the ω meson mass (700 MeV $< m_{\pi^0\gamma} <$ 850 MeV) has been applied. After this cut a clear peak around the proton mass can be seen. A missing mass cut according to eq. 5.14 was therefore placed in order to reduce the background. The missing mass cut is shown in red in fig. 5.49 (left).

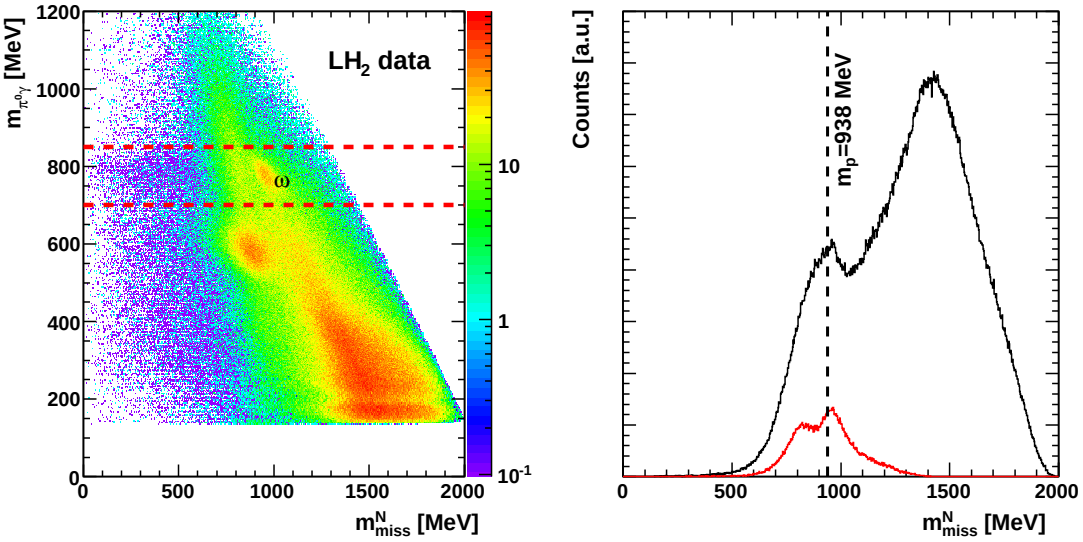

Figure 5.48: Left: The invariant mass of $\pi^0\gamma$ versus the missing mass for the event selection of three neutral hits and no further hits for the LH_2 target data. Right: The full projection on the x-axis (black) and the projection after a cut in the $\pi^0\gamma$ invariant mass around the ω mass shown (red).

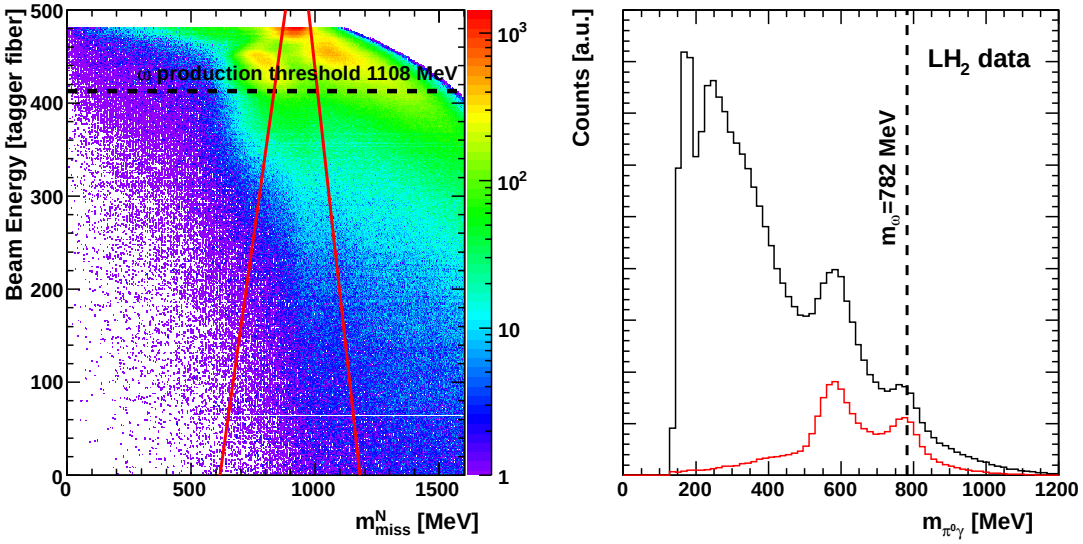

Figure 5.49: Left: The missing mass versus the incident beam energy in tagger fibers (the beam energy is increasing with decreasing fiber number) for the event selection of three neutral hits and no further hits for the LH_2 target data. The missing mass cut is drawn in red. Right: The invariant mass of $\pi^0\gamma$ above the production threshold of the ω meson without (black) and with (red) the missing mass cut.

Figure 5.49 (right) illustrates the effect of this cut on reducing the background. A clear reduction of the background can be seen.

An obvious feature in the invariant mass spectrum is a peak around 550 MeV. This peak was not removed by the missing mass cut and that was the motivation for the last cut, a cut on the opening angle between the π^0 and the γ originating from the ω meson in the center-of-mass system, $\theta_{c.m.}^{\pi^0,\gamma}$. The cut was dependent on the momentum of the ω meson in the center-of-mass system, $p_{c.m.}^{\omega}$, according to

$$p_{c.m.}^{\omega} < -11.11 \cdot \theta_{c.m.}^{\pi^0\gamma} \frac{\text{MeV}/c}{\text{deg}} + 2000 \text{ MeV}/c\,. \tag{5.26}$$

Events outside of this cut were discarded. Figure 5.50 (upper left) shows this cut together with a $\gamma p \to \omega p$ simulation and even though some of the events ended up outside of this cut, it is clear that most of the ω mesons satisfied this cut. The situation for the data (upper right) was completely different to the simulation. Here, a considerable part of the events ended up outside of this cut, in two distinct areas. The lower figures shows the invariant mass for the simulation (left) and the data (right) before and after the opening angle cut. The peak around 550 MeV in the data was successfully removed by this cut.

A simulation of the single pion production ($\gamma p(n) \to \pi^0 p(n) \to \gamma\gamma p(n)$) showed that this was indeed the background channel responsible for this peak. Figure 5.51 (left) illustrates that this simulated channel exactly reproduces the intensities outside of the cut that were seen in the data. Figure 5.51 (right) shows the invariant mass of the single π^0 production channel for the simulation and the peak around 550 MeV can clearly be seen before the cut and that it was successfully removed with this cut. This strong peak originated from events where a proton was mis-identified as a neutral particle and was assumed to be the third photon. Even though the probability for this mis-identification was small, the contribution was still large due to the large cross-section for the single pion production. Removal of this background peak was crucial in order to get a reliable fit of the background in the invariant mass spectra.

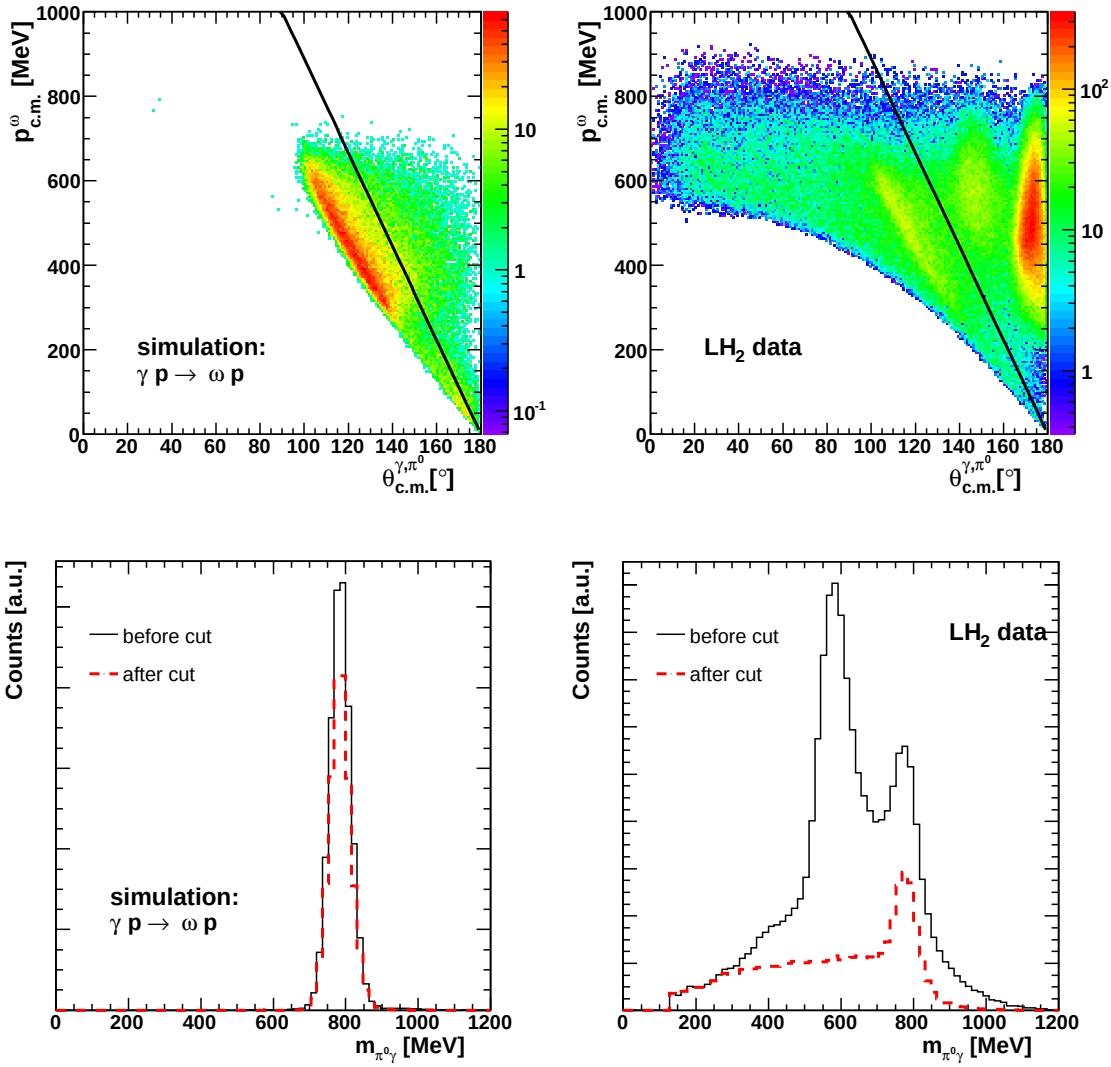

Figure 5.50: Top: The opening angle between the π^0 and γ versus the momentum of the reconstructed ω meson in the center-of-mass system for events with three neutral hits and no further hits for simulation (left) and LH_2 target data (right). The cut is drawn in black. Lower: The $\pi^0\gamma$ invariant mass before (black solid) and after (red dashed) the opening angle cut for the simulation (left) and for the data (right).

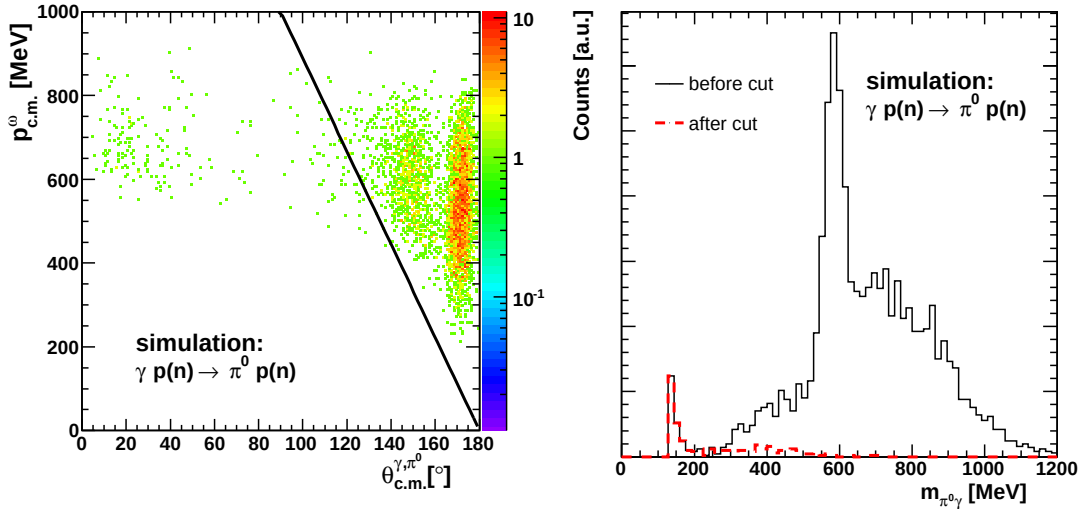

Figure 5.51: Left: The opening angle between the π^0 and γ (proton mis-identified as γ) versus the momentum of the reconstructed ω meson in the center-of-mass system for events with three neutral hits and no further hits for a simulation of single pion production off the bound proton, $\gamma p(n) \rightarrow \pi^0 p(n)$. The cut is drawn in black. Right: Invariant mass spectra for the same simulation outside (black soild) and inside (red dashed) the opening angle cut.

The events surviving these cuts were corrected for the detection efficiencies as described in sect. 5.12.1 for the phase space method and in sect. 5.12.2 for the grid method. In figure 5.52 some examples of invariant mass spectra before (left) and after (right) event-by-event efficiency correction can be seen for different bins of $\cos(\theta^{\omega}_{c.m.})$ for an incident beam energy E_γ = 1700-1800 MeV. All fits (with the function 5.16) to the $\pi^0\gamma$ invariant mass spectra (before and after event-wise efficiency correction) for the inclusive analysis of the LH_2 target data can be found in appendix E. The numbers of ω mesons before efficiency correction are shown in fig. 5.53.

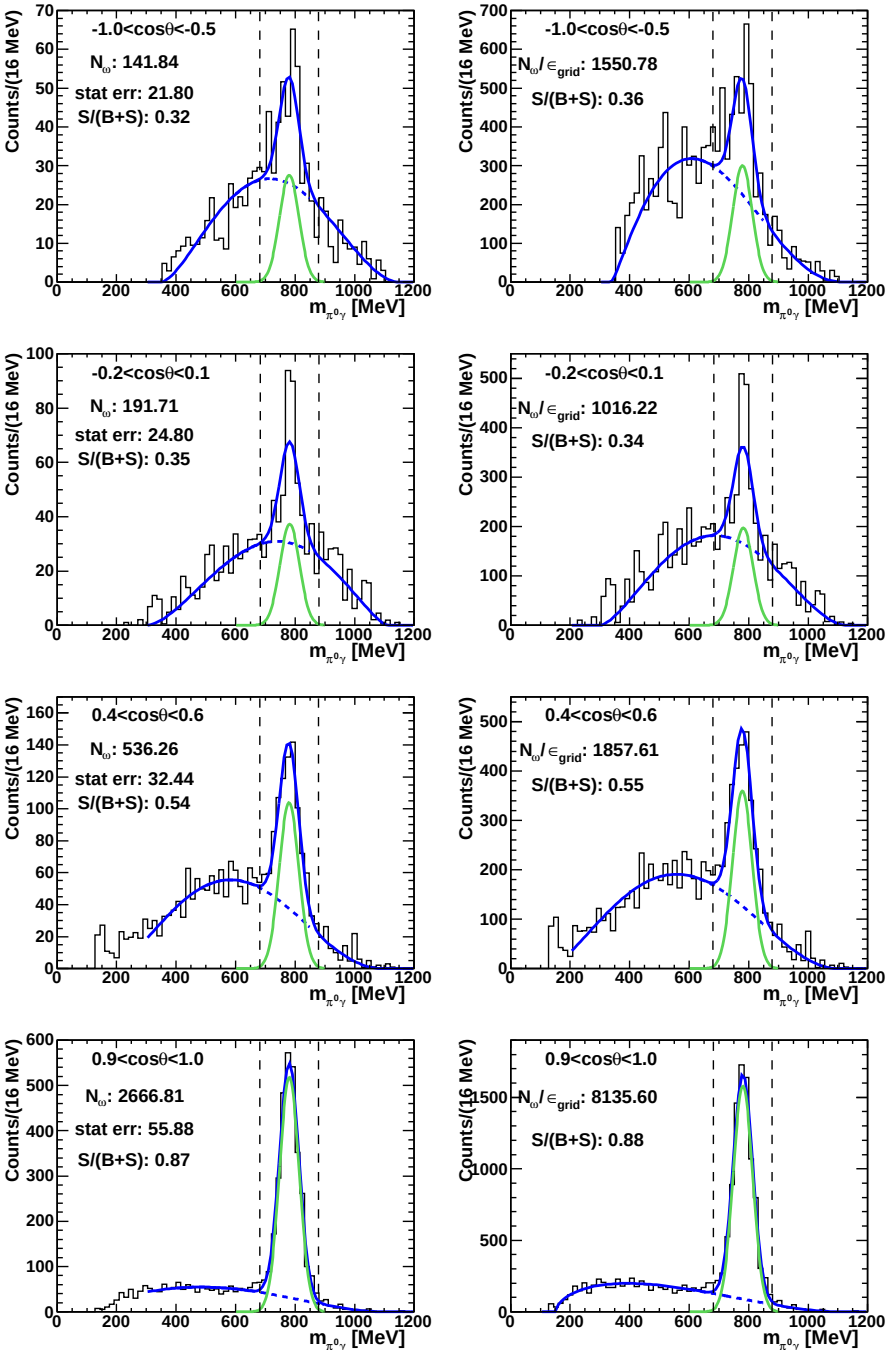

Figure 5.52: The $\pi^0\gamma$ invariant mass for a few different $\cos(\theta^{\omega}_{c.m.})$ angular bins for incident beam energy E_γ = 1700-1800 MeV for the inclusive analysis off the LH_2 target. The figures to the left are before efficiency correction and the figures to the right have been event-wise efficiency corrected depending on the $\theta_{lab.}$ and $T_{lab.}$ of the ω meson. The signal-to-background ratio obtained from the fits are shown.

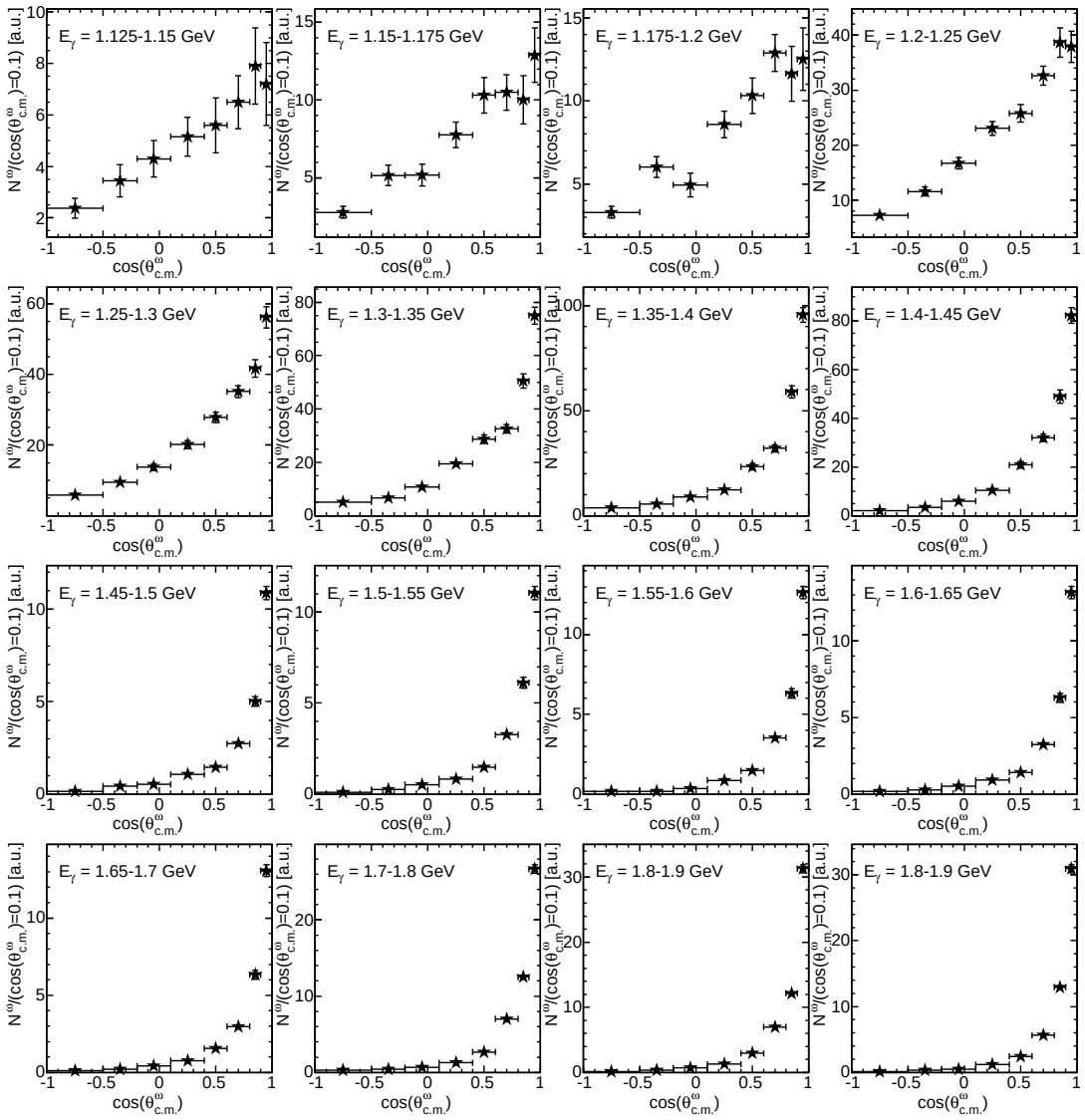

Figure 5.53: Number of ω mesons produced off the free proton as a function of $\cos(\theta^{\omega}_{c.m.})$ (with the different angular bin sizes taken into account) for the inclusive analysis. Note that the numbers are not yet corrected for detection efficiencies. The statistical errors are shown.

The average angular efficiency was recalculated from the grid method, ϵ_{grid}, and compared to the ones obtained from the phase space simulations,

$$\epsilon_{grid}(\Delta\cos(\theta^{\omega}_{c.m.}), \Delta E^{beam}_{\gamma}) = \frac{N^{detected}(\Delta\cos(\theta^{\omega}_{c.m.}), \Delta E^{beam}_{\gamma})}{N^{detected}_{corrected}(\Delta\cos(\theta^{\omega}_{c.m.}), \Delta E^{beam}_{\gamma})}, \tag{5.27}$$

where $N^{detected}$ are the number of detected events before efficiency correction and $N^{detected}_{corrected}$ are the number of detected events after event-by-event efficiency correction according to the grid efficiency. This was done for bins of $(\Delta\cos(\theta^{\omega}_{c.m.}), \Delta E^{beam}_{\gamma})$.

The grid efficiency did not take the signal losses due to the missing mass cut, $\epsilon^{misscut}_{loss}$, and due to the opening angle cut, $\epsilon^{oanglecut}_{loss}$, into account. The total loss $\epsilon_{loss} = \epsilon^{misscut}_{loss} \cdot \epsilon^{oanglecut}_{loss}$ had to be estimated and corrected for at a later stage. The signal loss in each bin of $\cos(\theta^{\omega}_{c.m.})$ was calculated by dividing the number of reconstructed ω mesons after the cut with the number of reconstructed ω mesons before the cut for the exclusive phase space simulation treated in an inclusive manner

$$\epsilon_{loss}(\Delta\cos(\theta^{\omega}_{c.m.}), \Delta E^{beam}_{\gamma}) = \frac{N^{after\,cuts}(\Delta\cos(\theta^{\omega}_{c.m.}), \Delta E^{beam}_{\gamma})}{N^{before\,cuts}(\Delta\cos(\theta^{\omega}_{c.m.}), \Delta E^{beam}_{\gamma})}. \tag{5.28}$$

The resulting signal losses from the missing mass cut and from the opening angle cut are shown in fig. 5.54.

Figure 5.55 shows the recalculated efficiencies from the grid method before the signal loss correction ϵ_{grid} and after the signal loss correction $\epsilon_{grid} \cdot \epsilon_{loss}$ in comparison to the efficiencies obtained from the phase space simulation treated in an inclusive manner. It shows that after the signal loss correction the recalculated grid efficiencies $\epsilon_{grid} \cdot \epsilon_{loss}$ agree well with the efficiencies from the phase space simulations treated inclusively, as expected.

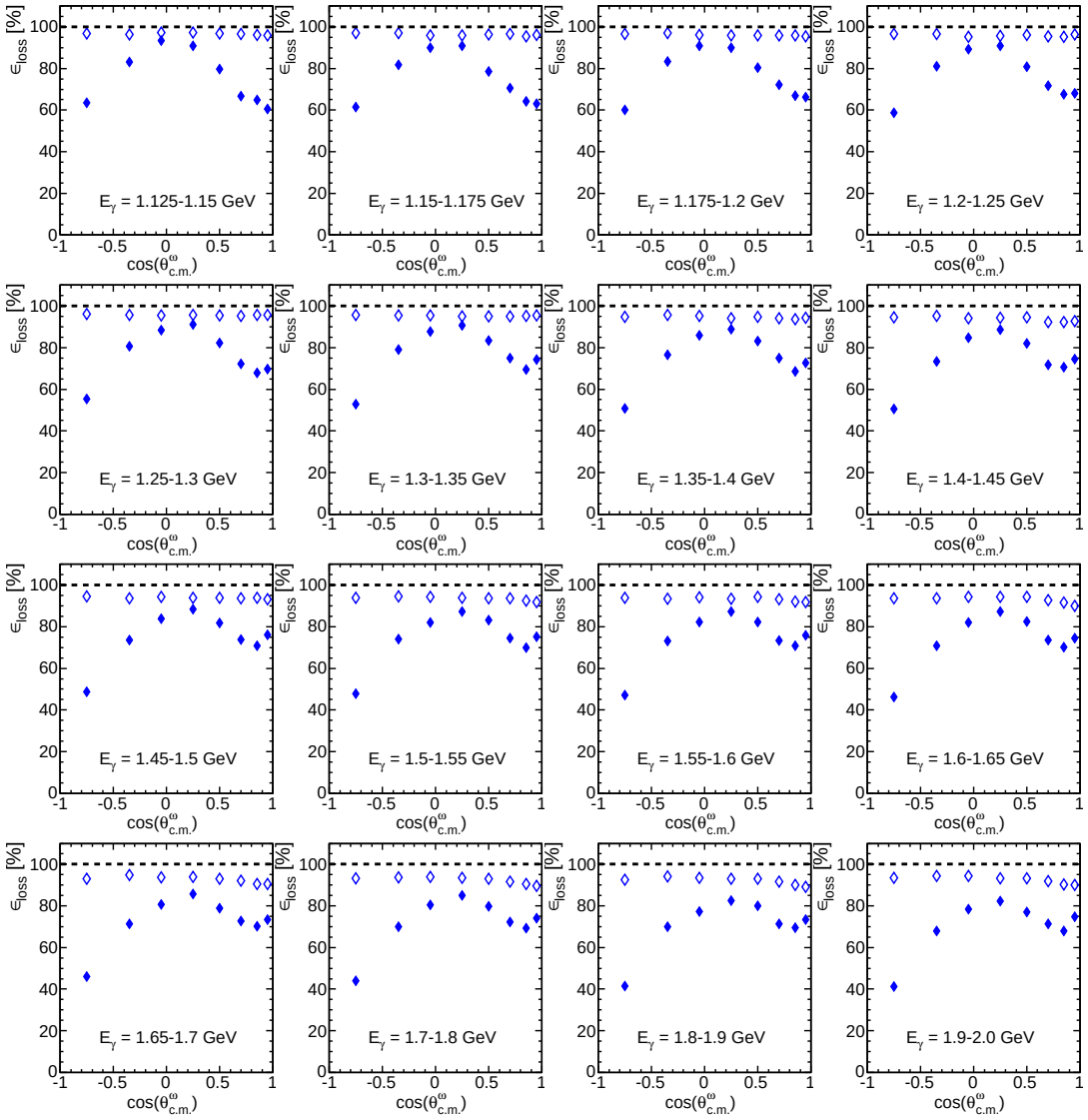

Figure 5.54: Signal loss as a function of $\cos(\theta^{\omega}_{c.m.})$ due to the missing mass cut (open symbols) and with the addition of the opening angle cut (full symbols) for the inclusive analysis of the LH_2 data. The signal losses have been obtained from the $\gamma p \to \omega p$ simulation.

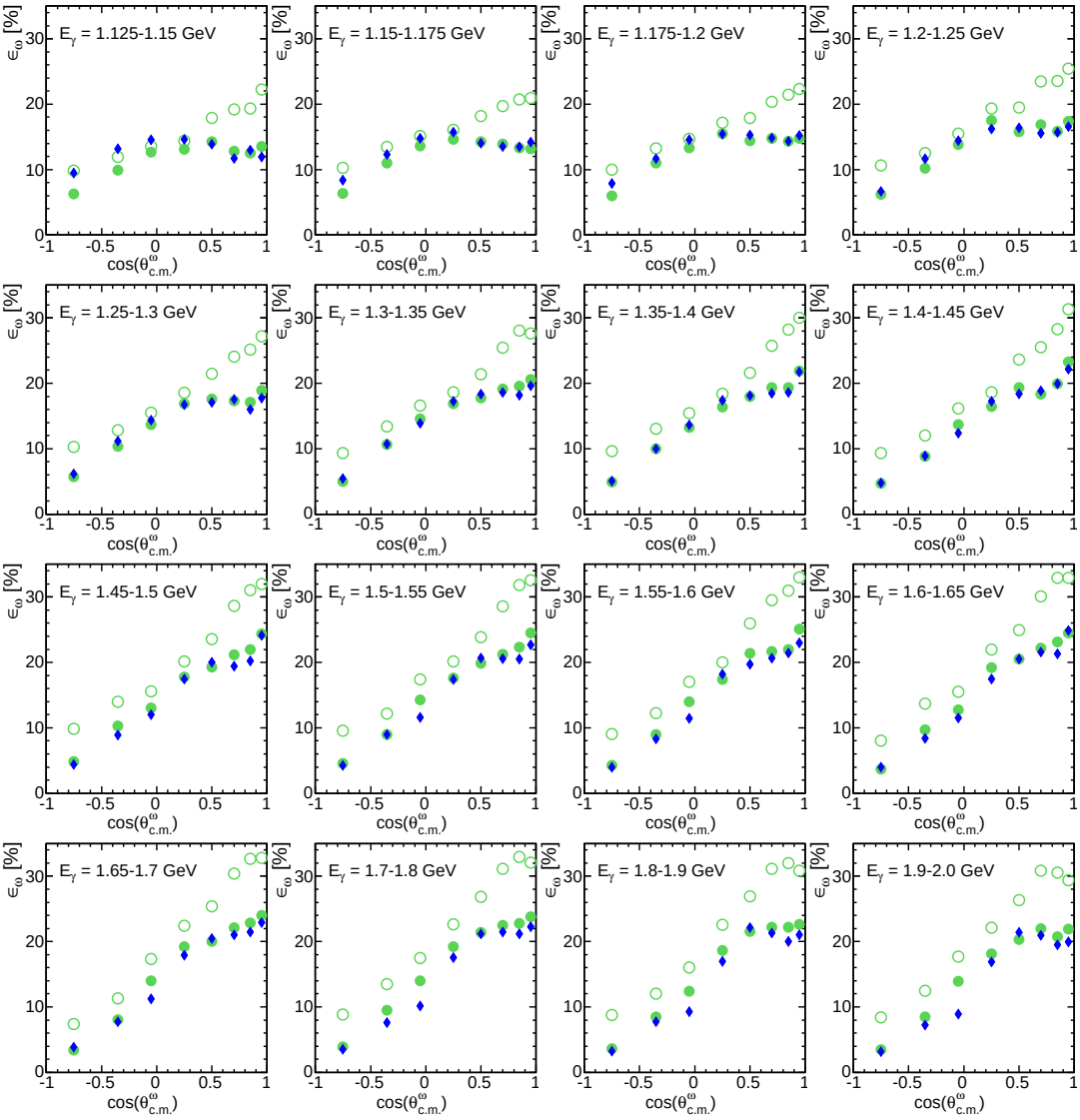

Figure 5.55: ω detection efficiency as a function of $\cos(\theta^{\omega}_{c.m.})$ for the inclusive reaction using the grid method before (green open) and after (green full) signal loss correction compared to using the phase space simulation ($\gamma p \rightarrow \omega p$ simulation treated inclusively in the analysis) for the reaction off free protons (blue).

5.12.4. The quasi-free inclusive production off LD_2

The quasi-free inclusive production off a deuterium target means that the ω meson was produced off either a proton or off a neutron. If the coherent contribution (production off a deuterium nucleus which stays intact) is negligible (which is thought to be the case, as will be shown in sect. 5.13), the quasi-free inclusive cross-section $\sigma_{incl}^{LD_2}$ is assumed to be close to the sum of the two exclusive cross-sections, *i.e.*

$$\sigma_{incl}^{LD_2} = \sigma_p^{bound} + \sigma_n^{bound}, \tag{5.29}$$

where σ_p^{bound} is the exclusive cross-section of the ω meson being produced off a bound proton and σ_n^{bound} is the exclusive cross-section of the ω meson being produced off a bound neutron. This equation holds for incident beam energies where no additional particles are produced, but such a contribution is, however, expected to be small. With this reasoning, subtracting σ_p^{bound} from the quasi-free inclusive cross-section is an alternative determination of the cross-section off a neutron, which is independent of the neutron detection efficiency.

The inclusive analysis of the LD_2 data was done in the exact same way as that of the LH_2 data. First, the two photons originating from the π^0 was identified with a χ^2 test (see eq. 5.9). Figure 5.56 shows the χ^2 (left) and the confidence level (right) for the simulation and for the data for three neutral hits events.

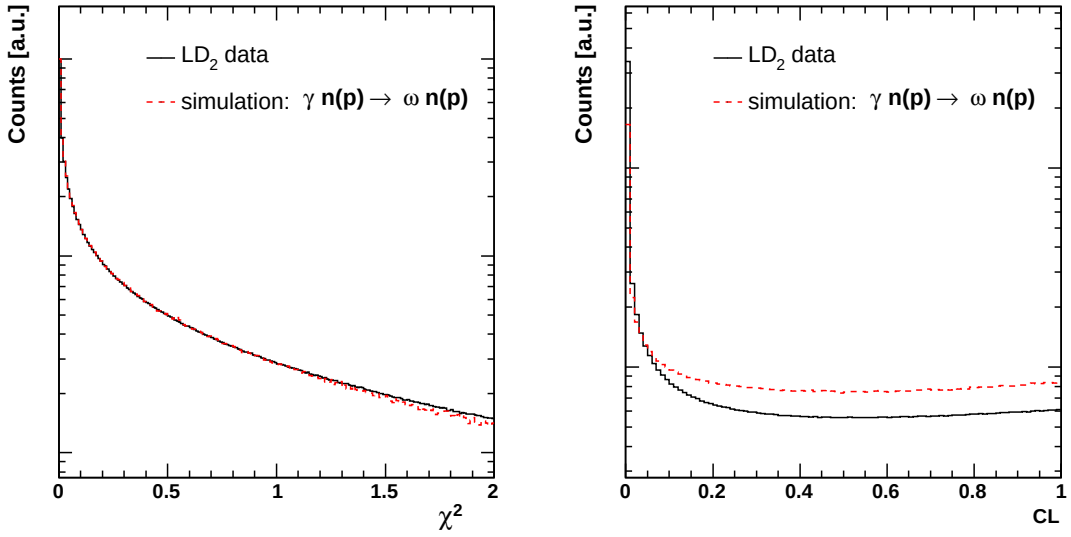

Figure 5.56: Left: The χ^2 distribution for the selection of the two photons originating from the π^0 for the inclusive analysis of ω production off LD_2 target for data (black solid line) and simulation (red dashed line). Right: The confidence level.

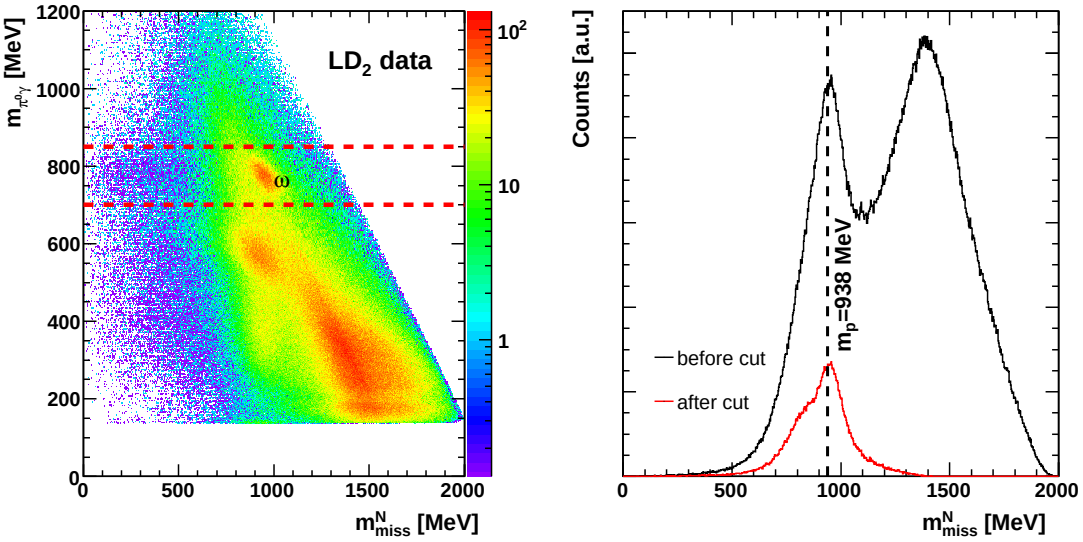

Figure 5.57: Left: The invariant mass of $\pi^0\gamma$ versus the missing mass for the event selection of three neutral hits and no further hits. Right: The full projection on the x-axis (black) and the projection after a cut in the $\pi^0\gamma$ invariant mass around the ω mass shown (red). With the cut applied a clear peak around the proton mass can be seen.

A cut around the pion mass (110 MeV $< m_{\gamma\gamma} <$ 160 MeV) was placed and the third neutral hit was added to the invariant mass. The missing mass was then calculated according to eq. 5.13. Figure 5.57 (left) shows the $\pi^0\gamma$ invariant mass versus the missing mass for the events where three neutral hits (and no further hits) have been registered . These are part of the events selected for the quasi-free inclusive channel (the other parts have been shown in the exclusive channels). Figure 5.57 (right) shows the projection onto the missing mass axis for the full range and for a cut around the ω mass indicated in the left figure. A peak around the proton (or neutron) mass can be seen after the cut, indicating the events of interest.

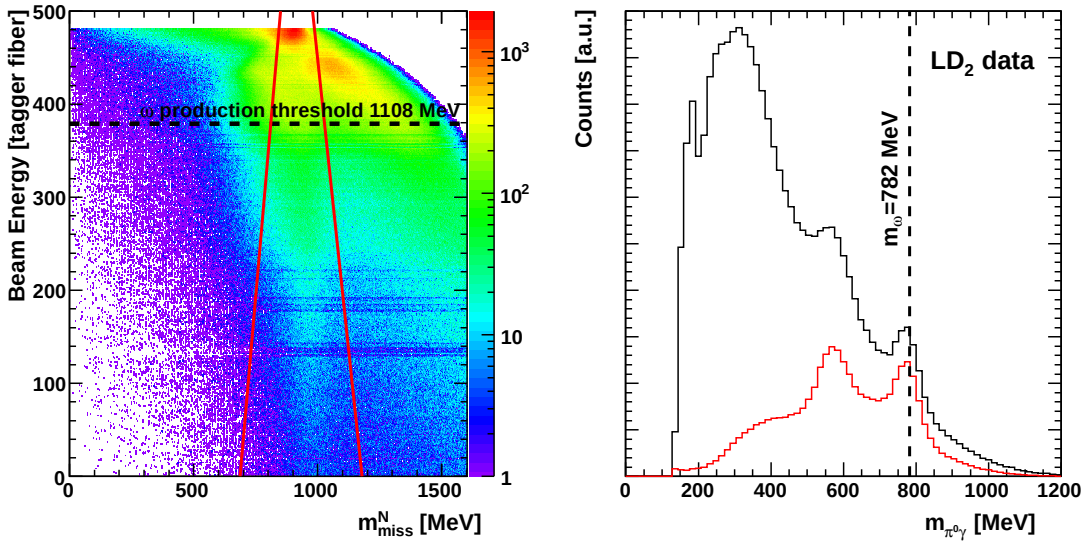

Figure 5.58: Left: The missing mass versus the incident beam energy in tagger fibers (the beam energy is increasing with decreasing fiber number) for the event selection of three neutral hits and no further hits. The missing mass cut is drawn in red. Right: The effect of the missing mass cut on removing background. The invariant mass of $\pi^0\gamma$ above the production threshold of the ω meson without a missing mass cut is shown (black) and with the missing mass cut (red).

As in the analysis of the exclusive channels, a missing mass cut depending on the incident beam energy (see eq. 5.15) was applied in order to reduce background in the $\pi^0\gamma$ invariant mass spectrum. In fig. 5.58 (left) shows this cut together with the data. Figure 5.58 (right) shows a clear reduction of the background when this cut was applied.

Just as in the inclusive analysis of ω mesons produced off the LH_2 target, a momentum dependent cut on the opening angle according to eq. 5.26 was placed in order to remove a strong contribution from single π^0 production (a simulation of the single π^0 production is shown in fig. 5.51). Figure 5.59 demonstrates the success of this cut on removing the single π^0 background channel which showed up as a peak around 550 MeV in the $\pi^0\gamma$ invariant mass spectrum. The origin of this peak was discussed further in sect. 5.12.3.

The events surviving these cuts were corrected for the detection efficiencies as described in sect. 5.12.1 for the phase space method and in sect. 5.12.2 for the grid method. In figure 5.60 some examples of invariant mass spectra before (left) and after (right) event-by-event efficiency correction can be seen for different bins of $\cos(\theta^{\omega}_{c.m.})$ for an incident beam energy E_γ = 1708-1808 MeV. All fits (with the function 5.16) to the $\pi^0\gamma$ invariant mass spectra (before and after event-wise efficiency correction) for the inclusive analysis of the LD_2 target data can be found in appendix H. The numbers of ω mesons before efficiency correction are shown in fig. 5.61.

The signal losses due to the missing mass cut, $\epsilon^{misscut}_{loss}$ and due to the opening angle cut $\epsilon^{oanglecut}_{loss}$ (they were not accounted for by the grid efficiency) had to be estimated and corrected for. The signal loss due to the missing mass and due to the opening angle cut in each bin of $\cos(\theta^{\omega}_{c.m.})$ was calculated with eq. 5.28. They are shown in fig. 5.62. The signal losses were calculated for both the simulation off the bound proton and off the bound neutron. From fig. 5.62 it is clear that the signal losses were independent of the simulated reaction channel used.

The average angular efficiencies were recalculated from the grid method using eq. 5.27. They are shown in fig. 5.63 before and after signal loss corrections. In the same figure the efficiencies obtained from the phase space simulations off protons and off neutrons treated inclusively are shown. They agree well with the average angular efficiencies from the grid method after signal loss corrections.

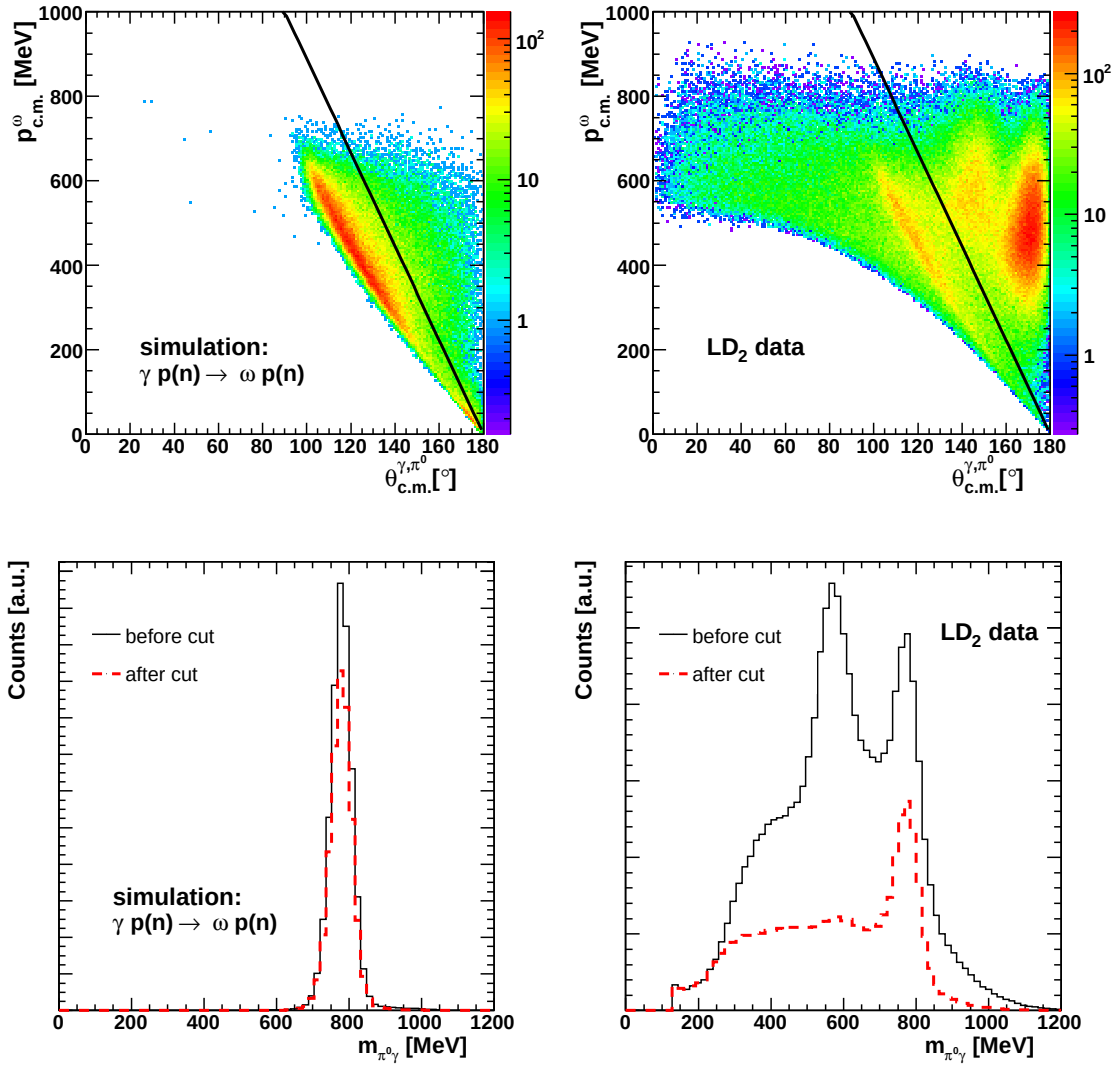

Figure 5.59: Top: The opening angle between the π^0 and γ versus the momentum of the reconstructed ω meson in the center-of-mass system for events with three neutral hits and no further hits for simulation (left) and LD_2 target data (right). The cut is drawn in black. Lower: The $\pi^0\gamma$ invariant mass before (black solid) and after (red dashed) the opening angle cut for the simulation (left) and for the data (right).

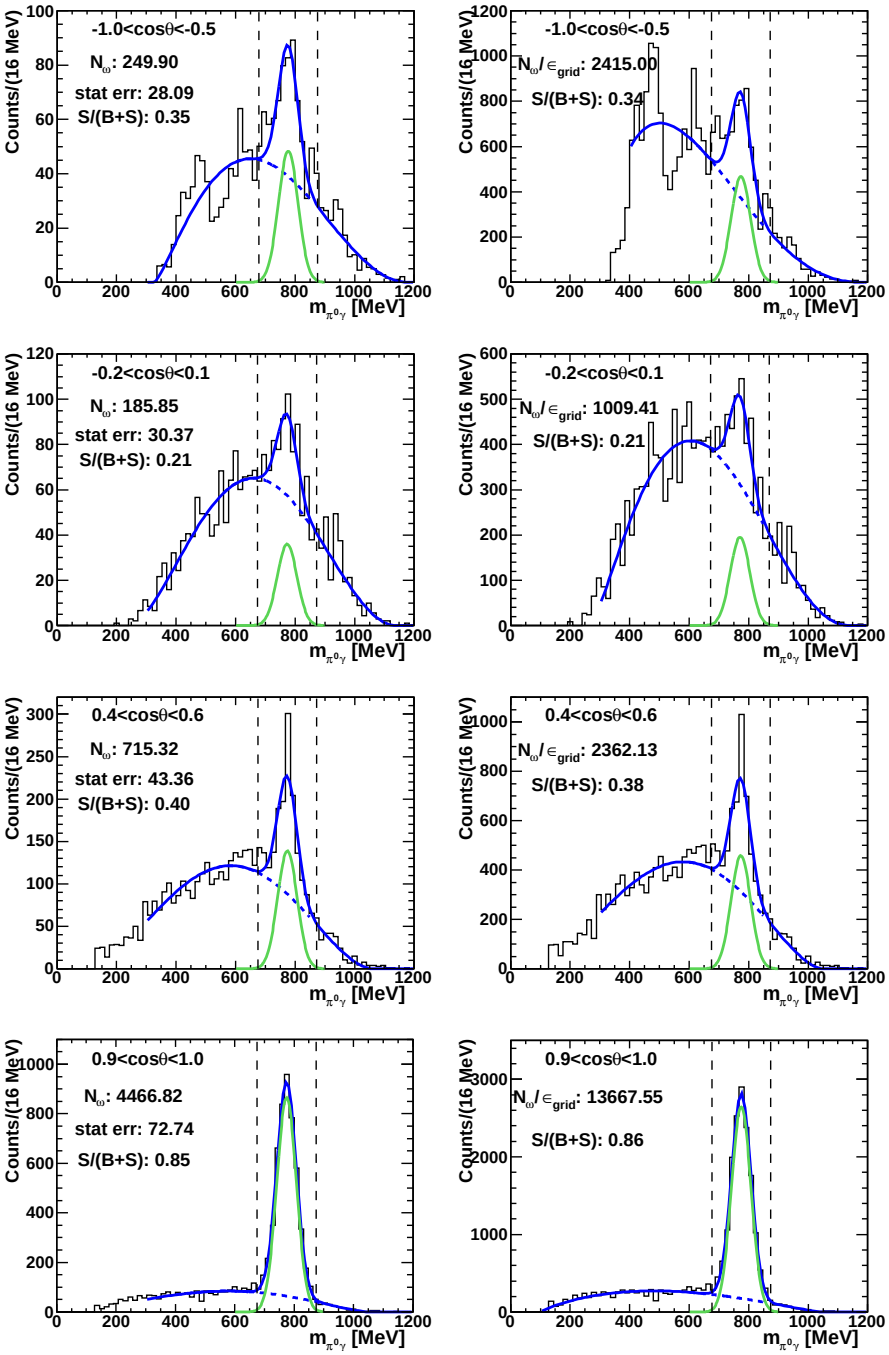

Figure 5.60: The $\pi^0\gamma$ invariant mass for a few different $\cos(\theta^{\omega}_{c.m.})$ angular bins for incident beam energy E_γ = 1708-1808 MeV for the inclusive analysis off the LD_2 target. The figures to the left are before efficiency correction and the figures to the right have been event-wise efficiency corrected depending on the $\theta_{lab.}$ and $T_{lab.}$ of the ω meson. The signal-to-background ratio obtained from the fits are shown.

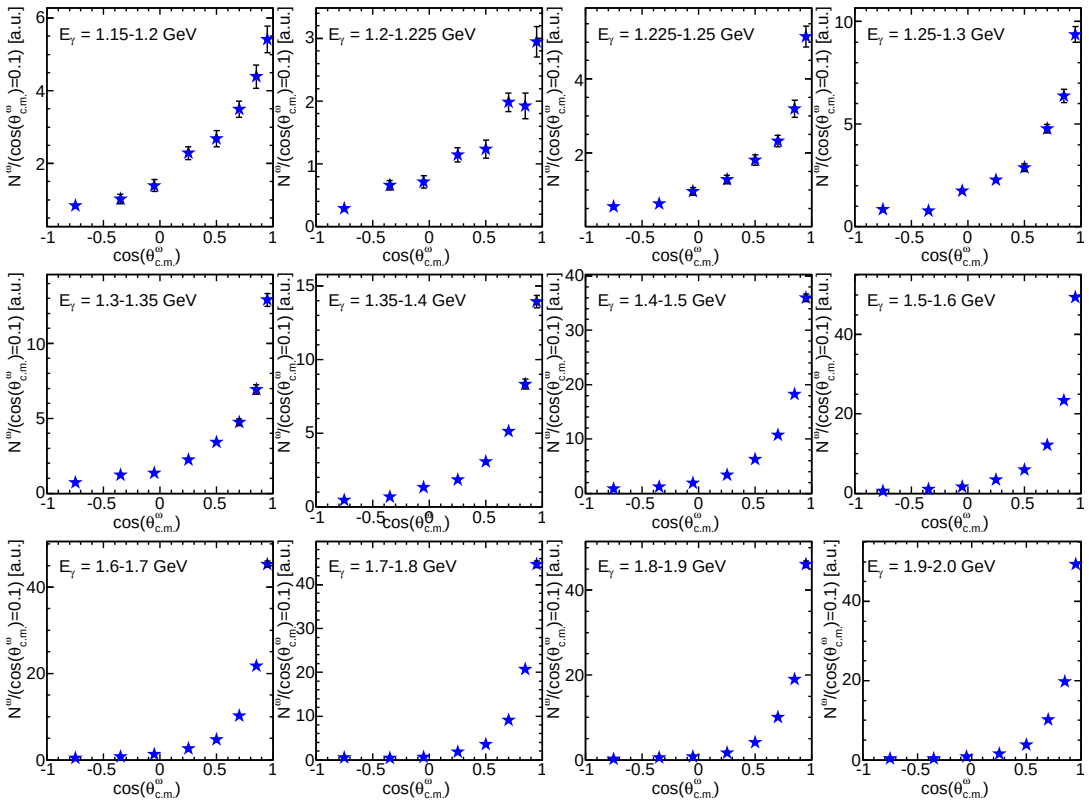

Figure 5.61: Number of ω mesons produced off LD_2 as a function of $\cos(\theta^{\omega}_{c.m.})$ (with the different angular bin sizes taken into account) for the inclusive analysis. Note that the numbers are not yet corrected for detection efficiencies. The statistical errors are shown.

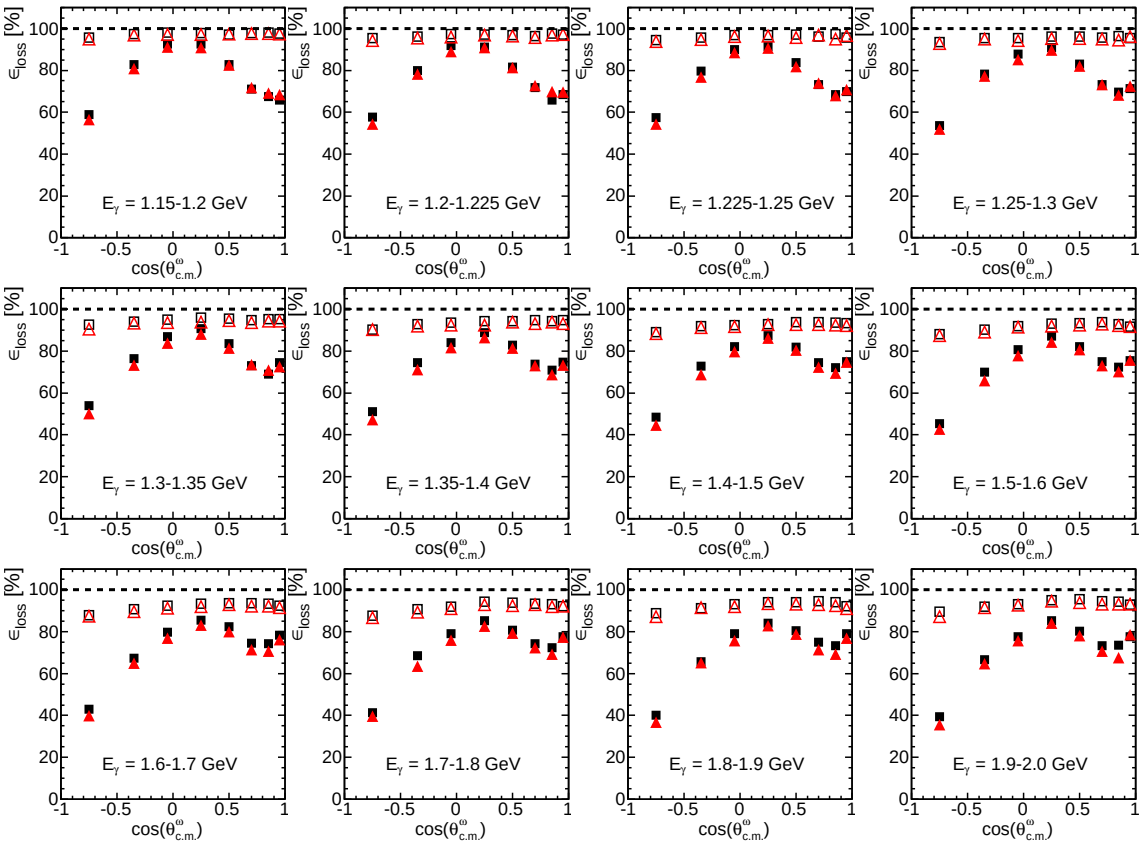

Figure 5.62: Signal loss as a function of $\cos(\theta^{\omega}_{c.m.})$ for the quasi-free inclusive reaction due to the missing mass cut (open symbols) and with the addition of the opening angle cut (full symbols). The signal loss have been calculated by using the $\gamma d \rightarrow \omega n(p)$ simulation (red triangles) and the $\gamma d \rightarrow \omega p(n)$ simulation (black squares) and they are in good agreement.

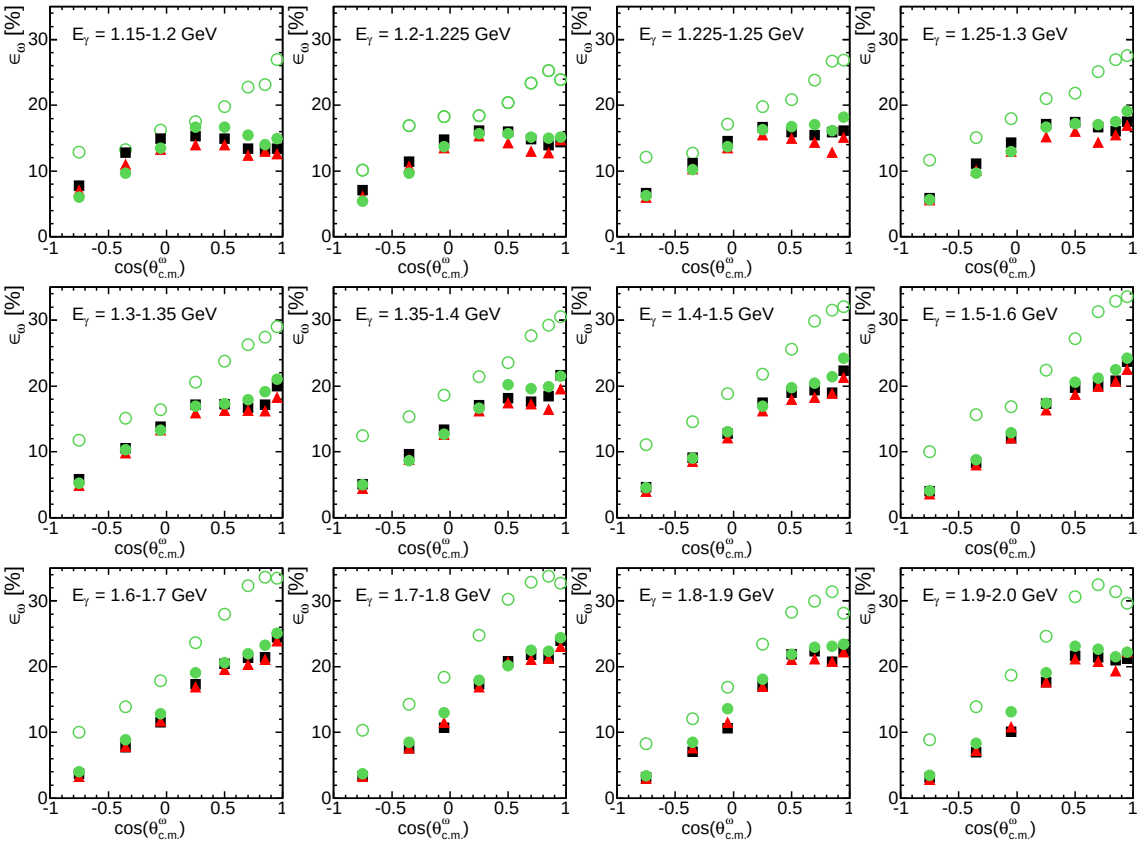

Figure 5.63: ω detection efficiency as a function of $\cos(\theta^{\omega}_{c.m.})$ for the quasi-free inclusive reaction using the grid method before (green open) and after (green full) signal loss correction compared to using the phase space simulation (quasi-free exclusive reaction simulation treated as inclusive in the analysis) for the reaction off protons (black) and for the reaction off neutrons (red).

Detection efficiency of protons

The detection efficiency of protons as a function of $\cos(\theta^{\omega}_{c.m.})$ was calculated by dividing the efficiency of the exclusive reaction of the ω meson being produced off a proton by the efficiency of the quasi-free inclusive channel

$$\frac{(\epsilon_{excl})_p}{\epsilon_{incl}} = \frac{\epsilon_\omega \cdot \epsilon_p}{\epsilon_\omega} \,. \tag{5.30}$$

However, since the analyses were done with different cuts the number of ω mesons had to be corrected for the signal losses giving

$$\epsilon_p = \frac{(N^{\omega}_{excl})_p / \epsilon^{\theta-cut}_{loss}}{N^{\omega}_{incl} / \epsilon^{oangle-cut}_{loss}} \,, \tag{5.31}$$

where $(N^{\omega}_{excl})_p$ is the number of ω mesons seen in the exclusive analysis off the proton (*i.e.* the event selection three neutral hits and one charged hit with the missing mass cut applied), N^{ω}_{incl} is the number of ω mesons seen in the inclusive analysis (*i.e.* the event selection with three neutral hits and no further hits or events with at least three neutral hits and four hits in total) and $\epsilon^{\theta-cut}_{loss}$ (see fig. 5.16 for the free proton and fig. 5.17 for the bound proton) and $\epsilon^{oangle-cut}_{loss}$ are the signal losses due to the θ-cut and the opening angle cut (see eq. 5.26), respectively. Practically nothing was lost from the signal by the θ-cut in the case of the free proton, see fig. 5.64. For the LH_2 target, the free proton detection efficiency could be determined from the data and compared to the one from the simulation, see fig. 5.65. The data and simulation agree within errors in most cases. The reason for any discrepancy most likely comes from difficulties in the fitting of the invariant mass spectra. Obviously, a proton detection efficiency larger than 100% does not make sense. Figure 5.66 shows the proton efficiencies obtained from the simulation off the bound proton. Here, a calculation from the data for comparison was not possible.

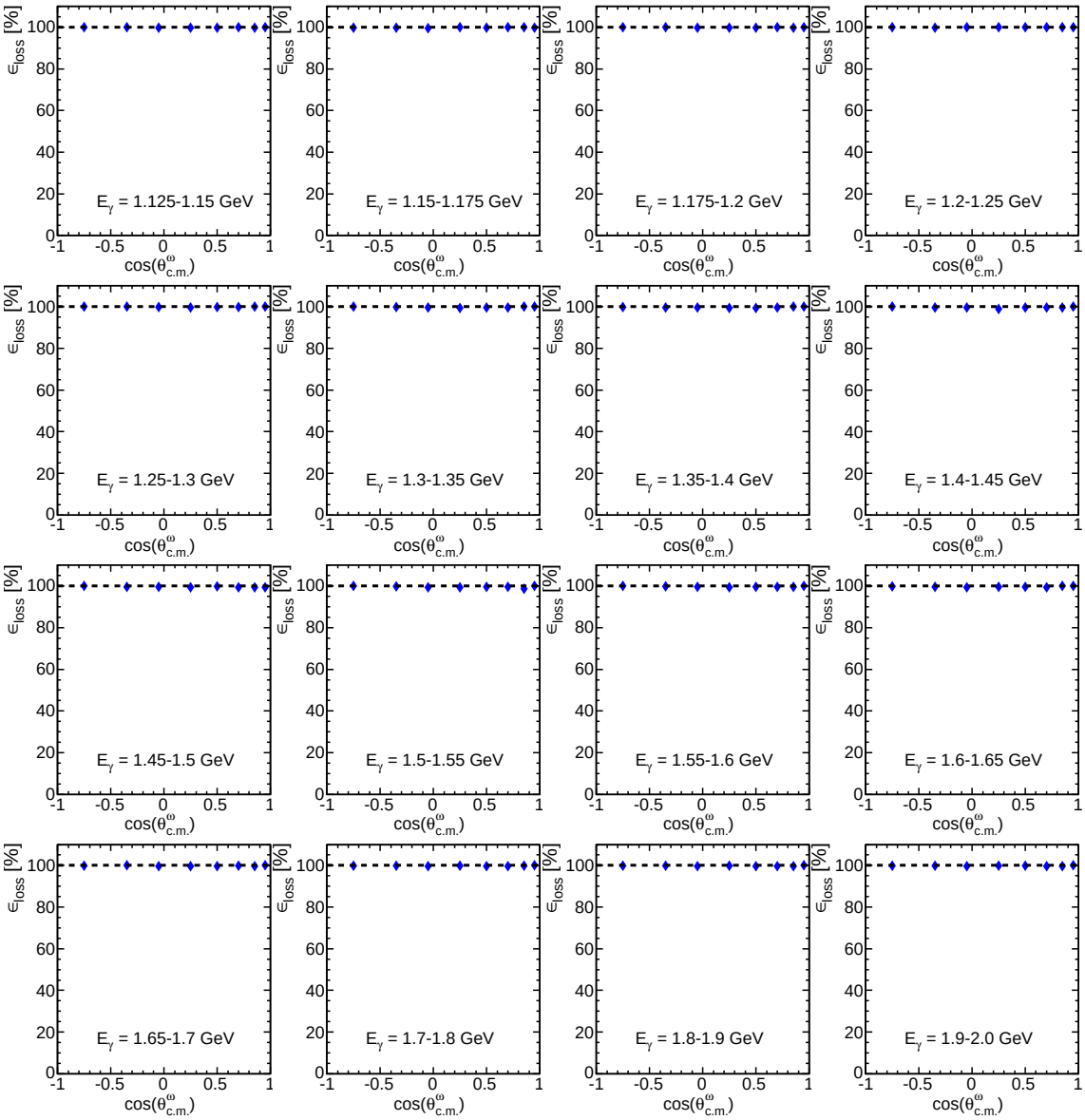

Figure 5.64: Loss of ω mesons as a function of $\cos(\theta^{\omega}_{c.m.})$ due to the $\theta_{lab.}$-cut of the recoil protons for LH_2 data, $\epsilon^{\theta-cut}_{loss}$ in eq. 5.31.

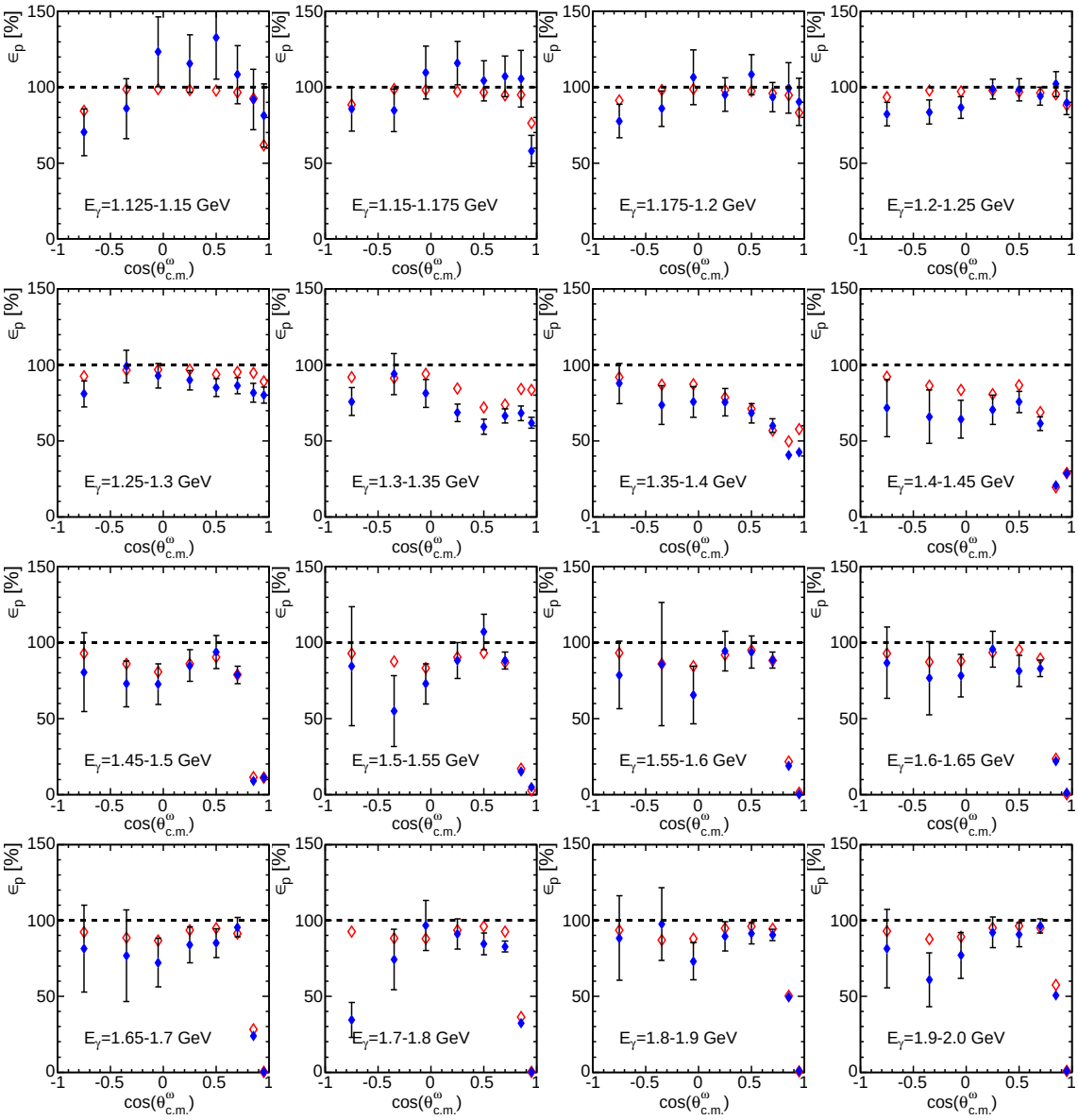

Figure 5.65: Proton detection efficiency as a function of $\cos(\theta^{\omega}_{c.m.})$ for the simulation (open diamonds) compared to data (full diamonds) for the reaction off free protons calculated using eq. 5.30.

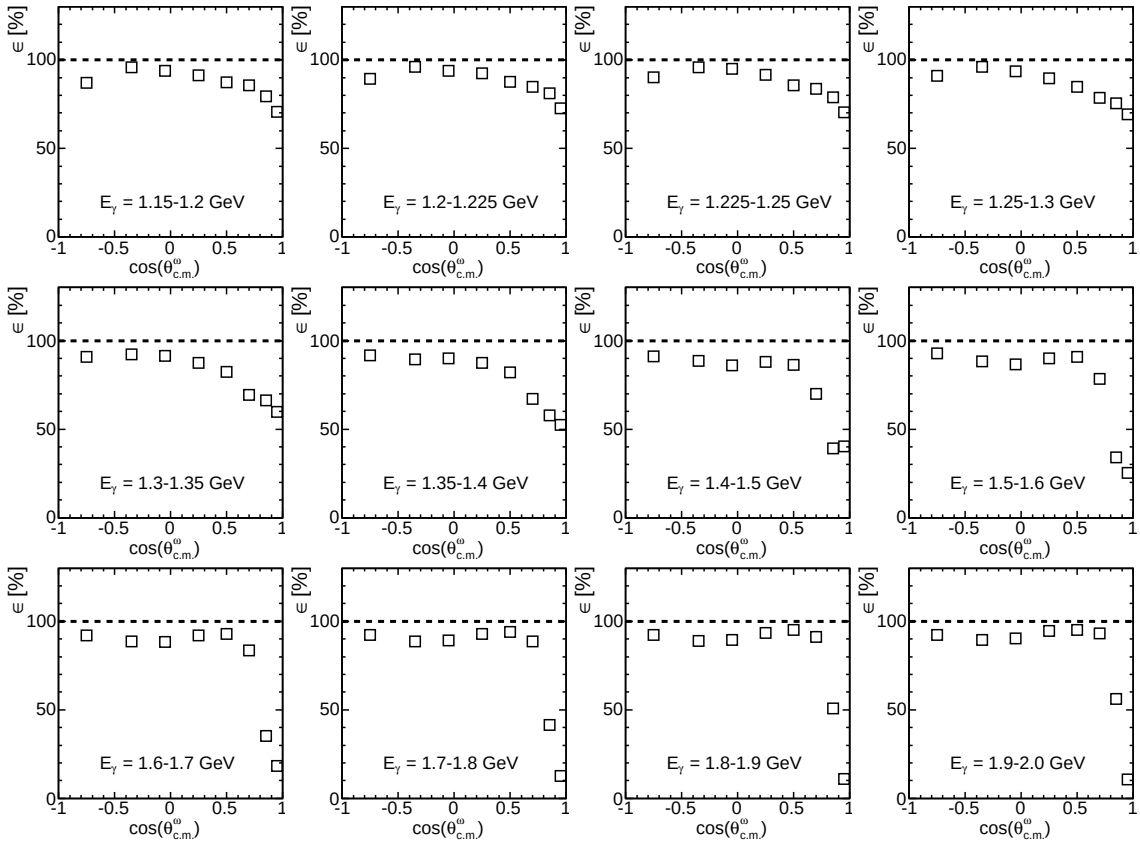

Figure 5.66: Proton detection efficiency, ϵ_p, as a function of $\cos(\theta^{\omega}_{c.m.})$ calculated from simulation of ω mesons produced off the bound proton using eq. 5.30.

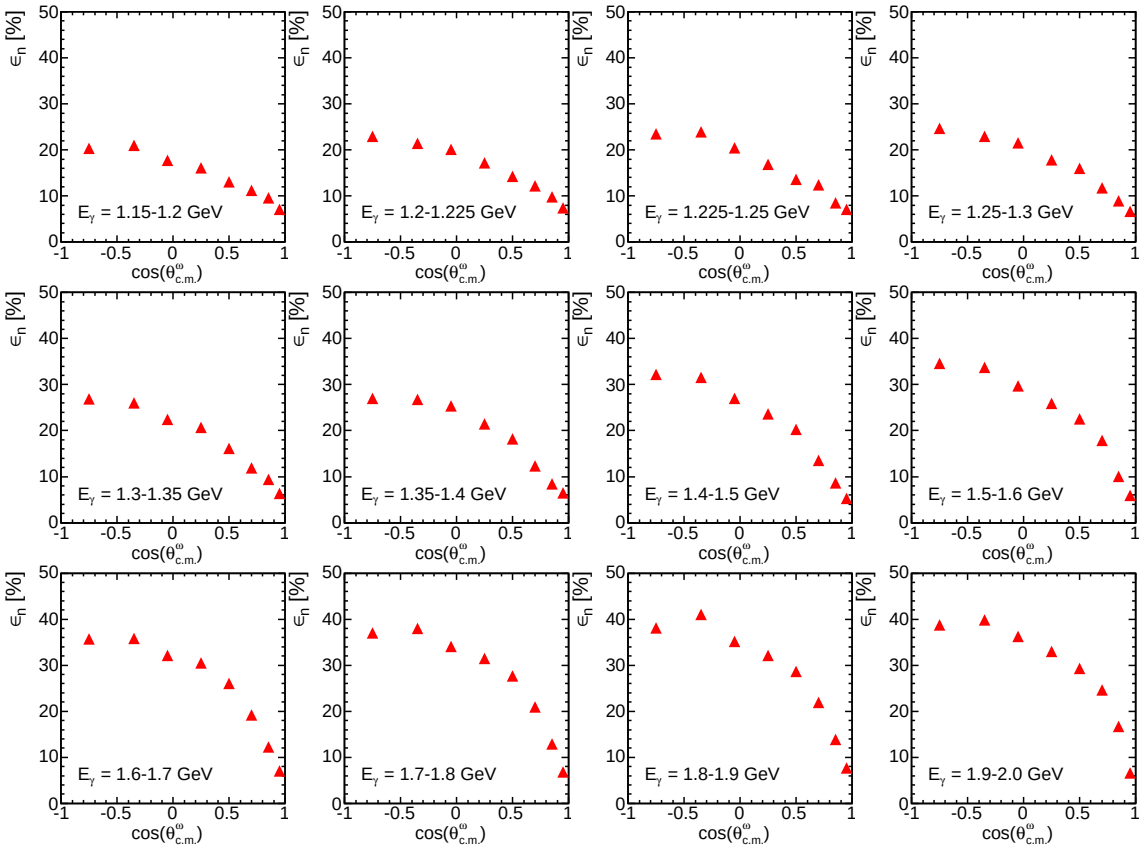

Figure 5.67: Neutron detection efficiency, ϵ_n, as a function of $\cos(\theta^{\omega}_{c.m.})$ calculated from simulation of ω mesons produced off the bound neutron using eq. 5.32.

Detection efficiency of neutrons

In the same way as in the case of the proton detection efficiency, the detection efficiency of neutrons as a function of $\cos(\theta^{\omega}_{c.m.})$ was calculated by dividing the efficiency of the exclusive reaction of the ω meson being produced off a neutron by the efficiency of the quasi-free inclusive channel

$$\frac{(\epsilon_{excl})_n}{\epsilon_{incl}} = \frac{\epsilon_\omega \cdot \epsilon_n}{\epsilon_\omega} \,. \tag{5.32}$$

The result can be seen in fig. 5.67.

Total detection efficiencies

The total efficiencies for detecting the nucleons and ω meson separately are shown in fig. 5.68 as a function of incident beam energy. They are the angle integrated efficiencies from simulations shown in figures 5.65, 5.66 and 5.67 and 5.63 (the efficiency from the grid method after signal loss correction).

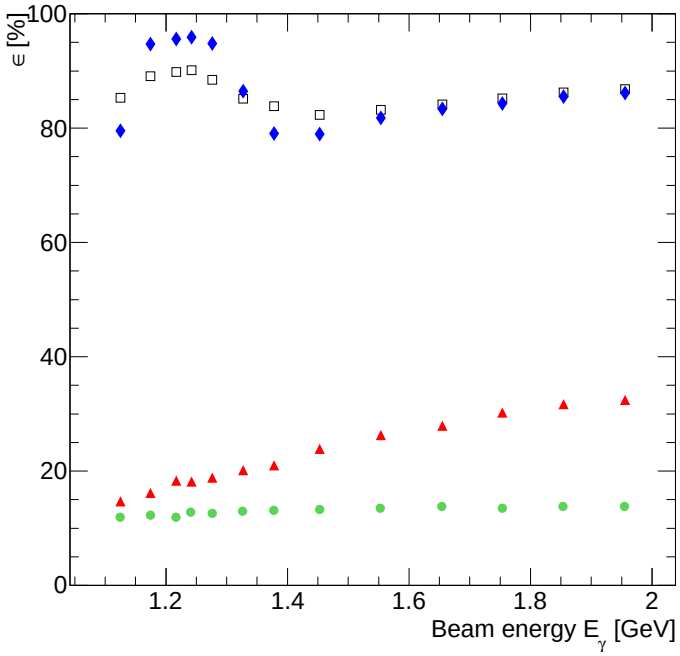

Figure 5.68: Total efficiencies for detecting a free proton (blue diamonds), a bound proton (black squares), a neutron (red triangles) and an ω meson (green circles) separately.

5.13. Search for coherent production

Coherent production means that the ω meson was formed without breaking up the deuterium nucleus. Because of the higher mass of the deuterium nucleus ($m_d = 1875.61$ MeV) compared to the proton the recoil nucleus will travel more slowly than a recoil proton and thus leave a different ionization trace in the E_{dep}-TOF spectrum. Figure 5.69 (left) illustrates this difference for a simulation of ω mesons produced off a bound proton and off a deuterium nucleus. Figure 5.69 (right) shows what was seen in the data. A cut was defined around the right part of the trace coming from coherent production in order to separate events from the ones produced via the quasi-free exclusive production. The cut is drawn in red in Fig. 5.69 (right).

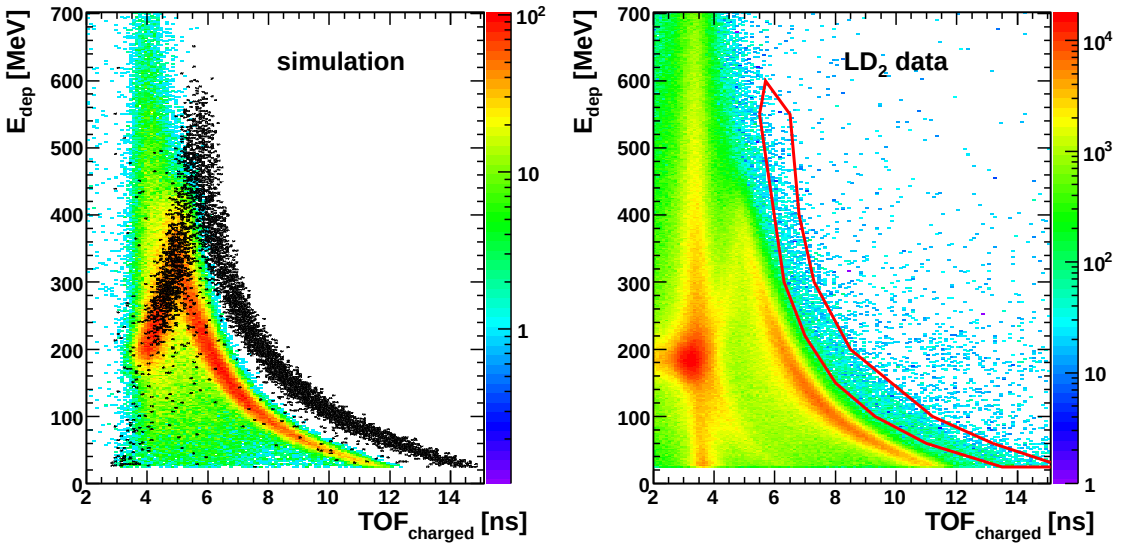

Figure 5.69: Deposited energy of the charged recoil particle versus its time-of-flight. Left: Simulation for ω production off a bound proton (in color) and off a deuterium nucleus (in black). Right: Data together with a cut around the band where the coherent production is expected to be seen.

Figure 5.70 shows the invariant mass after applying this cut. A small peak can be seen in the ω mass region. The missing mass assuming coherent production was calculated by

$$m^{d}_{miss} = |\mathbf{P}_{\gamma} + \mathbf{P}_{d} - \mathbf{P}_{\pi^0\gamma}|, \tag{5.33}$$

where $\mathbf{P}_{\gamma}$, $\mathbf{P}_{d}$ and $\mathbf{P}_{\pi^0\gamma}$ are the four-momenta of the incident photon, the initial state deuteron and the detected $\pi^0\gamma$. The missing mass was calculated for the events with invariant masses in the ω mass region, 700 MeV $< m_{\pi^0\gamma} <$ 850 MeV. The result is shown to the right in fig. 5.70. This was done for two different ranges of incident beam energy 946-1108 MeV (upper row) and 1108-2008 MeV (lower row). As expected, the ω mesons observed below 1108 MeV seems to originate from coherent production since they show a sharp peak in the missing mass spectrum around the deuteron mass. For the events in the incident beam energy 1108-2008 MeV the missing mass spectrum shows a broader peak (which indicates the presence of Fermi momentum) shifted to higher energies. By comparing to the simulations it seems like there could be a very small contribution from coherent production. This should not contribute much to the measured cross-section off the bound proton. Of course, this way of searching for the coherent production was not possible for the three neutral hits events, since the time of the nucleon was used. Therefore, the contribution to the inclusive cross-section was not investigated. To determine the absolute cross-section of the coherent production, the proper acceptance has to be taken into account, this was however not the aim of this work.

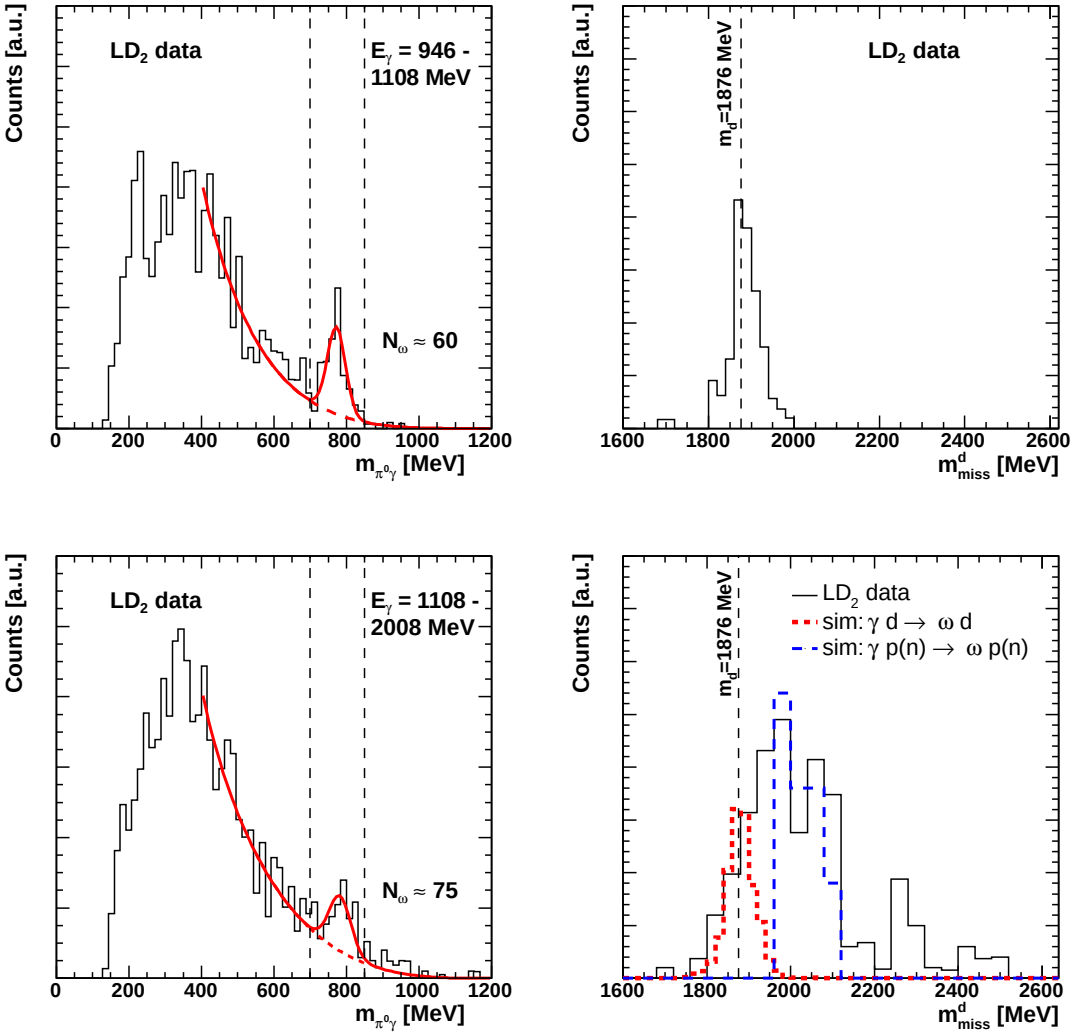

Figure 5.70: Left: The invariant mass of $\pi^0\gamma$ seen in the data after applying the cut shown in fig. 5.69 (right). Right: The missing mass assuming coherent production, applying the cut in fig. 5.69 (right) and requiring the invariant mass to be in the ω meson mass region (dashed lines in the left figure) for the data (black) and for the simulation of the coherent channel (red). A negligible contribution from coherent production can be seen.

5.14. Photon flux determination

The last necessary information needed in order to calculate absolute cross-sections was the photon flux, now that the number of ω mesons produced and the detection efficiencies have been determined. The photon flux, ϕ, is the number of photons in the beam that reached the target per second and thus had the possibility to produce a reaction. The tagging system recorded the number of scattered electrons, $N^{e^-}_{scaler}$. Figure 5.71 (upper left) shows the scaler spectrum (the number of electrons registered in each tagger fiber) for the LH_2 beam time. Scalers were recorded during the spill time, whereas the data acquisition was running during the life time. Therefore, the scalers had to be corrected for dead time effects. This was done by using the life time/spill time-ratio, see fig. 5.71 (upper right). It shows that the life time was ≈40 %. Figure 5.71 (lower left) shows the flux [e^-/MeV] as a function of the incident beam energy. It follows a $1/E_\gamma$ behavior, which characterizes Bremsstrahlung photon production. It is, however, only an approximate behavior and has to be corrected according to

$$\phi(E_\gamma) = (\frac{4}{3} - \frac{4}{3}\frac{E_\gamma}{E_b} + (\frac{E_\gamma}{E_b})^2)\frac{\phi_0}{E_\gamma}\,, \tag{5.34}$$

(for details see [46]). E_b is the electron beam energy, *i.e.* $E_b = 3.2$ GeV for the LH_2 beam time and $E_b = 2.6$ GeV for the LD_2 beam time. A fit of eq. 5.34 to the flux shows a good agreement. However, this fit was only used to illustrate the behavior, for flux correction in the cross-section calculations the integrated scaler spectrum was used.

Figure 5.72 shows the same as fig. 5.71, but for the LD_2 target beam time. For this beam time the beam was linearly polarized, which gave rise to a polarization peak at ≈ 1100 MeV. Equation 5.34 can obviously not describe the flux in the polarization region. Figure 5.72 (lower left) shows a fit of eq. 5.34 to the flux outside of the polarization peak ($E_\gamma > 1700$ MeV). It can bee seen that the effect of the polarization extends far from the peak position, as low as $E_\gamma < 500$ MeV. It also shows that there is a second maximum at ≈ 1550 MeV. This can be more clearly seen in fig. 5.72 (lower right), where the relative intensity (the ratio of the flux to the fit) is shown as a function of incident beam energy. This behavior seems to be consistent with previous findings and calculations (see [47]).

Due to the beam dispersion (and consequently, the usage of a collimator placed behind the bending magnet) $N^{e^-}_{scaler}$ does not directly correspond to the number of photons that reached the target. For that reason, one has to take the tagging efficiency, ϵ_γ, into account.

The tagging efficiency was calculated by

$$\epsilon_\gamma = \frac{N^\gamma_{\gamma-veto}}{N^{e^-}_{scaler}}\,, \tag{5.35}$$

where $N^\gamma_{\gamma-veto}$ is the number of photons that passed the target and were detected by the γ-veto detector in the beam dump (99,99 % of the photons that reach the target just pass through the target without undergoing any interaction). For a detailed description of the tagging efficiency determination (for the beam times with LD_2 target), see [41]. The tagging efficiencies for the beam times used in this thesis were estimated to be on average 72% for the data with LH_2 target and 85% for the data with LD_2 target.

The photon flux was determined by

$$\phi(E_\gamma) = \frac{N^{e^-}_{scaler}(E_\gamma)\cdot\epsilon_\gamma(E_\gamma)}{\Delta E_\gamma \cdot \Delta t}\,, \tag{5.36}$$

where ΔE_γ is a bin in incident photon beam energy and Δt is the number of seconds of beam time.

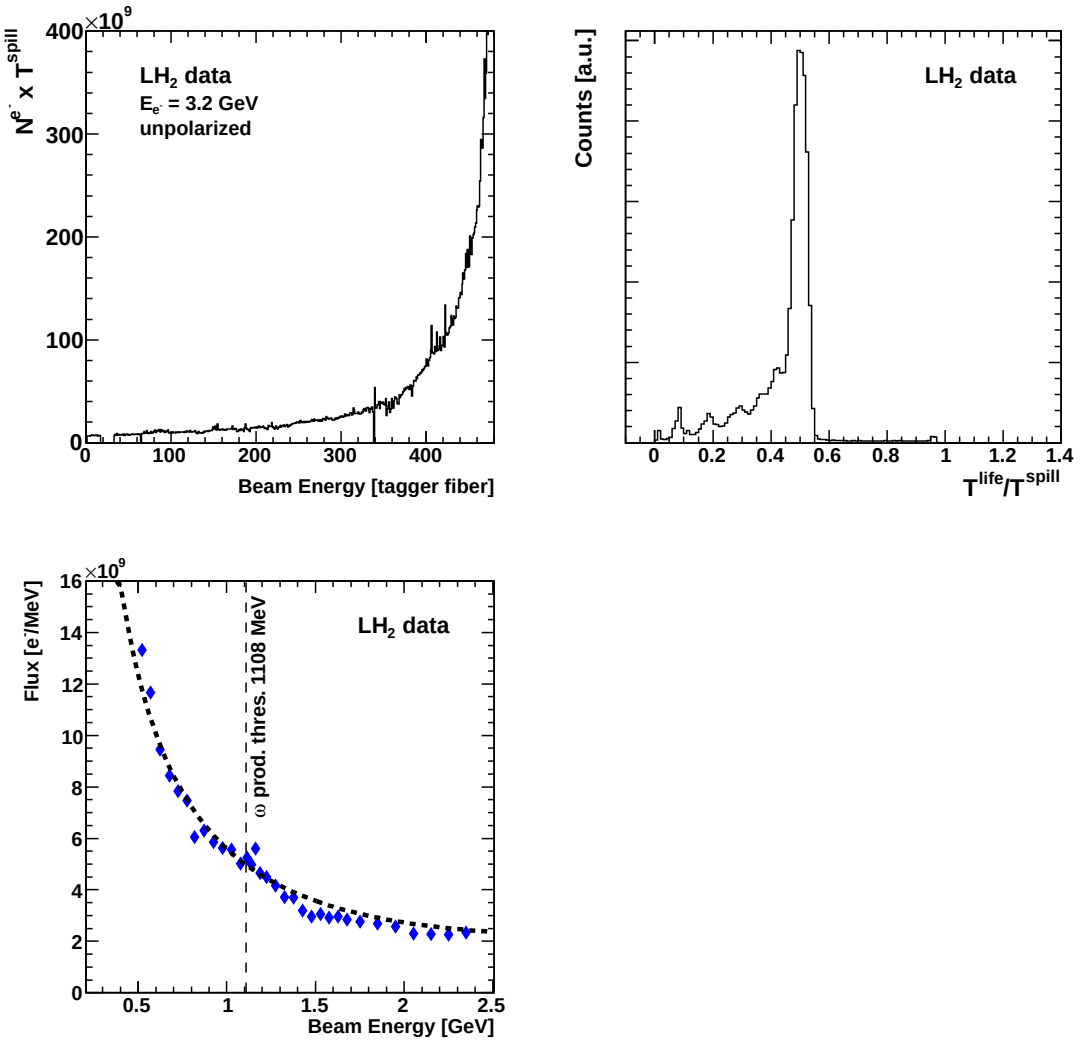

Figure 5.71: Top left: Raw scaler spectrum for the LH_2 beam time. Top right: The normalisation factor T^{life}/T^{spill} used to correct for dead time effects. The average life time was ≈40 %. Lower left: The flux $[e^-/\text{MeV}]$ for the LH_2 data together with a fit according to eq. 5.34 (dashed curve).

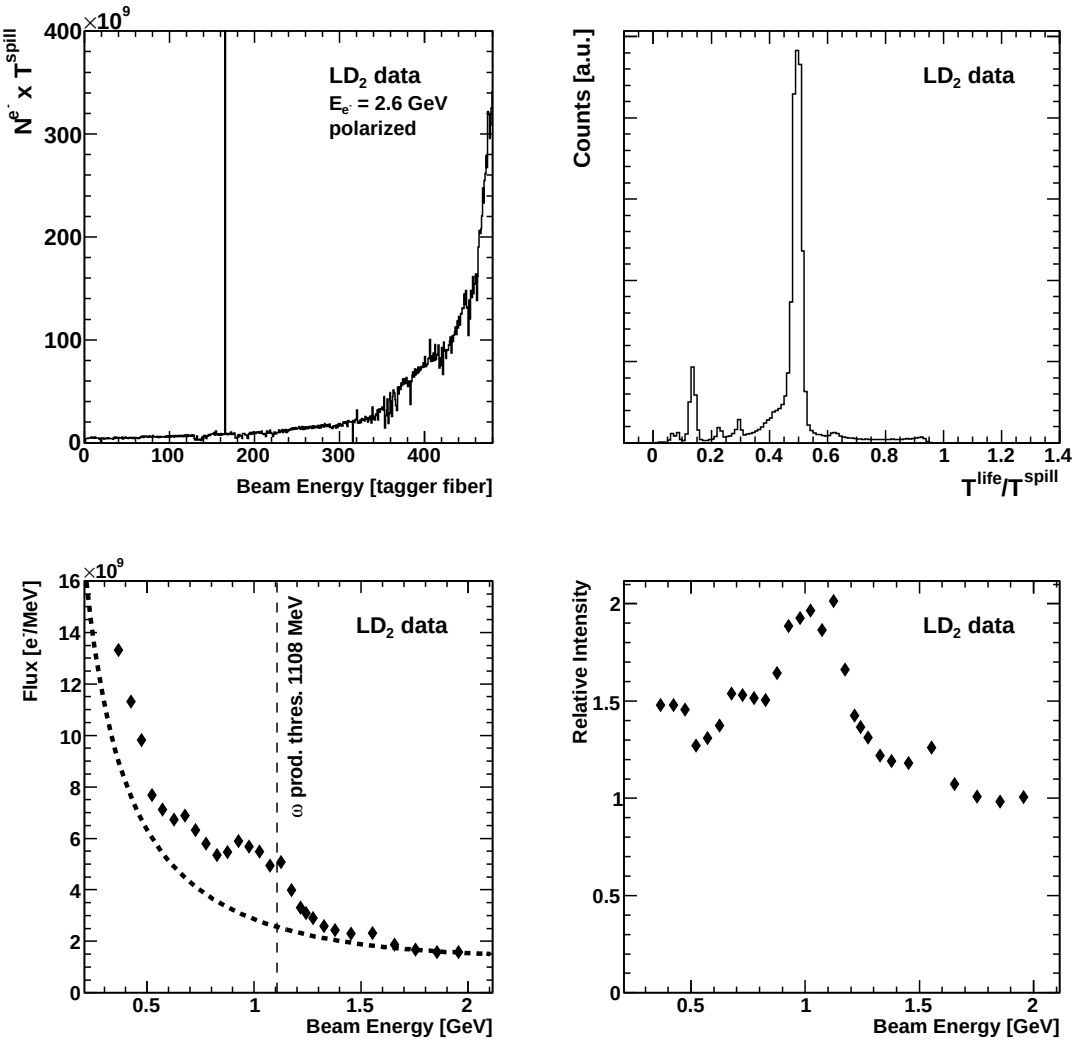

Figure 5.72: Top left: Raw scaler spectrum for the LD_2 beam time. Fiber 166 was not functioning properly. This was corrected for by setting it to the mean of the values registered by the two neighboring fibers. Top right: The normalisation factor T^{life}/T^{spill} used to correct for dead time effects. The life time was $\approx$ 40 %. Lower left: The flux $[e^-/\text{MeV}]$ for the LD_2 data together with a fit according to eq. 5.34 (dashed curve). Lower right: The relative intensity showing a main polarisation peak at $\approx$ 1100 MeV and a second maximum at $\approx$ 1550 MeV

6. Results

In this chapter the results on differential cross-sections and total cross-sections of ω mesons produced by the following reactions will be shown:

- **The production off the free proton** $\gamma p \rightarrow \omega p$ (exclusive and inclusive analyses)
- **The quasi-free production off the bound proton** $\gamma d \rightarrow \omega p(n)$
- **The quasi-free production off the bound neutron** $\gamma d \rightarrow \omega n(p)$
- **The quasi-free inclusive production** $\gamma d \rightarrow \omega(np)$

6.1. Differential cross-sections

To determine cross-sections for reactions where the particle is not isotropically produced, it is necessary to study the angular distributions, determine the differential cross-section and integrate it in order to obtain the total cross-section. This is the case for the photoproduction of ω mesons off protons and off neutrons, since the production is favored for ω mesons emitted in the forward direction.

The differential cross-sections were calculated by

$$\frac{\mathrm{d}\sigma}{\mathrm{d}\cos\theta}(E_\gamma, \cos\theta) = \frac{N_\omega(E_\gamma, \cos\theta)}{\varepsilon(E_\gamma, \cos\theta) \cdot \xi \cdot N_\gamma(E_\gamma) \cdot \Gamma_{br} \cdot \Delta\cos\theta}\,, \tag{6.1}$$

where $\mathrm{N}_\omega(E_\gamma, \cos\theta)$ is the number of ω meson events seen in a certain window of incident beam energy and window of $\cos\theta$ (where $\theta = \theta^\omega_{c.m.}$), $\varepsilon(E_\gamma, \cos\theta)$ is the detection efficiency of the reaction (obtained from simulation), ξ is the target density (see eq. 2.36 and table 3.1), $N_\gamma(E_\gamma)$ is the number of incident beam photons in the selected energy window and Γ_{br} is the branching ratio of the chosen channel.

Due to the strong exponential rise in the differential cross-sections, they were scaled with the momentum transfer to the nucleon, t, for a better visualization. The scaling procedure

is described in appendix C. The t-scaled differential cross-sections, $d\sigma/dt$, were fitted with the function

$$F(|t - t_{min}|) = a + \exp(b + c \cdot |t - t_{min}|)\,, \tag{6.2}$$

where the parameter c quantifies the t-channel contribution and a quantifies the contributions from resonances to the cross-section.

The error bars shown in the figures of this section are all purely statistical.

6.1.1. The production off the free and bound proton

Figure 6.1 shows the differential cross-sections of the free proton from the exclusive analysis as a function of $\cos(\theta^{\omega}_{c.m.})$ for different bins of incident beam energy, E_γ, in comparison to published data by CLAS [19]. A strong exponential behavior at higher incident beam energies is observed as the ω mesons are moving in forward direction, which is characteristic of t-channel exchange. The comparison between CB-ELSA data and CLAS data shows a good agreement in the resonance region (the region where the ω mesons are moving backward in the c.m. system). However, in the region where the ω mesons are moving forward in the c.m. system the CB-ELSA data lies above the CLAS data in the full incident beam energy range.

The differential cross-sections were also determined through an inclusive analysis. The result is shown in fig. 6.2 for the two different acceptance correction methods, with the phase space acceptance (described in sect. 5.12.1) and with the grid acceptance (described in sect. 5.12.2). The two different methods seem to give very similar results. However, when looking at the total cross-sections a slight discrepancy was seen which reflects the systematic uncertainty in the ω acceptance, which was $\approx$6%.

The mean values for the inclusive differential cross-sections from the two methods were calculated and scaled with the momentum transfer to the nucleon. The resulting differential cross-sections, $d\sigma/dt$, are shown in fig. 6.3 together with the t-scaled differential cross-sections from the exclusive analysis and the published data by SAPHIR [18]. In general, they come close to each other, however, the CBELSA/TAPS data lie above the previously published data in the small momentum transfer region for almost all incident photon energy bins. For a comparison of the total cross-sections off the free proton, see fig. 6.14.

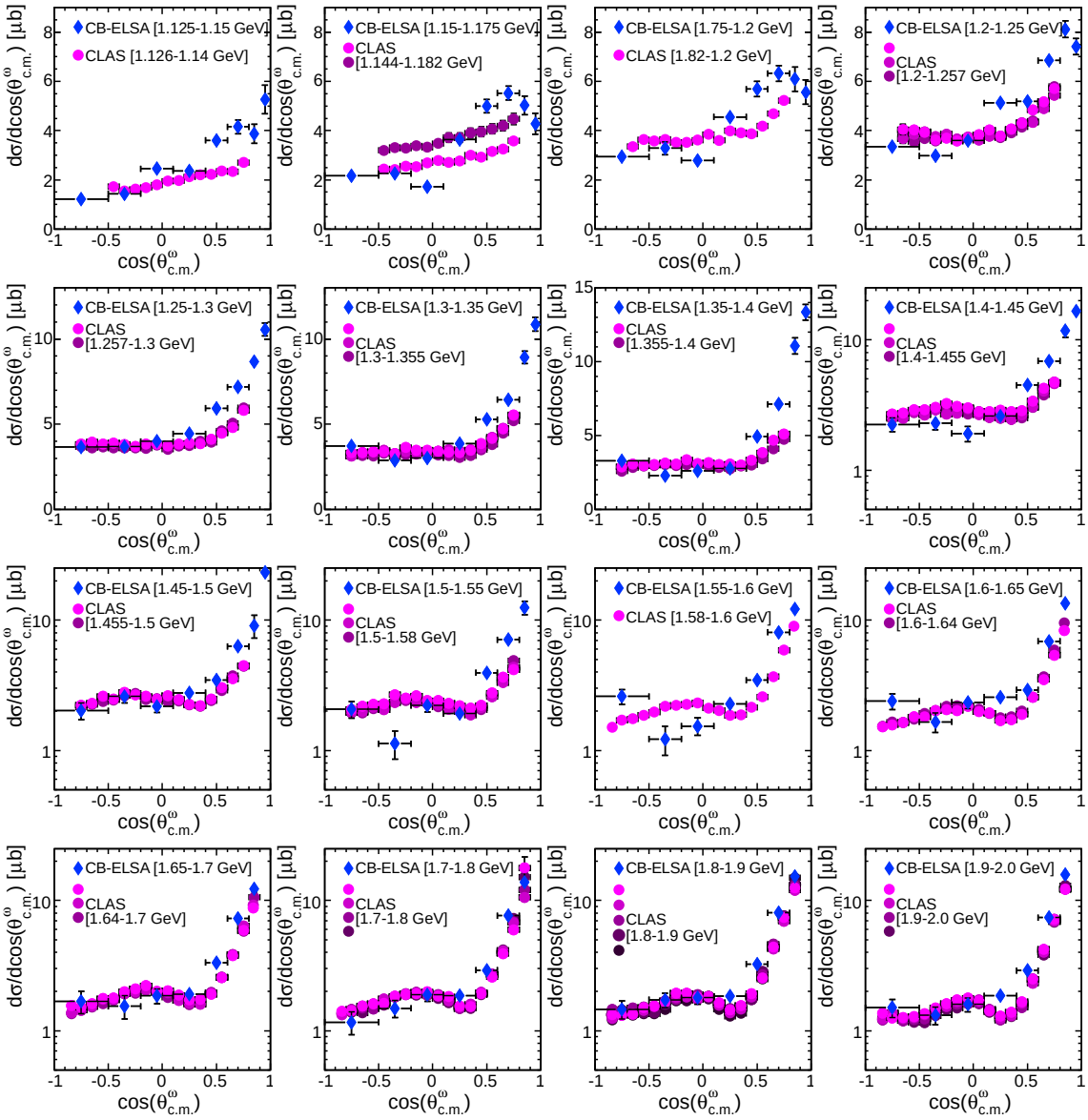

Figure 6.1: Differential cross-sections, $d\sigma/d\cos(\theta^{\omega}_{c.m.})$ versus $\cos(\theta^{\omega}_{c.m.})$, of ω mesons produced off the free proton for different bins of incident beam energy, E_γ. The results of this thesis for the exclusive analysis (blue diamonds) are compared to CLAS data (magenta circles)[19]. Since the incident energy binning of the present work does not coincide with that in [19] several CLAS data sets are shown for the incident energy intervals given in this figure.

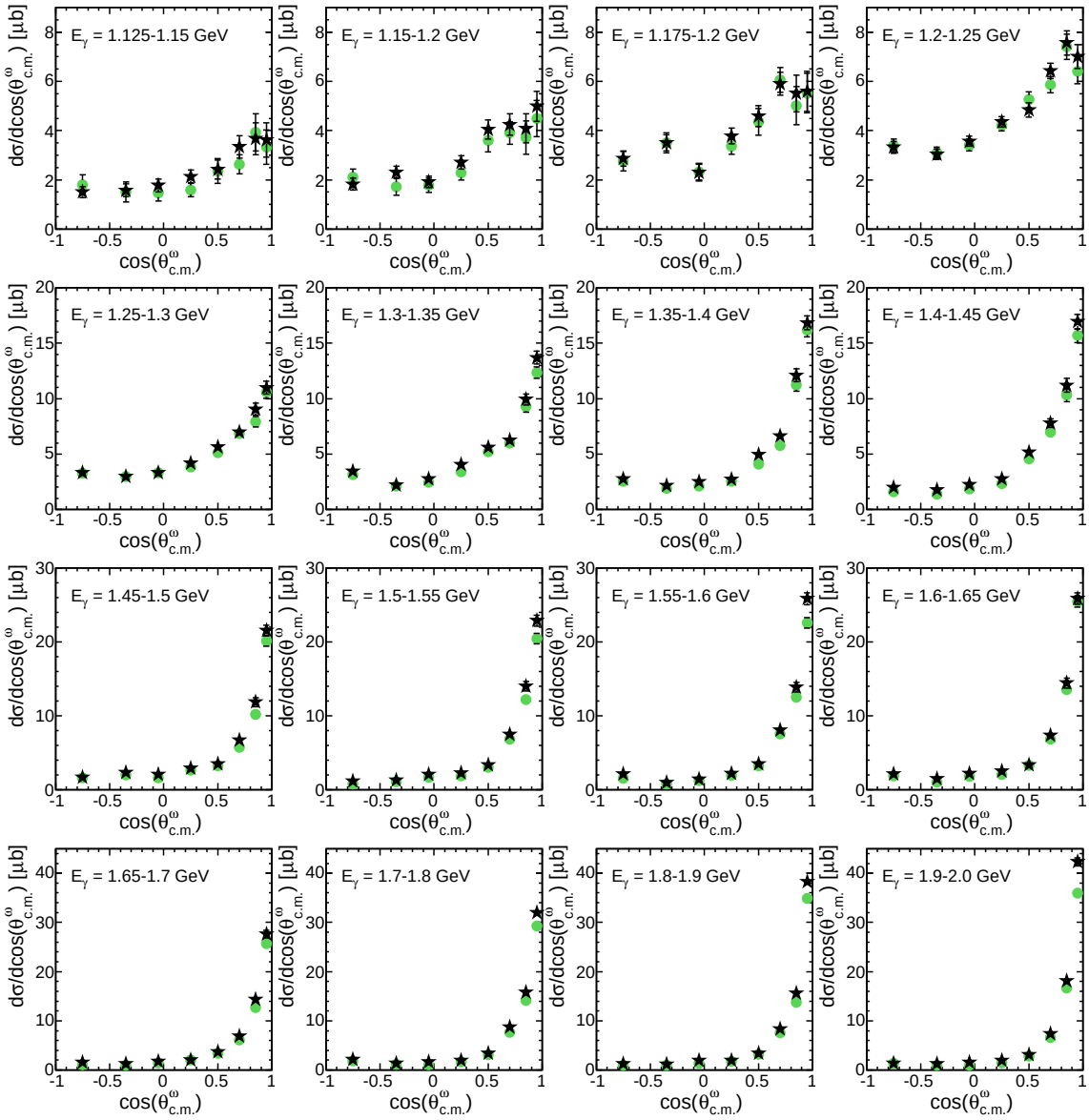

Figure 6.2: Differential cross-sections, $d\sigma/d\cos(\theta^{\omega}_{c.m.})$ versus $\cos(\theta^{\omega}_{c.m.})$, of ω mesons produced off the free proton for different bins of incident beam energy, E_{γ}. The results of inclusive analysis using the grid acceptance (green circles) and using the phase space simulated acceptances (black stars).

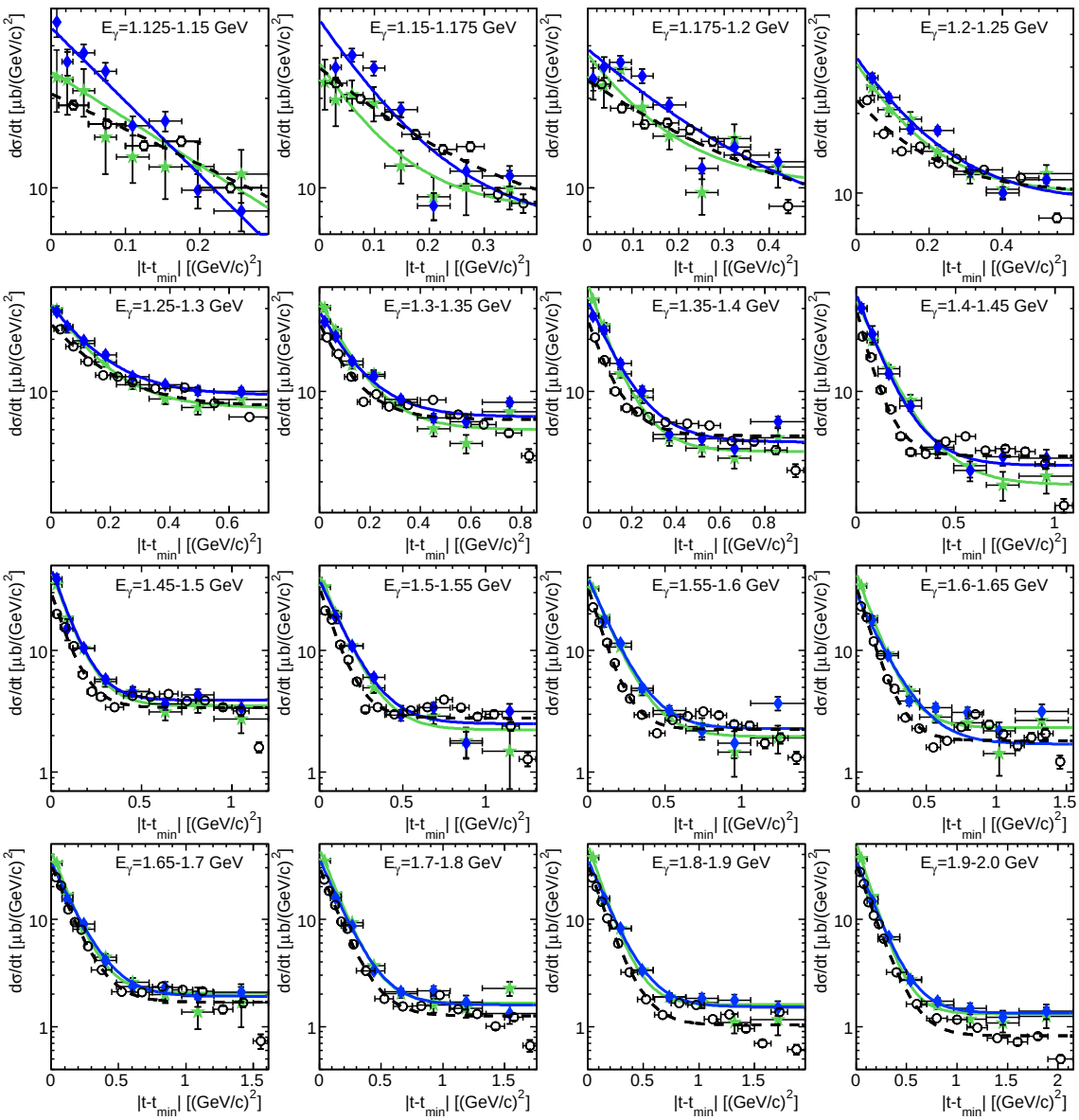

Figure 6.3: Differential cross-sections of ω mesons produced off the free proton versus the momentum transfer to the nucleon, t. The results of this work from the exclusive analysis (blue diamonds) and from the inclusive analysis (green stars) are compared to results from SAPHIR (open circles)[18]. The lines are fits to the CBELSA/TAPS data (solid) and SAPHIR data (dashed) according to eq. 6.2.

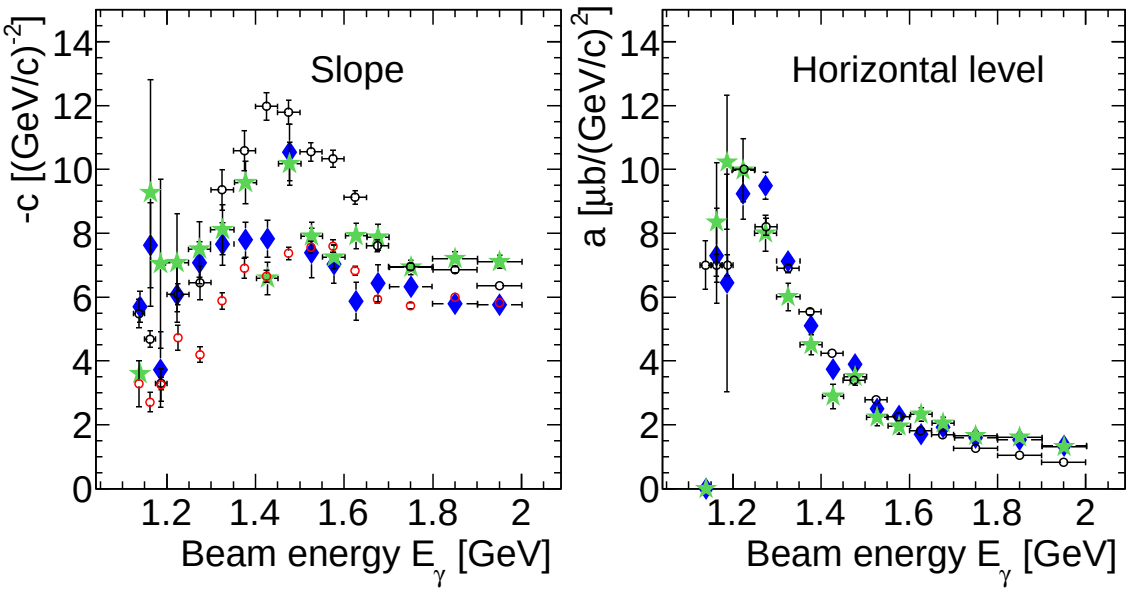

Figure 6.4: Slope parameter (left) and horizontal level (right) from function 6.2 that were fit to the t-scaled differential cross-sections for ω photoproduction off the free proton in fig. 6.3. The result of this thesis for the exclusive analysis (blue diamonds), for the inclusive analysis (green stars) are compared to SAPHIR data (open circles). The slope parameter for SAPHIRs data determined from the fit in fig. 6.3 (black open circles) and the values published in [18] (red open circles).

The t-scaled differential cross-sections in fig. 6.3 were fitted with eq. 6.2 and the parameters a and c of the fits are shown in fig. 6.4. For the slope parameter from the SAPHIR data two different values are drawn, the slope obtained from the fits in fig. 6.1 and the values published by SAPHIR [18]. The latter values were obtained by an exponential fit in the small momentum transfer region. For this fit there is no clear definition of where the fit region ends though. A better choice is to use the slope in the function 6.2 and to be consistent, the comparison should be done to that slope. Figure 6.4 (left) shows that the slopes from the different analysis methods (exclusive and inclusive) are generally in good agreement. In view of the uncertainty of determining the slope, seen by the difference in the slopes obtained from the SAPHIR data using different fits, they can be said to also agree with the SAPHIR data. At energies $E_\gamma > 1.5$ GeV the inclusive analysis gives somewhat steeper slopes than the exclusive analysis. In this energy region, the differential cross-section for the most forward-going ω mesons, $0.9 \leq \cos(\theta^{\omega}_{c.m.}) \leq 1.0$, could not be determined in the exclusive analysis due to vanishing proton acceptance. In this region, an extrapolation had to be used which could explain the discrepancy in slopes.

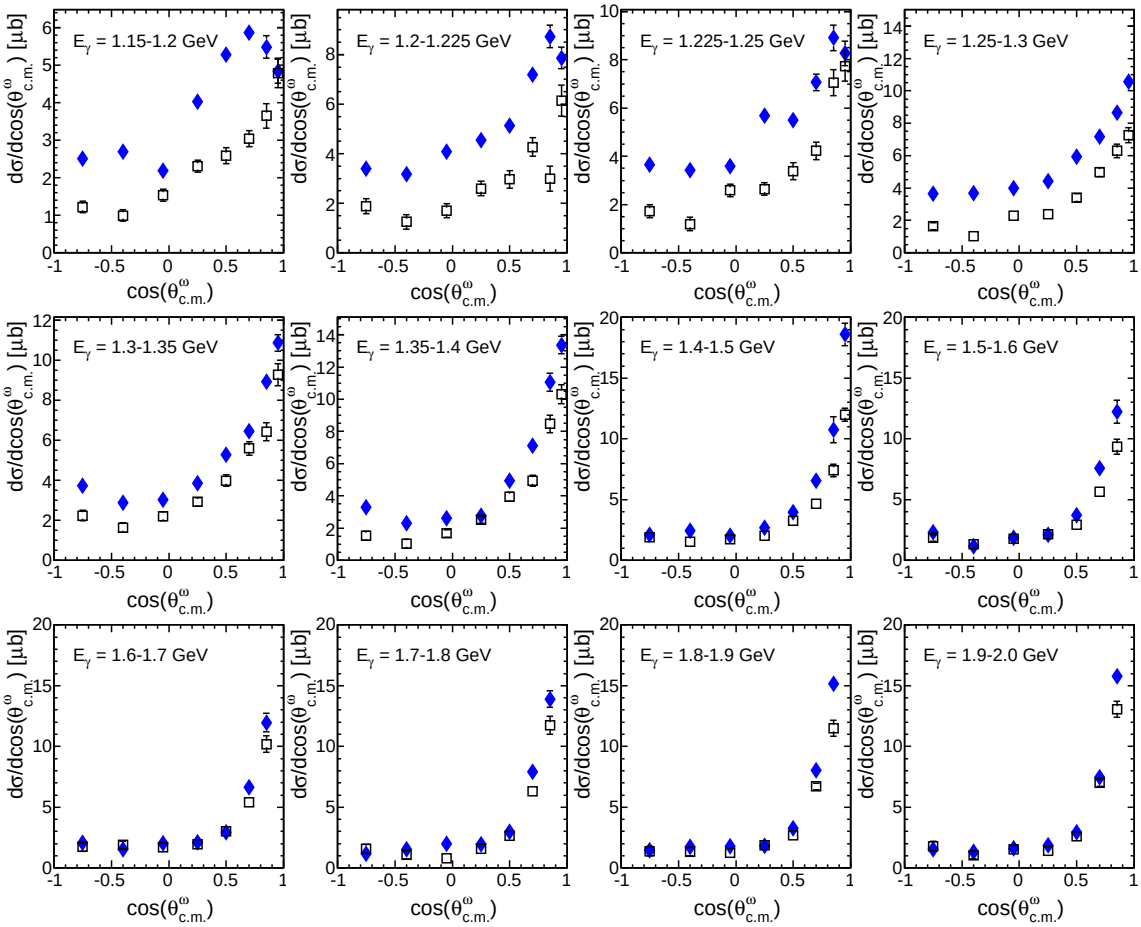

Figure 6.5: Differential cross-sections $d\sigma/d\cos(\theta^{\omega}_{c.m.})$ of ω mesons produced off the bound proton (open squares) compared to off the free proton (blue diamonds).

The horizontal level in $d\sigma/dt$, which is related to the ω meson production via resonances, can be seen to be in good agreement with the previously published data. Only for $E_\gamma >$ 1.6 GeV the horizontal level lies slightly above the SAPHIR data. In this region also the CLAS data was seen to lie above the SAPHIR data (for that comparison see fig. 1.4). The present data comes close to the CLAS data in this region.

The differential cross-section off the bound proton $d\sigma/d\cos(\theta^{\omega}_{c.m.})$ is shown in fig. 6.5 in comparison to the previous result off the free proton. The differential cross-sections were scaled with the momentum transfer to the nucleon, t. The resulting $d\sigma/dt$ can be

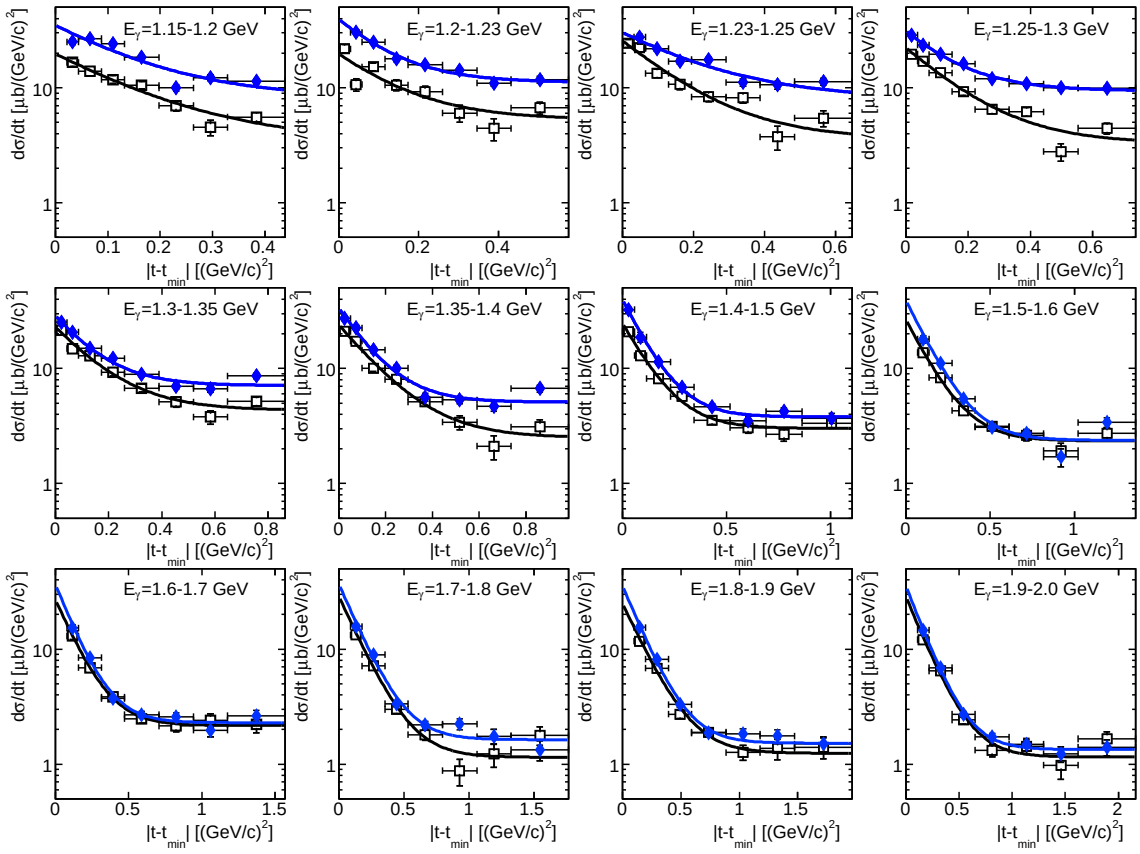

Figure 6.6: Differential cross-section versus the momentum transfer to the nucleon for ω mesons produced off the bound proton (open squares) and for ω mesons produced off the free proton (blue diamonds). The curves are fits to the data according to eq. 6.2.

seen in fig. 6.6, where it is compared to the differential cross-section off the free proton. Both figures show that in the low energy region, where production via resonances makes a substantial contribution to the cross-section, the differential cross-section off the bound proton lies below the one off the free proton. At higher incident beam energies the differential cross-sections off bound and off free protons come close to each other.

The differential cross-sections $d\sigma/d\cos(\theta^{\omega}_{c.m.})$ and $d\sigma/dt$ for ω production off the free proton and off the bound proton are listed in tables in appendices I and J.1, respectively.

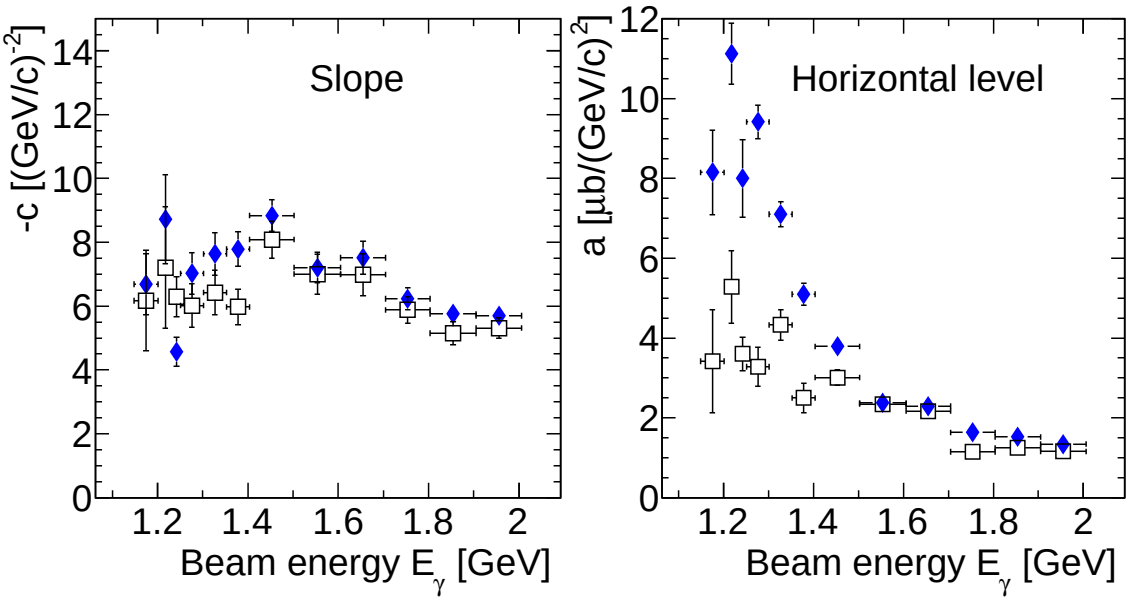

Figure 6.7: Left: slope parameter and right: horizontal level from the fit of eq. 6.2 to $d\sigma/dt$ for ω mesons produced off the bound proton (open squares) and for ω mesons produced off the free proton (blue diamonds).

The parameters of the fits (eq. 6.2) to the differential cross-sections $d\sigma/dt$ shown in fig. 6.7 confirm that at higher energies ($E_\gamma > 1.4$ GeV) the bound proton becomes quasi-free and the production mechanism is almost the same as off a free proton giving equal slopes and horizontal levels.

At low energies the proton-neutron interaction becomes particularly relevant. In this energy region the exponential slope is difficult to determine because of the strong resonance contributions. The horizontal levels in this energy region indicate stronger resonance contribution for ω production off the free proton compared to off the bound proton. This can partly be explained by a smearing due to the Fermi motion of a bound proton. For a comparison of the total cross-sections together with the cross-section off the free proton folded with Fermi motion, see fig. 6.15.

6.1.2. The quasi-free production off the bound neutron

The differential cross-sections off the bound neutron are shown in fig. 6.8 as a function of $\cos(\theta^{\omega}_{c.m.})$ and in fig. 6.9 as a function of the momentum transfer to the nucleon $d\sigma/dt$. In both figures the differential cross-section off the bound neutron is compared to the

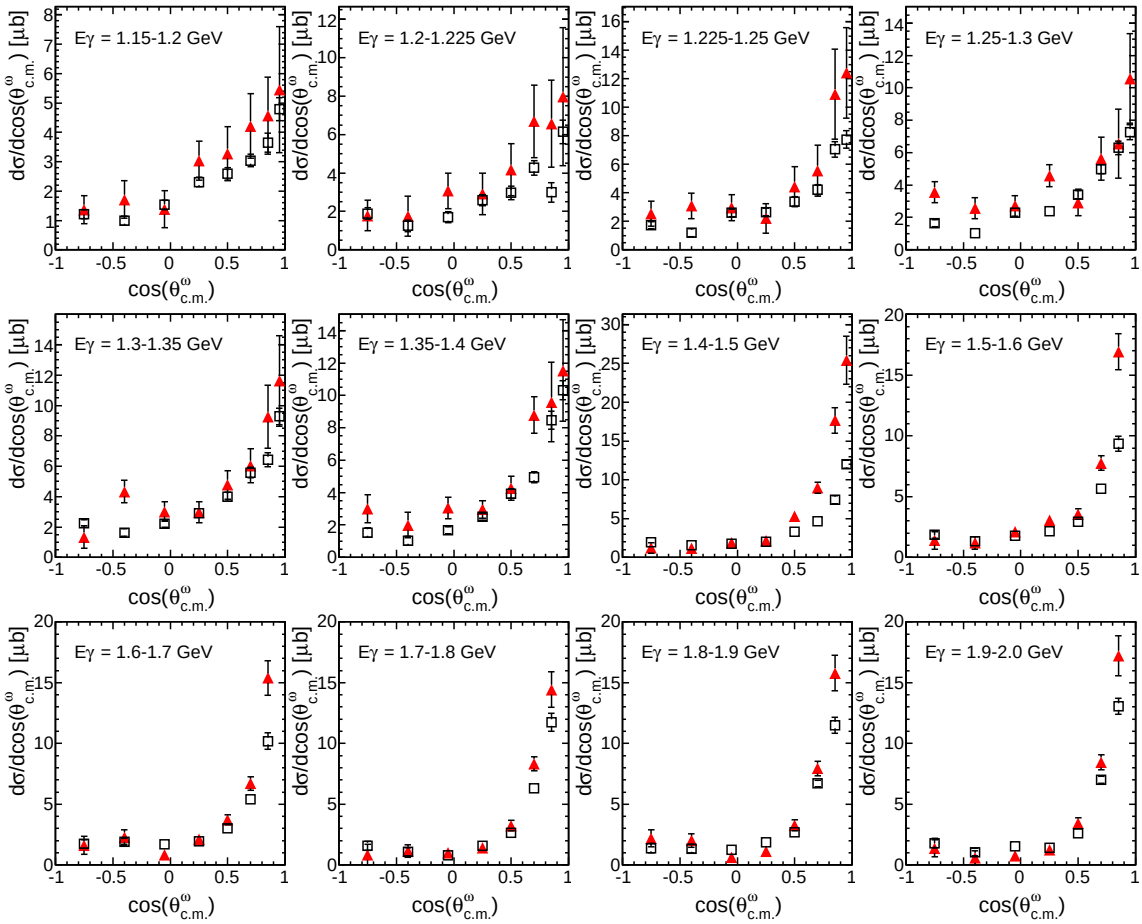

Figure 6.8: Differential cross-sections $d\sigma/d\cos(\theta^{\omega}_{c.m.})$ of ω mesons produced off the bound neutron (red triangles) compared to off the bound proton (open squares).

differential cross-section off the bound proton. Both figures show that the differential cross-section off the bound neutron is larger than that off the bound proton. For incident beam energies $E_\gamma > 1.6$ GeV the difference in the differential cross-sections off protons and off neutrons becomes smaller. For a comparison of the total cross-sections off the bound neutron to that off the bound proton see fig. 6.16.

The differential cross-sections $d\sigma/dt$ were fitted with eq. 6.2 and the parameters of the fits are shown in fig. 6.10. The exponential slopes (left), which characterize the t-channel exchange, can be seen to agree within the precision of determination for ω mesons produced

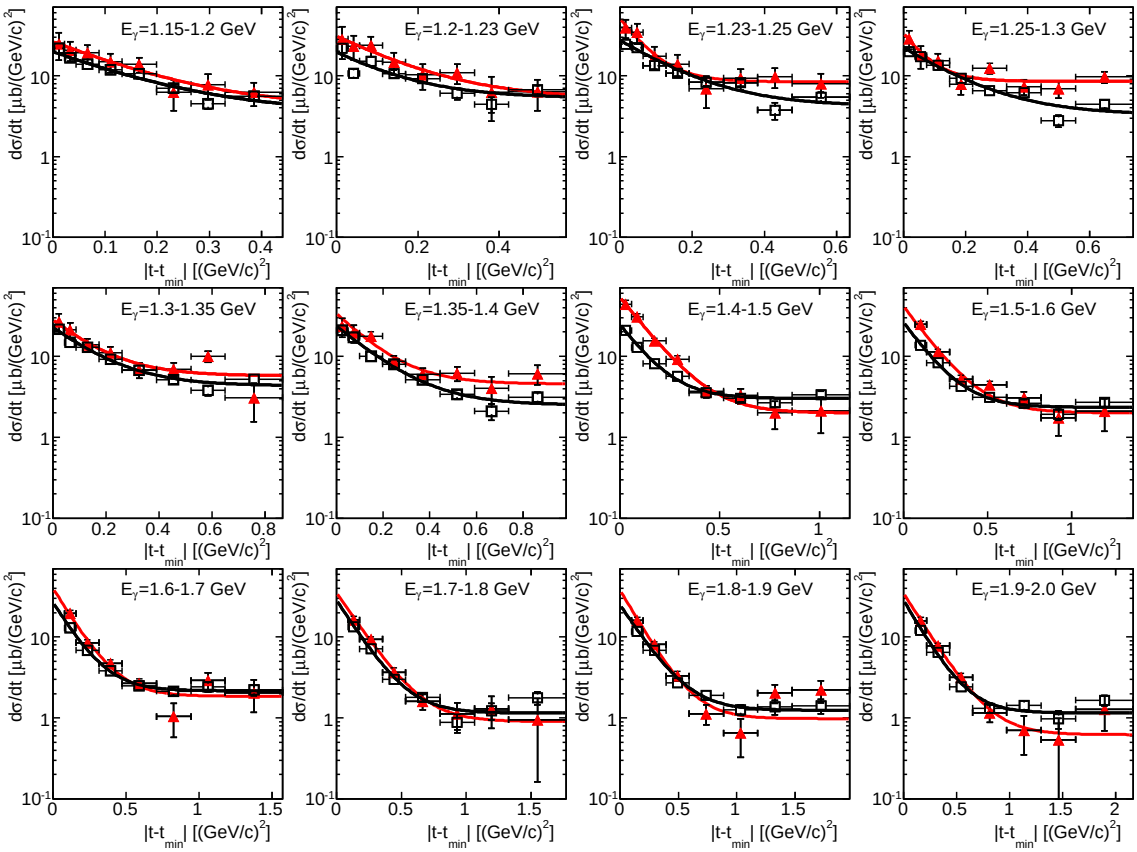

Figure 6.9: Differential cross-section versus the momentum transfer to the nucleon for ω mesons produced off the bound proton (open squares) and for ω mesons produced off the bound neutron (red triangles). The curves are fits to the data according to eq. 6.2.

off the bound neutron and off the bound proton. The comparison of the horizontal levels (right) show stronger resonance contribution for ω meson production off the neutron than for the production off the proton for incident beam energies $E_\gamma < 1.4$ GeV. At higher incident beam energies both slopes and horizontal levels become identical, indicating a production mechanism independent of isospin.

The differential cross-sections $d\sigma/d\cos(\theta^{\omega}_{c.m.})$ and $d\sigma/dt$ for ω production off the neutron are listed in tables in appendix J.2.

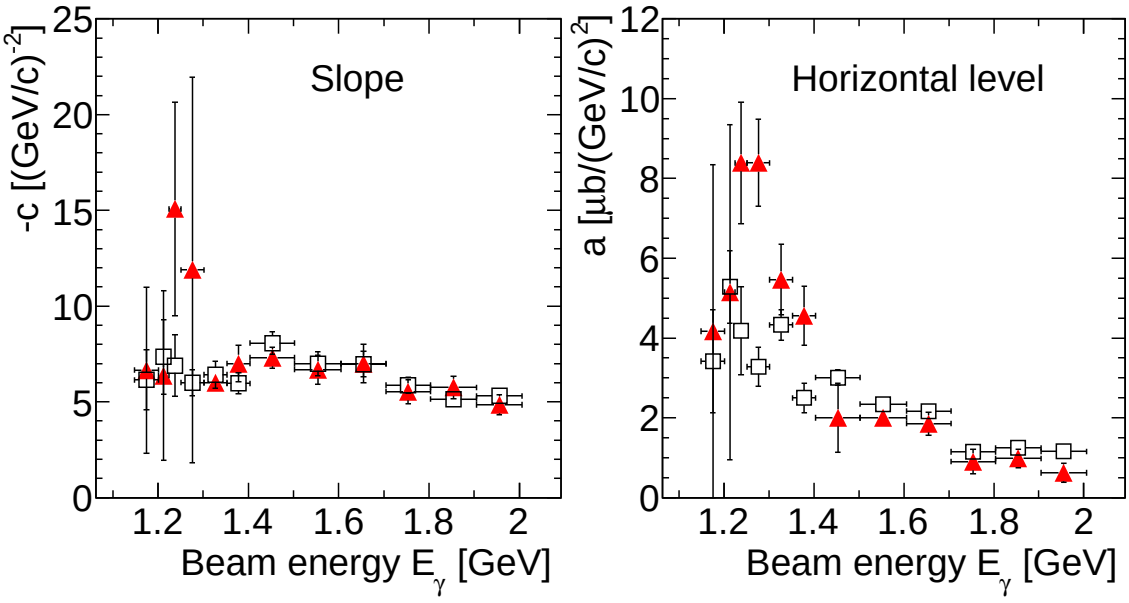

Figure 6.10: Left: slope parameter and right: horizontal level from the fit of eq. 6.2 to $d\sigma/dt$ for ω mesons produced off the bound proton (open squares) and off the bound neutron (red triangles).

6.1.3. The quasi-free inclusive production off LD_2

The differential cross-sections for the quasi-free inclusive production were calculated with two different methods for the efficiency correction, as discussed in sect. 5.12. Figure 6.11 shows that the two different methods are in good agreement. However, integration of the fits showed a slight discrepancy which reflects the systematic error in the ω acceptance.

The mean values for the differential cross-sections from the two methods were calculated and scaled with the momentum transfer to the nucleon. The resulting $d\sigma/dt$ are shown in fig. 6.12 together with the sum of the two exclusive differential cross-sections, $\frac{d\sigma_p}{dt} + \frac{d\sigma_n}{dt}$. This comparison was made in order to check the validity of the cross-sections determined by the exclusive analysis. The sum of the two exclusive cross-sections should not exceed the inclusive cross-section. As shown in fig. 6.12 the sum agrees with the inclusive cross-section, within errors. Only for incident beam energies $E_\gamma > 1.6$ GeV a slight discrepancy in the exponential slopes for small momentum transfers is seen. For the lowest point in t a reliable neutron identification was not ensured, thus the exclusive differential cross-sections had to be extrapolated, which could possibly explain the observed discrepancy. For the effect of this discrepancy on the total cross-sections, see fig. 6.17.

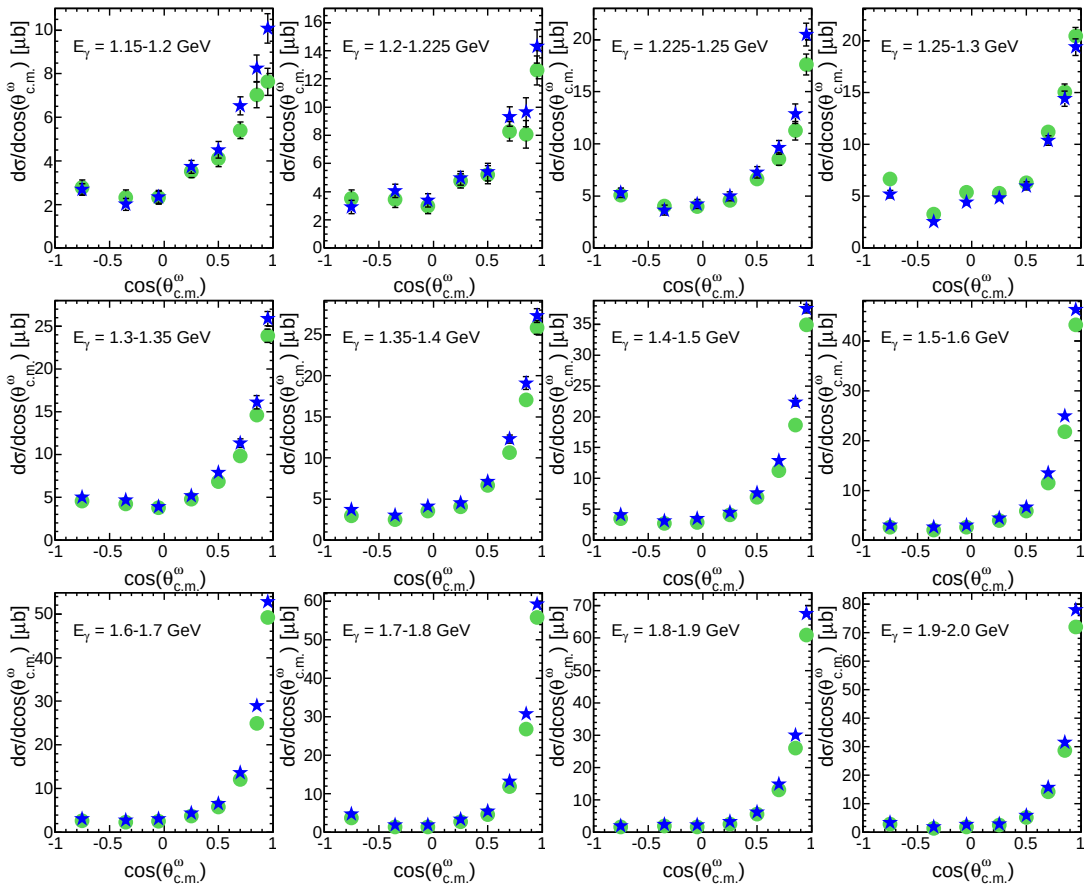

Figure 6.11: Differential cross-sections, $d\sigma/d\cos(\theta^{\omega}_{c.m.})$ versus $\cos(\theta^{\omega}_{c.m.})$, of ω mesons determined with inclusive analysis off LD_2 for different bins of incident beam energy, E_γ using the grid acceptance (green circles) and using the phase space simulated acceptances (blue stars).

The inclusive differential cross-sections $d\sigma/d\cos(\theta^{\omega}_{c.m.})$ and $d\sigma/dt$ for ω production off LD_2 are listed in tables in appendix J.3.

6.1.4. Comparison to a coupled-channel calculation

Figure 6.13 shows the differential cross-sections determined by exclusive analysis off the free proton, bound proton and bound neutron compared to a coupled-channel calculation performed by Vitaly Shklyar [48] for ω mesons produced off the free proton and off the free neutron for four bins of incident beam energy. For the lowest bin (E_γ = 1.1-1.15 MeV),

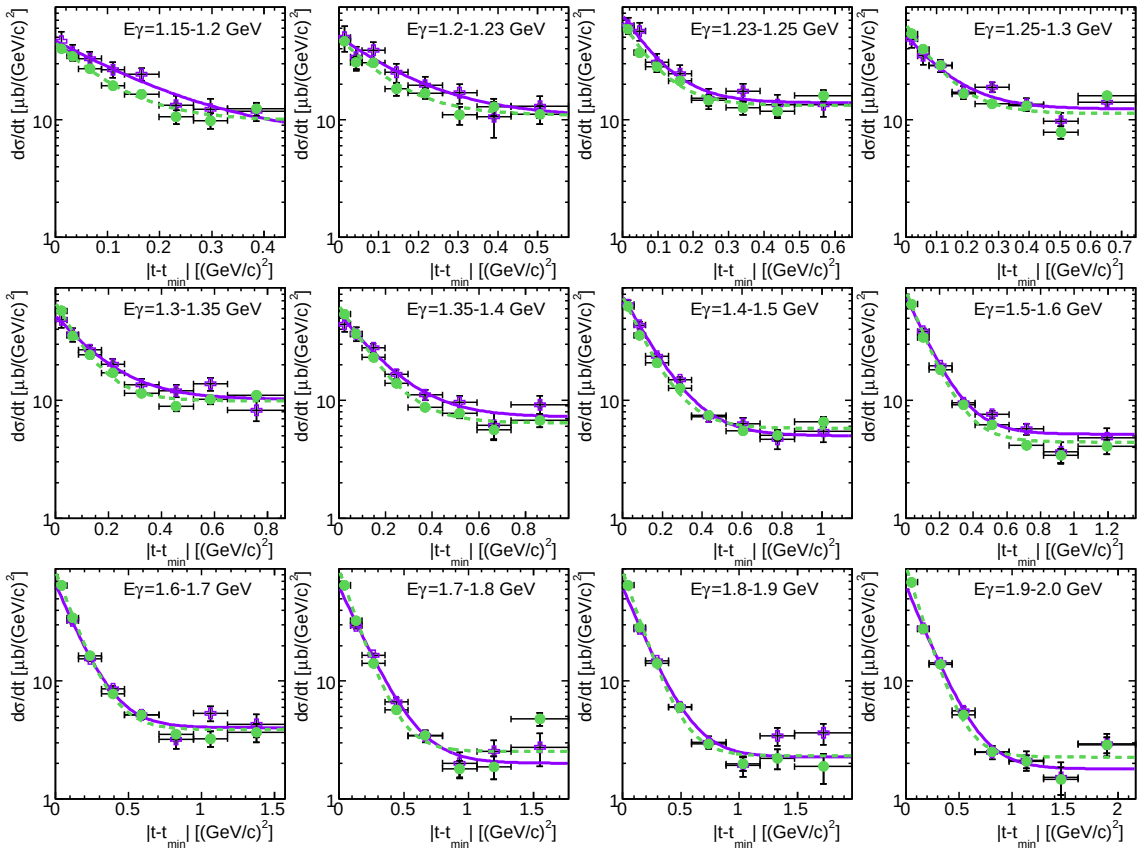

Figure 6.12: Differential cross-section versus the momentum transfer to the nucleon for the quasi-free inclusive channel off deuterium (green circles) compared to the sum of the two exclusive production channels, $\sigma_p^{bound}/dt + \sigma_n^{bound}/dt$, (purple crosses).

reasonable fits to the $\pi^0\gamma$ invariant mass spectra was not possible, hence no data is shown in this bin. It can be seen that the calculation yields a much larger cross-sections for ω mesons off the free neutron than off the free proton for all incident beam energies. In the incident beam energy range 1.25-1.3 GeV a the data off the free proton comes close to the calculation. In this energy bin the differential cross-section off the bound proton lies below the calculation and the data off the free proton. The differential cross-section off the bound neutron is larger than that off the bound proton, however, not with the same magnitude as is seen for the calculation.

At higher incident beam energies the data for all three reaction channels come close to

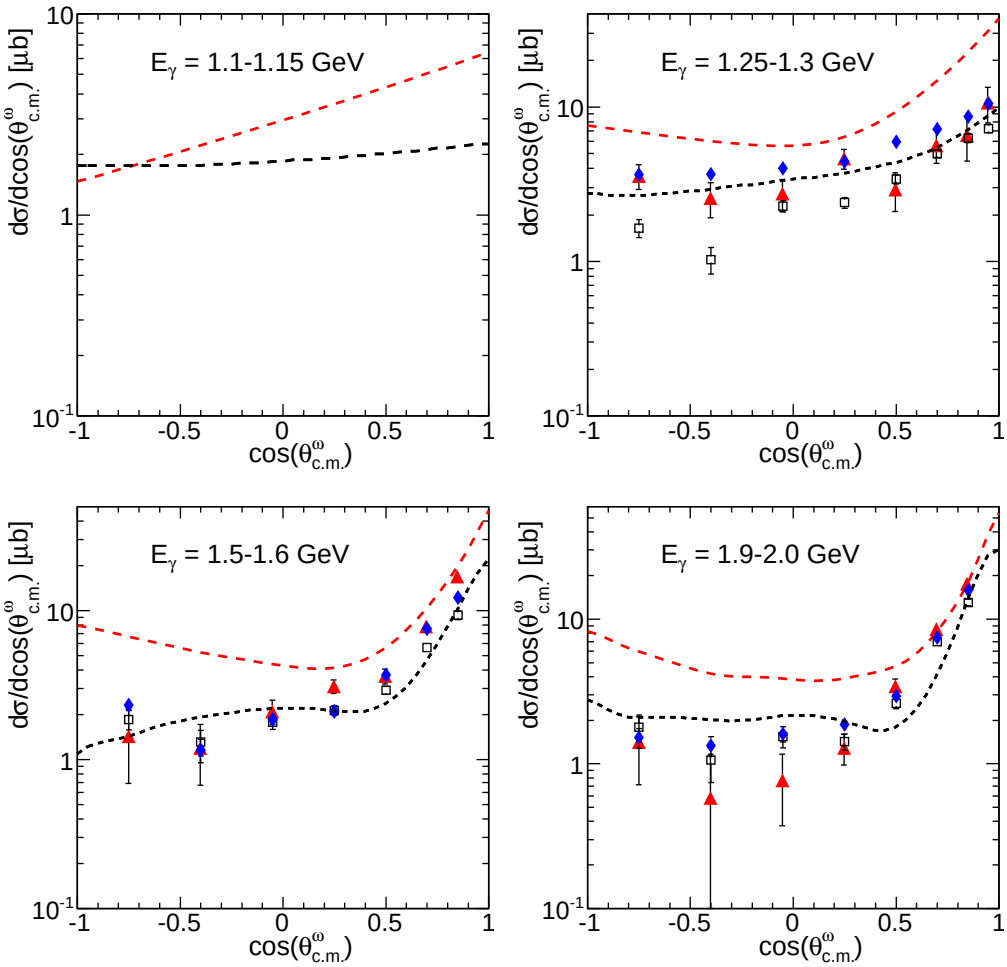

Figure 6.13: Differential cross-sections $d\sigma/d\cos(\theta^{\omega}_{c.m.})$ for ω mesons produced off the free proton (blue diamonds), off the bound proton (open squares) and off the bound neutron (red triangles) compared to coupled-channel calculations off the free proton (black dashed) and the free neutron (red dashed).

each other showing a slightly lower contribution in the resonance dominated region (ω mesons going backward in the c.m.-system) and in the region where the ω mesons goes forward in the c.m.-system the data lie above the calculation off the free proton. The differential cross-section obtained from calculation off the free neutron is much larger than the data. But, it is important to note that the calculation is very crude (no neutron data is entered) and the fact that the neutron and proton are bound within a nucleus is not taken into account.

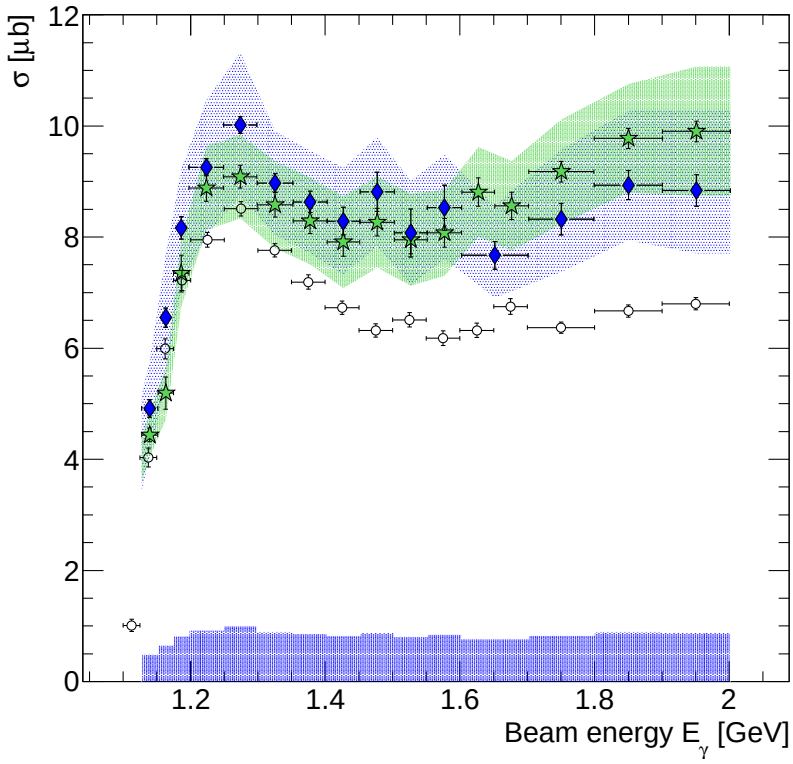

Figure 6.14: Total cross-section as a function of the incident photon energy for ω mesons produced off the free proton. The results of this work for the exclusive analysis (blue diamonds) and for the inclusive analysis (green stars) are compared to results from SAPHIR (open circles) [18]. The systematic errors of the present analysis which affect the overall normalization are shown as bar histogram. The bands indicate the systematic errors in the data analysis.

A comparison of the total cross-sections off the bound proton and off the bound neutron to the calculation is shown in fig. 6.16.

6.2. Total cross-sections

The total cross-sections were obtained by integration of the fits to the t-scaled differential cross-sections from 0 to $|t_{max} - t_{min}|$. The values of the total cross-sections are listed in appendix K. The statistical errors were calculated using the Gaussian propagation rule described in appendix A.2. The sources of systematic errors are described in appendix A.3.

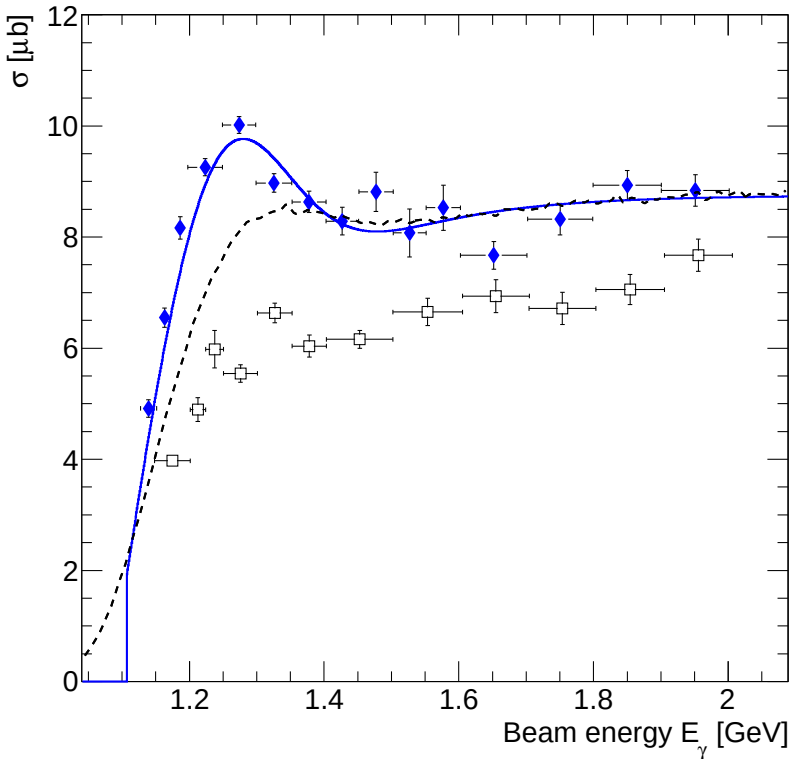

Figure 6.15: Total cross-sections as a function of the incident photon energy for ω mesons produced off the free proton from exclusive analysis (blue diamonds) and off the bound proton (open squares). Folding the cross-section off the free proton, fitted by the solid blue curve, with the Fermi motion of nucleons in deuterium leads to the dashed black curve.

6.2.1. The cross-section off the free and bound proton

The total cross-sections for ω mesons produced off the free proton from the inclusive and exclusive analyses were obtained by integration of the fits in fig. 6.3. They are shown in fig. 6.14 together with data from SAPHIR [18] (the CLAS collaboration has not published any total cross-sections since they had a limited angular coverage). For incident beam energies $E_\gamma < 1.3$ GeV agreement is found between the present data and the SAPHIR data, within the systematic errors. However, at higher incident beam energies the total cross-sections from the exclusive analysis lies generally 1-2 μb above the data published by SAPHIR. For incident beam energies $E_\gamma > 1.7$ GeV the cross-section from the inclusive analysis tend to be larger than the exclusive cross-section by $\approx$10%. This difference is attributed to the

extrapolation of the fits in the small momentum transfer region, which was necessary for the exclusive analysis. Within the systematic errors quoted, the inclusive and exclusive cross-sections are in agreement.

The cross-section of ω mesons produced off the bound proton was obtained by integration of the differential cross-sections depicted in fig. 6.6. It is shown in fig. 6.15 in comparison to the previous result of ω mesons produced off the free proton. It can be seen that the resonance peak observed in the free proton case is hardly visible in the bound proton case. In order to see if this feature could be explained by the Fermi motion of the bound proton, the free proton data was fitted (with the restriction that $\sigma = 0$ under the production threshold $E_\gamma < 1108$ MeV) and folded with the Fermi motion of nucleons in deuterium. This indeed shows a smearing of the resonance peak, however, not enough to account for the difference in cross-sections which amounts to $\approx$30%. The folding was done statistically by recalculating the initial state energy using impulse approximation (described in sect. 2.4) where the target proton was given a randomly generated momentum from the Fermi distribution for a nucleon in the deuteron. The code for this folding with the Fermi motion was written by Igal Jaegle [50].

6.2.2. The quasi-free cross-section off the bound neutron

Figure 6.16 shows the total cross-sections of ω mesons produced off the bound neutron and off the bound proton obtained by integration of the fits in fig. 6.9. The cross-section off the bound neutron is clearly larger than that off the bound proton in the low energy region. At higher energies they become almost equal. The dashed lines in the figure are coupled channel calculations performed by Vitaly Shklyar [48] of the cross-sections of ω mesons produced off the free neutron and off the free proton. It is a crude calculation with parameters adjusted to reproduce the SAPHIR data but without fitting to any neutron data. The effect of the Fermi motion was also not included. Still, it illustrates that due to isospin differences, leading to interference effects on the amplitude level, a larger cross-section is obtained for ω mesons produced off neutrons compared to off protons. The difference in cross-sections from this calculation is, however, larger than the one observed in the CB-ELSA data. The ratio of the cross-sections σ_n/σ_p is shown in fig. 6.18 and discussed in sect. 6.2.3.

6.2.3. The quasi-free inclusive cross-section off LD_2

The quasi-free inclusive cross-section was obtained by integration of the fits in fig. 6.12. Figure 6.17 shows that the inclusive cross-section agrees, within errors, with the the sum

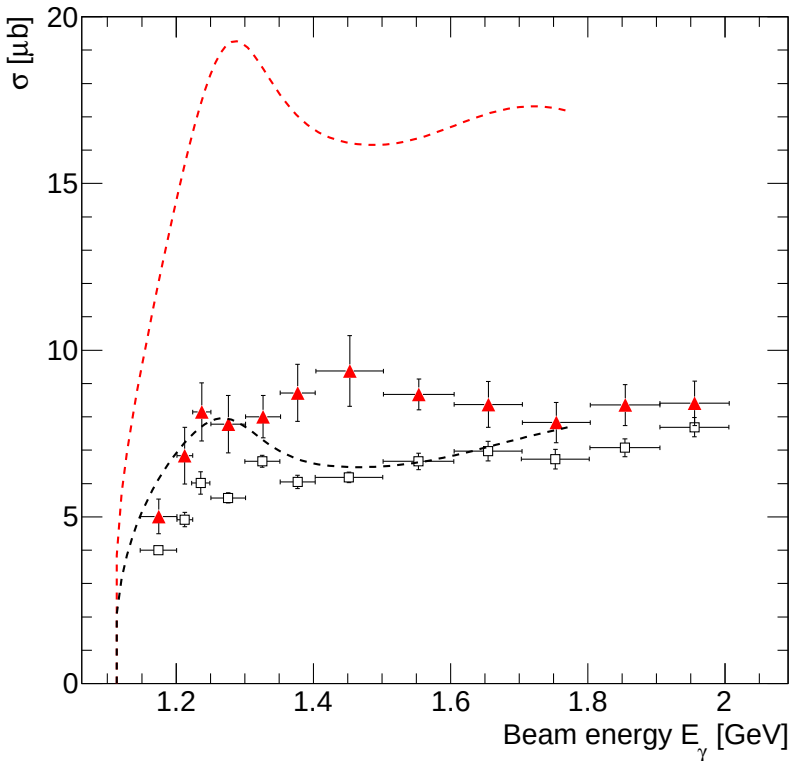

Figure 6.16: Total cross-section as a function of the incident photon energy for ω mesons produced off the bound neutron (red triangles) compared to the total cross-section for ω mesons produced off the bound proton (open squares). The dashed curves are coupled-channel calculations of the cross-section of ω mesons produced off the free proton (black) and off the free neutron (red) performed by Vitaly Shklyar [48].

of the angle integrated cross-sections for exclusive ω production off the bound proton and bound neutron, $\sigma_p + \sigma_n$. For energies $E_\gamma > 1.6$ GeV the inclusive cross-section is slightly larger than the sum of the two exclusive cross-sections. This difference may be due to the extrapolation of the differential cross-section at low momentum for the exclusive analyses.

An alternative determination of the the cross-section off the neutron was made by subtracting the cross-section off the bound proton from the inclusive cross-section, *i.e.*

$$\sigma_n^{indirect} = \sigma_{incl} - \sigma_p \,. \tag{6.3}$$

The resulting cross-section, which is independent of the neutron detection efficiency, is also shown in fig. 6.17. This cross-section is seen to be larger than the cross-section off the

bound proton, consistent with the exclusively determined cross-section off the neutron. The difference in the two determinations of the production cross-section off the bound neutron mainly reflects the systematic error in the neutron identification.

In order to quantify how much larger the cross-section off the neutron is than the cross-section off the proton the ratio , σ_n/σ_p was calculated, see fig. 6.18, for the indirect determination and for the direct (exclusive) measurement. For incident beam energies 1.2 GeV $<E_\gamma <$ 1.6 GeV the average ratio is $< \sigma_n/\sigma_p > \approx 1.3$. For incident beam energies $E_\gamma >$ 1.6 GeV the ratio from the indirect measurement is $\approx$1.4 whereas the ratio from the direct determination decreases to $\approx$1.1 at 2.0 GeV. This difference is within the systematic errors quoted for the cross-section determinations.

Figure 6.18 also shows the ratio of the cross-sections from the coupled channel calculations which were shown in fig. 6.16. They yield a ratio $< \sigma_n/\sigma_p > \approx 2.3$ in the range from threshold up to 1.8 GeV. This is clearly larger than what was observed in the data. Still, it shows that there exist theoretical models that predict a larger cross-section for ω mesons produced off neutrons compared to the production off protons.

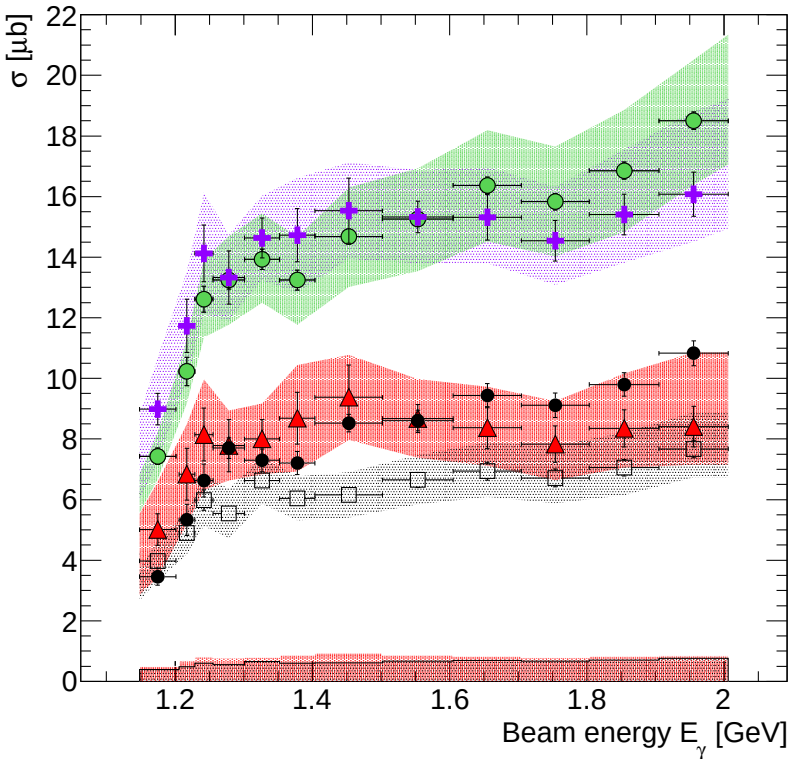

Figure 6.17: Total cross-section as a function of the incident photon energy for ω mesons produced off the bound proton (open squares) and off the bound neutron (red triangles), the sum of the two exclusive cross-sections $\sigma_p^{bound} + \sigma_n^{bound}$ (purple crosses), the quasi-free inclusive cross-section σ_{incl} (green circles) and the cross-section off the neutron calculated by $\sigma_{incl} - \sigma_p^{bound}$ (black circles). The systematic errors which affect the overall normalization are shown as bar histograms. The bands indicate the systematic errors in the data analysis.

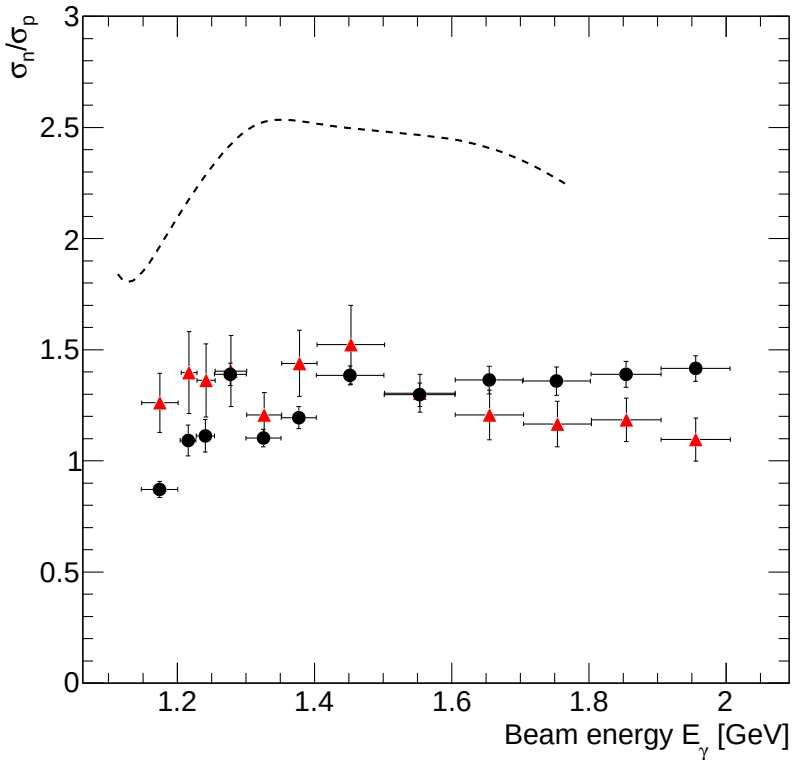

Figure 6.18: The ratio of the total cross-section for an ω meson produced off a bound neutron to the total cross-section for an ω meson produced off a bound proton, σ_n/σ_p for the exclusive analysis (red triangles) and the ratio from the indirectly determined neutron cross-section using the inclusive analysis (black circles). The dashed curve show the ratio σ_n/σ_p for a coupled channel calculation.

7. Conclusions

7.1. ω photoproduction off the free and bound proton

The differential cross-section off the free proton was determined through both exclusive and inclusive analyses and the results generally agree quite well. The inclusive analysis gives somewhat higher values, in particular the exponential slope is slightly steeper than that for the exclusive analysis in the region for small momentum transfer to the nucleus. The exponential rise in this region is characteristic of the t-channel exchange process. In the region where $0.9 \leq \cos(\theta^{\omega}_{c.m.}) \leq 1.0$ the differential cross-section for incident beam energies $E_{\gamma} \geq 1500$ MeV could not be determined due to vanishing proton acceptance. Hence, extrapolation had to be used in this region which could explain this discrepancy. The total cross-section obtained from the inclusive analysis were found to be ≈10% higher than the cross-sections obtained from the exclusive analysis in this high energy region. This discrepancy is within the quoted systematic errors.

Comparison to data by SAPHIR [18] and CLAS [19] on the ω photoproduction off the free proton shows a slight disagreement in the small momentum transfer region, where the differential cross-sections from this work lie above the previously published data. This gives total cross-sections that were on average 30% higher at an incident beam energy of 2.0 GeV than the cross-sections published by SAPHIR.

The cross-section off the bound proton is smaller than the one off the free proton. In the resonance peak region of ≈1.3 GeV incident beam energy the cross-section off the bound proton is ≈ 6.5 μb. The discrepancy to the cross-section off the free proton amounts to ≈30%. This difference cannot be attributed to a mere smearing due to the Fermi motion, showing that at energies close to the production threshold the interaction with the neutron plays a role. Only at higher energies the ω meson production cross-section off the bound proton comes close to that off the free proton.

The average cross-sections off the bound proton is 6.6±0.1 μb in the incident photon energy range 1.2-2.0 GeV with a systematic error of ≈15-20%.

7.2. ω photoproduction off the bound neutron

The determination of the ω photoproduction cross-section off the neutron proved to be a difficult matter. Corrections had to be made due to mis-identification of the neutron. In order to avoid the uncertainty originating from the neutron detection this cross-section was also determined indirectly by subtracting the cross-section off the bound proton from the inclusive quasi-free cross-section, $\sigma_n^{indirect} = \sigma_{incl} - \sigma_p$. In this way the neutron acceptance does not enter.

Both determinations yield a cross-section off the bound neutron which is larger than that off the bound proton. For photon energies 1.2-1.6 GeV the ratio is $< \sigma_n/\sigma_p > \approx 1.3$. In this energy region the excitation and decay of nucleon resonances play a dominant role. A stronger resonance contribution to the cross-section for ω production off the bound neutron compared to that off the bound proton is observed. At higher energies $E_\gamma >$ 1.7 GeV the cross-sections come close to each other, indicating production mechanisms independent of isospin.

The average cross-section off the bound neutron is 8.4±0.2 μb in the incident photon energy range 1.2-2.0 GeV. The systematic error was estimated to ≈20-35%.

7.3. Comparison to calculations

The cross-sections of this work were compared to coupled-channel calculations [48] of the ω production off the free proton and off the free neutron. The calculated cross-sections were much larger than the ones observed off the bound proton and bound neutron in this work. This is not surprising, though, since the calculation used the cross-section off the free proton as input and - as already stated - the cross-sections off the bound proton were seen to be lower by ≈30% than the ones off the free proton. For this reason a comparison of the σ_n/σ_p-ratio is a better choice. The coupled-channel calculation yields an average value of the ratio $< \sigma_n/\sigma_p > \approx 2.3$ in the range from the production threshold up to 1.8 GeV. This is larger than what was observed in the data. However, it is important to note that the calculation is crude, since it did not take any of the available neutron data into account. Still, it shows that there exist theoretical models that predict a larger cross-section for ω mesons produced off neutrons compared to that off protons, as observed experimentally in this thesis.

It is hoped that the present work will motivate further theoretical studies, for a deeper understanding of the production mechanisms of the ω meson.

A. Error Estimation

A.1. Statistical error

The statistical error, $\Delta\sigma_{stat}$, was estimated to be the square root of signal and background in the 3σ region around the ω peak in the $\pi^0\gamma$ invariant mass spectra, *i.e.*

$$\Delta\sigma_{stat} = \sqrt{S+B}\,. \tag{A.1}$$

A.2. Gaussian error propagation

The t-scaled differential cross-sections $\frac{\mathrm{d}\sigma}{\mathrm{d}t}(|t-t_{min}|)$ in this thesis were fitted with the function

$$f(x) = a + \exp(b+cx) \tag{A.2}$$

where $x = |t - t_{min}|$. The total cross-section is obtained from the integral of the fit

$$F(x) = ax + \frac{1}{c}\exp(b+cx) \tag{A.3}$$

and the area A under the fit is then

$$A = \int_0^{\Delta t} f(x)dx = \Big[F(x)\Big]_0^{\Delta t} = a\Delta t + \frac{1}{c}\exp(b+c\Delta t) - \frac{1}{c}\exp b\,, \tag{A.4}$$

where $\Delta t = |t_{max} - t_{min}|$. The error of the area ΔA, where $A = g(a,b,c)$, can be approximated by the Gaussian error propagation rule

$$\Delta A \approx \sqrt{\Big(\frac{\partial A}{\partial a}\Delta a\Big)^2 + \Big(\frac{\partial A}{\partial b}\Delta b\Big)^2 + \Big(\frac{\partial A}{\partial c}\Delta c\Big)^2} + \tag{A.5}$$

$$2\Big(Cov(a,b)\frac{\partial A}{\partial a}\frac{\partial A}{\partial b} + Cov(a,c)\frac{\partial A}{\partial a}\frac{\partial A}{\partial c} + Cov(b,c)\frac{\partial A}{\partial b}\frac{\partial A}{\partial c}\Big)\,, \tag{A.6}$$

where $Cov(a,b)$ is the covariance between a and b describing the correlation between the variables. The covariance is positive if the variables vary together and negative if they

vary in opposite directions. If the variables are uncorrelated (which is not the case here) the covariance is zero. Partial integration of eq. A.4 gives

$$\frac{\partial A}{\partial a} = \Delta t\,, \tag{A.7}$$

$$\frac{\partial A}{\partial b} = \frac{1}{c}\Big(\exp(b + c\Delta t) - \exp(b)\Big) \tag{A.8}$$

and

$$\frac{\partial A}{\partial c} = \exp(b + c\Delta t)\Big(\frac{\Delta t}{c} - \frac{1}{c^2}\Big) + \frac{\exp b}{c^2}\,. \tag{A.9}$$

Δa,Δb and Δc are the errors of the corresponding variables.

A.3. Systematic uncertainties

Systematic uncertainties which affect the overall normalization of the cross-sections have been estimated to ≈10% [51]. This uncertainty stems mainly from the photon flux determination. The uncertainty of the target thickness is comparably small (few percent) and the uncertainty of the decay branching ratio is negligible. This type of systematic uncertainty cancels out when comparing the cross-section off the bound proton with the one off the bound neutron.

Comparison between the two different methods used to determine the inclusive cross-sections indicate a ≈6% systematic uncertainty arising from the ω acceptance. Systematic uncertainties from fits and analysis cuts were estimated to be in the range ≈5-10% giving a total systematic error of ≈10-15% for the ω meson reconstruction.

The extrapolation needed in the exclusive analyses in the small momentum transfer region for incident beam energies $E_\gamma < 1.5$ GeV also introduced a systematic uncertainty. Deliberately removing the most forward point (small t) in the inclusive differential cross-section and using extrapolation showed that the systematic error introduced was at most 10%. For incident beam energies $E_\gamma > 1.7$ GeV the cross-section obtained by extrapolation was 10% lower than the one where the full angular range was used.

In addition, the systematic uncertainty due to the use of the exponential fit to the differential cross-section (integral of which gave the total cross-section) was estimated to be ≈5% in the full incident beam energy range.

Apart from incident photon energies near the production threshold the systematic uncertainty of the proton detection, derived from the comparison between the inclusive and exclusive cross-sections off the free proton target, is ≈10-15%. The comparison between the cross-section off the neutron from the exclusive analysis and calculated by subtraction of the cross-section off the proton from the inclusive cross-section (see fig. 6.17) indicate a systematic uncertainty of the neutron detection of ≈10-30%.

Table A.1 summarizes the sources of systematic errors. They add up to a total systematic uncertainty averaged for all incident beam energies of ≈15-20% and ≈20-35% in the cross-section determination off protons and neutrons, respectively. The systematic uncertainties related to the data analysis and the overall normalization are shown separately as bands and bar histograms, respectively, in fig. 6.14 and 6.17.

Table A.1: Sources of systematic errors.

Source	$\gamma d \to \omega p(n)$	$\gamma d \to \omega n(p)$
Analysis:		
Signal fits and cuts	≈5-10%	≈5-10%
Exponential fits	≈5%	≈5%
Extrapolation ($E_\gamma > 1.5$ GeV)	<10%	<10%
ω acceptance	≈6%	≈6%
Recoil nucleon detection	≈5-10%	≈10-30%
Overall normalization	≈10%	≈10%
Total	≈15-20%	≈20-35%

B. Kinematics Calculation

Here follows a calculation of the maximum angle allowed by relativistic kinematics for the outgoing neutron in the ω meson photoproduction reaction, both for the assumption that the neutron in the target is at rest and for the case when the target neutron is moving with a certain momentum.

B.1. Target neutron at rest

The invariant mass, s, for a photon beam hitting a neutron at rest is given by

$$s = m_n^2 + 2E_\gamma m_n \,, \tag{B.1}$$

where m_n is the neutron mass and E_γ is the energy of the incident beam photon.

$$\beta^{cm} = \frac{E_\gamma}{E_\gamma + m_n} \tag{B.2}$$

$$\gamma^{cm} = \frac{1}{\sqrt{1-\beta^2}} \tag{B.3}$$

The momenta in the center-of-mass system for the outgoing particles are

$$|p_n^{cm}| = |p_\omega^{cm}| = \frac{\sqrt{(s-(m_n+m_\omega)^2)(s-(m_n-m_\omega)^2)}}{2\sqrt{s}} \,. \tag{B.4}$$

Using equations B.2, B.3 and B.4 the energy of the neutron in the lab-system E_n^{lab} can be calculated as

$$E_n^{lab} = \gamma^{cm}\beta^{cm}E_n^{cm} = \gamma^{cm}\beta^{cm}\sqrt{m_n^2 + (p_n^{cm})^2} \,. \tag{B.5}$$

The kinematics can be illustrated as in fig. B.1, where the circle describes the cm-system and the ellipse the lab-system. The maximum θ angle allowed for the outgoing neutron θ_n^{max} corresponds to a minimum momentum transferred to the neutron p_n^{min}, where

$$p_n^{min} = \gamma^{cm}(\beta^{cm}E_n^{cm} - p_n^{cm}) \,. \tag{B.6}$$

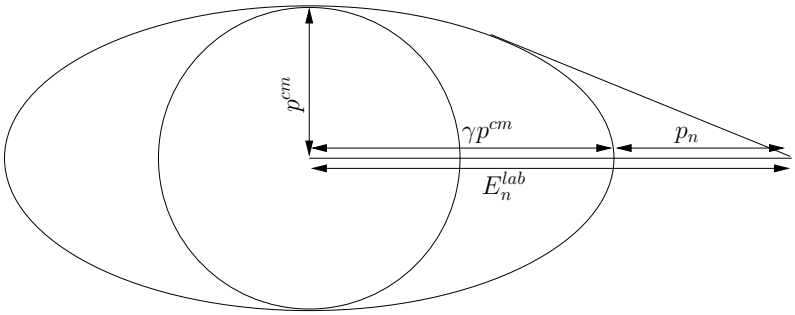

Figure B.1: An illustration of the relativistic kinematics. The circle represents the cm-system and the ellipse the lab-system.

From fig. B.2 the maximum θ angle for the neutron θ_n^{max} can be calculated. An ellipse is described by

$$\frac{x^2}{a^2} + \frac{y^2}{b^2} = 1\,, \tag{B.7}$$

which gives

$$y = \frac{a}{b}\sqrt{a^2 - x^2} \tag{B.8}$$

and

$$\frac{dy}{dx} = \frac{-xb}{a\sqrt{a^2 - x^2}}\,. \tag{B.9}$$

The coordinates (x,y) of a point on the ellipse connected by a straight line tangent to the ellipse to the point (A,0), where A=E_n^{lab}=$\gamma\beta E_n^{cm}$, can be calculated to be

$$x = \frac{a^2}{A} \tag{B.10}$$

and

$$y = b\sqrt{1 - \frac{a^2}{A^2}}\,. \tag{B.11}$$

Then the maximum θ angle of the neutron is given by

$$\theta_n^{max} = \arctan\frac{y}{A - x} = \arctan\frac{b}{\sqrt{A^2 - a^2}}\,, \tag{B.12}$$

where $a = \gamma^{cm} p^{cm}$ and $b = |p_n^{cm}|$, as can be seen in fig. B.1.

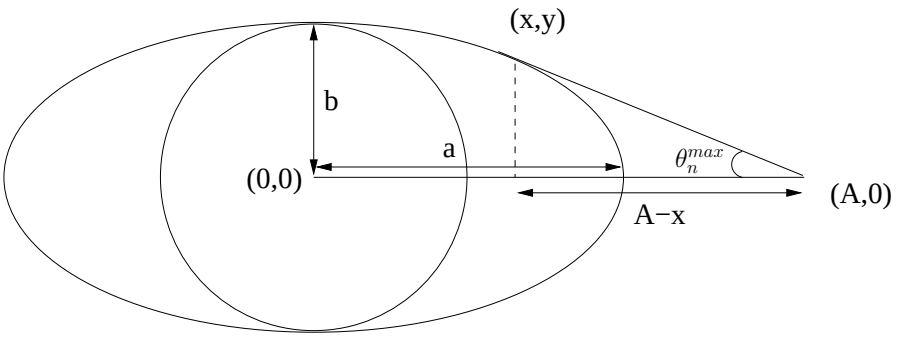

Figure B.2: The maximum θ angle for the outgoing neutron, θ_n^{max}, allowed by kinematics can be calculated using this figure.

B.2. Target neutron in motion

Taking into account that a bound nucleon is not at rest but has some momentum, the so-called Fermi momentum p_f, the calculation in the previous section has to be somewhat altered. Now the invariant mass is given by

$$s = m_n^2 + 2E_\gamma E_n - 2\vec{p_\gamma}\vec{p_f}\,, \tag{B.13}$$

where E_n is the energy of a neutron bound in deuterium

$$E_n = m_d - \sqrt{m_p^2 + p_f^2}\,, \tag{B.14}$$

where m_d and m_p is the mass of deuterium and proton, respectively. The mass of the neutron is no longer considered to be constant but rather has to be calculated by

$$m_n = \sqrt{E_n^2 - p_f^2}\,. \tag{B.15}$$

The maximum s and consequently the maximum θ angle of the scattered neutron is obtained when p_f is directed opposite to the beam, which gives

$$s = m_n^2 + 2E_\gamma E_n + 2E_\gamma p_f\,. \tag{B.16}$$

When introducing a momentum of the target neutron eq. B.2 will be modified into

$$\beta^{cm} = \frac{E_\gamma + p_f}{E_\gamma + E_n}\,. \tag{B.17}$$

The equations B.3 to B.12 remain the same and the maximum θ angle of the scattered neutron is calculated as described in the previous section.

C. t-scaling

Contributions to the differential cross-section by the t-channel exchange process can be seen as a strong rise in the differential cross-section at angles when the ω meson is going forward. The so-called t-scaling is then a better way of visualizing the differential cross-section by transforming $\frac{\mathrm{d}\sigma}{\mathrm{d}\cos\theta}$ into $\frac{\mathrm{d}\sigma}{\mathrm{d}t}$, where t is the momentum transfer to the target. This differential cross-section is then plotted against $|t - t_{min}|$, the difference between the actual momentum transfer and minimum momentum transfer allowed by the kinematics. The four-momentum transfer can range between t_{min} and t_{max}, which for ω mesons produced by γp is given by

$$t_{min}, t_{max} = \left[\frac{m_\omega^2}{2\sqrt{s}}\right]^2 - \left[\frac{s - m_p^2}{2\sqrt{s}} \mp \sqrt{\frac{(s + m_\omega^2 - m_p^2)^2}{4s} - m_\omega^2}\right]^2 , \tag{C.1}$$

where $s = m_p^2 + 2m_p E_\gamma$ and t_{min} corresponds to forward and t_{max} to backward production of the ω meson. The momentum transfer is given by

$$t = t_{min} - \frac{s - m_p^2}{s}\sqrt{(s - (m_\omega + m_p)^2)} \times \sqrt{(s - (m_\omega - m_p)^2)}\sin^2\frac{\theta_{cm}}{2} , \tag{C.2}$$

where θ_{cm} is the emission angle of the ω meson in the center-of-mass system. The differential cross-section $\mathrm{d}\sigma/\mathrm{d}(\cos\theta_{cm})$ is related to $\mathrm{d}\sigma/\mathrm{d}t$ by

$$\frac{\mathrm{d}\sigma}{\mathrm{d}(\cos\theta_{cm})} = \frac{\mathrm{d}\sigma}{\mathrm{d}t}\frac{\mathrm{d}t}{\mathrm{d}(\cos\theta_{cm})} . \tag{C.3}$$

On differentiating eq. C.2 one obtains

$$\frac{\mathrm{d}t}{\mathrm{d}(\cos\theta_{cm})} = \frac{(s - m_p^2)\sqrt{(s - (m_\omega + m_p)^2)(s - (m_\omega - m_p)^2)}}{2s} . \tag{C.4}$$

Inserting that into eq. C gives

$$\frac{\mathrm{d}\sigma}{\mathrm{d}t} = \frac{2s}{(s - m_p^2)\sqrt{(s - (m_\omega + m_p)^2)(s - (m_\omega - m_p)^2)}}\frac{\mathrm{d}\sigma}{\mathrm{d}(\cos\theta_{cm})} . \tag{C.5}$$

For small momentum transfers, corresponding to the region where the t-channel exchange is dominant, the differential cross-section can be fitted with a first order exponential. At

larger momentum transfers other phenomena, like s-channel resonances, dominate and the exponential behavior cannot be seen. Instead, in this region the differential cross-section is nearly constant, thus the fit function chosen to describe the t-dependent differential cross-section was

$$\frac{\mathrm{d}\sigma}{\mathrm{d}t}(|t - t_{min}|) = a + \exp(b + c \cdot |t - t_{min}|)\,, \tag{C.6}$$

where the slope parameter c is negative.

D. Fits for LH_2 exclusive analysis

Here, all the fits to the $\pi^0\gamma$ invariant mass spectra that were used to determine the cross-sections for ω photoproduction off the free proton are shown. The ω signals after background subtraction are also shown. The parameters of each fit with the function $f(x) = p_4(x-p_0)^{p_1}(x-p_2)^{p_3} + p_5 e^{-\frac{(x-p_6)^2}{2p_7^2}}$ are listed. The number of ω mesons for each angular and incident beam energy bin, N_ω, the statistical error and the signal-to-background ratio are given. The upper left spectra in each figure show the sum of all angular bins for the respective incident beam energy bin, -1.0$\leq \cos(\theta^{\omega}_{c.m.}) \leq$1.0. In the lower right figure the sum of ω mesons obtained from the fits in each angular bin is shown, N^{sum}_{ω}. Due to an acceptance hole for protons, the 0.9$\leq \cos(\theta^{\omega}_{c.m.}) \leq$1.0 bin could not be used for incident beam energies $E_\gamma > 1550$ MeV.

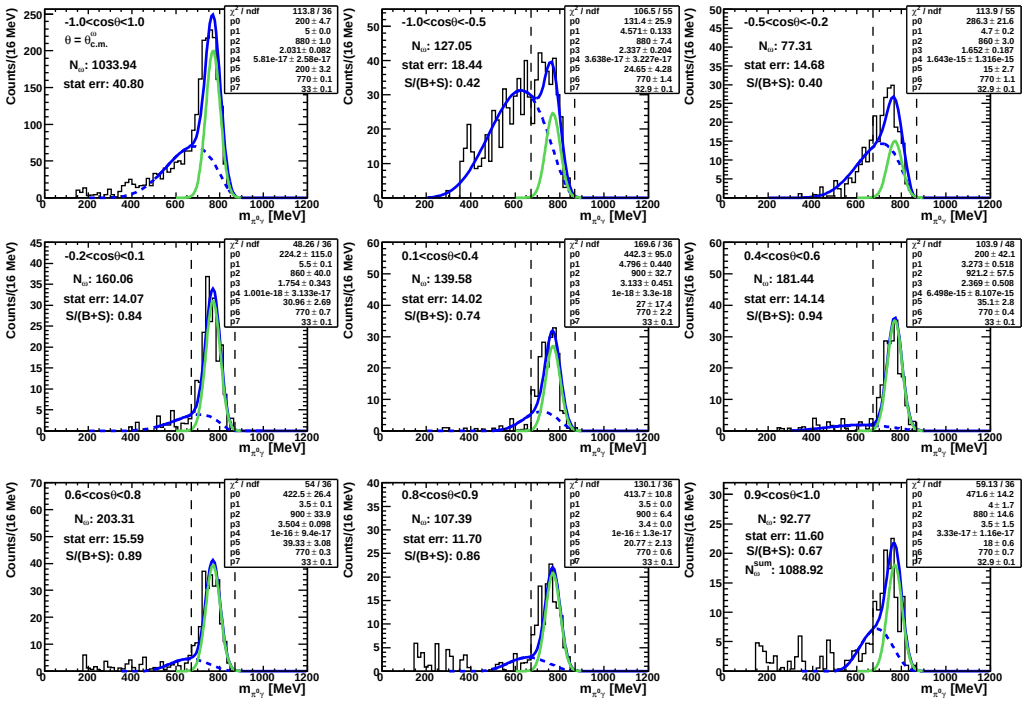

Figure D.1: Fits to the $\pi^0\gamma$ invariant mass spectra for the $\cos(\theta^{\omega}_{c.m.})$ angular bins with incident beam energy E_γ = 1125-1150 MeV.

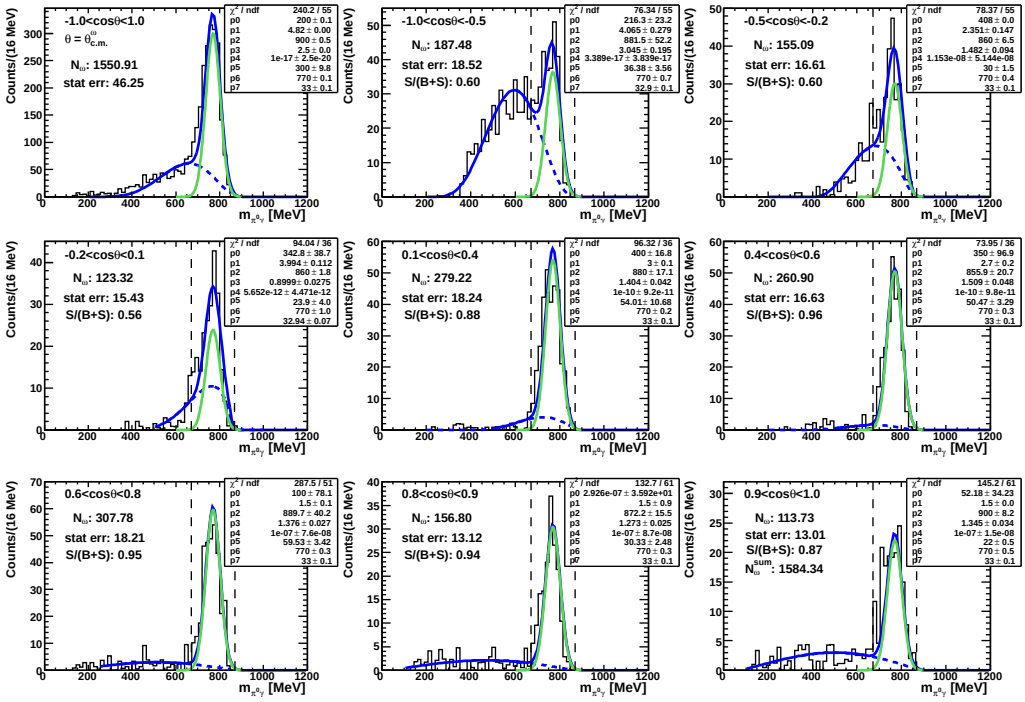

Figure D.2: Fits to the $\pi^0\gamma$ invariant mass spectra for the $\cos(\theta^{\omega}_{c.m.})$ angular bins with incident beam energy E_γ = 1150-1175 MeV.

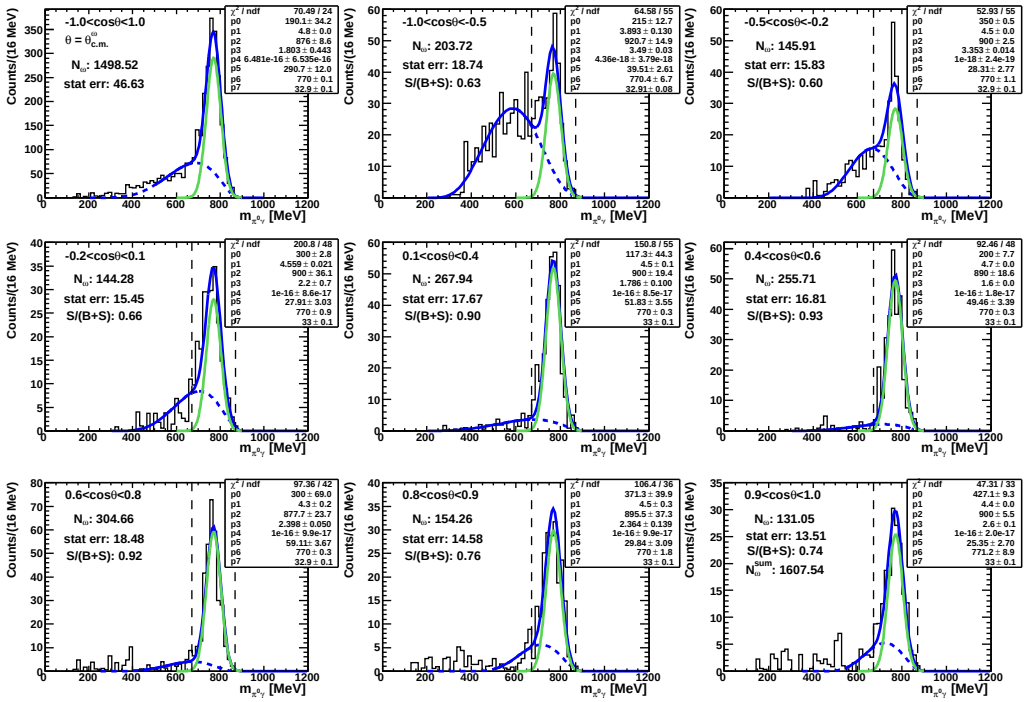

Figure D.3: Fits to the $\pi^0\gamma$ invariant mass spectra for the $\cos(\theta^{\omega}_{c.m.})$ angular bins with incident beam energy E_γ = 1175-1200 MeV.

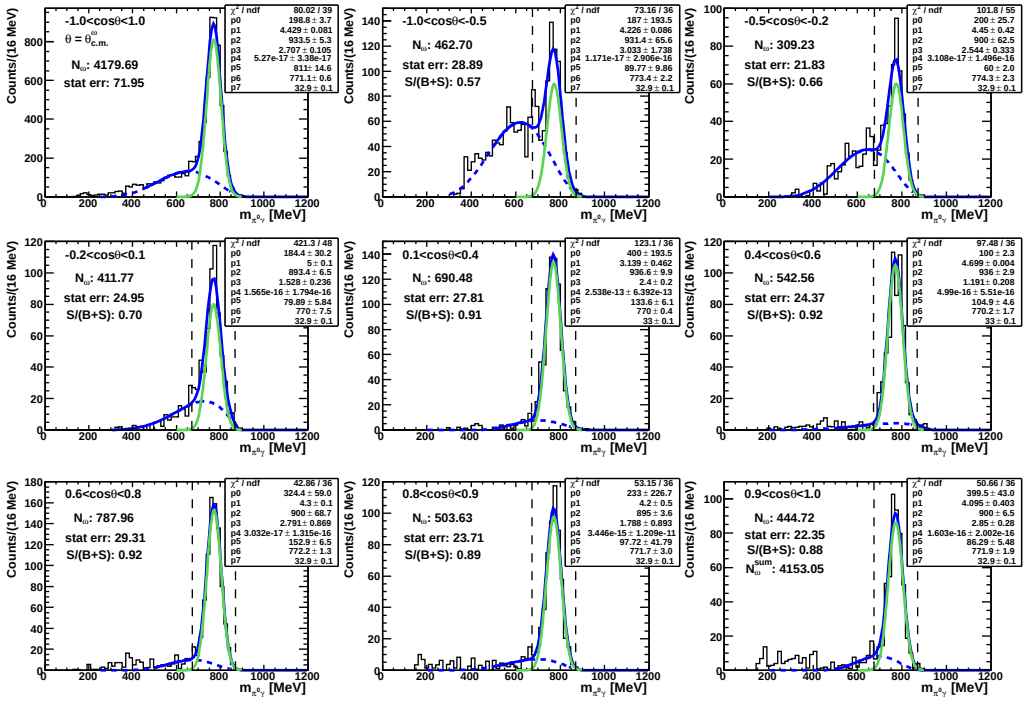

Figure D.4: Fits to the $\pi^0\gamma$ invariant mass spectra for the $\cos(\theta^{\omega}_{c.m.})$ angular bins with incident beam energy E_γ = 1200-1250 MeV.

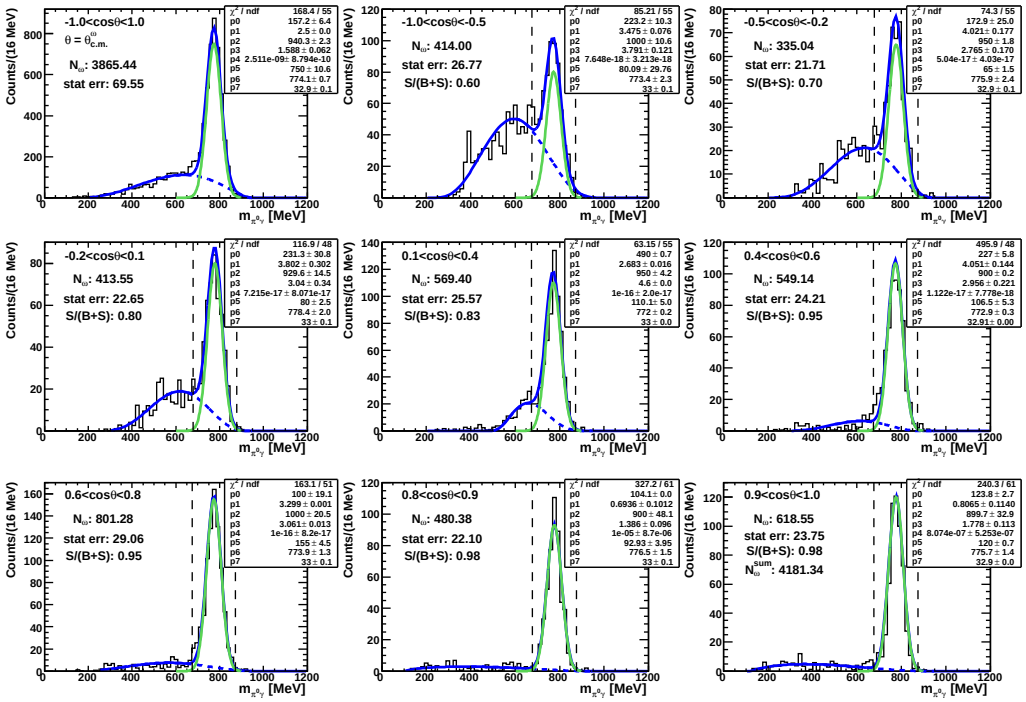

Figure D.5: Fits to the $\pi^0\gamma$ invariant mass spectra for the $\cos(\theta^{\omega}_{c.m.})$ angular bins with incident beam energy E_γ = 1250-1300 MeV.

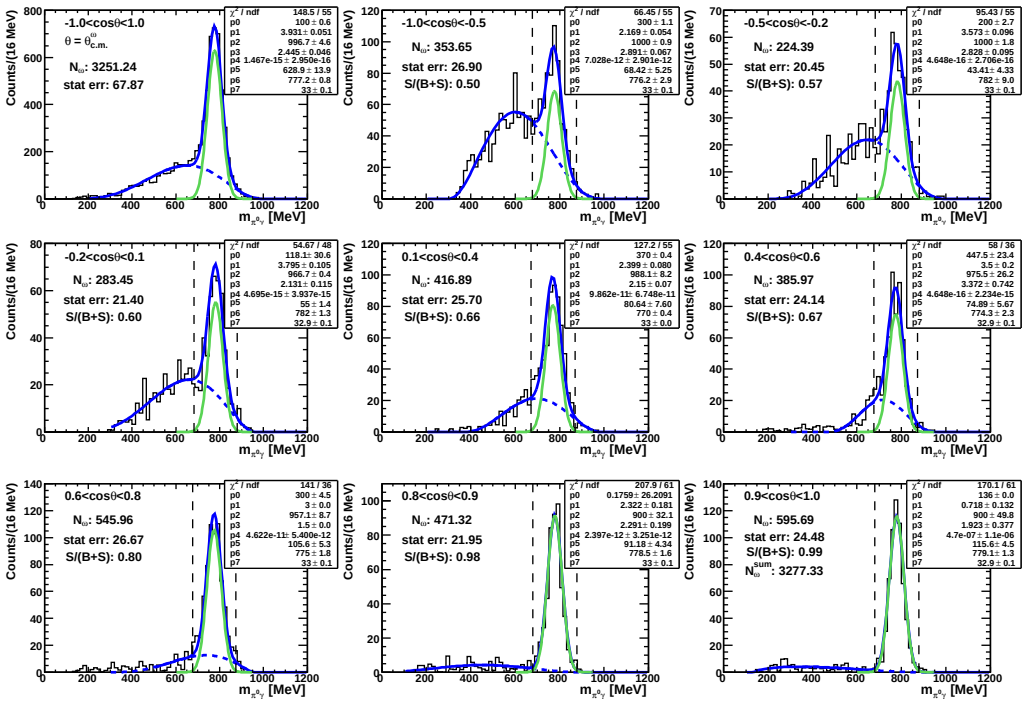

Figure D.6: Fits to the $\pi^0\gamma$ invariant mass spectra for the $\cos(\theta^{\omega}_{c.m.})$ angular bins with incident beam energy E_γ = 1300-1350 MeV.

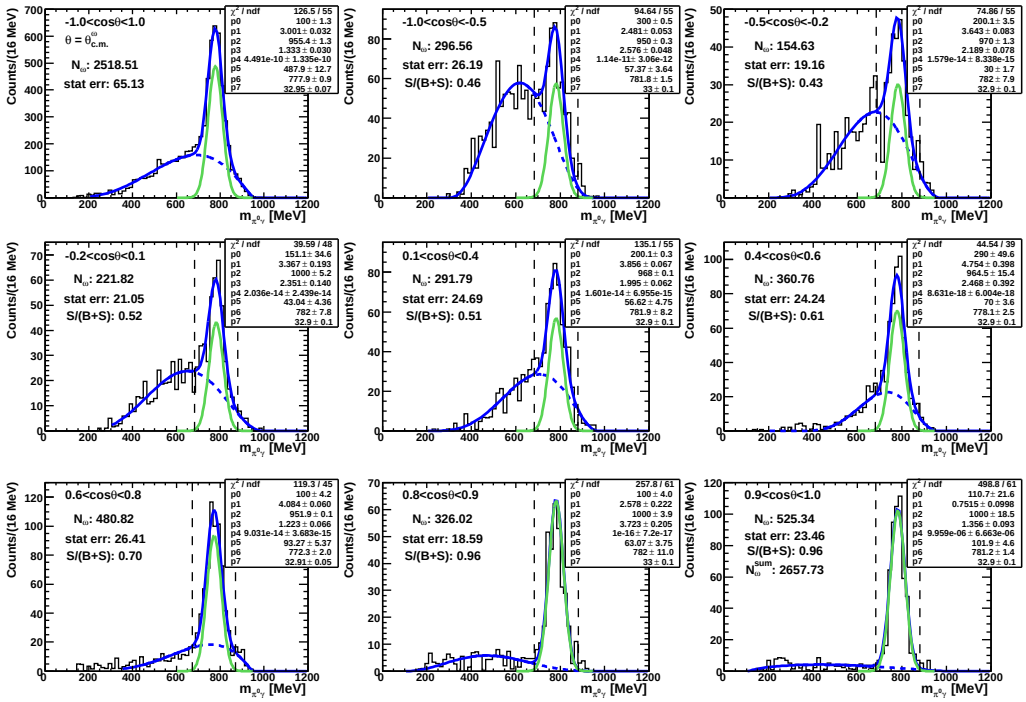

Figure D.7: Fits to the $\pi^0\gamma$ invariant mass spectra for the $\cos(\theta^{\omega}_{c.m.})$ angular bins with incident beam energy E_γ = 1350-1400 MeV.

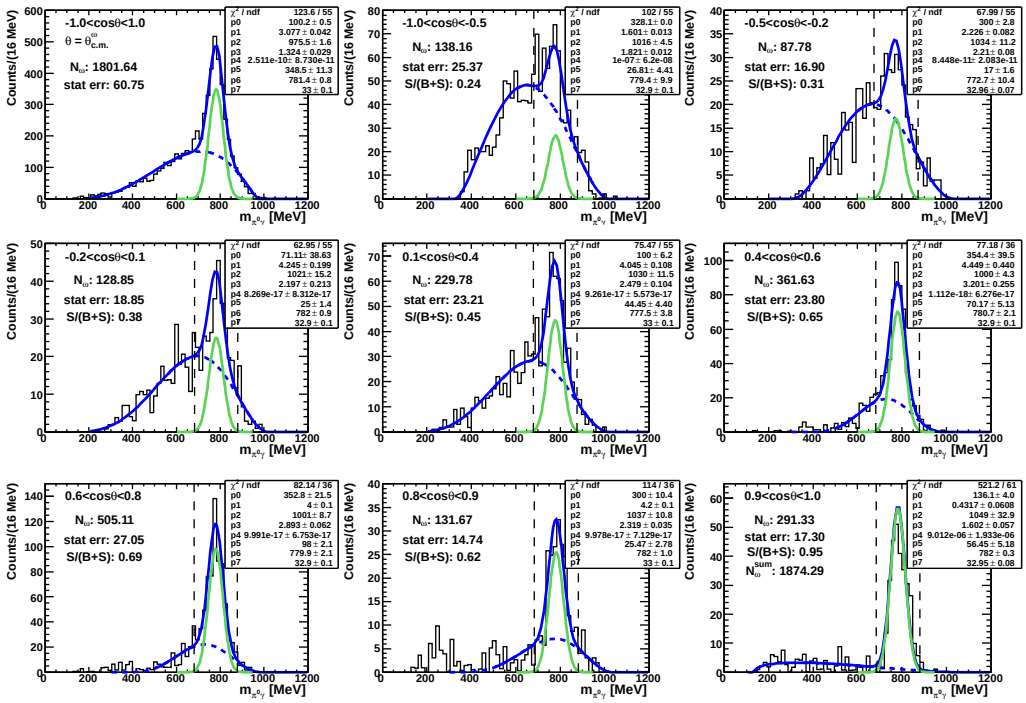

Figure D.8: Fits to the $\pi^0\gamma$ invariant mass spectra for the $\cos(\theta^{\omega}_{c.m.})$ angular bins with incident beam energy E_γ = 1400-1450 MeV.

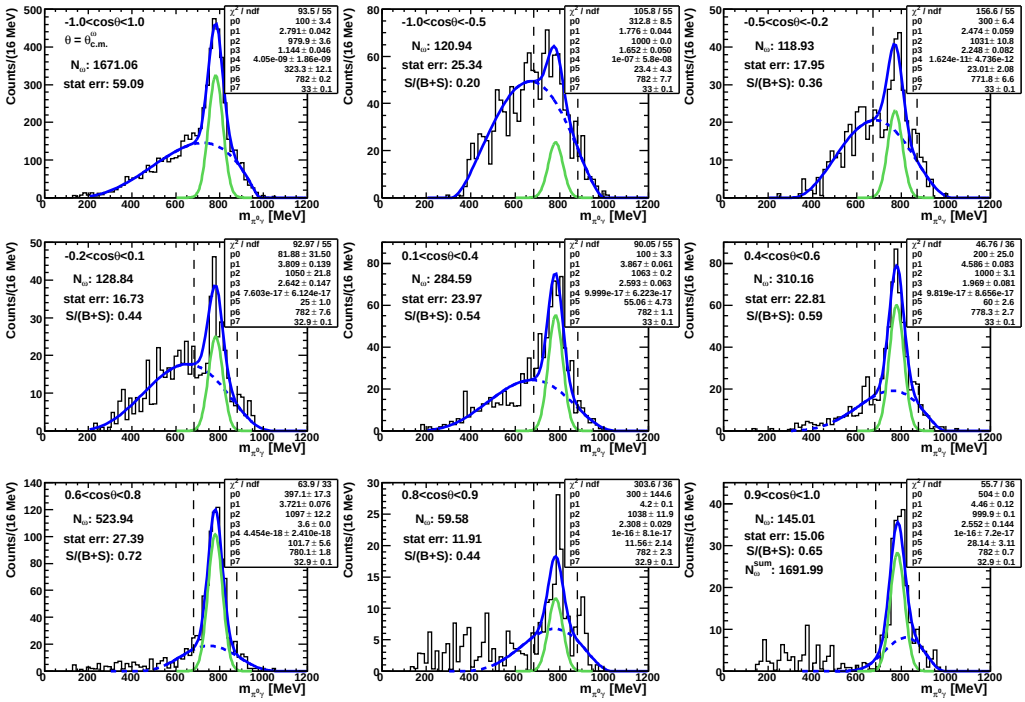

Figure D.9: Fits to the $\pi^0\gamma$ invariant mass spectra for the $\cos(\theta^{\omega}_{c.m.})$ angular bins with incident beam energy E_γ = 1450-1500 MeV.

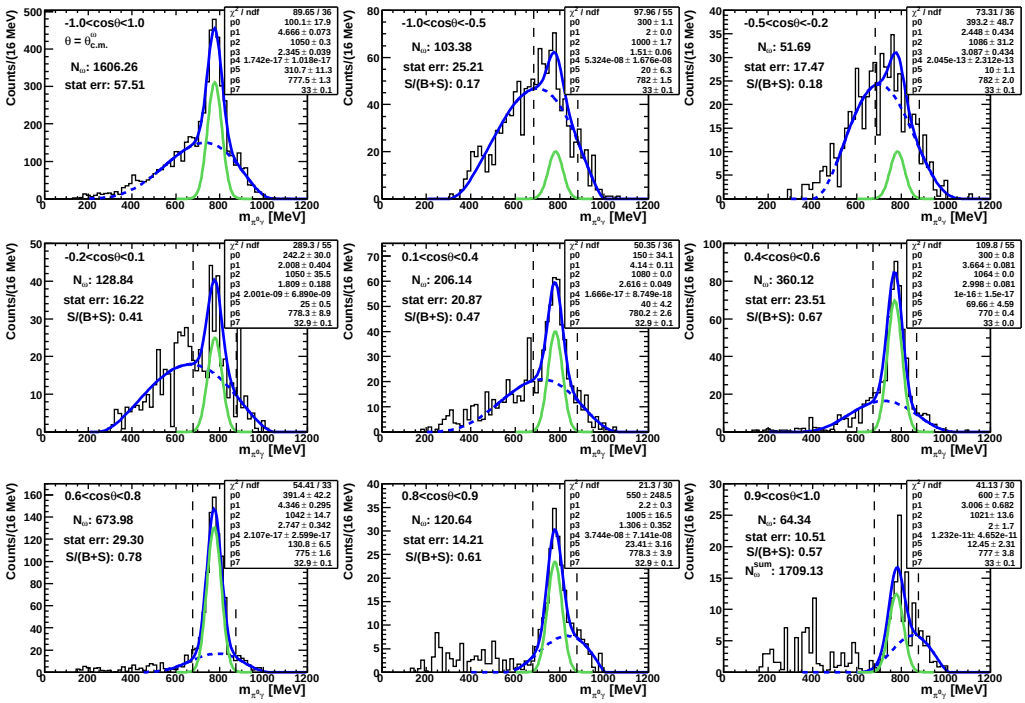

Figure D.10: Fits to the $\pi^0\gamma$ invariant mass spectra for the $\cos(\theta^{\omega}_{c.m.})$ angular bins with incident beam energy E_γ = 1500-1550 MeV.

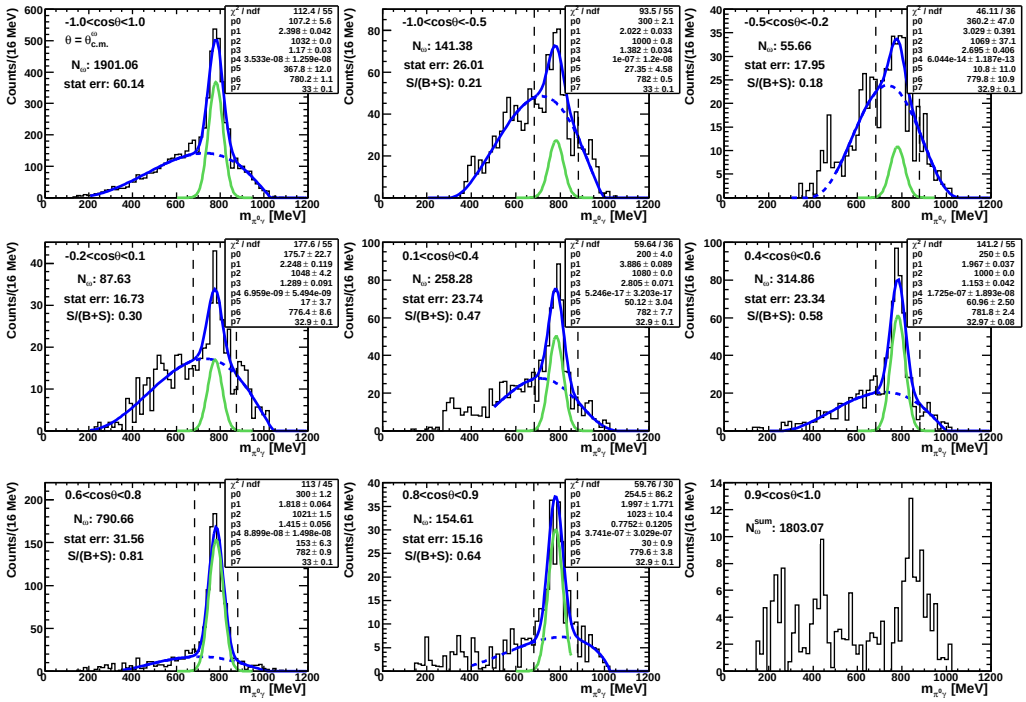

Figure D.11: Fits to the $\pi^0\gamma$ invariant mass spectra for the $\cos(\theta^{\omega}_{c.m.})$ angular bins with incident beam energy E_γ = 1550-1600 MeV.

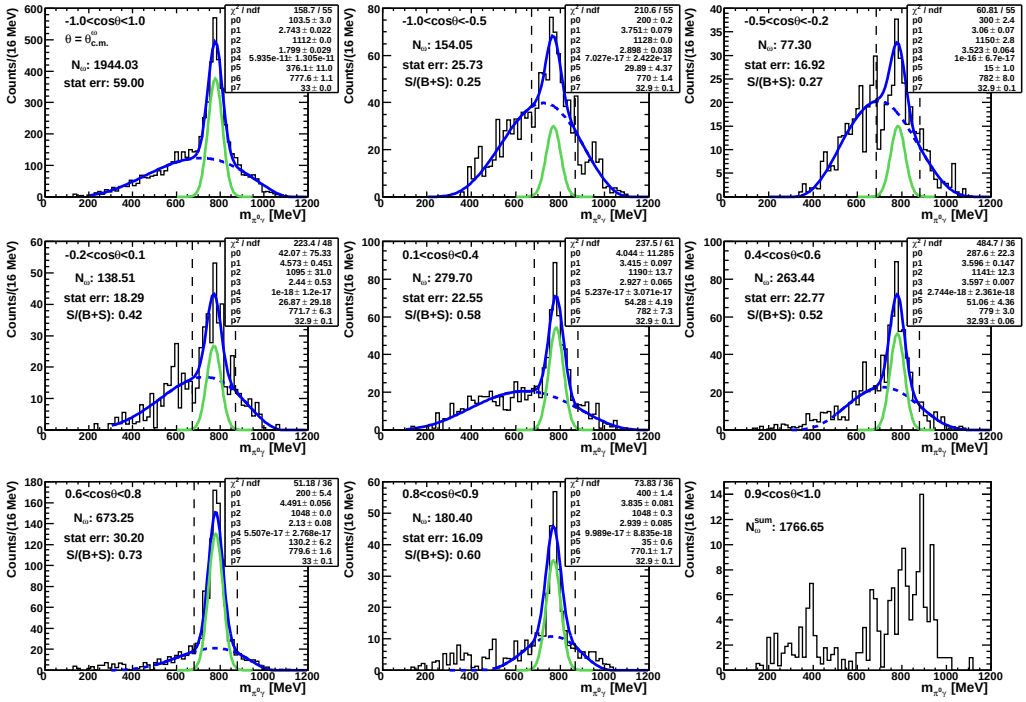

Figure D.12: Fits to the $\pi^0\gamma$ invariant mass spectra for the $\cos(\theta^{\omega}_{c.m.})$ angular bins with incident beam energy E_γ = 1600-1650 MeV.

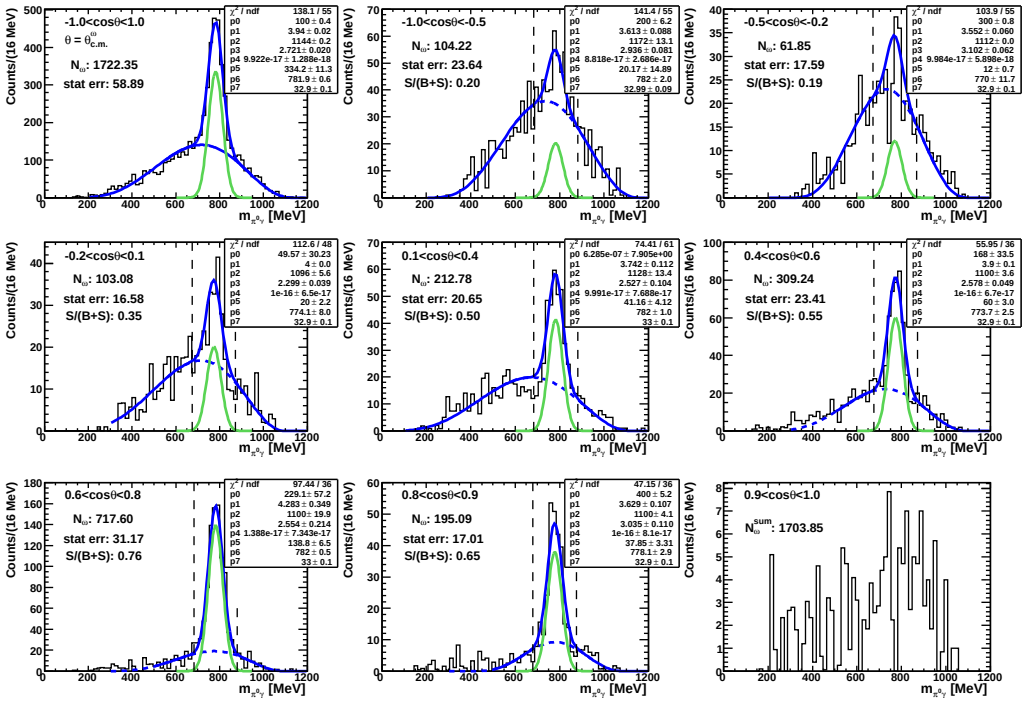

Figure D.13: Fits to the $\pi^0\gamma$ invariant mass spectra for the $\cos(\theta^{\omega}_{c.m.})$ angular bins with incident beam energy E_γ = 1650-1700 MeV.

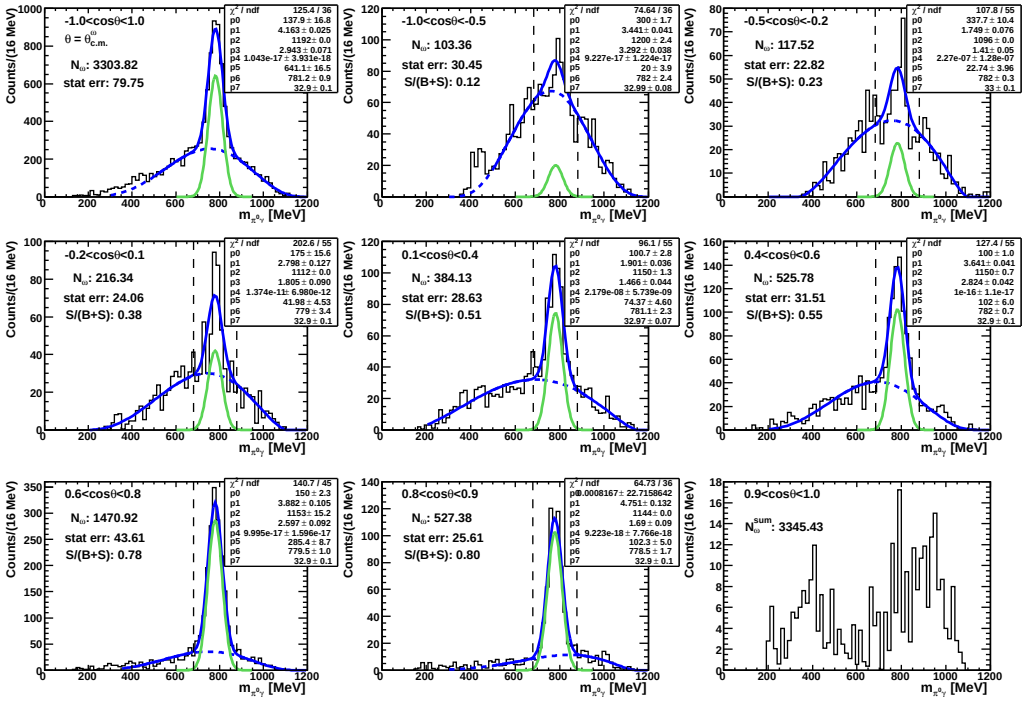

Figure D.14: Fits to the $\pi^0\gamma$ invariant mass spectra for the $\cos(\theta^{\omega}_{c.m.})$ angular bins with incident beam energy E_γ = 1700-1800 MeV.

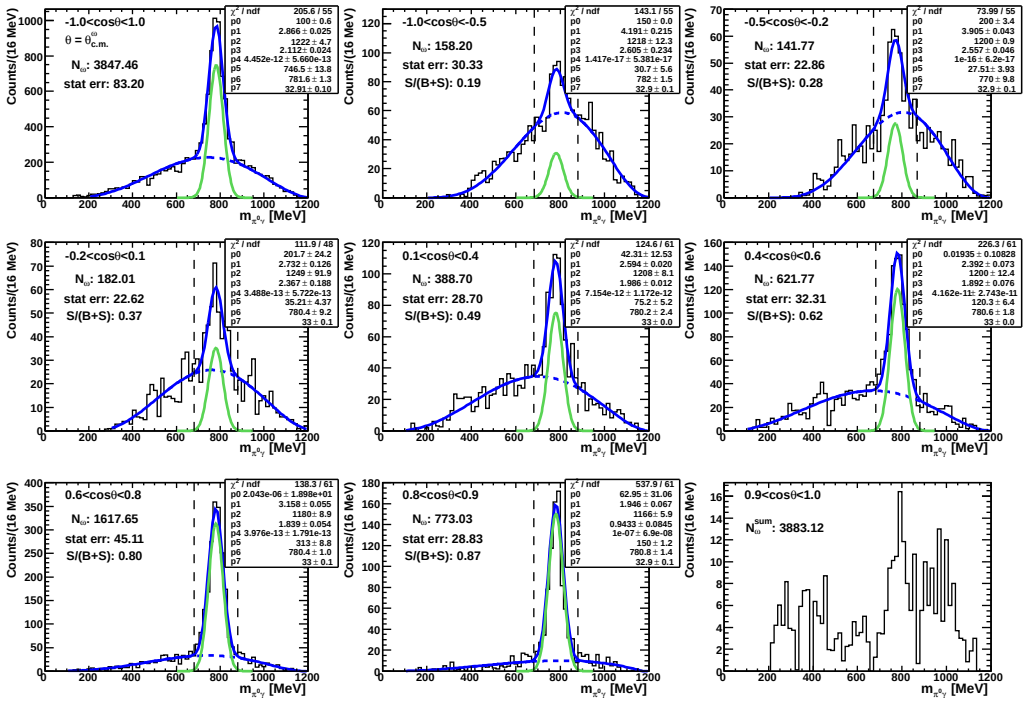

Figure D.15: Fits to the $\pi^0\gamma$ invariant mass spectra for the $\cos(\theta^{\omega}_{c.m.})$ angular bins with incident beam energy E_γ = 1800-1900 MeV.

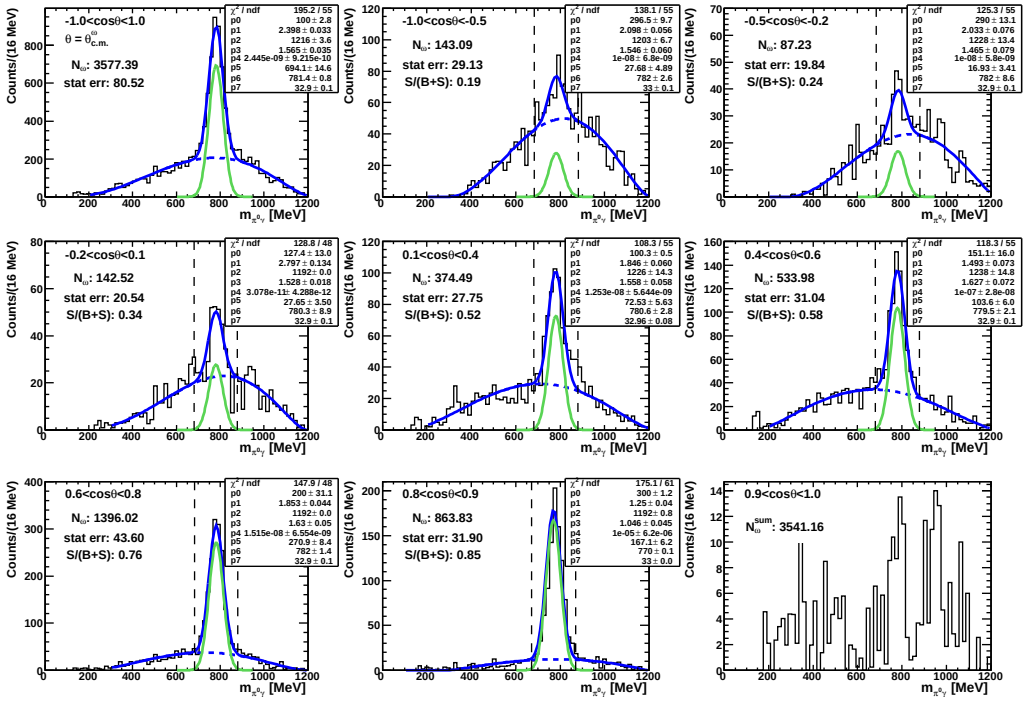

Figure D.16: Fits to the $\pi^0\gamma$ invariant mass spectra for the $\cos(\theta^{\omega}_{c.m.})$ angular bins with incident beam energy E_γ = 1900-2000 MeV.

E. Fits for LH_2 inclusive analysis

Here, all the fits to the $\pi^0\gamma$ invariant mass spectra that were used to determine the inclusive cross-sections for ω photoproduction off the LH_2 target are shown. The ω signals after background subtraction are also shown. The parameters of each fit with the function $f(x) = p_4(x-p_0)^{p_1}(x-p_2)^{p_3} + p_5 e^{-\frac{(x-p_6)^2}{2p_7^2}}$ are listed. The number of ω mesons for each angular and incident beam energy bin, N_ω, the statistical error and the signal-to-background ratio are given. The upper left spectra in each figure show the sum of all angular bins for the respective incident beam energy bin, -1.0$\leq \cos(\theta^\omega_{c.m.}) \leq$1.0. In the lower right figure the sum of ω mesons obtained from the fits in each angular bin is shown, N^{sum}_ω. Figure (a) shows the spectra before an efficiency correction was made and fig. (b) shows them after an event-by-event efficiency correction with $\epsilon(T^\omega_{lab.}, \theta^\omega_{lab.})$.

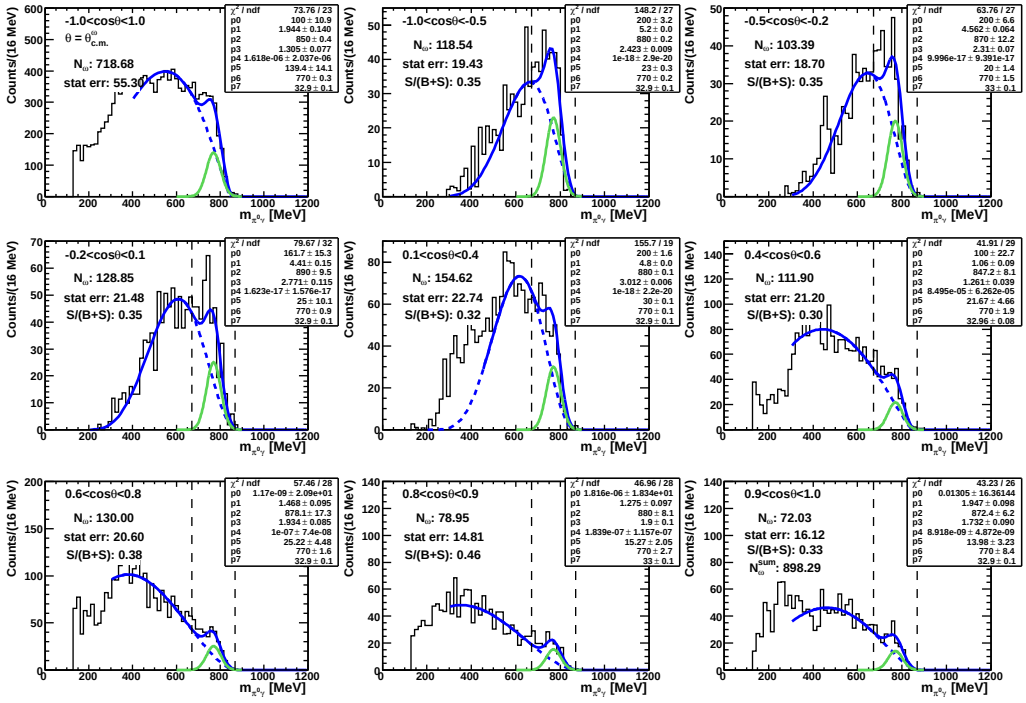

(a) Before efficiency correction

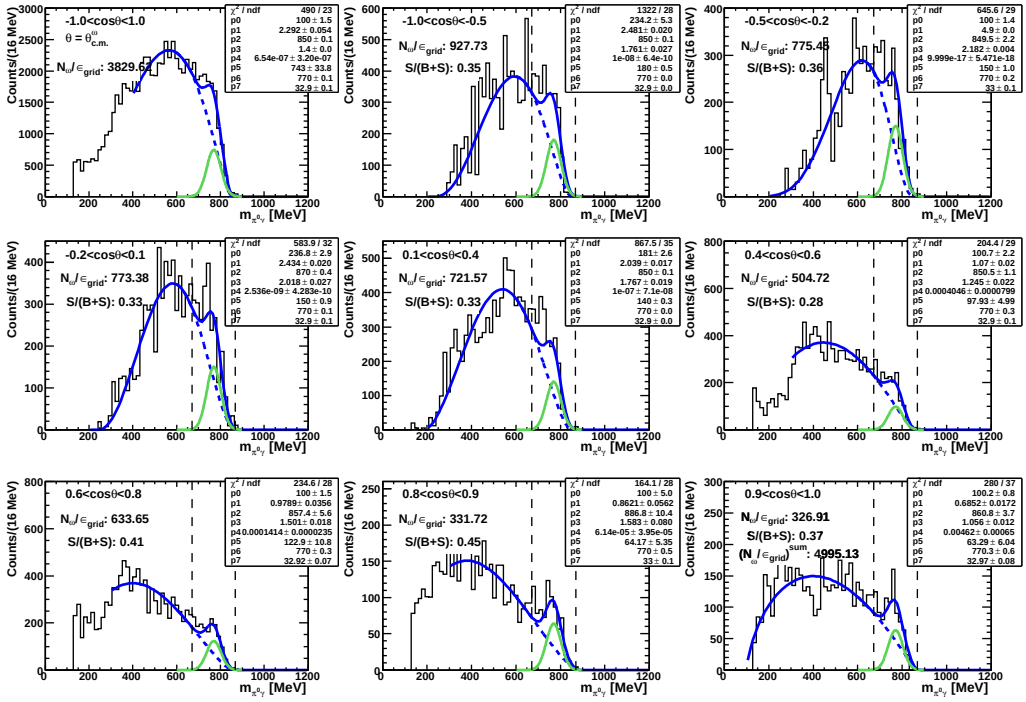

(b) After event-by-event efficiency correction with $\epsilon(T^{\omega}_{lab.}, \theta^{\omega}_{lab.})$

Figure E.1: Fits to the $\pi^0\gamma$ invariant mass spectra for the $\cos(\theta^{\omega}_{c.m.})$ angular bins with incident beam energy E_γ = 1125-1150 MeV.

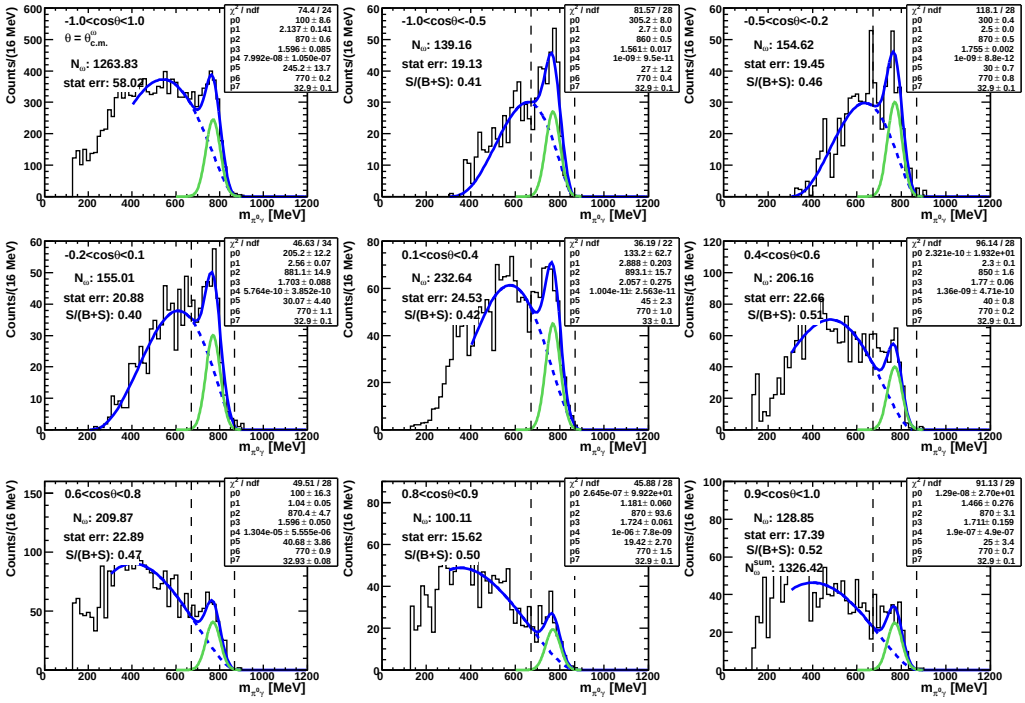

(a) Before efficiency correction

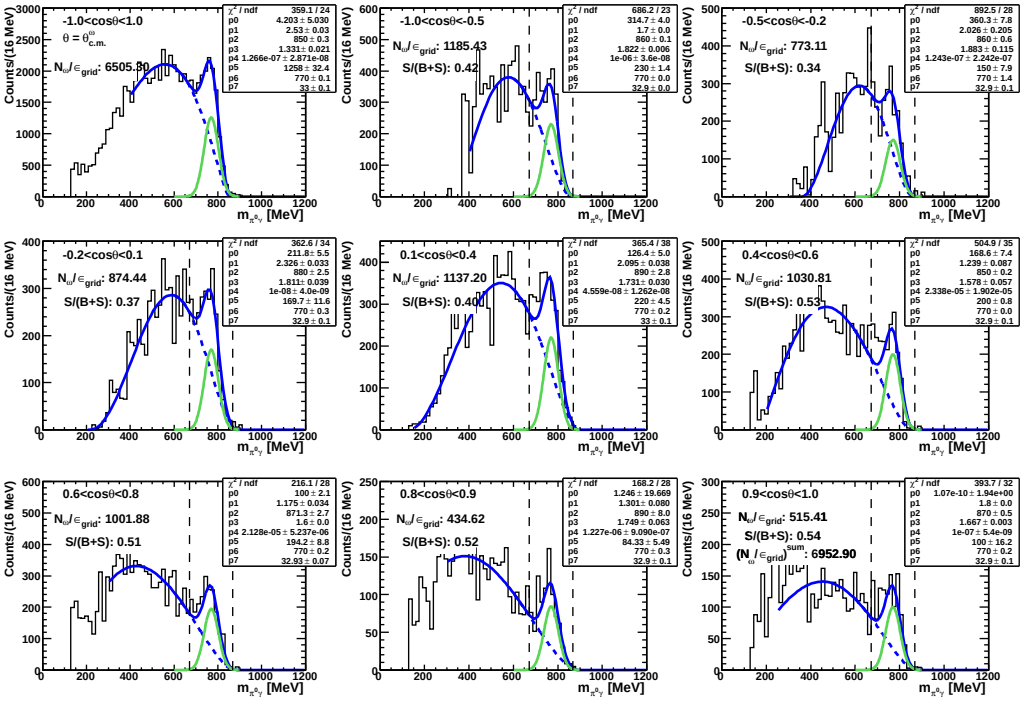

(b) After event-by-event efficiency correction with $\epsilon(T^{\omega}_{lab.}, \theta^{\omega}_{lab.})$

Figure E.2: Fits to the $\pi^0\gamma$ invariant mass spectra for the $\cos(\theta^{\omega}_{c.m.})$ angular bins with incident beam energy E_γ = 1150-1175 MeV.

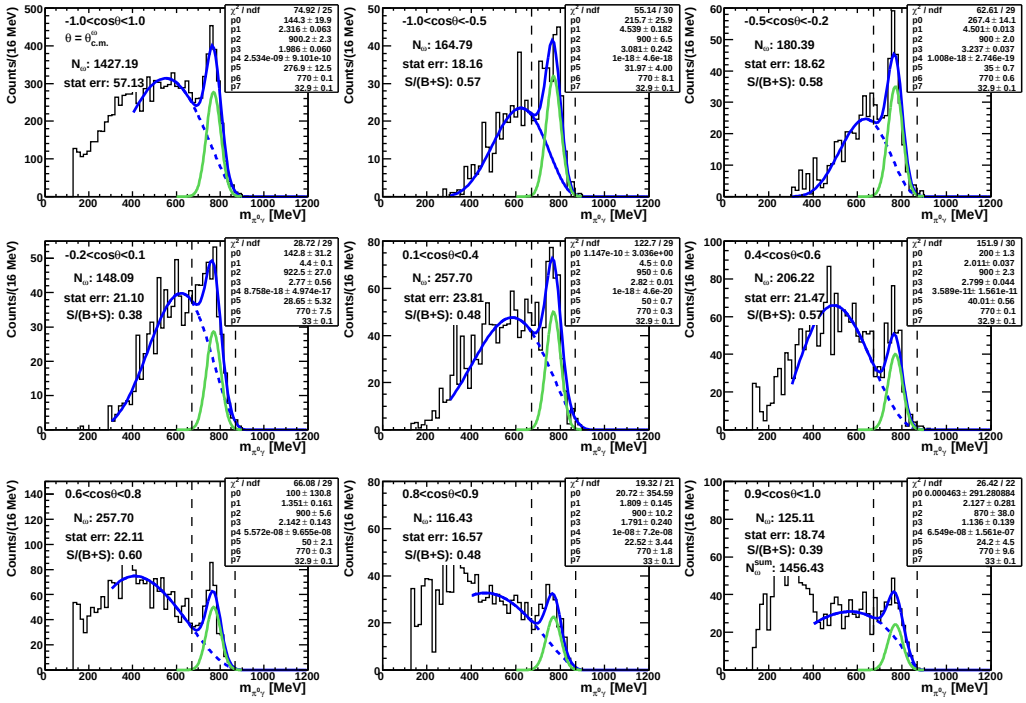

(a) Before efficiency correction

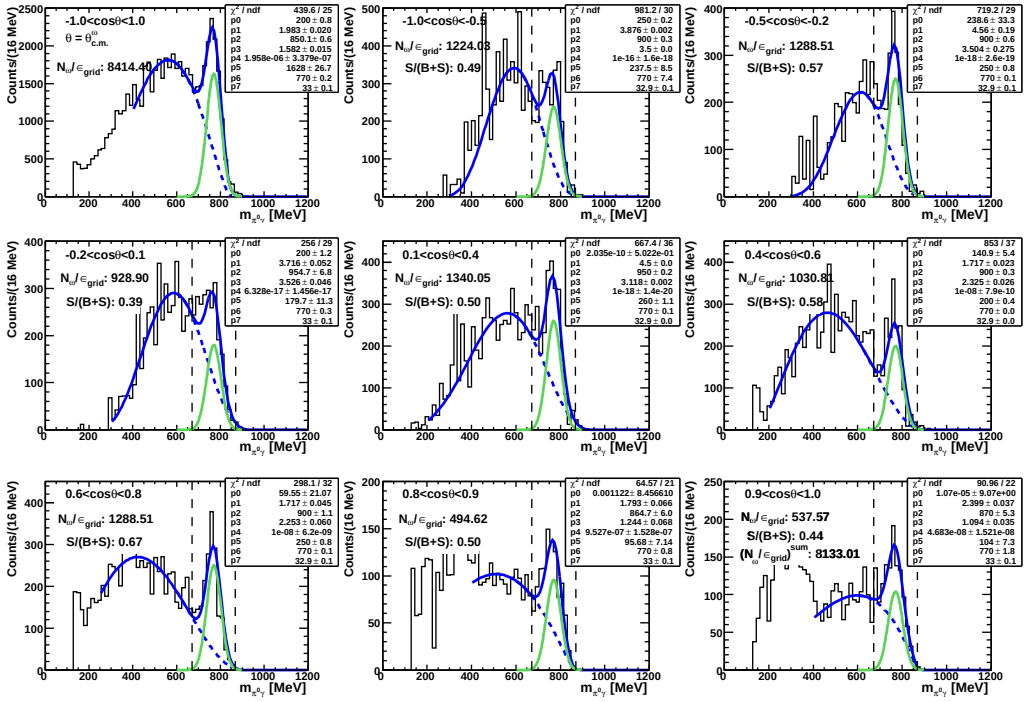

(b) After event-by-event efficiency correction with $\epsilon(T^{\omega}_{lab.}, \theta^{\omega}_{lab.})$

Figure E.3: Fits to the $\pi^0\gamma$ invariant mass spectra for the $\cos(\theta^{\omega}_{c.m.})$ angular bins with incident beam energy E_γ = 1175-1200 MeV.

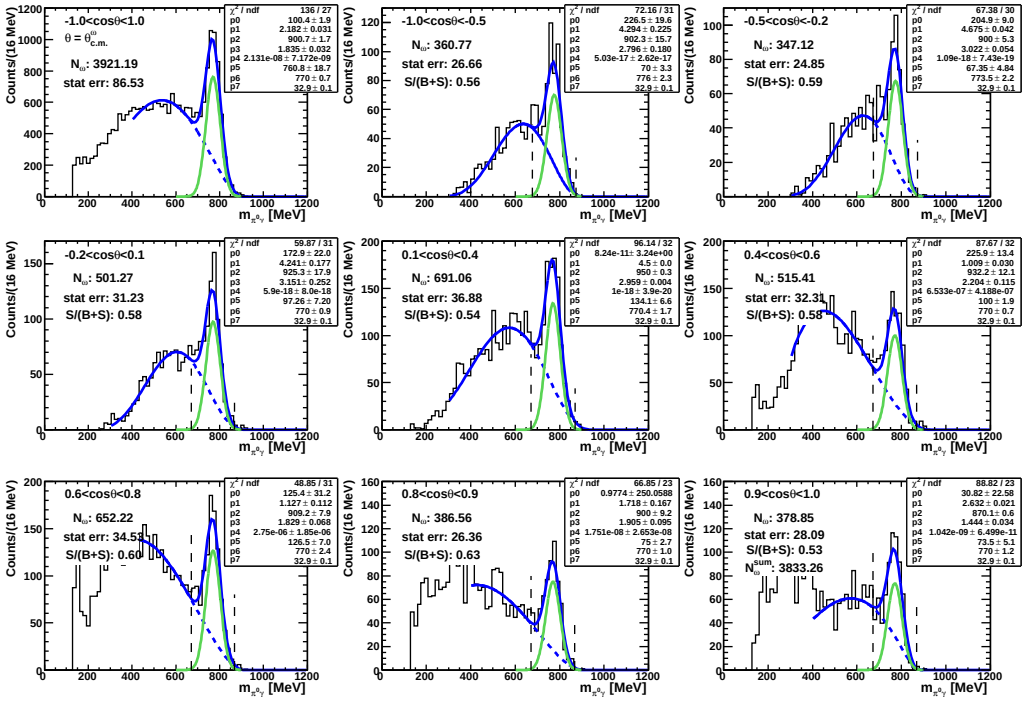

(a) Before efficiency correction

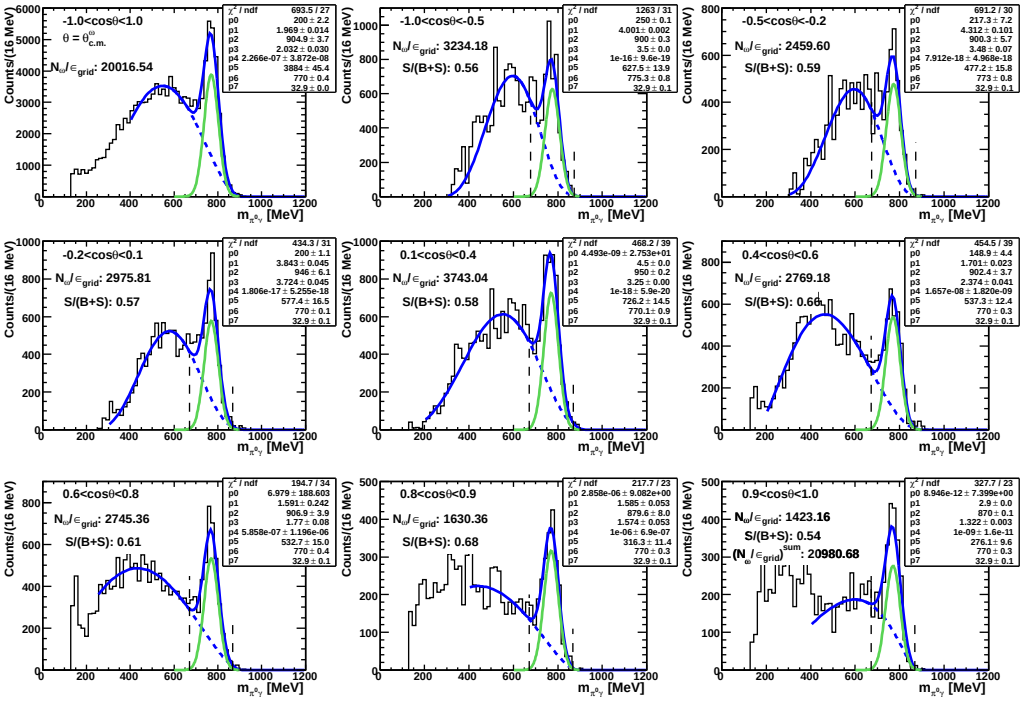

(b) After event-by-event efficiency correction with $\epsilon(T^{\omega}_{lab.}, \theta^{\omega}_{lab.})$

Figure E.4: Fits to the $\pi^0\gamma$ invariant mass spectra for the $\cos(\theta^{\omega}_{c.m.})$ angular bins with incident beam energy E_γ = 1200-1250 MeV.

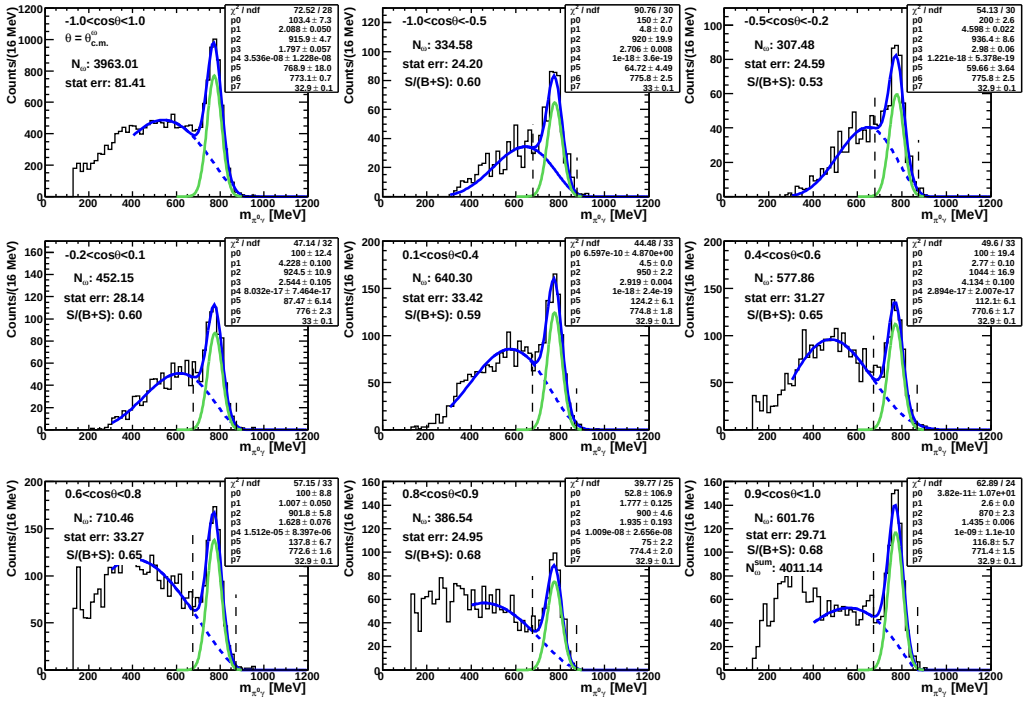

(a) Before efficiency correction

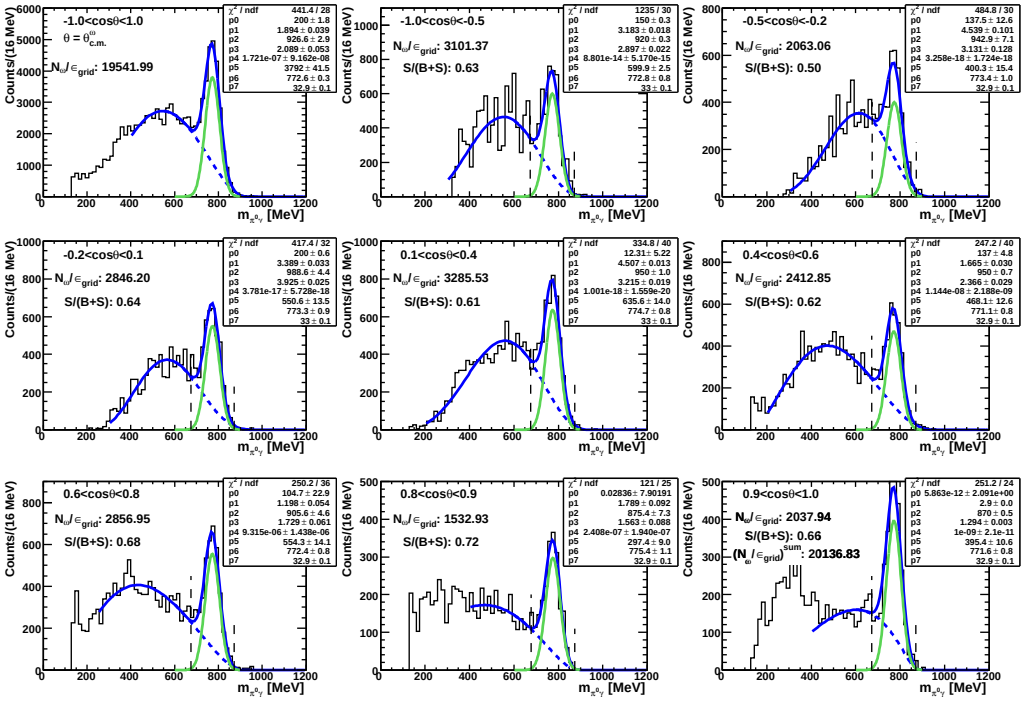

(b) After event-by-event efficiency correction with $\epsilon(T^{\omega}_{lab.}, \theta^{\omega}_{lab.})$

Figure E.5: Fits to the $\pi^0\gamma$ invariant mass spectra for the $\cos(\theta^{\omega}_{c.m.})$ angular bins with incident beam energy E_γ = 1250-1300 MeV.

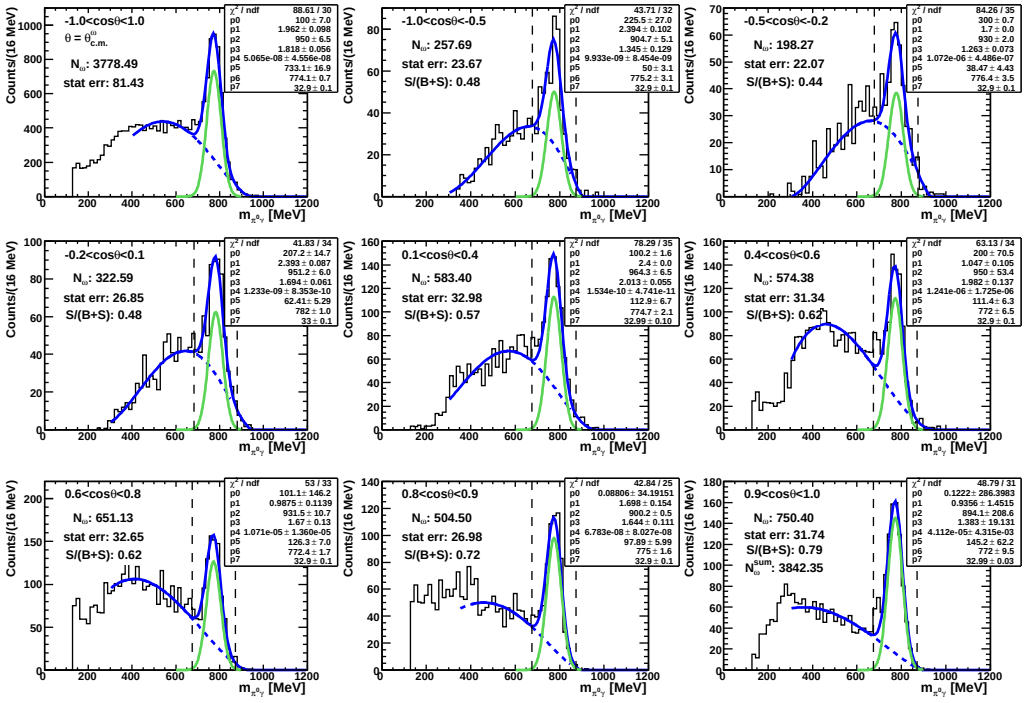

(a) Before efficiency correction

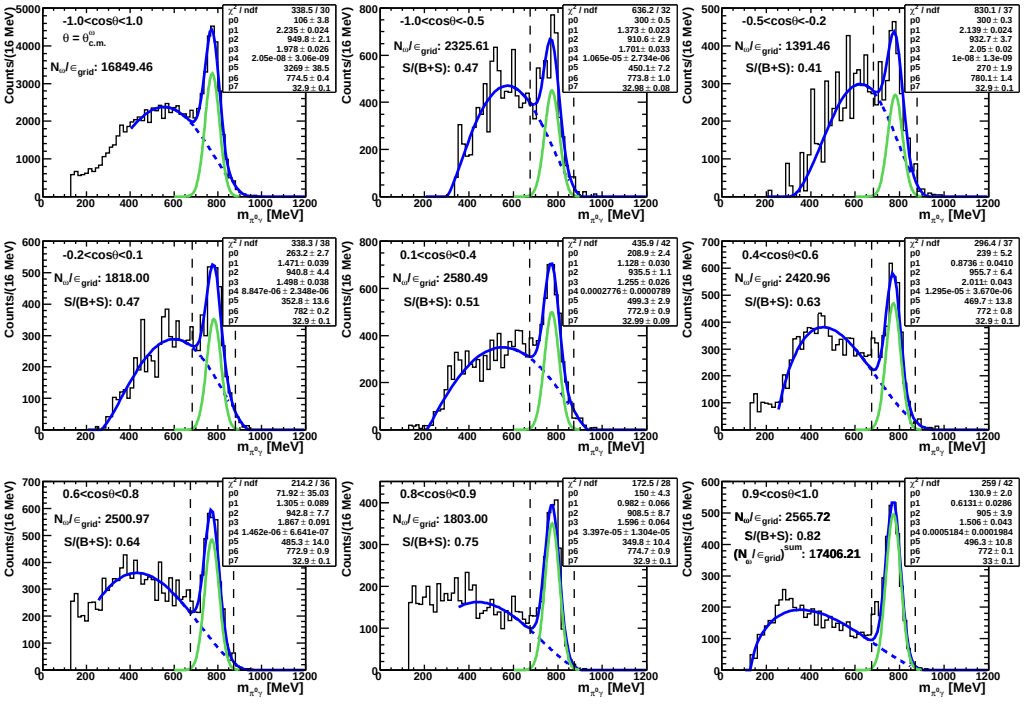

(b) After event-by-event efficiency correction with $\epsilon(T^{\omega}_{lab.}, \theta^{\omega}_{lab.})$

Figure E.6: Fits to the $\pi^0\gamma$ invariant mass spectra for the $\cos(\theta^{\omega}_{c.m.})$ angular bins with incident beam energy E_γ = 1300-1350 MeV.

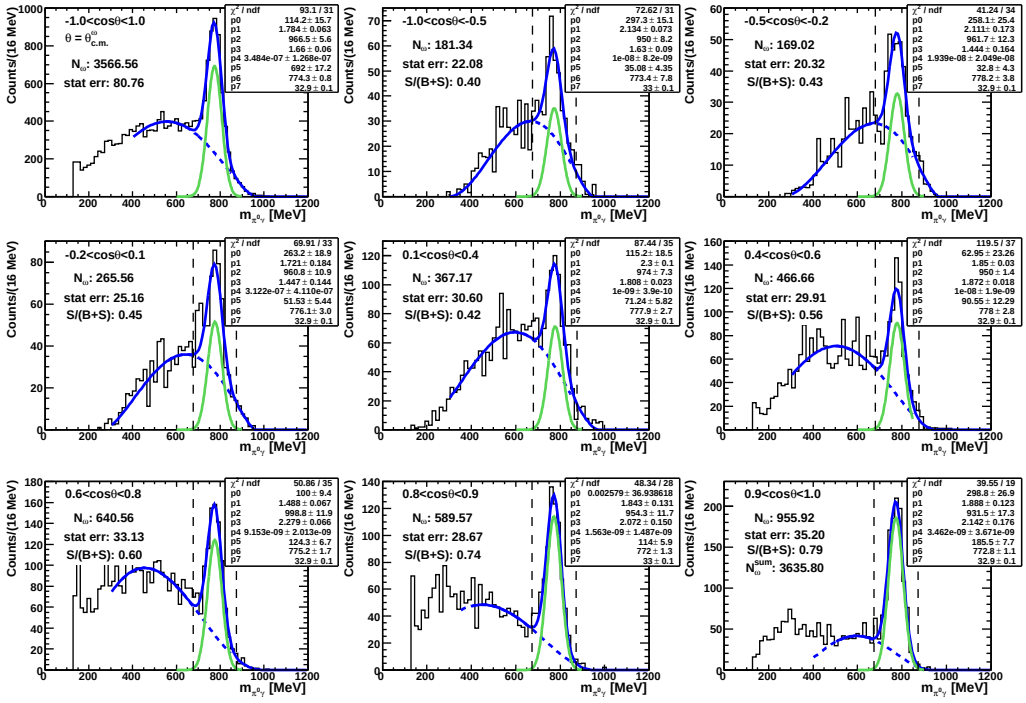

(a) Before efficiency correction

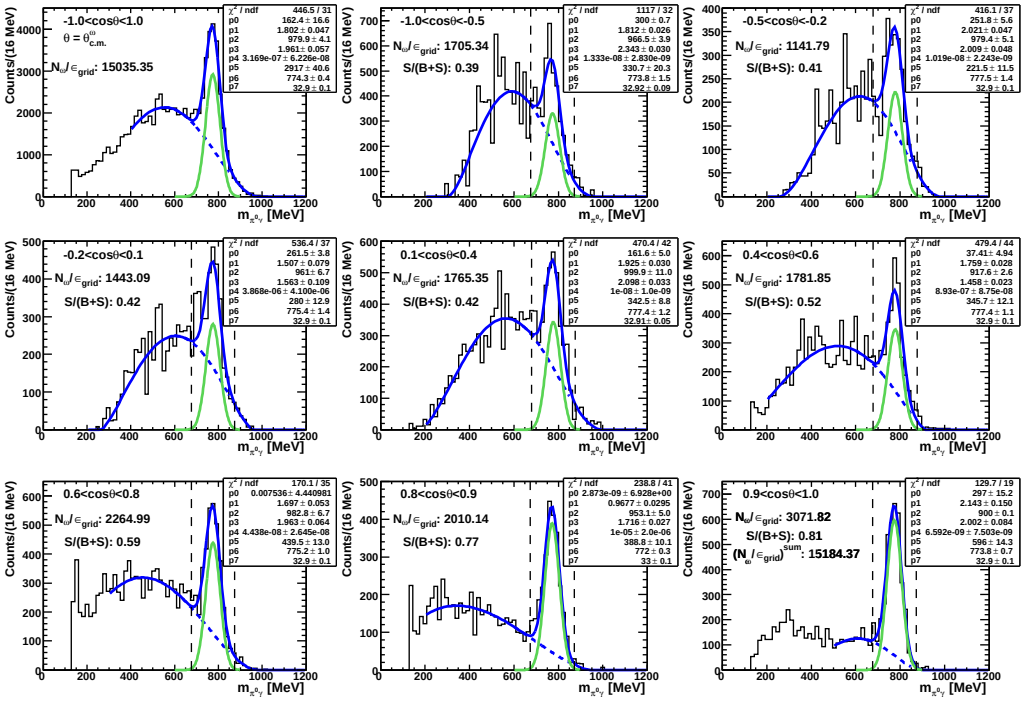

(b) After event-by-event efficiency correction with $\epsilon(T^{\omega}_{lab.}, \theta^{\omega}_{lab.})$

Figure E.7: Fits to the $\pi^0\gamma$ invariant mass spectra for the $\cos(\theta^{\omega}_{c.m.})$ angular bins with incident beam energy E_γ = 1350-1400 MeV.

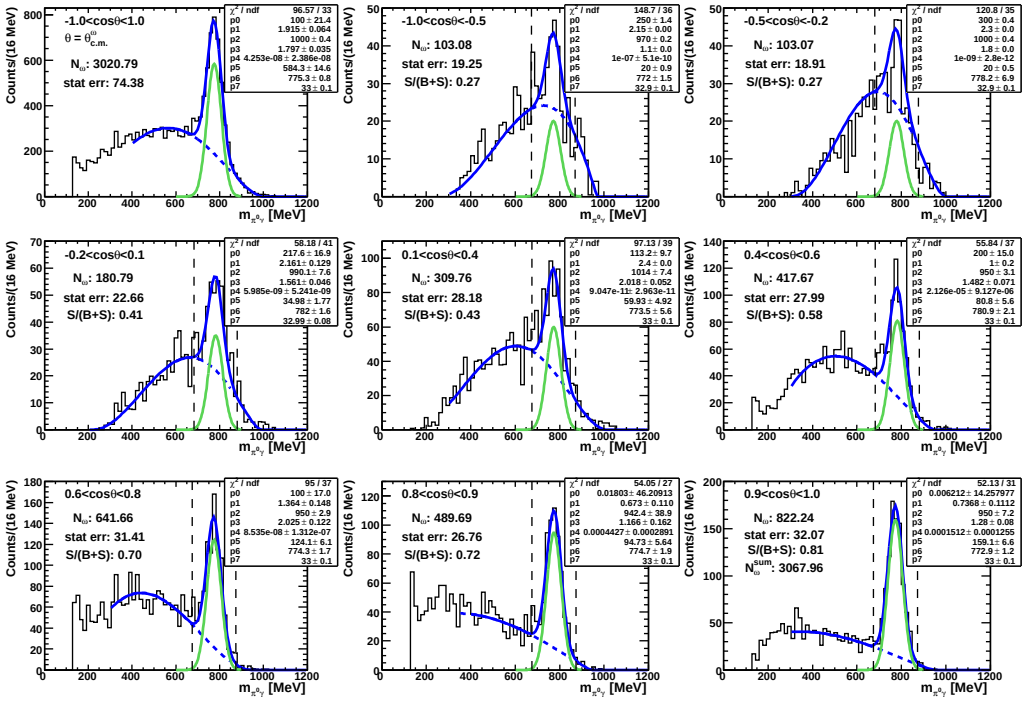

(a) Before efficiency correction

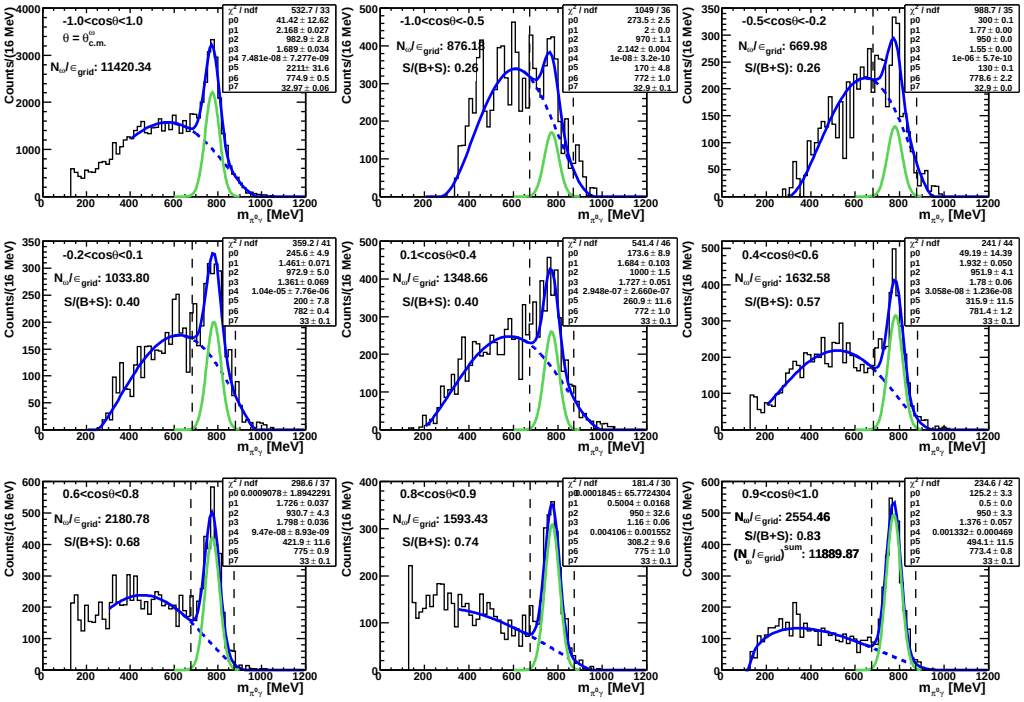

(b) After event-by-event efficiency correction with $\epsilon(T^{\omega}_{lab.}, \theta^{\omega}_{lab.})$

Figure E.8: Fits to the $\pi^0\gamma$ invariant mass spectra for the $\cos(\theta^{\omega}_{c.m.})$ angular bins with incident beam energy E_γ = 1400-1450 MeV.

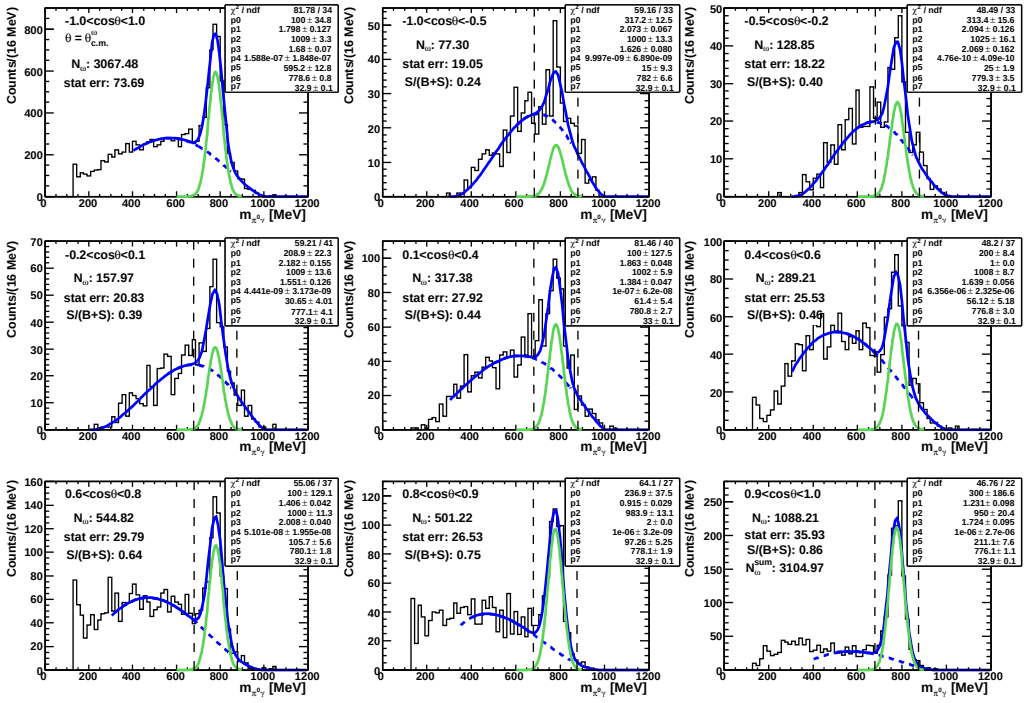

(a) Before efficiency correction

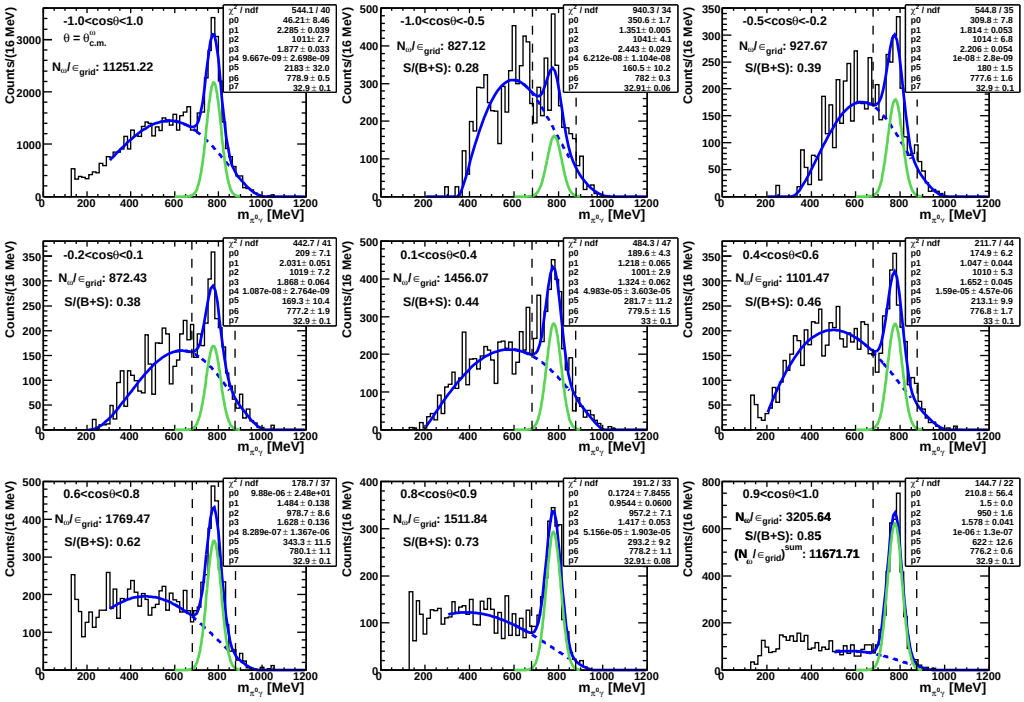

(b) After event-by-event efficiency correction with $\epsilon(T^{\omega}_{lab.}, \theta^{\omega}_{lab.})$

Figure E.9: Fits to the $\pi^0\gamma$ invariant mass spectra for the $\cos(\theta^{\omega}_{c.m.})$ angular bins with incident beam energy E_γ = 1450-1500 MeV.

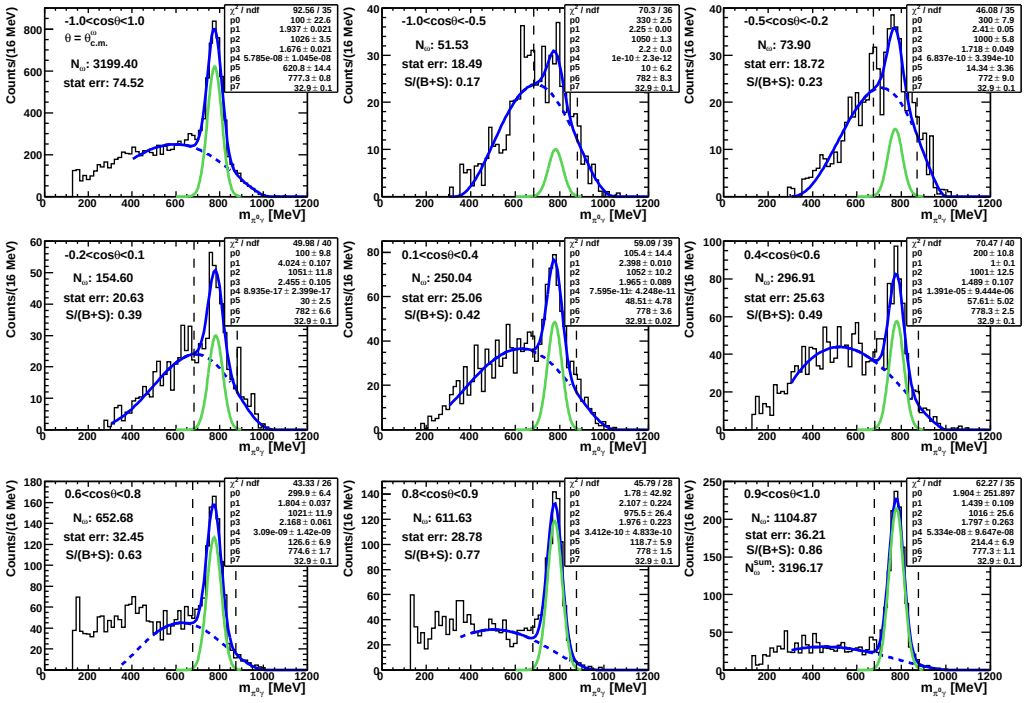

(a) Before efficiency correction

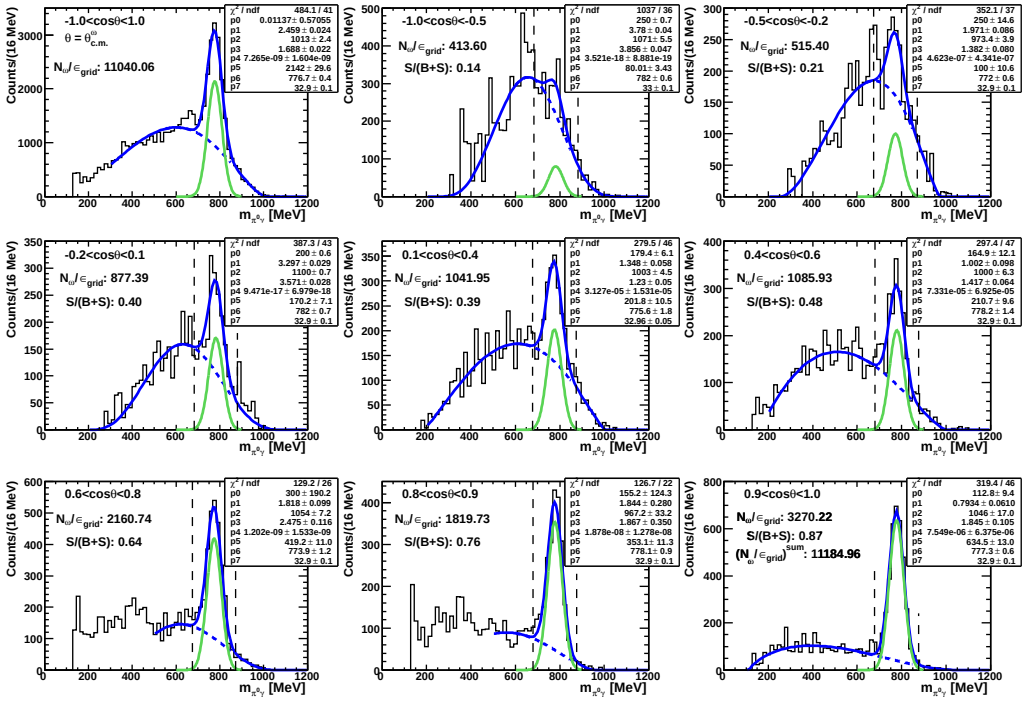

(b) After event-by-event efficiency correction with $\epsilon(T^{\omega}_{lab.}, \theta^{\omega}_{lab.})$

Figure E.10: Fits to the $\pi^0\gamma$ invariant mass spectra for the $\cos(\theta^{\omega}_{c.m.})$ angular bins with incident beam energy E_γ = 1500-1550 MeV.

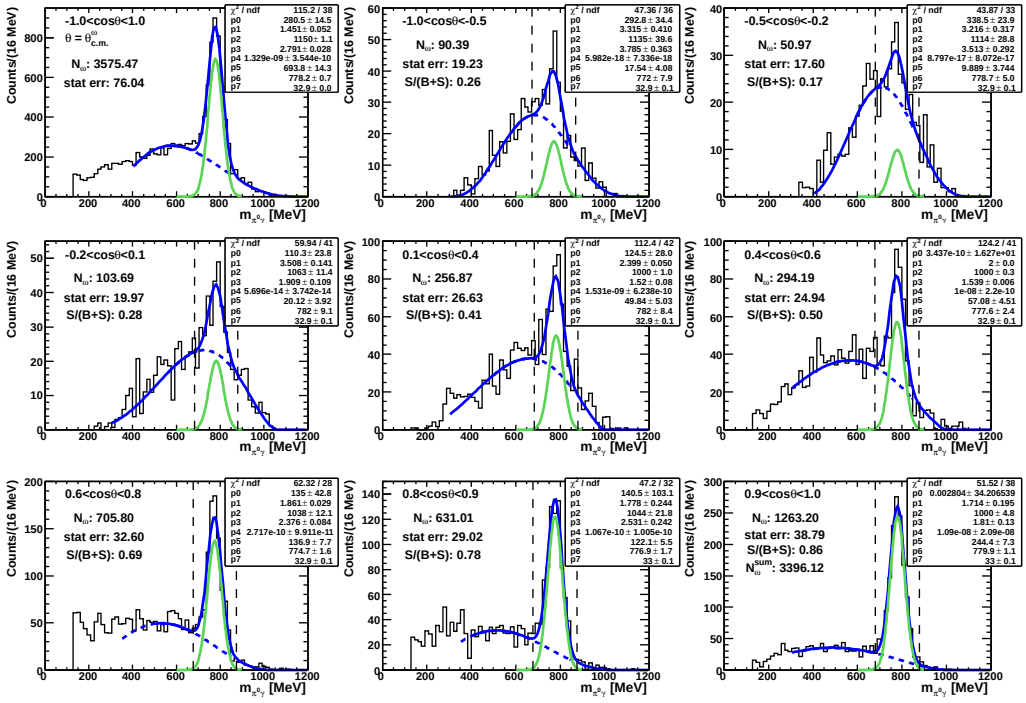

(a) Before efficiency correction

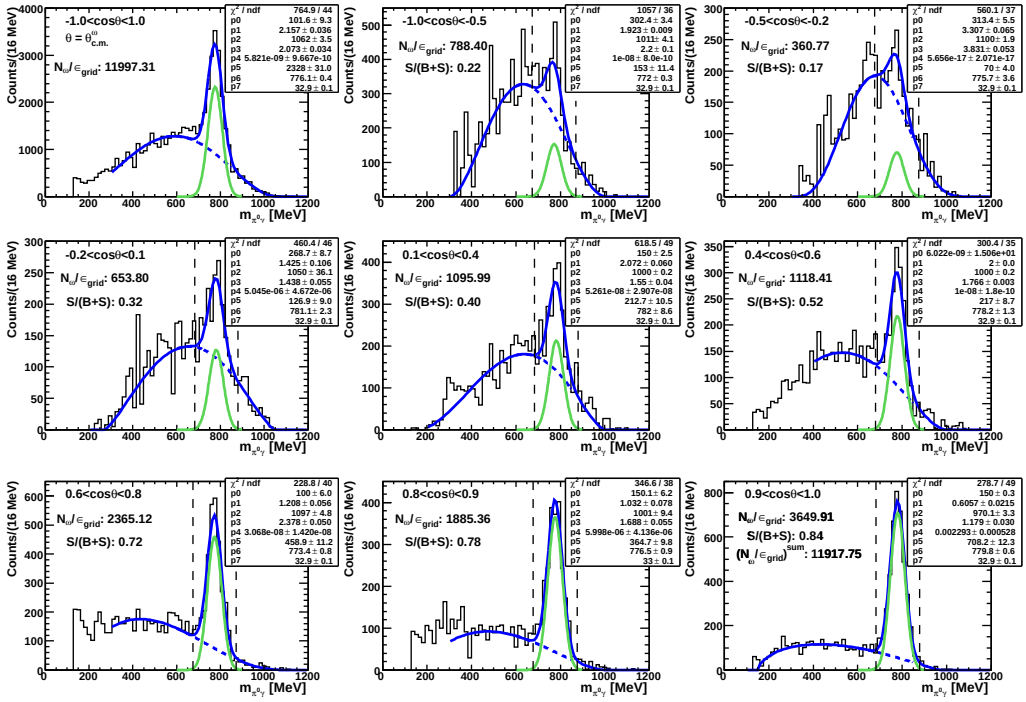

(b) After event-by-event efficiency correction with $\epsilon(T^{\omega}_{lab.}, \theta^{\omega}_{lab.})$

Figure E.11: Fits to the $\pi^0\gamma$ invariant mass spectra for the $\cos(\theta^{\omega}_{c.m.})$ angular bins with incident beam energy E_γ = 1550-1600 MeV.

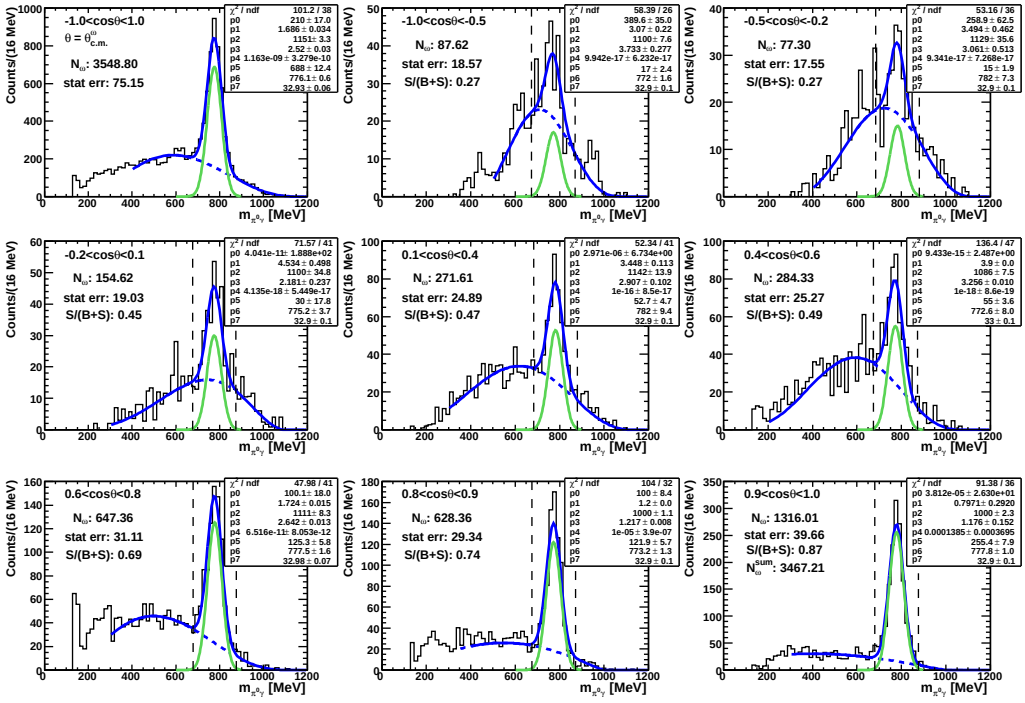

(a) Before efficiency correction

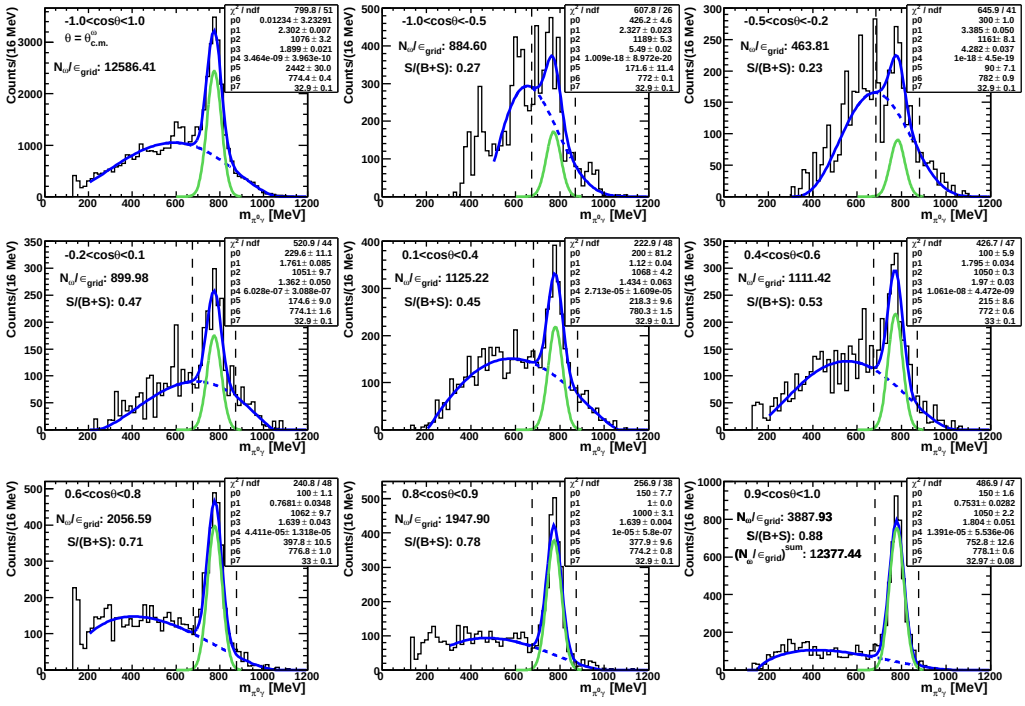

(b) After event-by-event efficiency correction with $\epsilon(T^{\omega}_{lab.}, \theta^{\omega}_{lab.})$

Figure E.12: Fits to the $\pi^0\gamma$ invariant mass spectra for the $\cos(\theta^{\omega}_{c.m.})$ angular bins with incident beam energy E_γ = 1600-1650 MeV.

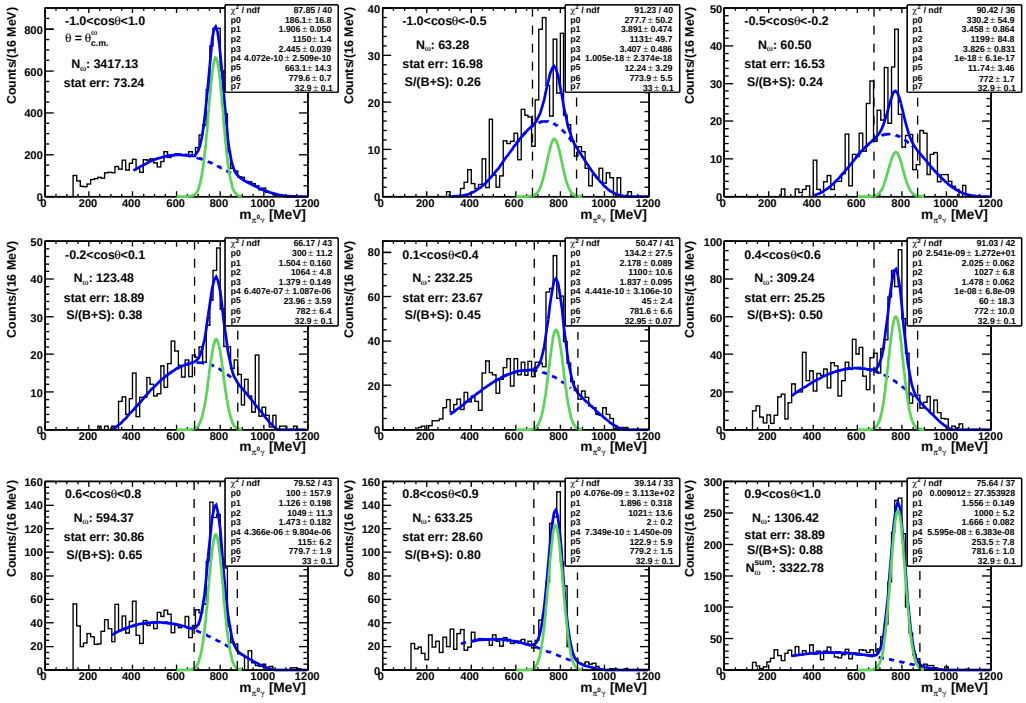

(a) Before efficiency correction

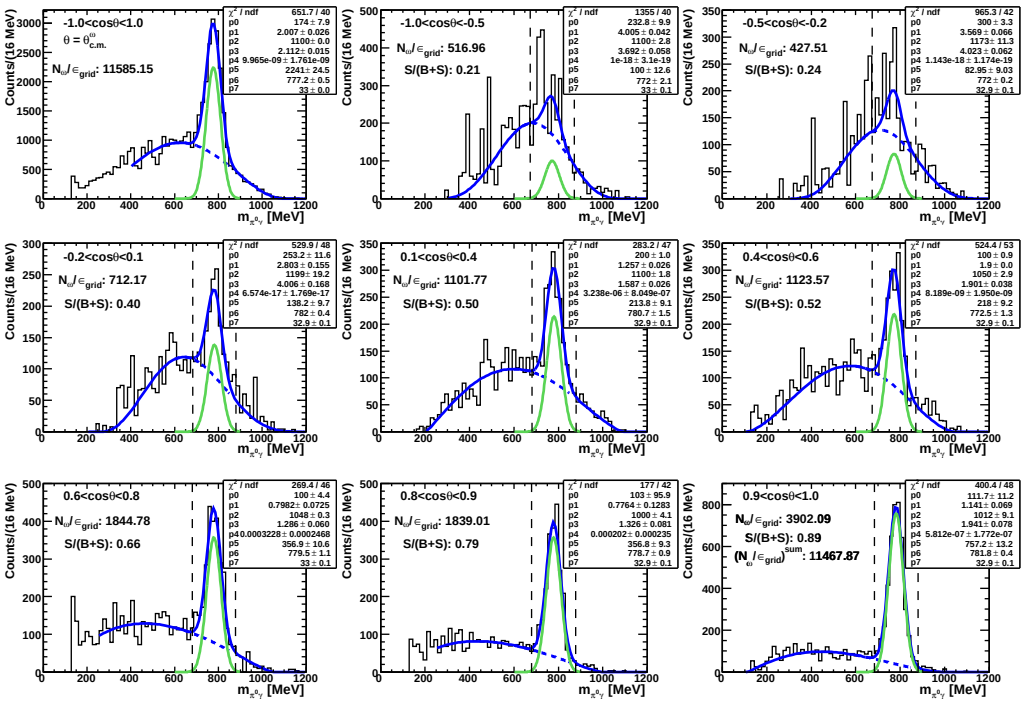

(b) After event-by-event efficiency correction with $\epsilon(T^{\omega}_{lab.}, \theta^{\omega}_{lab.})$

Figure E.13: Fits to the $\pi^0\gamma$ invariant mass spectra for the $\cos(\theta^{\omega}_{c.m.})$ angular bins with incident beam energy E_γ = 1650-1700 MeV.

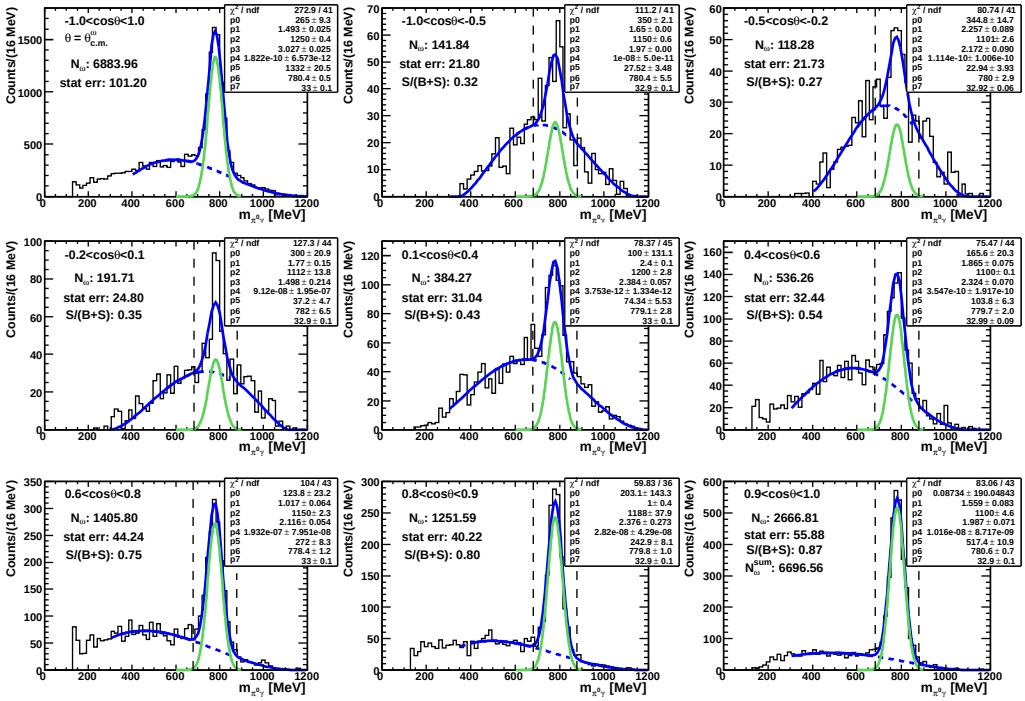

(a) Before efficiency correction

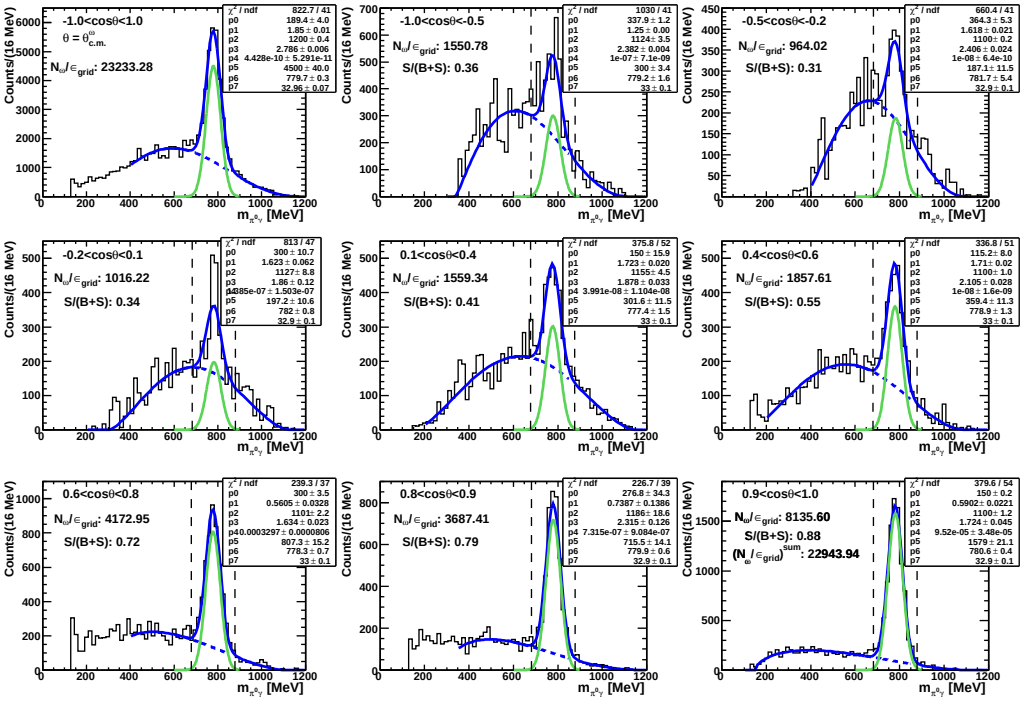

(b) After event-by-event efficiency correction with $\epsilon(T^{\omega}_{lab.}, \theta^{\omega}_{lab.})$

Figure E.14: Fits to the $\pi^0\gamma$ invariant mass spectra for the $\cos(\theta^{\omega}_{c.m.})$ angular bins with incident beam energy E_γ = 1700-1800 MeV.

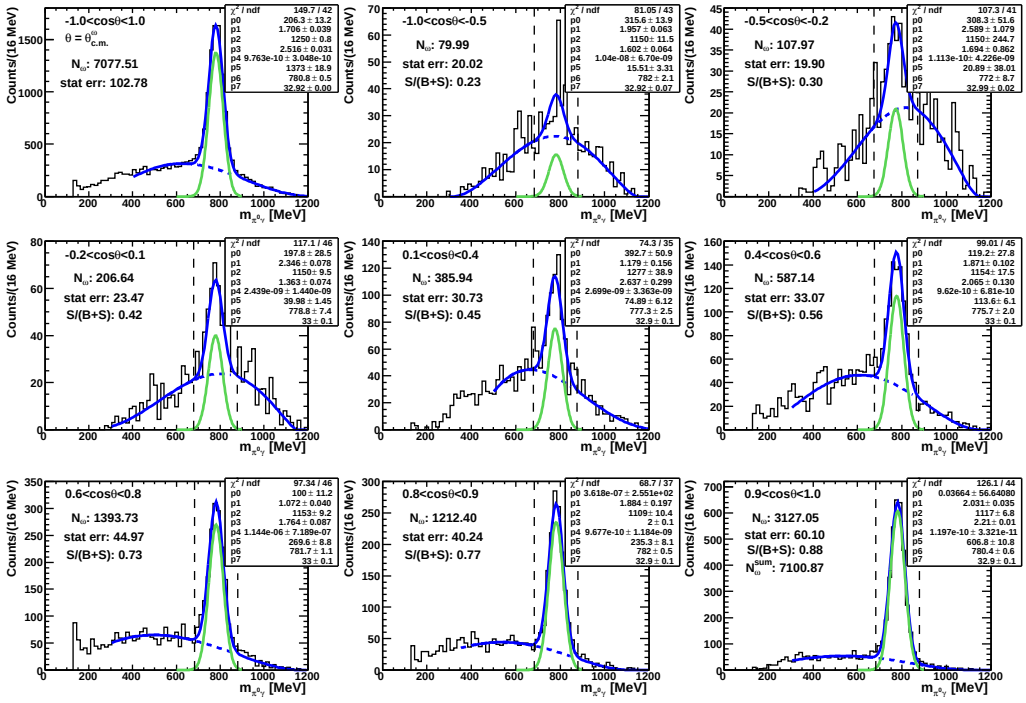

(a) Before efficiency correction

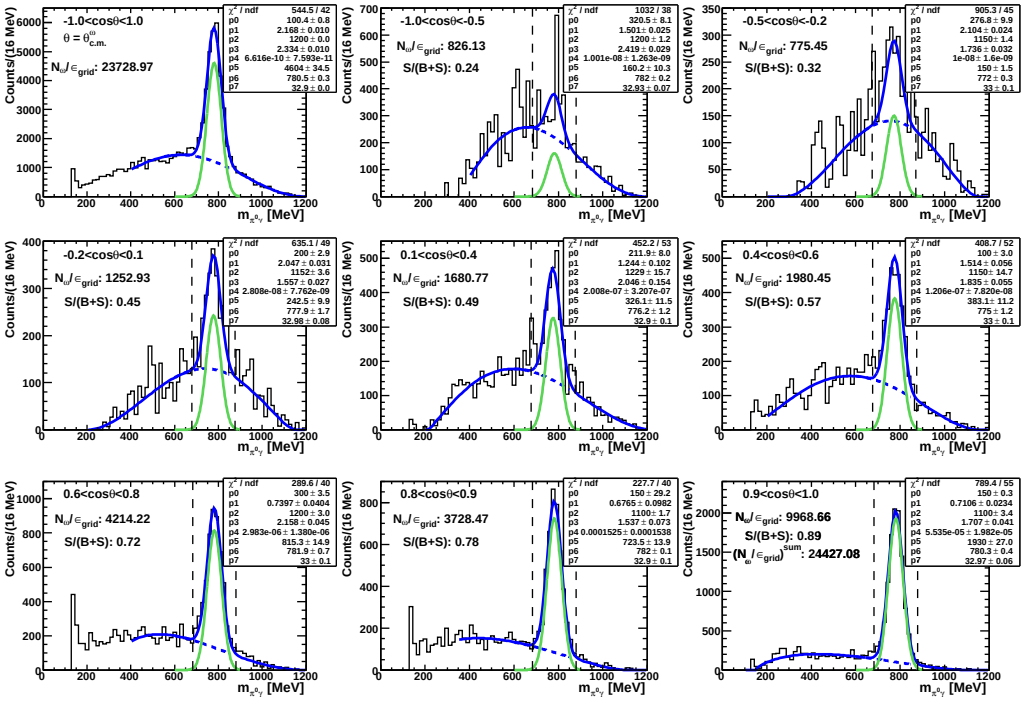

(b) After event-by-event efficiency correction with $\epsilon(T^{\omega}_{lab.}, \theta^{\omega}_{lab.})$

Figure E.15: Fits to the $\pi^0\gamma$ invariant mass spectra for the $\cos(\theta^{\omega}_{c.m.})$ angular bins with incident beam energy E_γ = 1800-1900 MeV.

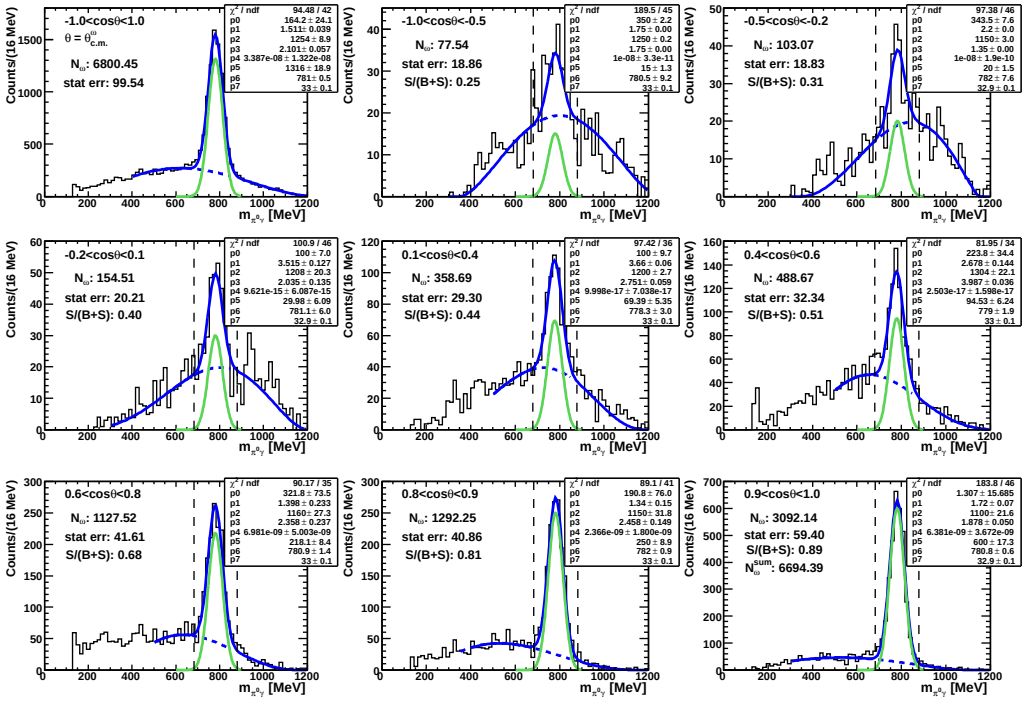

(a) Before efficiency correction

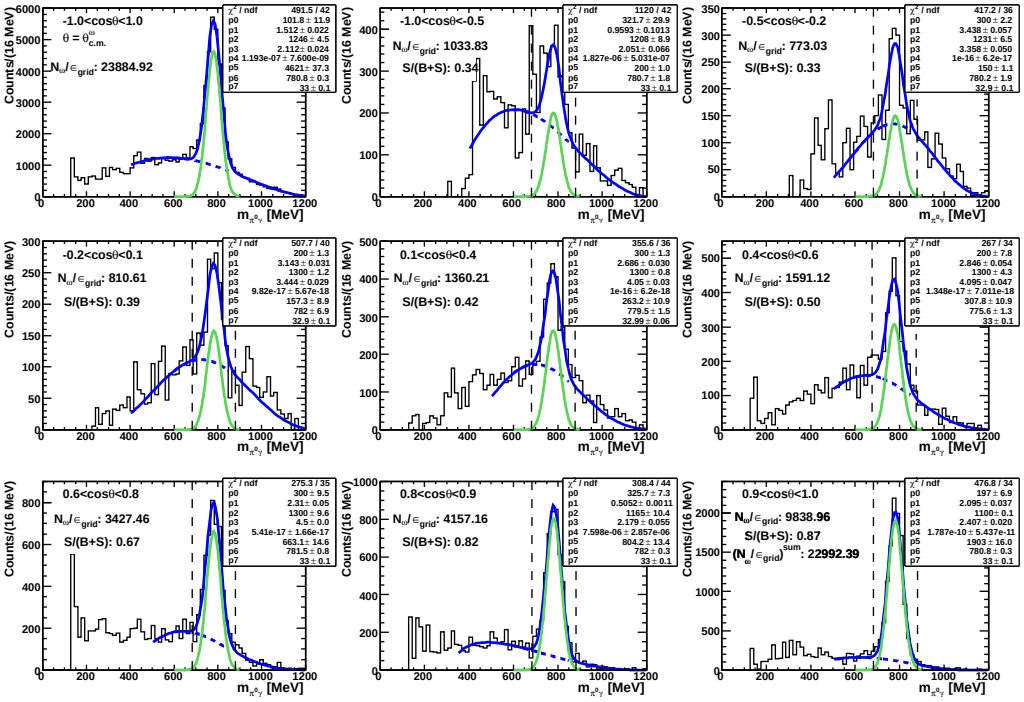

(b) After event-by-event efficiency correction with $\epsilon(T^{\omega}_{lab.}, \theta^{\omega}_{lab.})$

Figure E.16: Fits to the $\pi^0\gamma$ invariant mass spectra for the $\cos(\theta^{\omega}_{c.m.})$ angular bins with incident beam energy E_γ = 1900-2000 MeV.

F. Fits for LD_2 exclusive analysis off the proton

Here, all the fits to the $\pi^0\gamma$ invariant mass spectra that were used to determine the exclusive cross-sections for ω photoproduction off the bound neutron are shown. The ω signals after background subtraction are also shown. The parameters of each fit with the function $f(x) = p_4(x-p_0)^{p_1}(x-p_2)^{p_3} + p_5 e^{-\frac{(x-p_6)^2}{2p_7^2}}$ are listed. The number of ω mesons for each angular and incident beam energy bin, N_ω, the statistical error and the signal-to-background ratio are given. The upper left spectra in each figure show the sum of all angular bins for the respective incident beam energy bin, -1.0$\leq \cos(\theta^{\omega}_{c.m.}) \leq$1.0. In the lower right figure the sum of ω mesons obtained from the fits in each angular bin is shown, N^{sum}_{ω}.

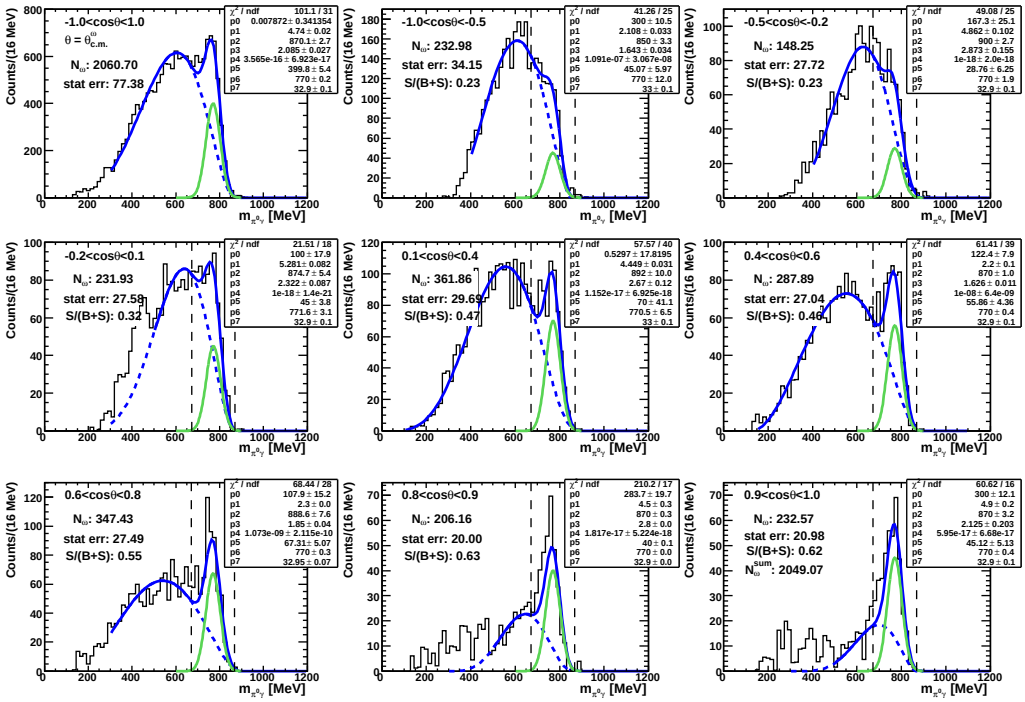

Figure F.1: Fits to the $\pi^0\gamma$ invariant mass spectra for the $\cos(\theta^{\omega}_{c.m.})$ angular bins with incident beam energy E_γ = 1158-1208 MeV.

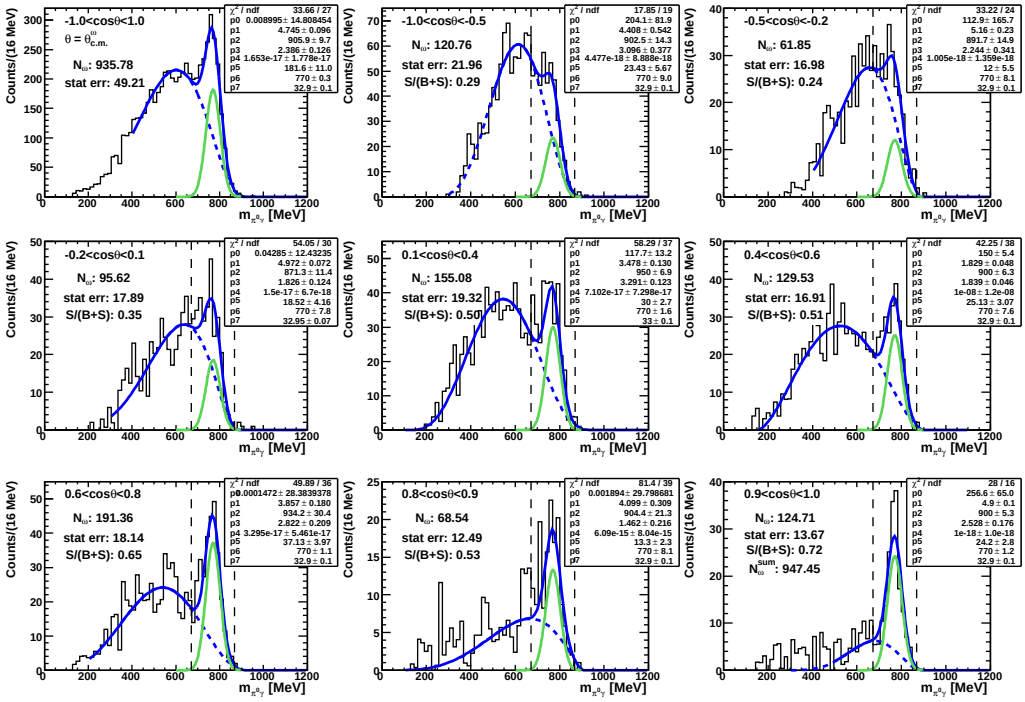

Figure F.2: Fits to the $\pi^0\gamma$ invariant mass spectra for the $\cos(\theta^{\omega}_{c.m.})$ angular bins with incident beam energy E_γ = 1208-1233 MeV.

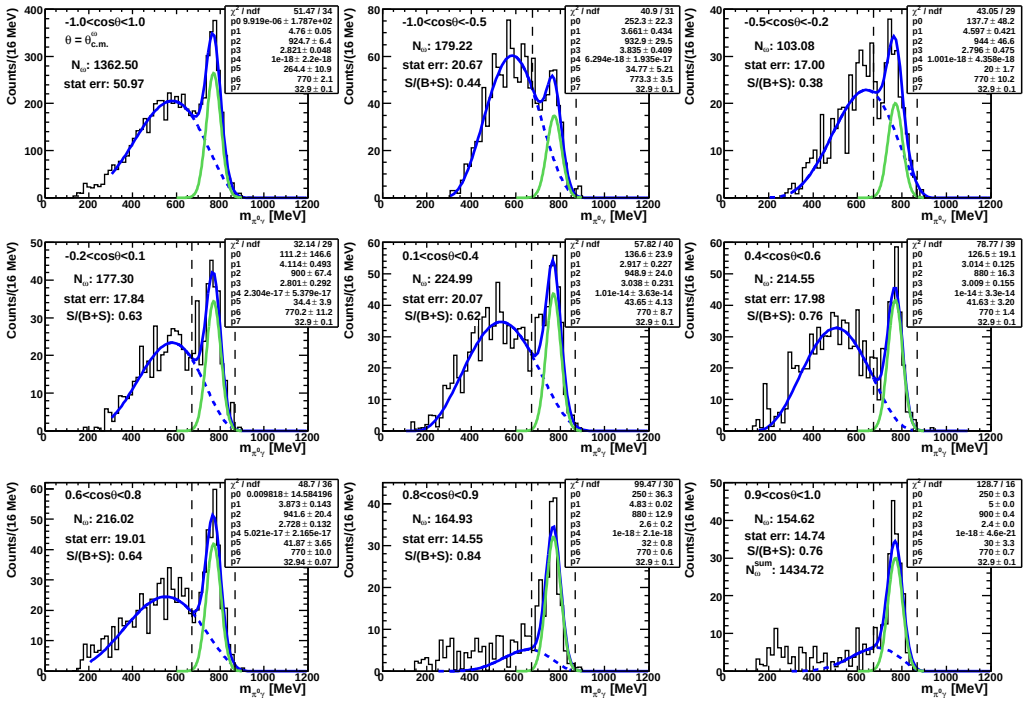

Figure F.3: Fits to the $\pi^0\gamma$ invariant mass spectra for the $\cos(\theta^{\omega}_{c.m.})$ angular bins with incident beam energy E_γ = 1233-1258 MeV.

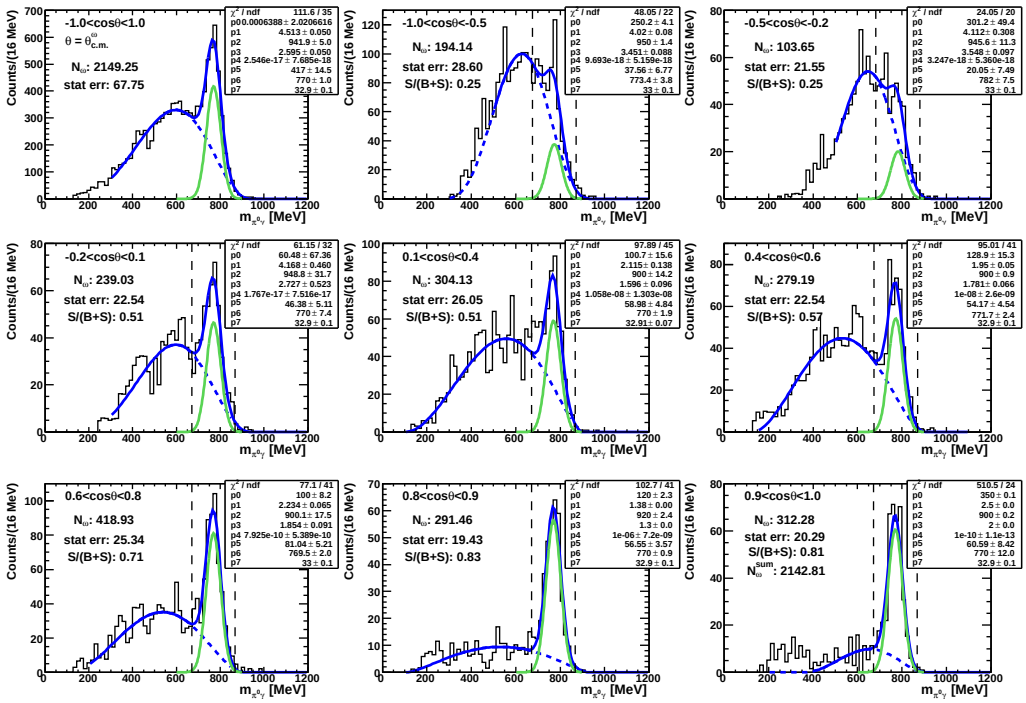

Figure F.4: Fits to the $\pi^0\gamma$ invariant mass spectra for the $\cos(\theta^{\omega}_{c.m.})$ angular bins with incident beam energy E_γ = 1258-1308 MeV.

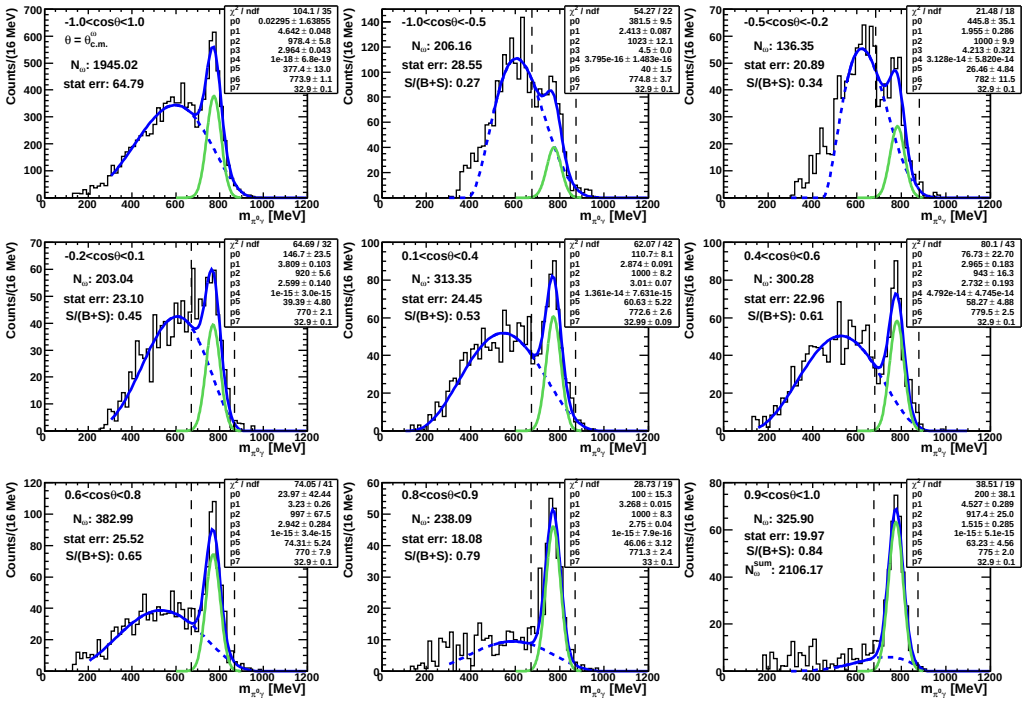

Figure F.5: Fits to the $\pi^0\gamma$ invariant mass spectra for the $\cos(\theta^{\omega}_{c.m.})$ angular bins with incident beam energy E_γ = 1308-1358 MeV.

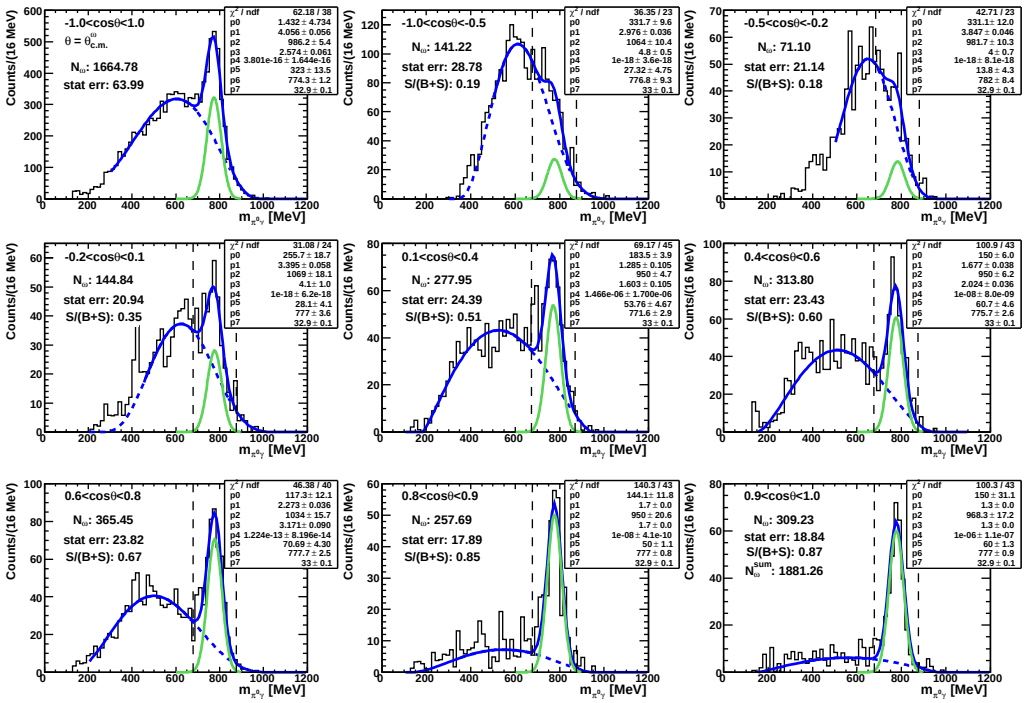

Figure F.6: Fits to the $\pi^0\gamma$ invariant mass spectra for the $\cos(\theta^{\omega}_{c.m.})$ angular bins with incident beam energy E_γ = 1358-1408 MeV.

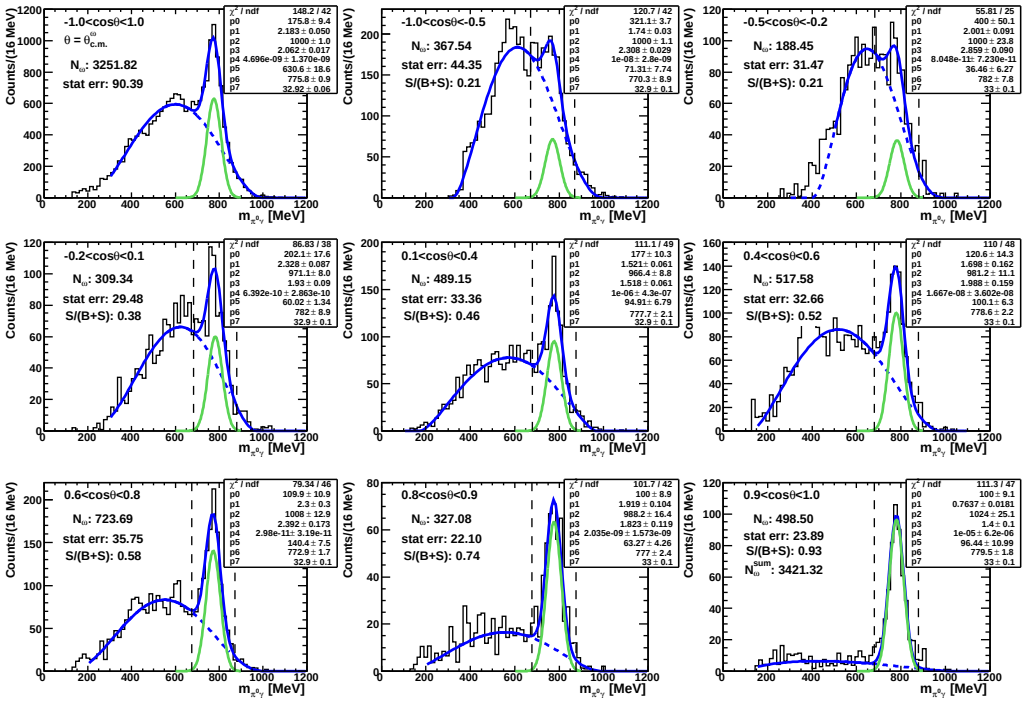

Figure F.7: Fits to the $\pi^0\gamma$ invariant mass spectra for the $\cos(\theta^{\omega}_{c.m.})$ angular bins with incident beam energy E_γ = 1408-1508 MeV.

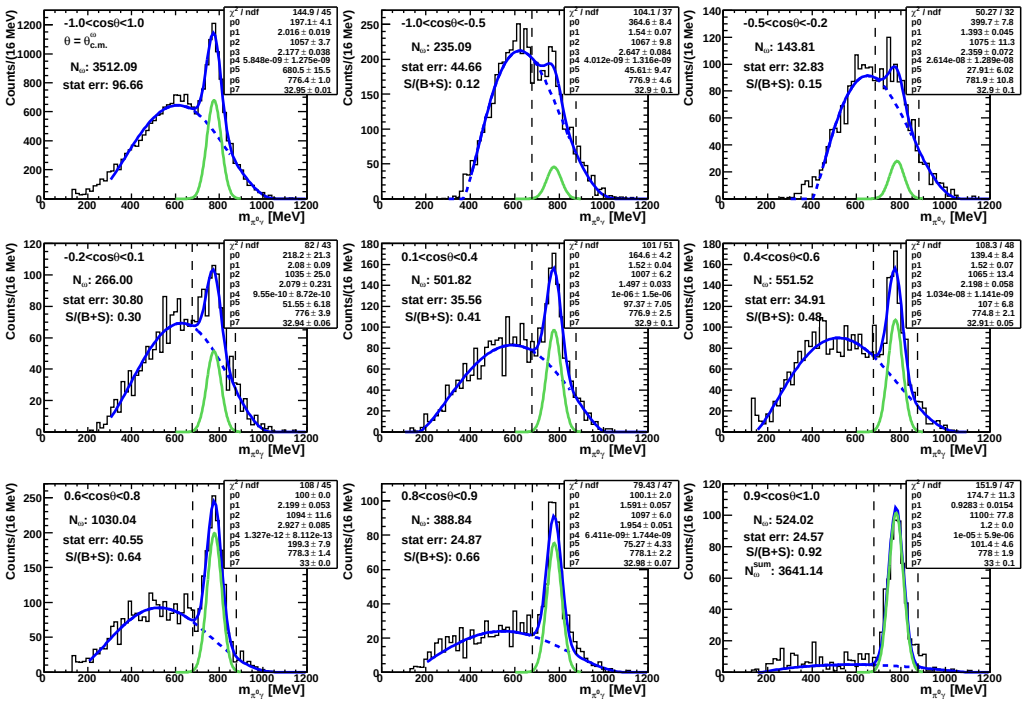

Figure F.8: Fits to the $\pi^0\gamma$ invariant mass spectra for the $\cos(\theta^{\omega}_{c.m.})$ angular bins with incident beam energy E_γ = 1508-1608 MeV.

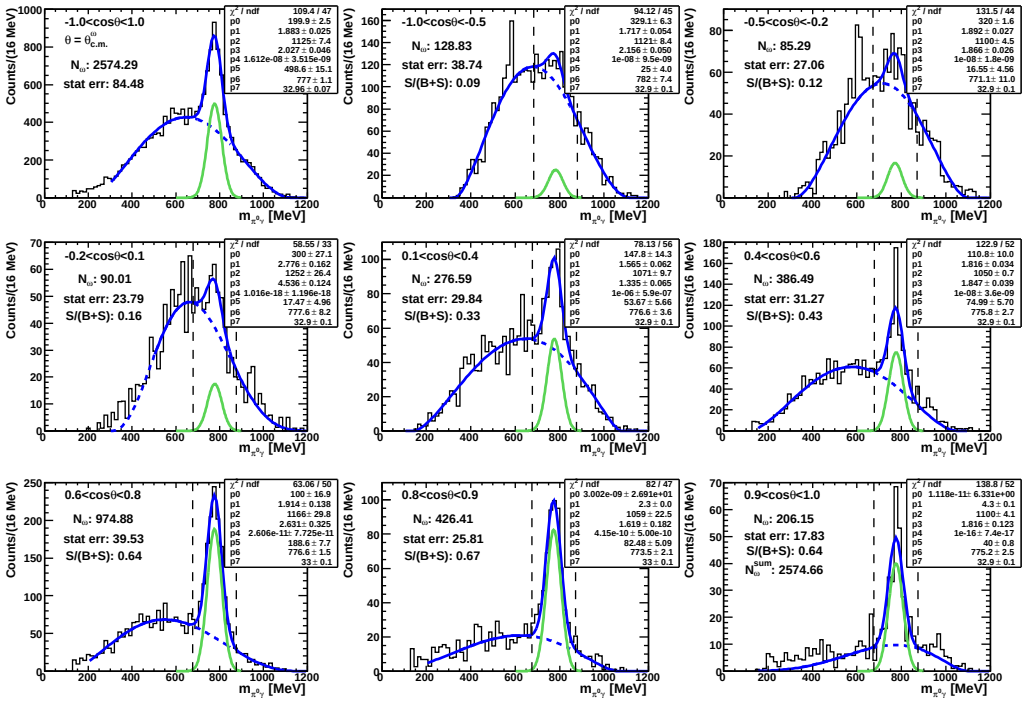

Figure F.9: Fits to the $\pi^0\gamma$ invariant mass spectra for the $\cos(\theta^{\omega}_{c.m.})$ angular bins with incident beam energy E_γ = 1608-1708 MeV.

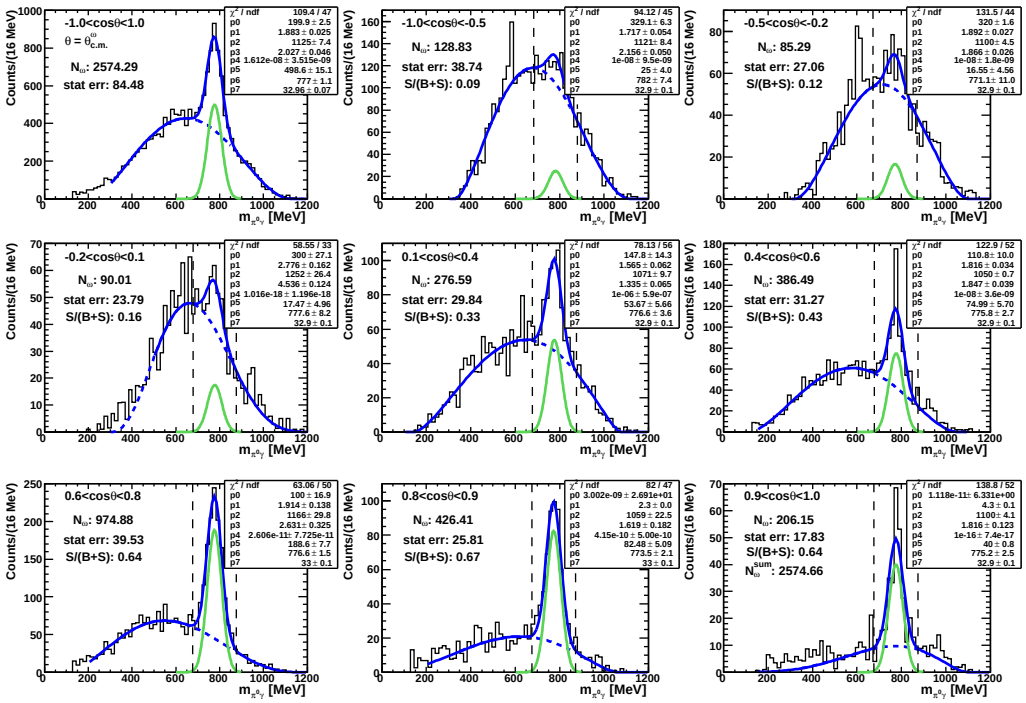

Figure F.10: Fits to the $\pi^0\gamma$ invariant mass spectra for the $\cos(\theta^{\omega}_{c.m.})$ angular bins with incident beam energy E_γ = 1708-1808 MeV.

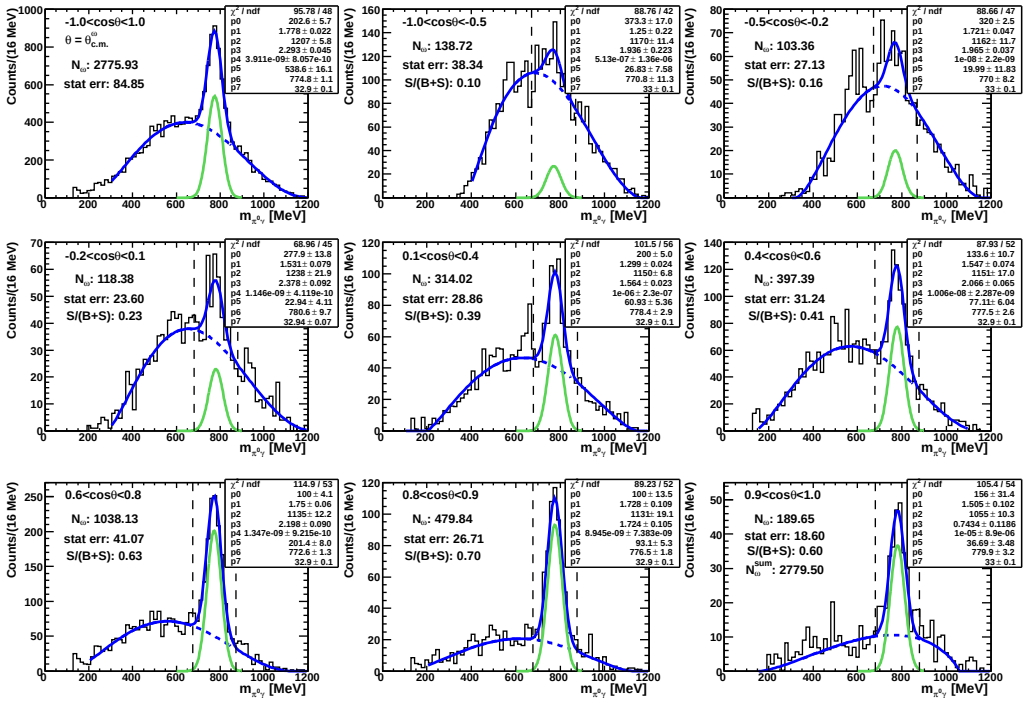

Figure F.11: Fits to the $\pi^0\gamma$ invariant mass spectra for the $\cos(\theta^{\omega}_{c.m.})$ angular bins with incident beam energy E_γ = 1808-1908 MeV.

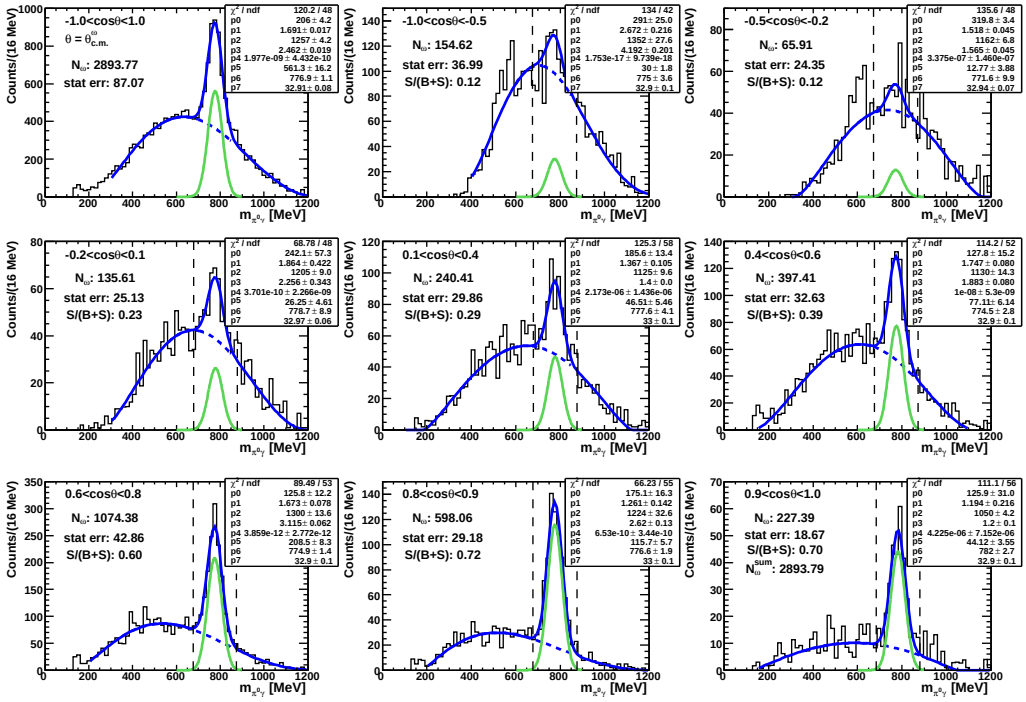

Figure F.12: Fits to the $\pi^0\gamma$ invariant mass spectra for the $\cos(\theta^{\omega}_{c.m.})$ angular bins with incident beam energy E_γ = 1908-2008 MeV.

G. Fits for LD_2 exclusive analysis off the neutron

Here, all the fits to the $\pi^0\gamma$ invariant mass spectra that were used to determine the exclusive cross-sections for ω photoproduction off the bound neutron are shown. The ω signals after background subtraction are also shown. The parameters of each fit with the function $f(x) = p_4(x-p_0)^{p_1}(x-p_2)^{p_3} + p_5 e^{-\frac{(x-p_6)^2}{2p_7^2}}$ are listed. The number of ω mesons for each angular and incident beam energy bin, N_ω, the statistical error and the signal-to-background ratio are given. The upper left spectra in each figure show the sum of all angular bins for the respective incident beam energy bin, -1.0$\leq \cos(\theta^{\omega}_{c.m.}) \leq$1.0. In the lower right figure the sum of ω mesons obtained from the fits in each angular bin is shown, N^{sum}_{ω}.

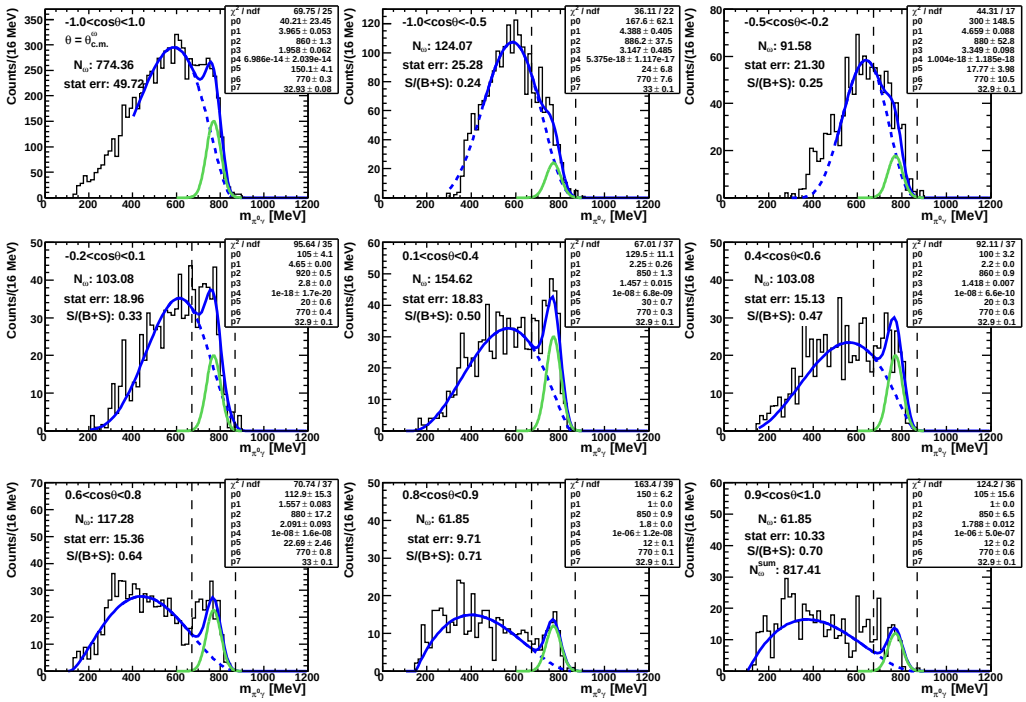

Figure G.1: Fits to the $\pi^0\gamma$ invariant mass spectra for the $\cos(\theta^{\omega}_{c.m.})$ angular bins with incident beam energy E_γ = 1158-1208 MeV.

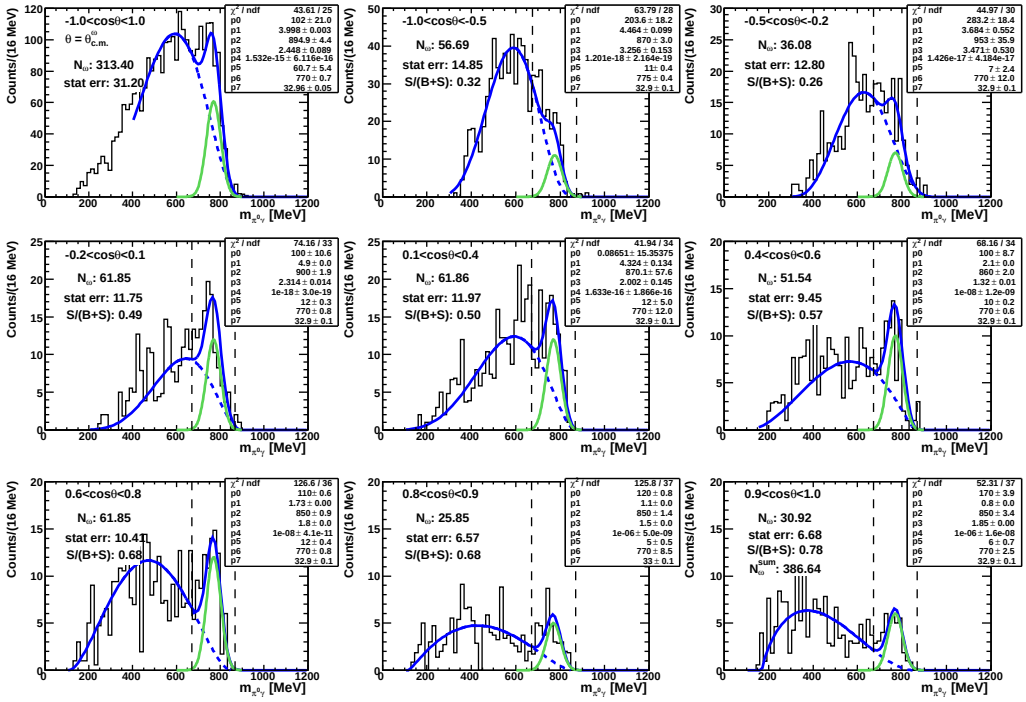

Figure G.2: Fits to the $\pi^0\gamma$ invariant mass spectra for the $\cos\theta_\theta c.m.^{\omega}$ angular bins with incident beam energy E_γ = 1208-1233 MeV.

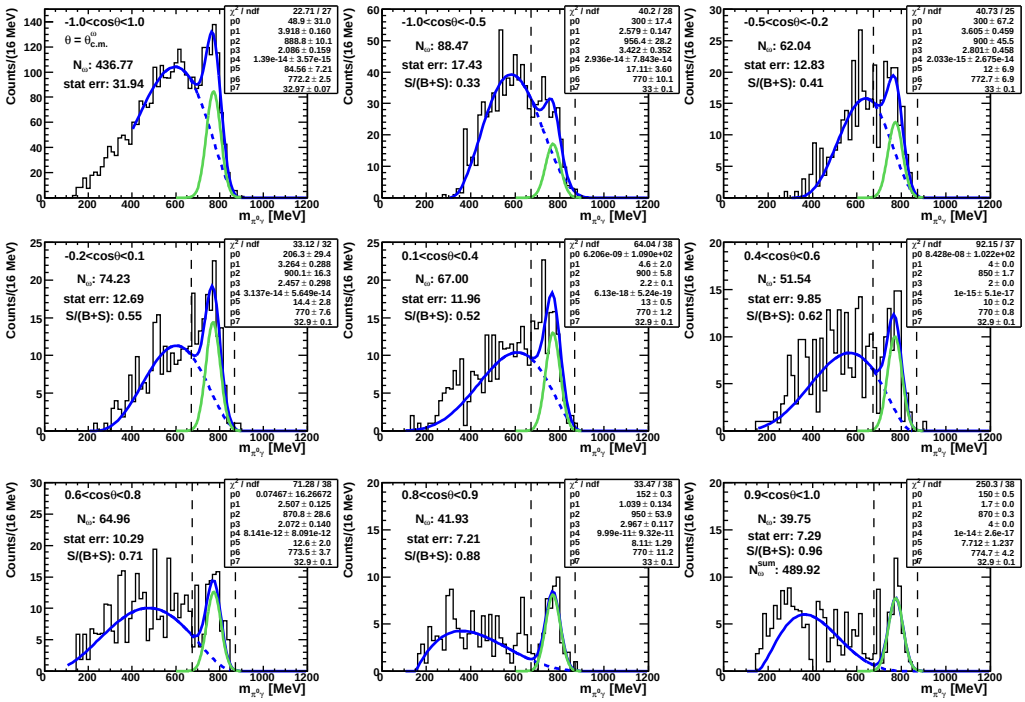

Figure G.3: Fits to the $\pi^0\gamma$ invariant mass spectra for the $\cos(\theta^{\omega}_{c.m.})$ angular bins with incident beam energy E_γ = 1233-1258 MeV.

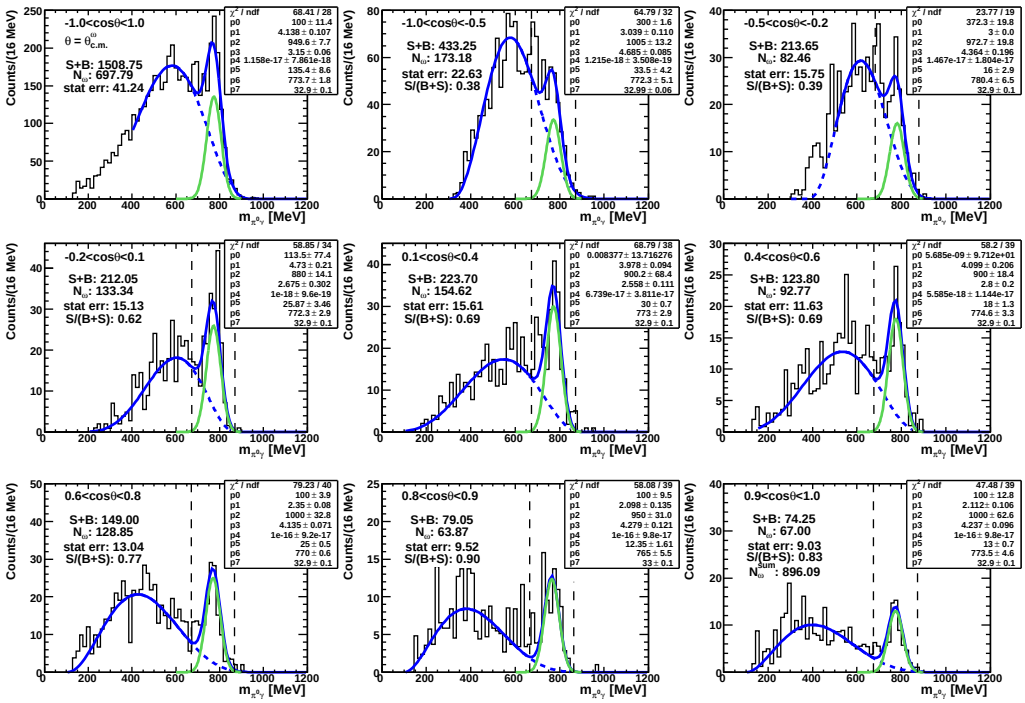

Figure G.4: Fits to the $\pi^0\gamma$ invariant mass spectra for the $\cos(\theta^{\omega}_{c.m.})$ angular bins with incident beam energy E_γ = 1258-1308 MeV.

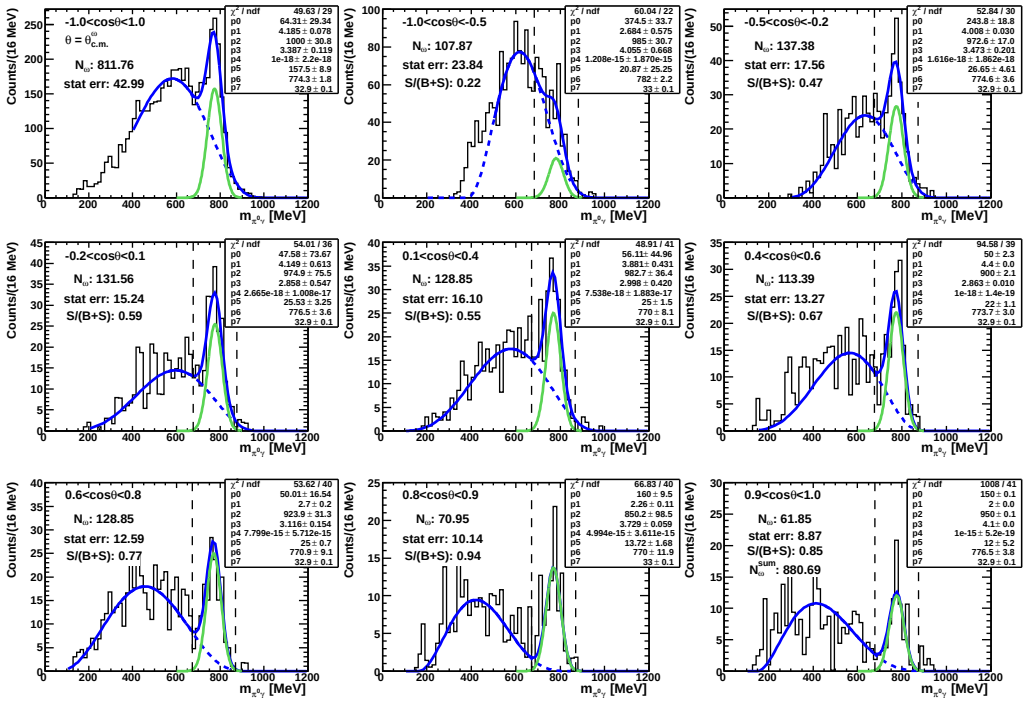

Figure G.5: Fits to the $\pi^0\gamma$ invariant mass spectra for the $\cos(\theta^{\omega}_{c.m.})$ angular bins with incident beam energy E_γ = 1308-1358 MeV.

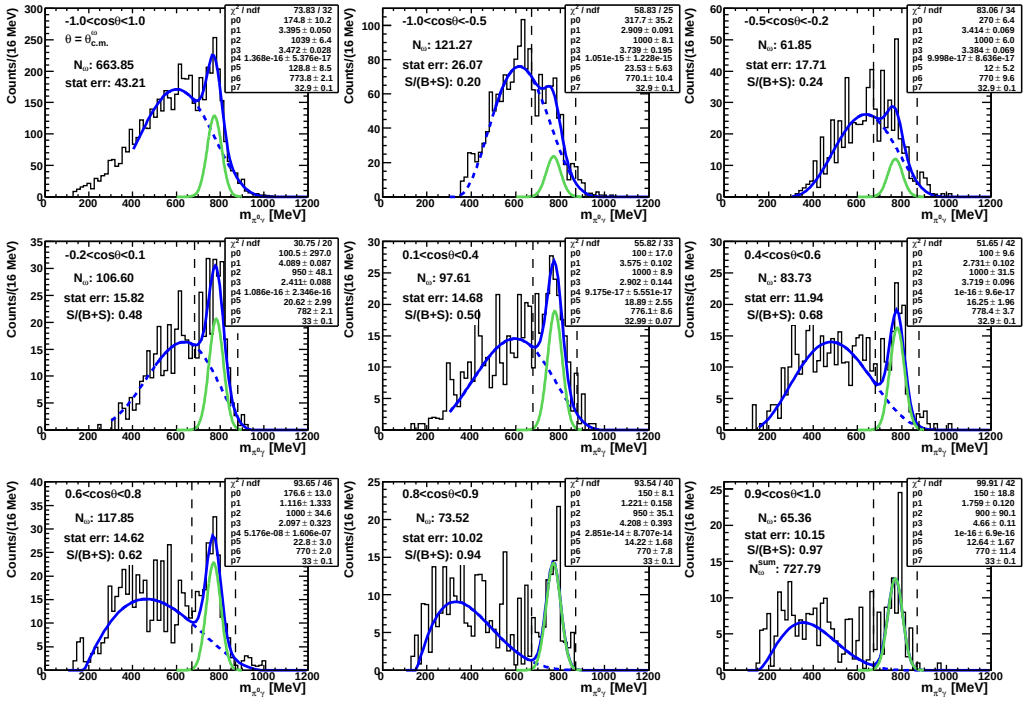

Figure G.6: Fits to the $\pi^0\gamma$ invariant mass spectra for the $\cos(\theta^{\omega}_{c.m.})$ angular bins with incident beam energy E_γ = 1358-1408 MeV.

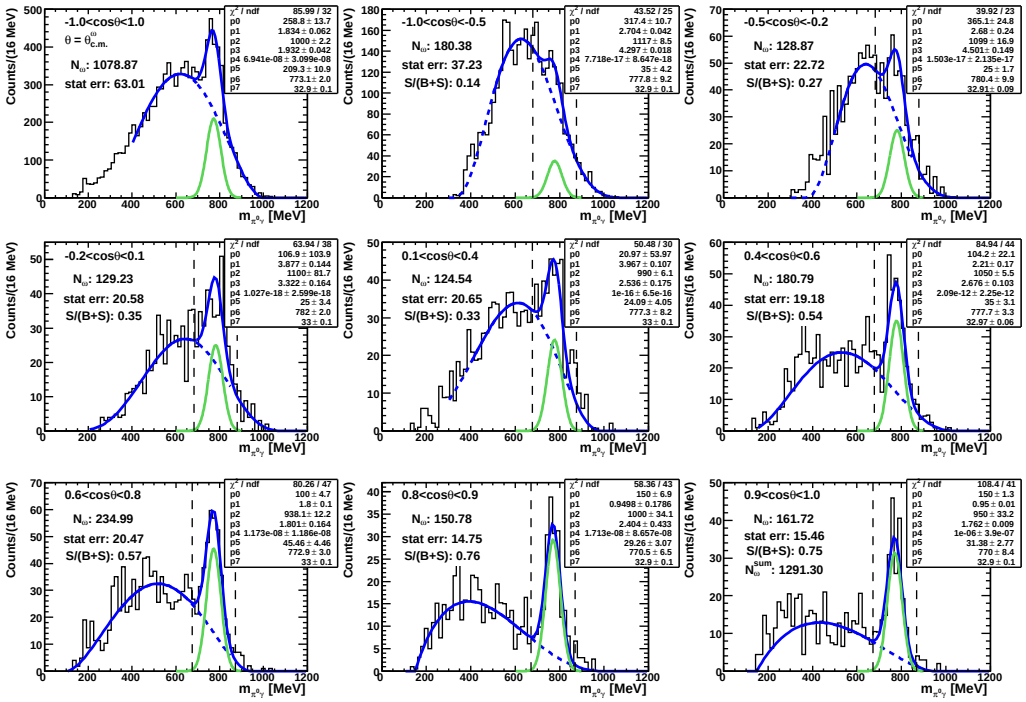

Figure G.7: Fits to the $\pi^0\gamma$ invariant mass spectra for the $\cos(\theta^{\omega}_{c.m.})$ angular bins with incident beam energy E_γ = 1408-1508 MeV.

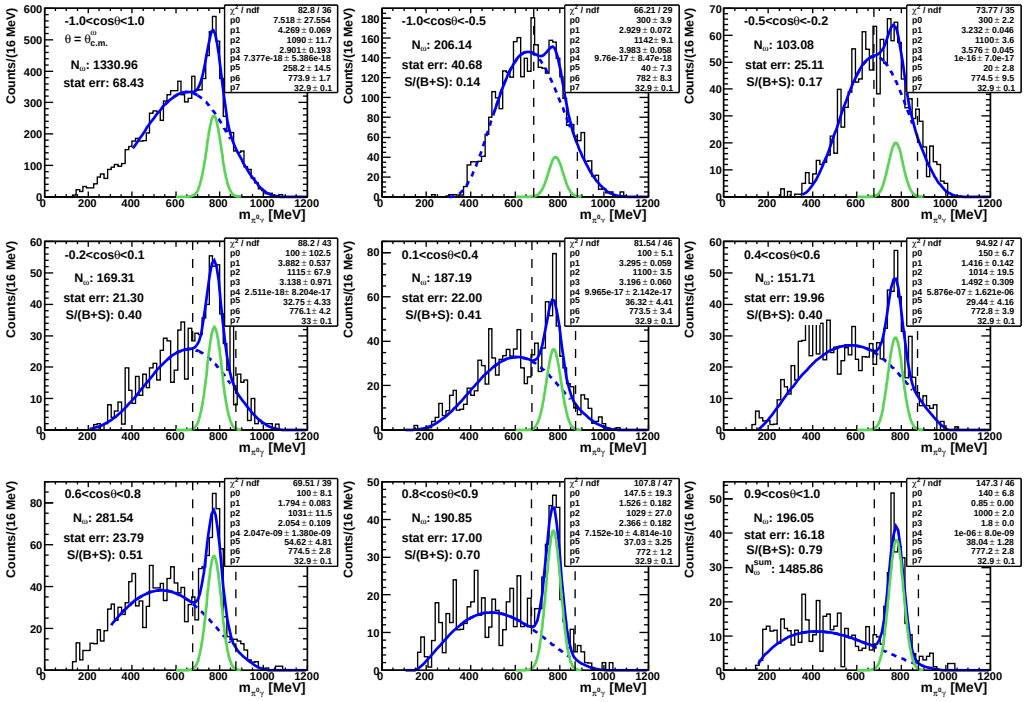

Figure G.8: Fits to the $\pi^0\gamma$ invariant mass spectra for the $\cos(\theta^{\omega}_{c.m.})$ angular bins with incident beam energy E_γ = 1508-1608 MeV.

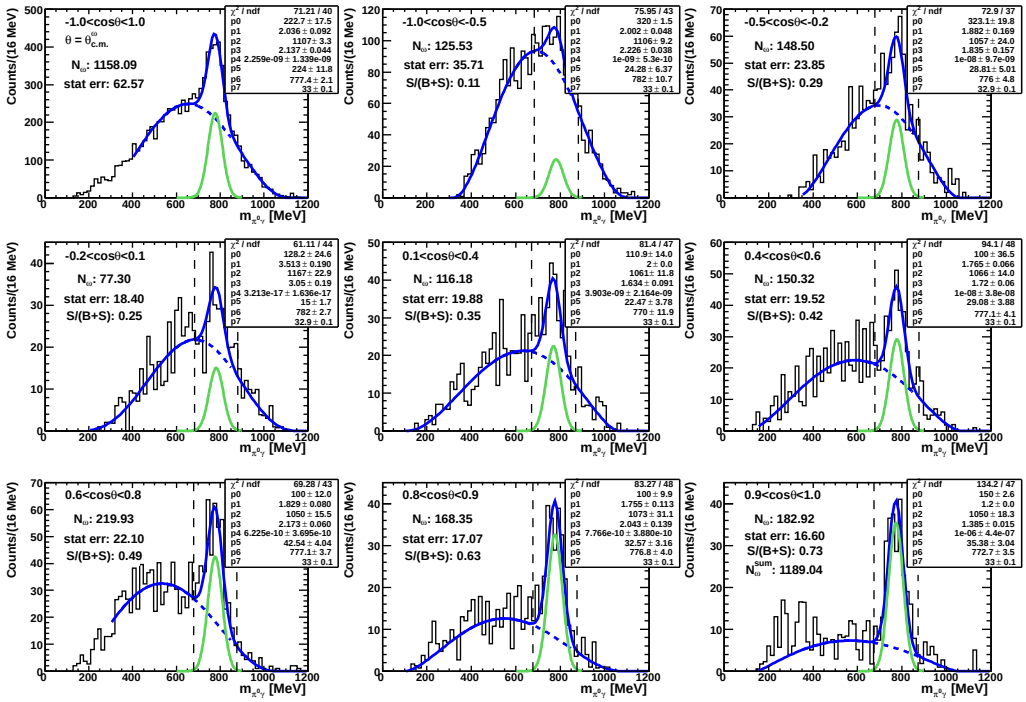

Figure G.9: Fits to the $\pi^0\gamma$ invariant mass spectra for the $\cos(\theta^{\omega}_{c.m.})$ angular bins with incident beam energy E_γ = 1608-1708 MeV.

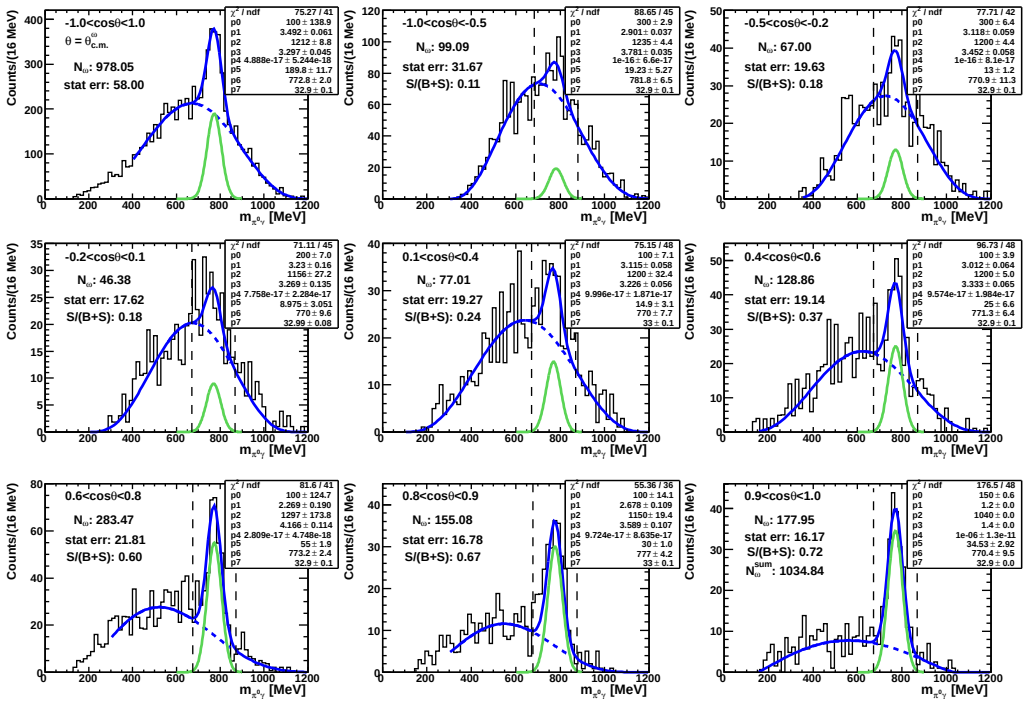

Figure G.10: Fits to the $\pi^0\gamma$ invariant mass spectra for the $\cos(\theta^{\omega}_{c.m.})$ angular bins with incident beam energy E_γ = 1708-1808 MeV.

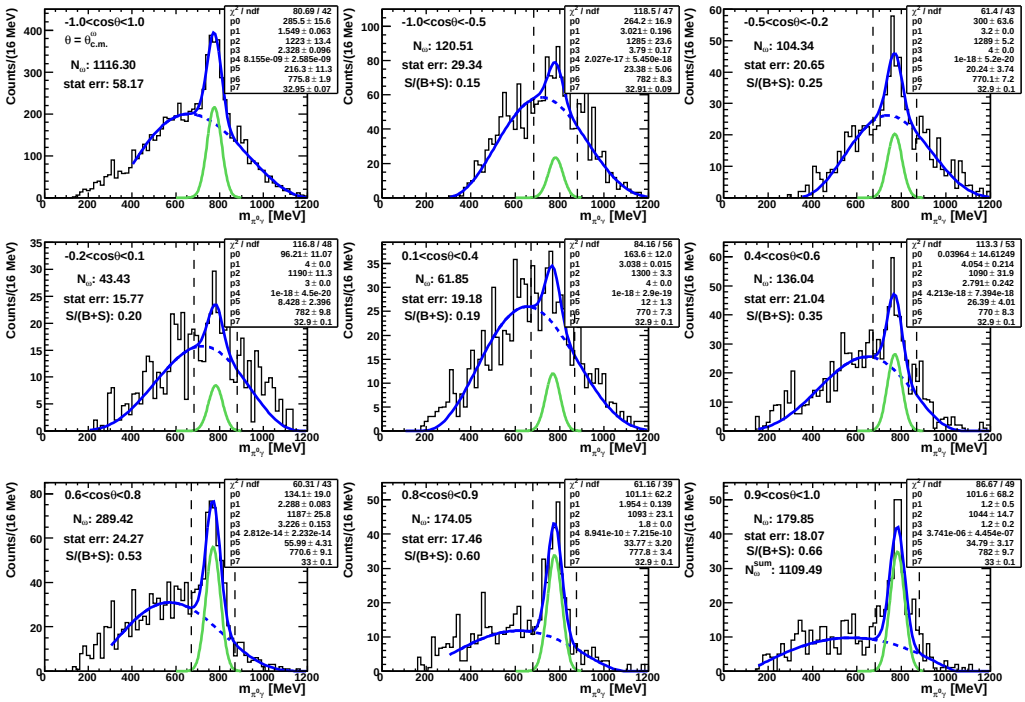

Figure G.11: Fits to the $\pi^0\gamma$ invariant mass spectra for the $\cos(\theta^{\omega}_{c.m.})$ angular bins with incident beam energy E_γ = 1808-1908 MeV.

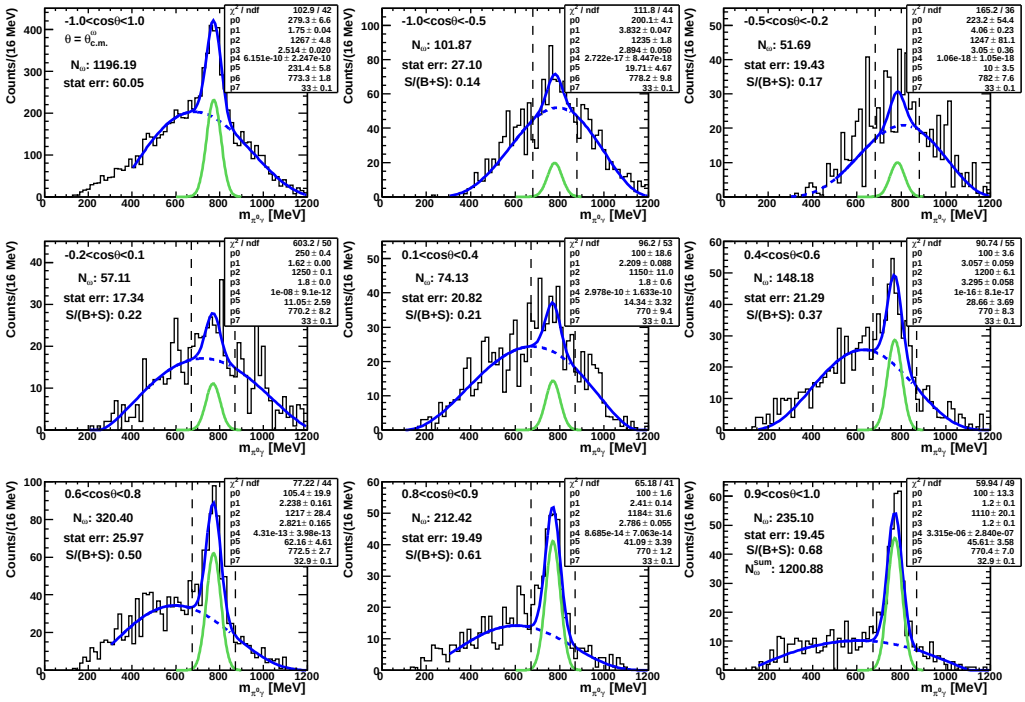

Figure G.12: Fits to the $\pi^0\gamma$ invariant mass spectra for the $\cos(\theta^{\omega}_{c.m.})$ angular bins with incident beam energy E_γ = 1908-2008 MeV.

H. Fits for LD_2 inclusive analysis

Here, all the fits to the $\pi^0\gamma$ invariant mass spectra that were used to determine the inclusive cross-sections for ω photoproduction off the LD_2 target are shown. The ω signals after background subtraction are also shown. The parameters of each fit with the function $f(x) = p_4(x-p_0)^{p_1}(x-p_2)^{p_3} + p_5 e^{-\frac{(x-p_6)^2}{2p_7^2}}$ are listed. The number of ω mesons for each angular and incident beam energy bin, N_ω, the statistical error and the signal-to-background ratio are given. The upper left spectra in each figure show the sum of all angular bins for the respective incident beam energy bin, -1.0$\leq \cos(\theta^{\omega}_{c.m.}) \leq$1.0. In the lower right figure the sum of ω mesons obtained from the fits in each angular bin is shown, N^{sum}_{ω}. Figure (a) shows the spectra before an efficiency correction was made and fig. (b) shows them after an event-by-event efficiency correction with $\epsilon(T^{\omega}_{lab.}, \theta^{\omega}_{lab.})$.

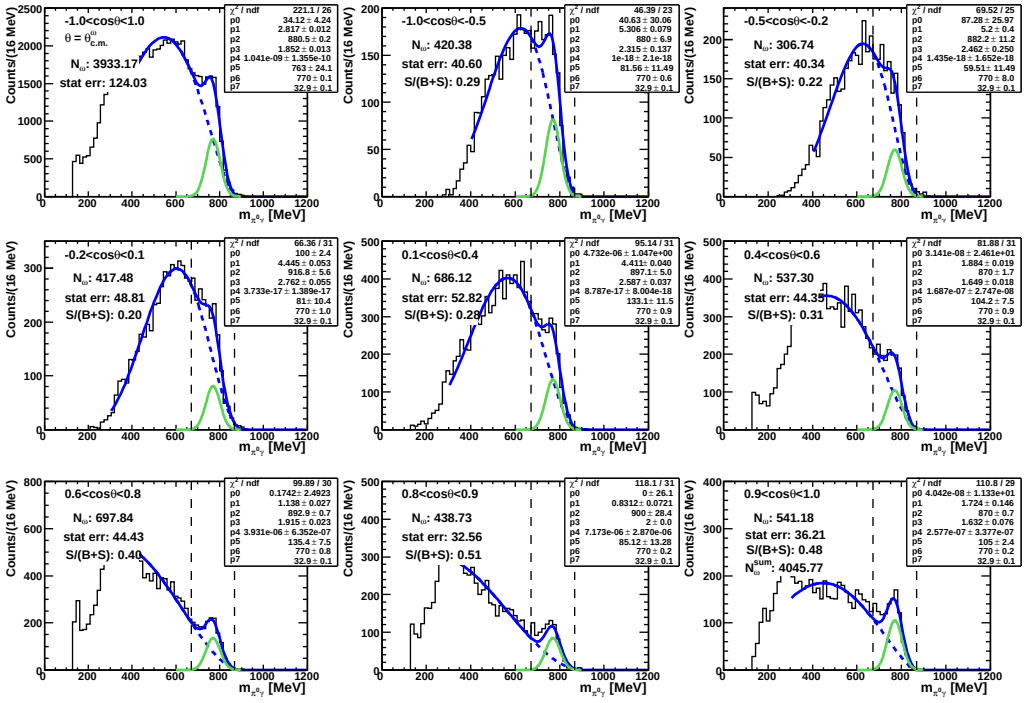

(a) Before efficiency correction

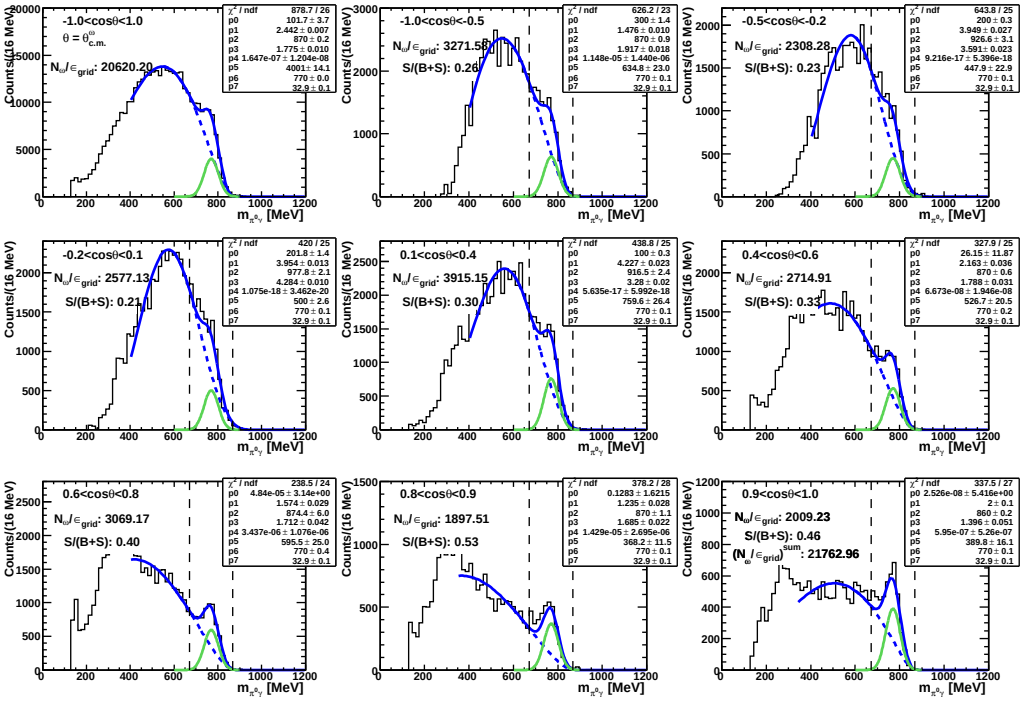

(b) After event-by-event efficiency correction with $\epsilon(T^{\omega}_{lab.}, \theta^{\omega}_{lab.})$

Figure H.1: Fits to the $\pi^0\gamma$ invariant mass spectra for the $\cos(\theta^{\omega}_{c.m.})$ angular bins with incident beam energy E_γ = 1158-1208 MeV.

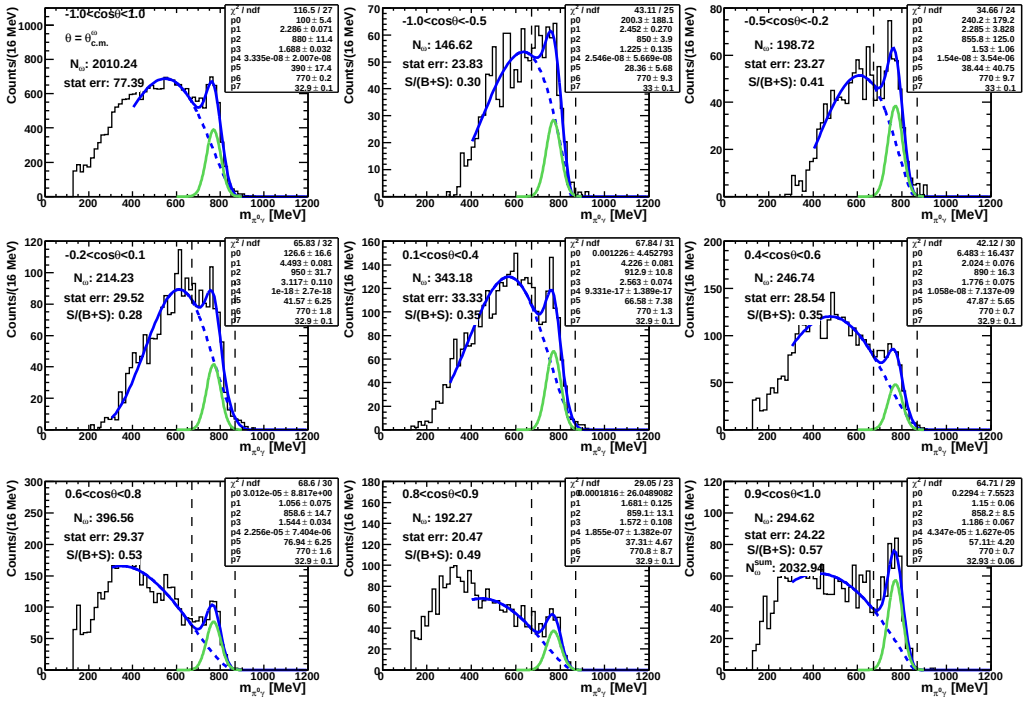

(a) Before efficiency correction

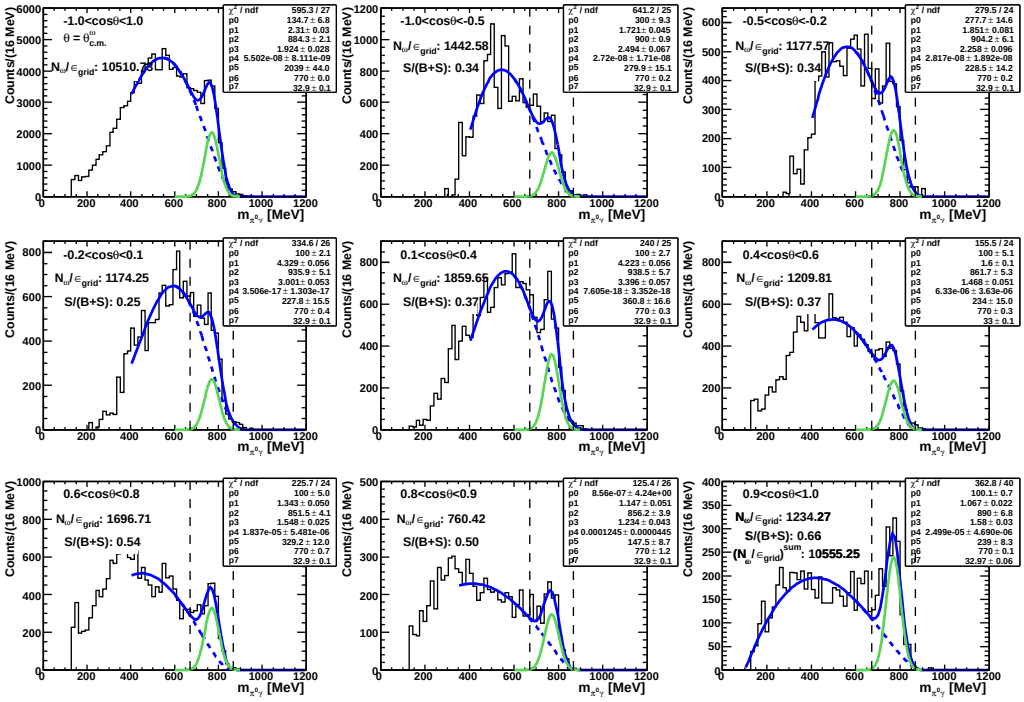

(b) After event-by-event efficiency correction with $\epsilon(T^{\omega}_{lab.}, \theta^{\omega}_{lab.})$

Figure H.2: Fits to the $\pi^0\gamma$ invariant mass spectra for the $\cos(\theta^{\omega}_{c.m.})$ angular bins with incident beam energy E_γ = 1208-1233 MeV.

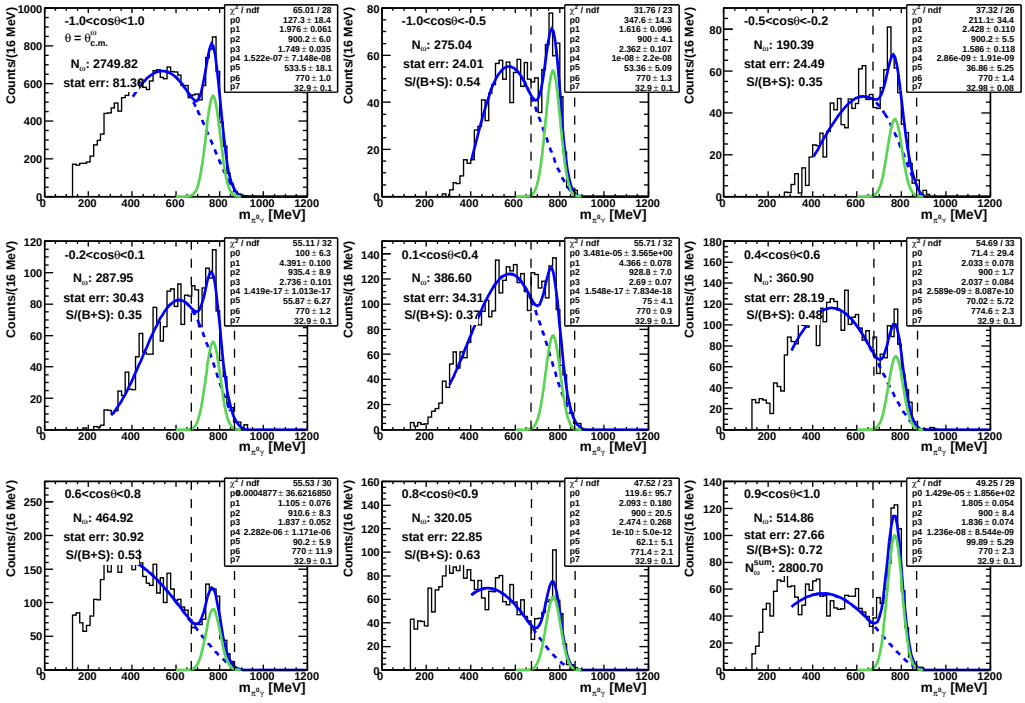

(a) Before efficiency correction

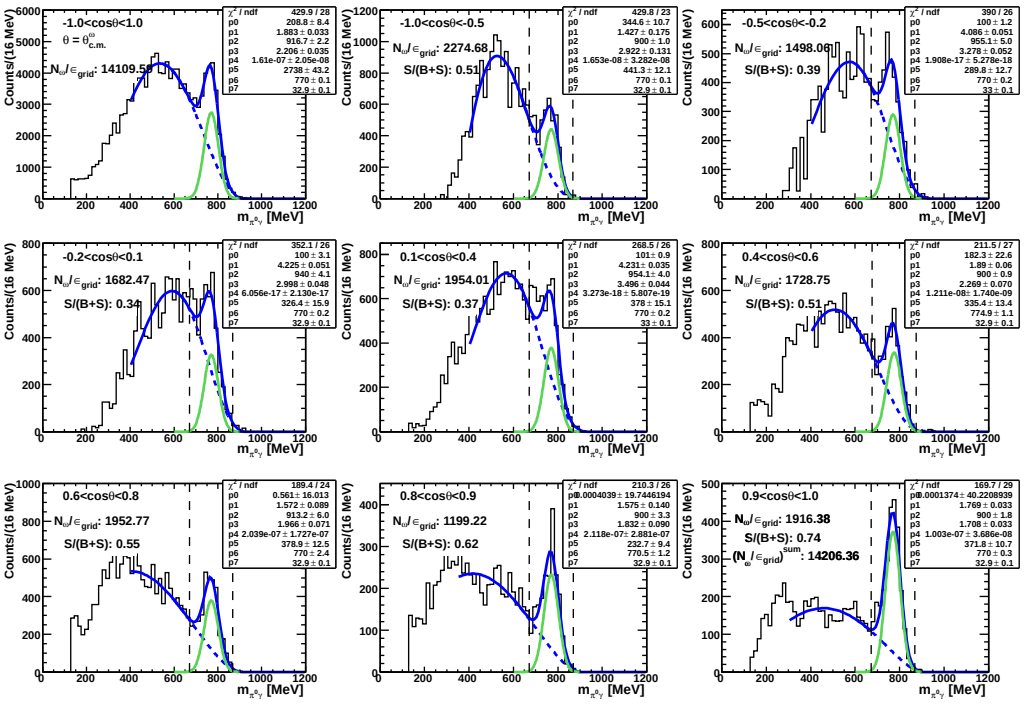

(b) After event-by-event efficiency correction with $\epsilon(T^{\omega}_{lab.}, \theta^{\omega}_{lab.})$

Figure H.3: Fits to the $\pi^0\gamma$ invariant mass spectra for the $\cos(\theta^{\omega}_{c.m.})$ angular bins with incident beam energy E_γ = 1233-1258 MeV.

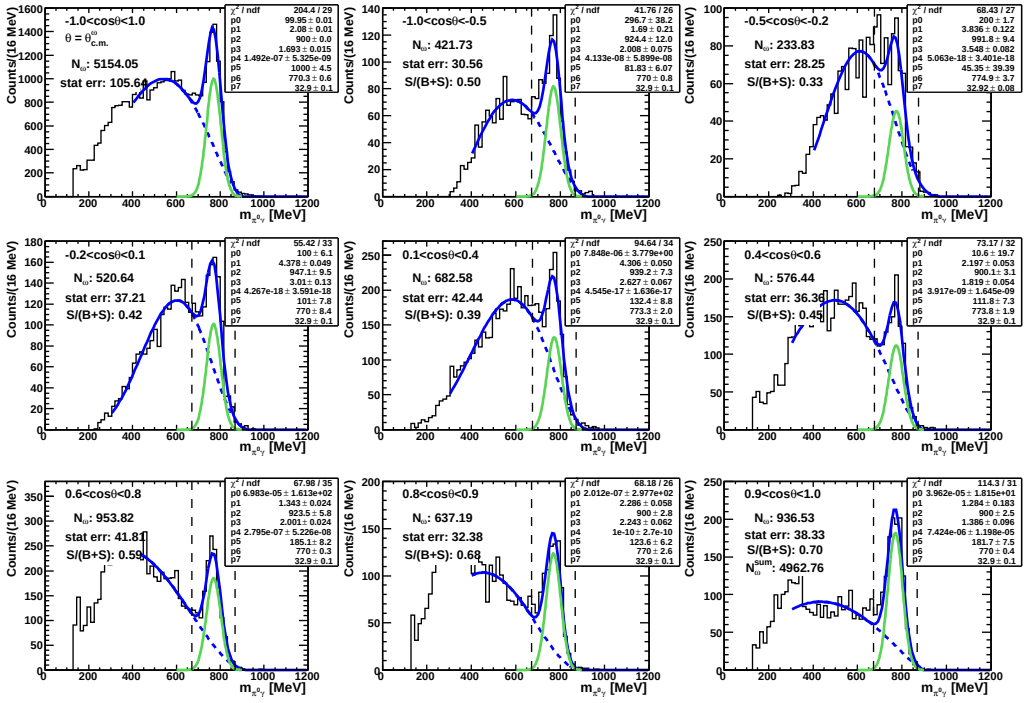

(a) Before efficiency correction

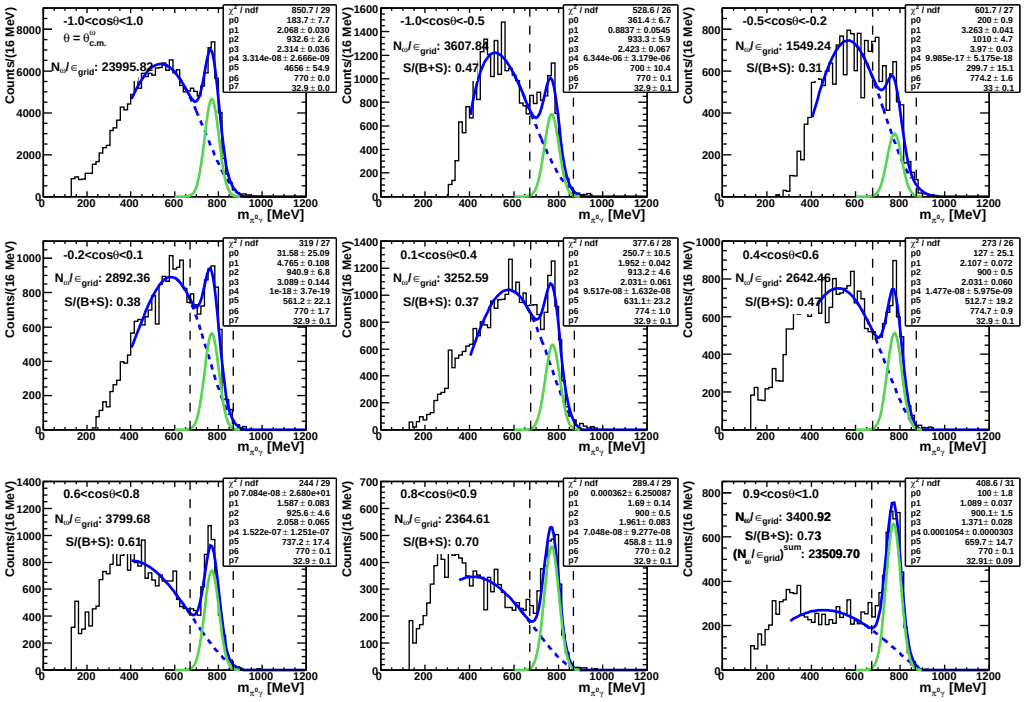

(b) After event-by-event efficiency correction with $\epsilon(T^{\omega}_{lab.}, \theta^{\omega}_{lab.})$

Figure H.4: Fits to the $\pi^0\gamma$ invariant mass spectra for the $\cos(\theta^{\omega}_{c.m.})$ angular bins with incident beam energy E_γ = 1258-1308 MeV.

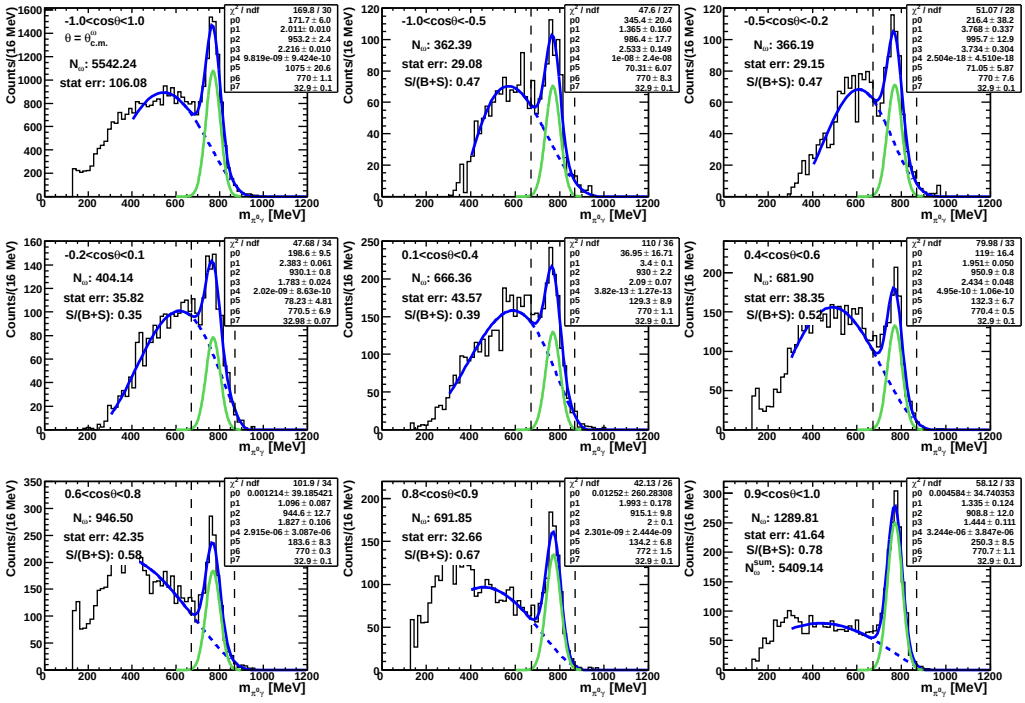

(a) Before efficiency correction

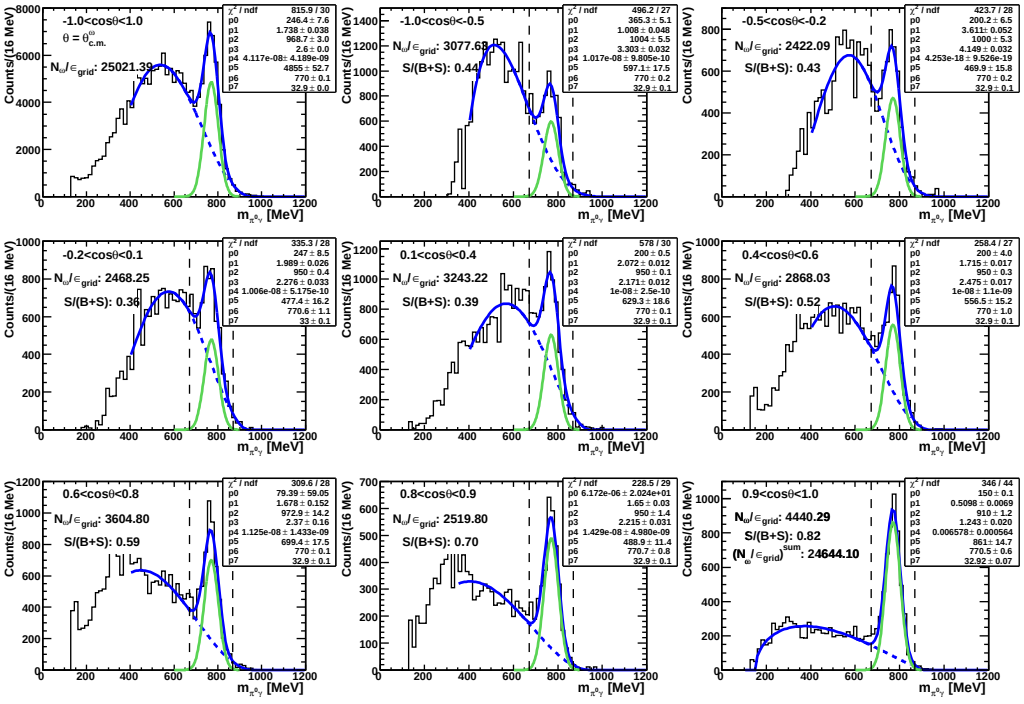

(b) After event-by-event efficiency correction with $\epsilon(T^{\omega}_{lab.}, \theta^{\omega}_{lab.})$

Figure H.5: Fits to the $\pi^0\gamma$ invariant mass spectra for the $\cos(\theta^{\omega}_{c.m.})$ angular bins with incident beam energy E_γ = 1308-1358 MeV.

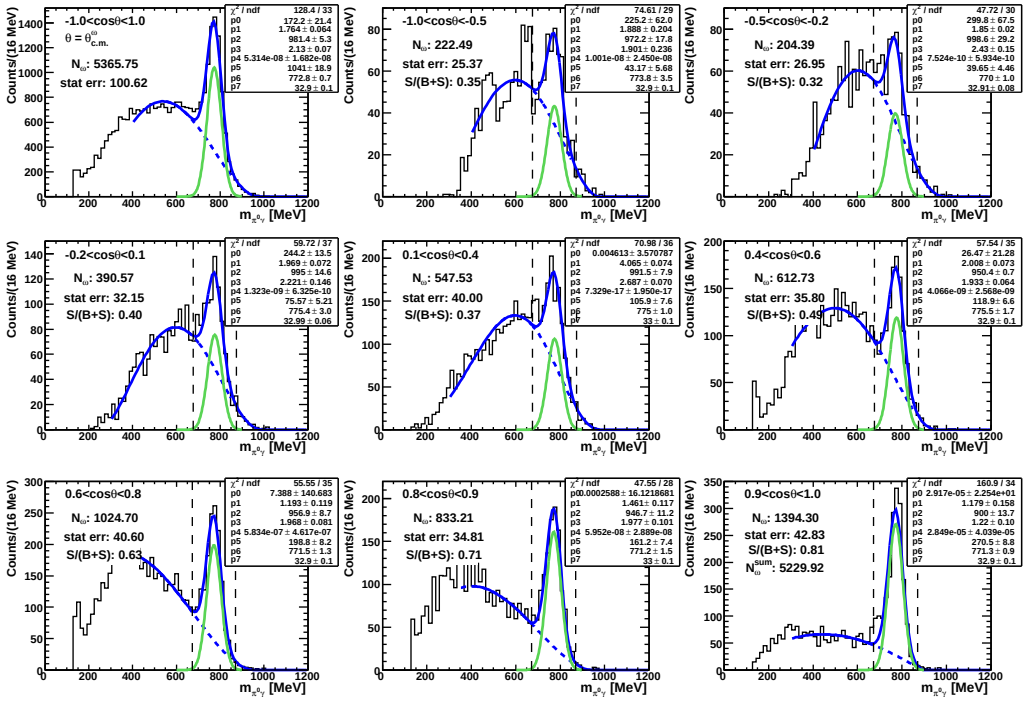

(a) Before efficiency correction

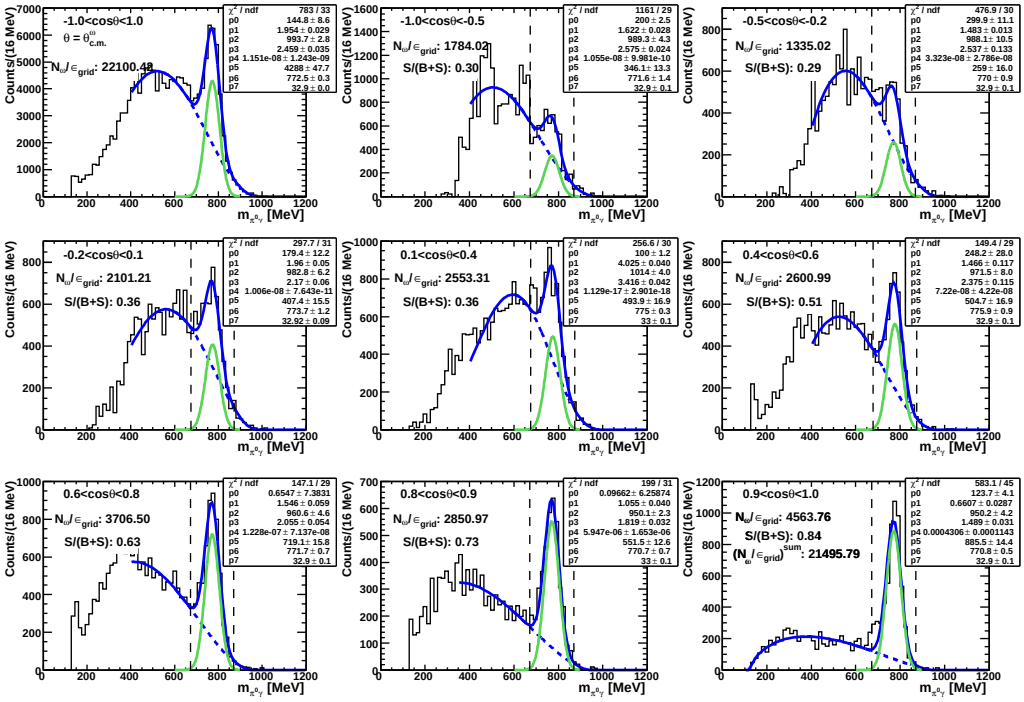

(b) After event-by-event efficiency correction with $\epsilon(T^{\omega}_{lab.}, \theta^{\omega}_{lab.})$

Figure H.6: Fits to the $\pi^0\gamma$ invariant mass spectra for the $\cos(\theta^{\omega}_{c.m.})$ angular bins with incident beam energy E_γ = 1358-1408 MeV.

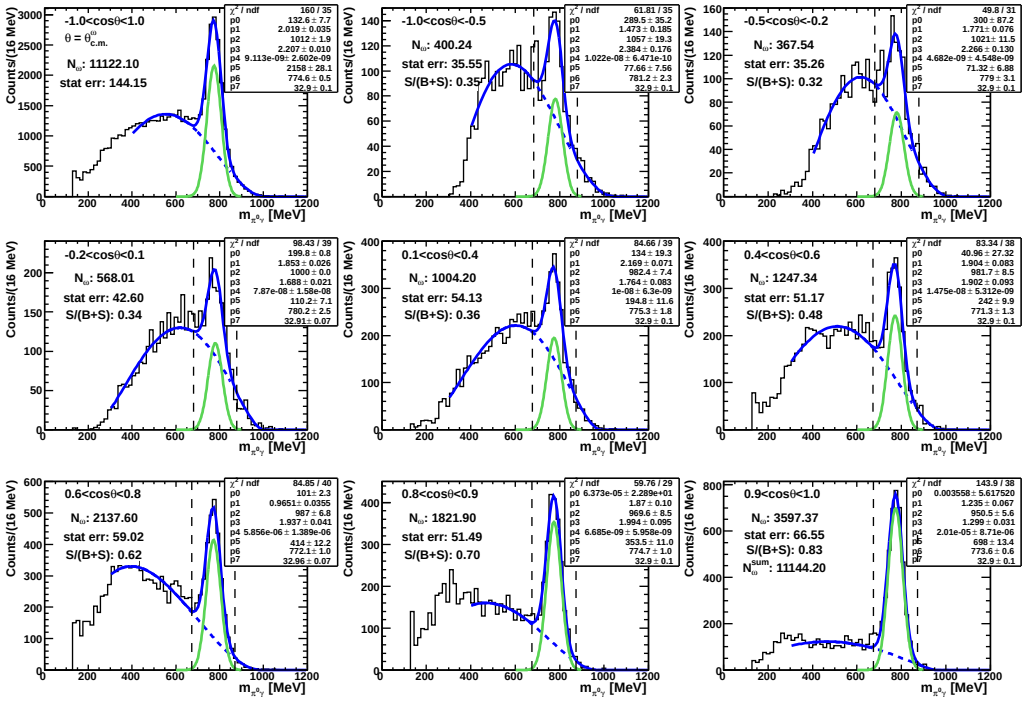

(a) Before efficiency correction

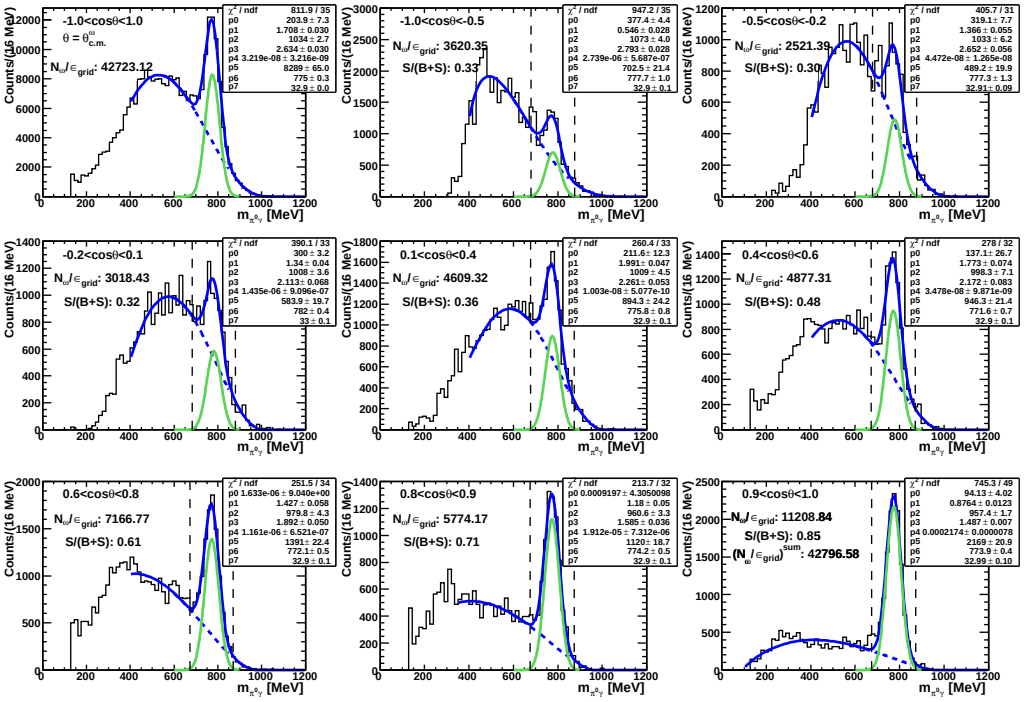

(b) After event-by-event efficiency correction with $\epsilon(T^{\omega}_{lab.}, \theta^{\omega}_{lab.})$

Figure H.7: Fits to the $\pi^0\gamma$ invariant mass spectra for the $\cos(\theta^{\omega}_{c.m.})$ angular bins with incident beam energy E_γ = 1408-1508 MeV.

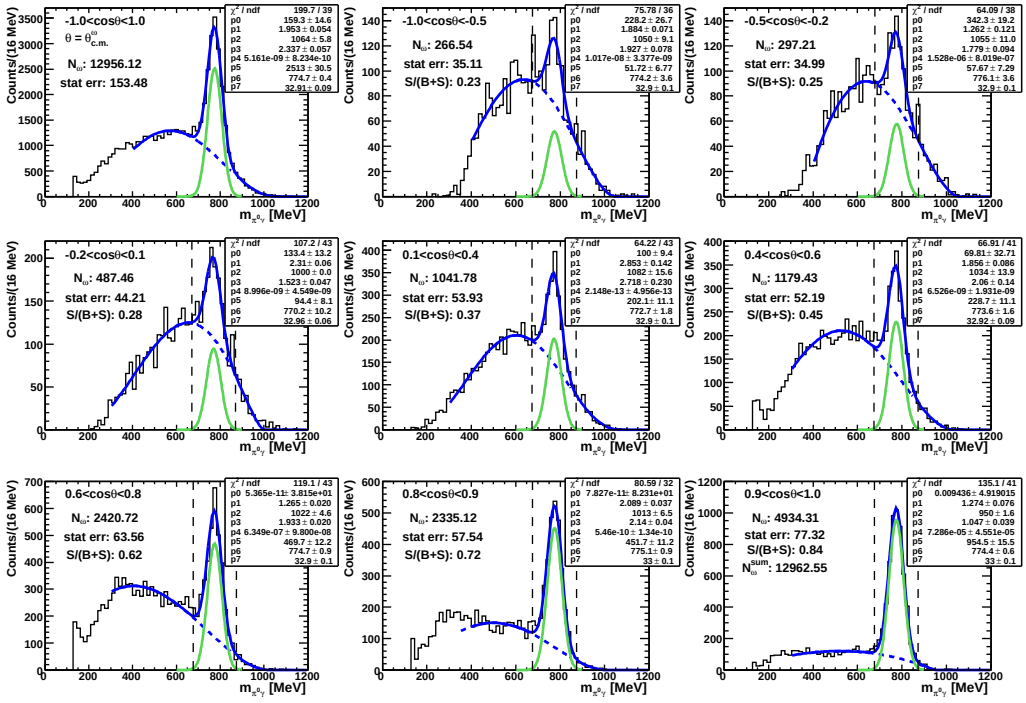

(a) Before efficiency correction

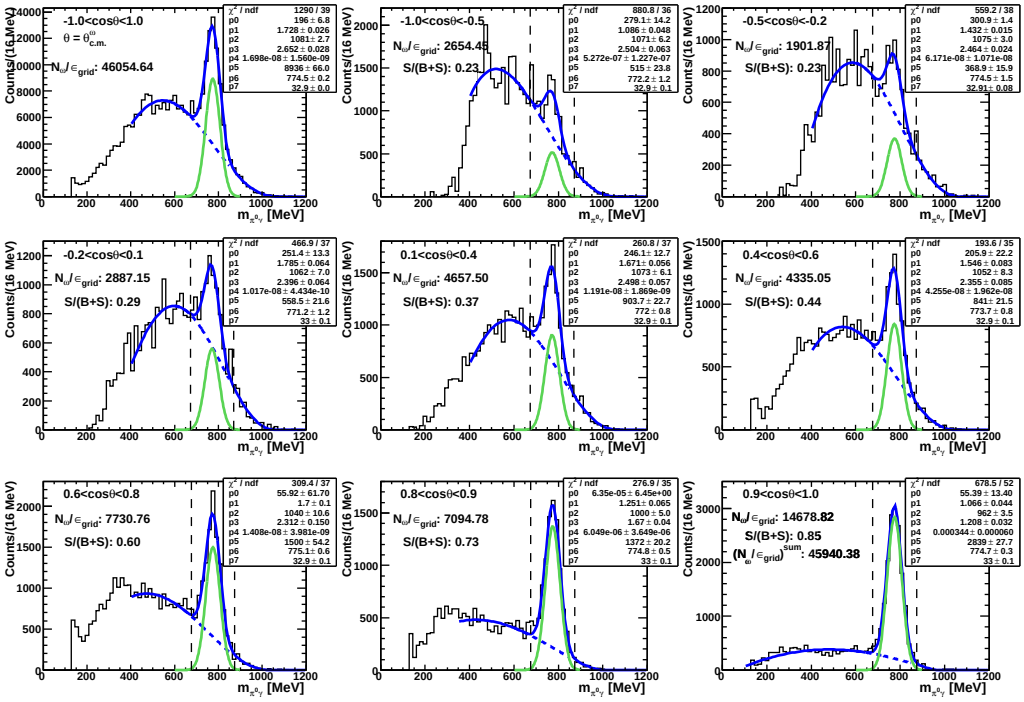

(b) After event-by-event efficiency correction with $\epsilon(T^{\omega}_{lab.}, \theta^{\omega}_{lab.})$

Figure H.8: Fits to the $\pi^0\gamma$ invariant mass spectra for the $\cos(\theta^{\omega}_{c.m.})$ angular bins with incident beam energy E_γ = 1508-1608 MeV.

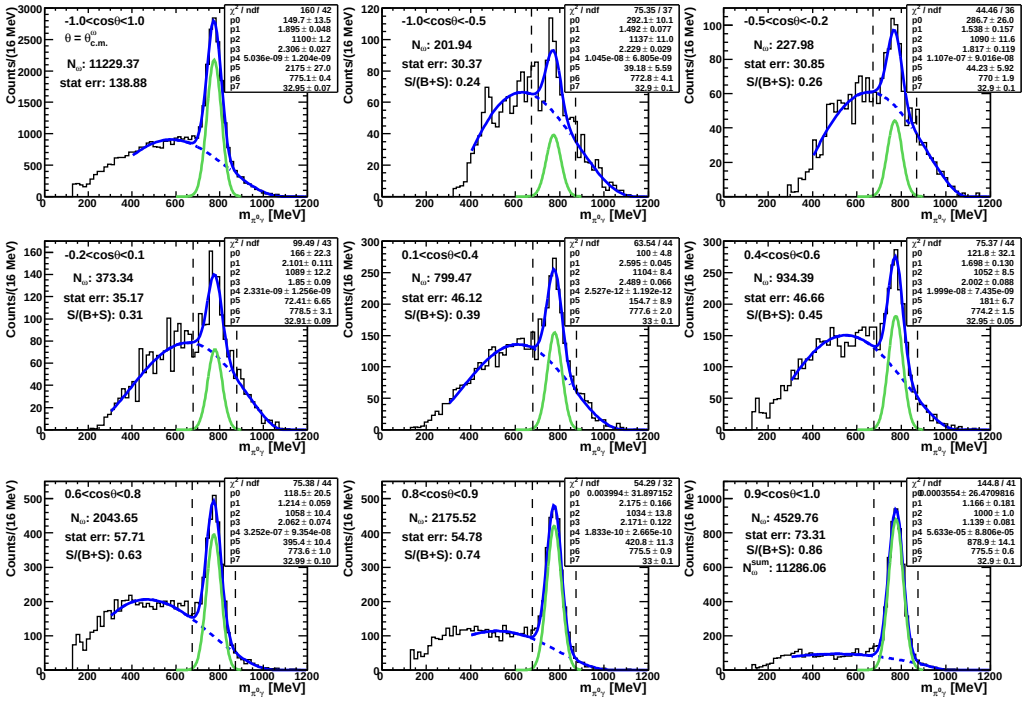

(a) Before efficiency correction

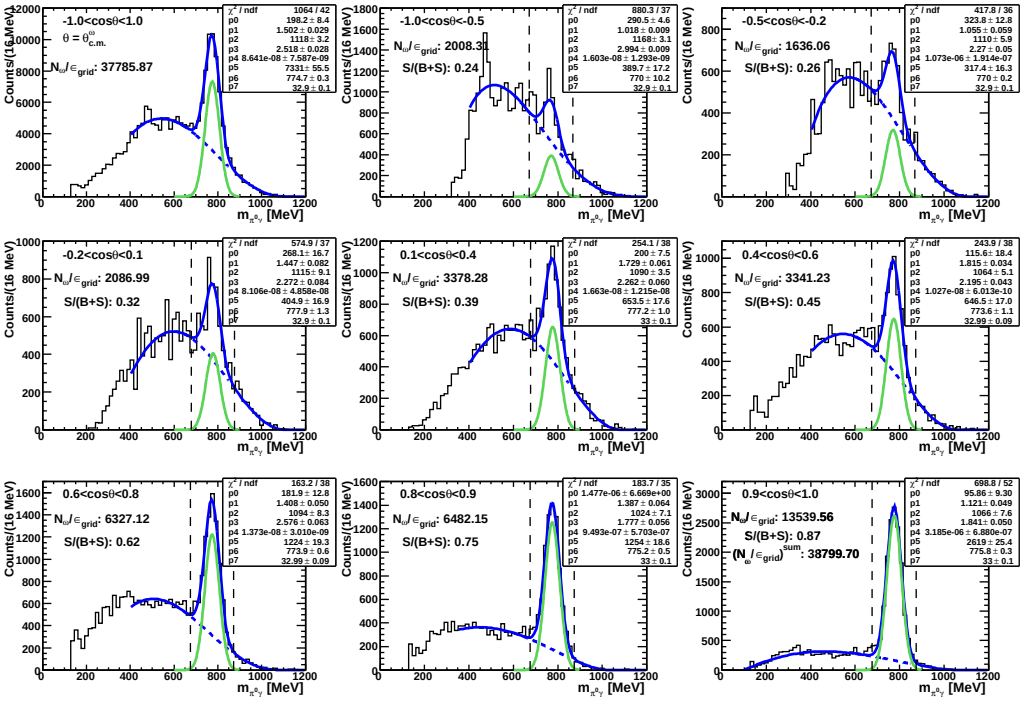

(b) After event-by-event efficiency correction with $\epsilon(T^{\omega}_{lab.}, \theta^{\omega}_{lab.})$

Figure H.9: Fits to the $\pi^0\gamma$ invariant mass spectra for the $\cos(\theta^{\omega}_{c.m.})$ angular bins with incident beam energy E_γ = 1608-1708 MeV.

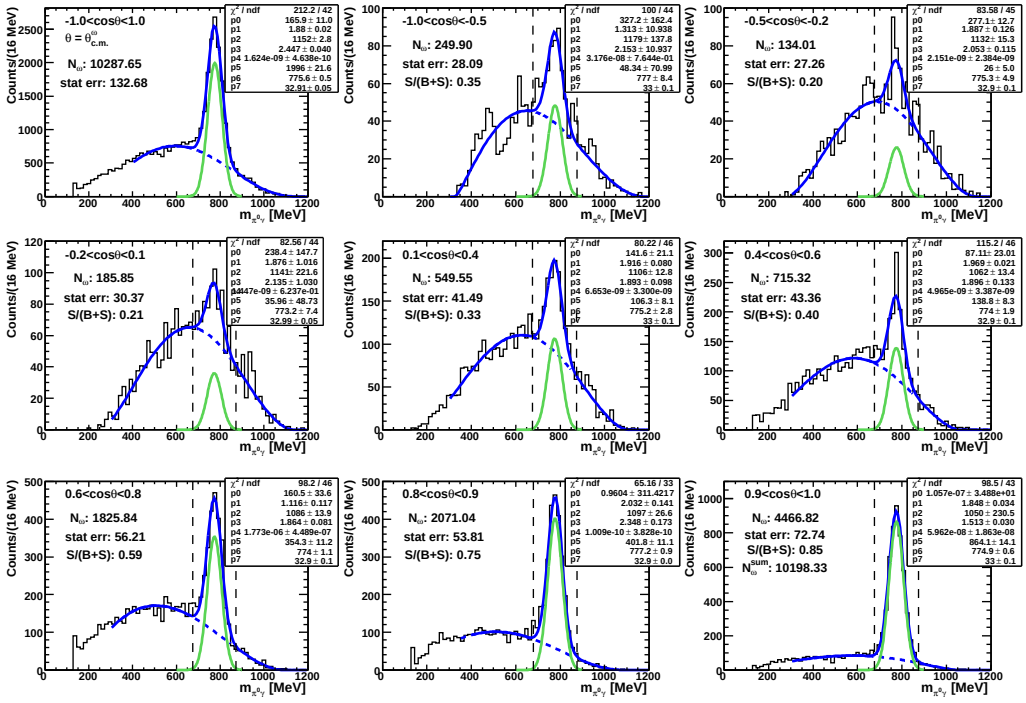

(a) Before efficiency correction

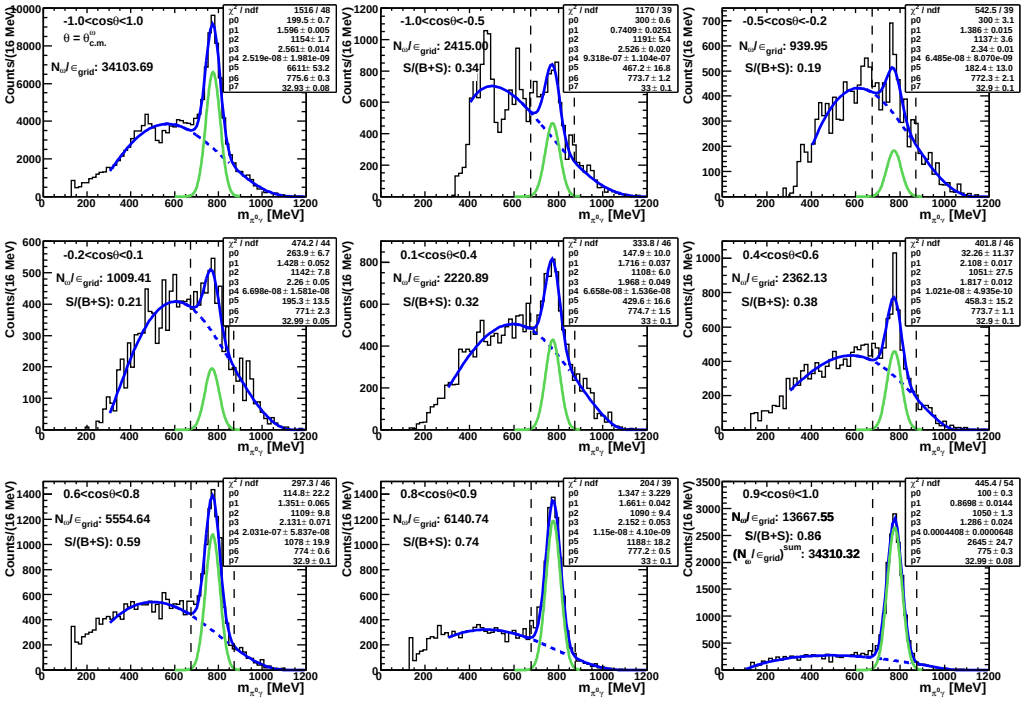

(b) After event-by-event efficiency correction with $\epsilon(T^{\omega}_{lab.}, \theta^{\omega}_{lab.})$

Figure H.10: Fits to the $\pi^0\gamma$ invariant mass spectra for the $\cos(\theta^{\omega}_{c.m.})$ angular bins with incident beam energy E_γ = 1708-1808 MeV.

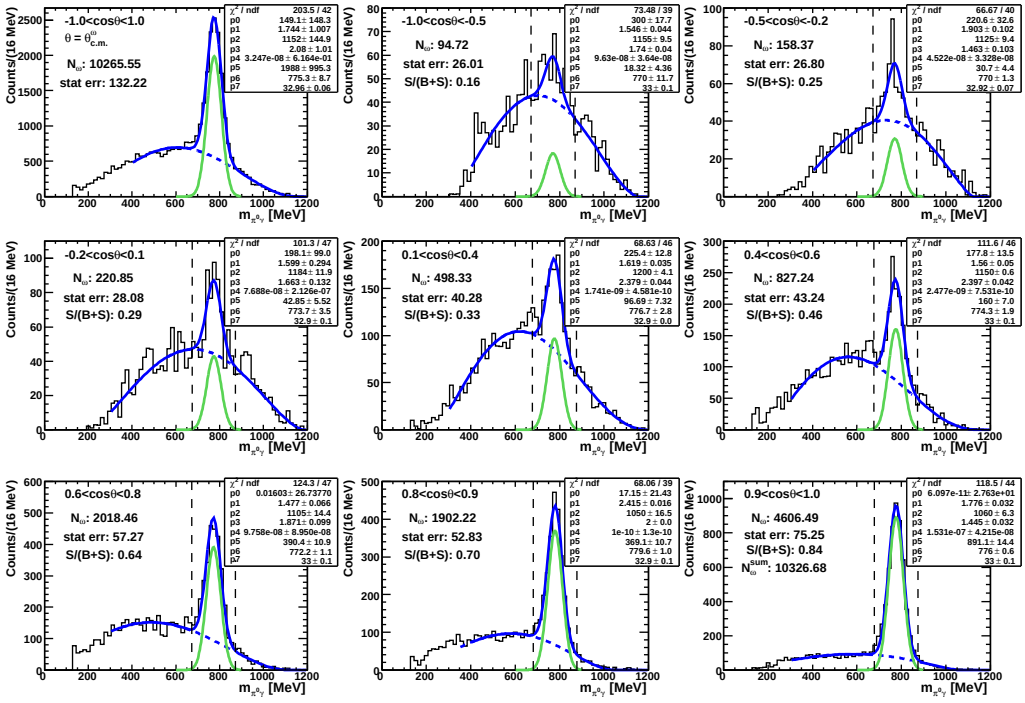

(a) Before efficiency correction

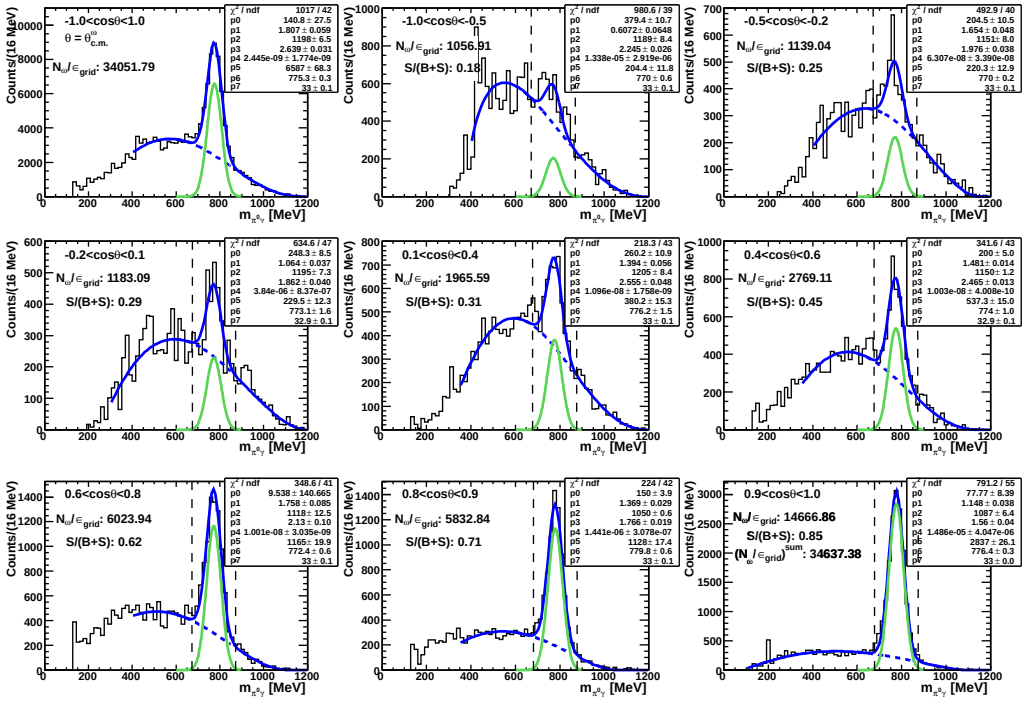

(b) After event-by-event efficiency correction with $\epsilon(T^{\omega}_{lab.}, \theta^{\omega}_{lab.})$

Figure H.11: Fits to the $\pi^0\gamma$ invariant mass spectra for the $\cos(\theta^{\omega}_{c.m.})$ angular bins with incident beam energy E_γ = 1808-1908 MeV.

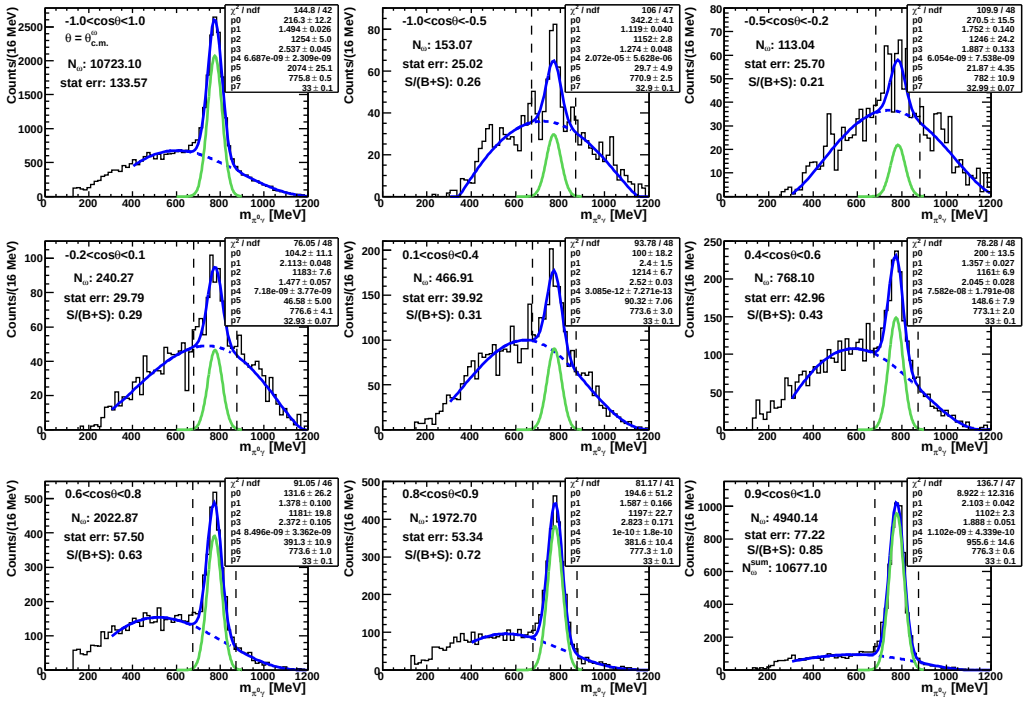

(a) Before efficiency correction

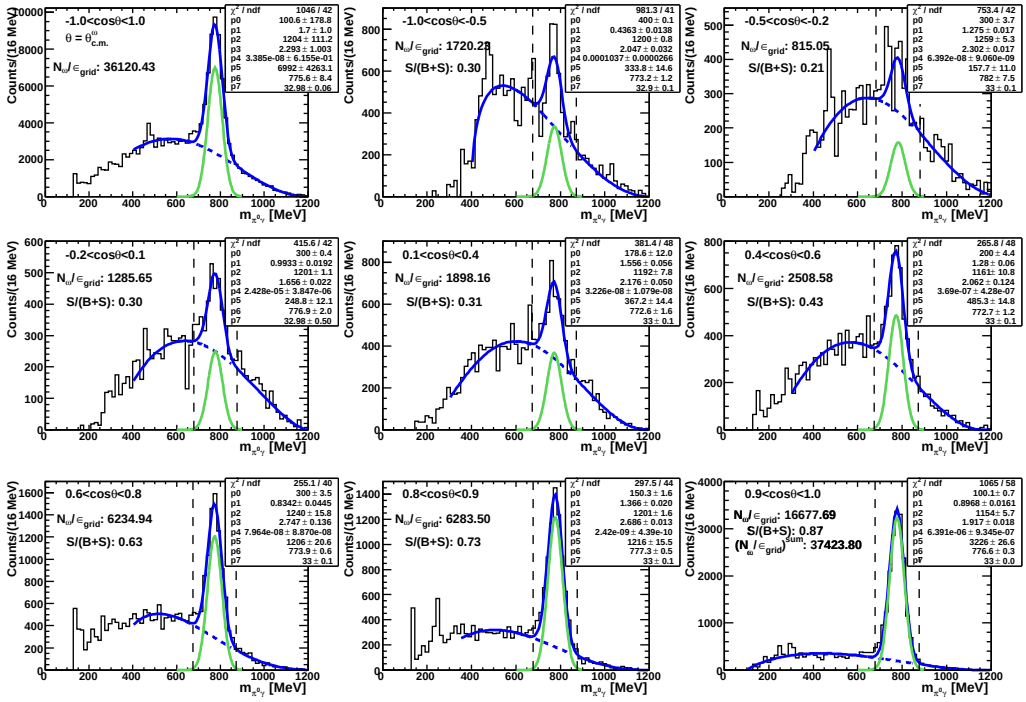

(b) After event-by-event efficiency correction with $\epsilon(T^{\omega}_{lab.}, \theta^{\omega}_{lab.})$

Figure H.12: Fits to the $\pi^0\gamma$ invariant mass spectra for the $\cos(\theta^{\omega}_{c.m.})$ angular bins with incident beam energy E_γ = 1908-2008 MeV.

I. Differential Cross-sections off LH_2

Here, the differential cross-sections for ω mesons produced free proton and the inclusive differential cross-section off the LH_2 target are listed in tables.

I.1. Exclusive differential cross-sections off the free proton

$\cos(\theta^{\omega}_{c.m.})$	$d\sigma/d\cos(\theta^{\omega}_{c.m.})$ $[\mu b]$	$\lvert t-t_{min}\rvert$ $[GeV^2]$	$d\sigma/dt$ $[\mu b/GeV^2]$
-1.0$\leq \cos\theta <$-0.5	1.22224±0.177379	0.219372-0.292496	8.35732±1.21287
-0.5$\leq \cos\theta <$-0.2	1.43664±0.190483	0.175497-0.219372	9.82332±1.30247
-0.2$\leq \cos\theta <$0.1	2.45031±0.184312	0.131623-0.175497	16.7545±1.26027
0.1$\leq \cos\theta <$0.4	2.36636±0.179069	0.0877487-0.131623	16.1805±1.22442
0.4$\leq \cos\theta <$0.6	3.60084±0.250816	0.0584991-0.0877487	24.6215±1.71501
0.6$\leq \cos\theta <$0.8	4.15574±0.280757	0.0292496-0.0584991	28.4157±1.91973
0.8$\leq \cos\theta <$0.9	3.8769±0.387554	0.0146248-0.0292496	26.5091±2.64998
0.9$\leq \cos\theta \leq$1.0	5.26278±0.582006	0-0.0146248	35.9854±3.97959

Table I.1: The differential cross-section off the free proton for incident beam energy E_γ =1125-1150 MeV.

$\cos(\theta^{\omega}_{c.m.})$	$d\sigma/d\cos(\theta^{\omega}_{c.m.})$ $[\mu b]$	$\lvert t-t_{min}\rvert$ $[GeV^2]$	$d\sigma/dt$ $[\mu b/GeV^2]$
-1.0$\leq \cos\theta <$-0.5	2.17355±0.171615	0.297011-0.396014	10.9771±0.866711
-0.5$\leq \cos\theta <$-0.2	2.25605±0.207472	0.237609-0.297011	11.3938±1.0478
-0.2$\leq \cos\theta <$0.1	1.72425±0.180338	0.178207-0.237609	8.70801±0.910765
0.1$\leq \cos\theta <$0.4	3.6296±0.203831	0.118804-0.178207	18.3306±1.02941
0.4$\leq \cos\theta <$0.6	4.99562±0.271914	0.0792029-0.118804	25.2295±1.37325
0.6$\leq \cos\theta <$0.8	5.52346±0.27959	0.0396014-0.0792029	27.8952±1.41202
0.8$\leq \cos\theta <$0.9	5.02726±0.374174	0.0198007-0.0396014	25.3893±1.8897
0.9$\leq \cos\theta \leq$1.0	4.27463±0.427806	0-0.0198007	21.5883±2.16056

Table I.2: The differential cross-section off the free proton for incident beam energy E_γ =1150-1175 MeV.

$\cos(\theta^{\omega}_{c.m.})$	$d\sigma/d\cos(\theta^{\omega}_{c.m.})$ $[\mu b]$	$\lvert t-t_{min}\rvert$ $[GeV^2]$	$d\sigma/dt$ $[\mu b/GeV^2]$
-1.0$\leq \cos\theta <$-0.5	2.93293±0.215221	0.359213-0.478951	12.2473±0.898718
-0.5$\leq \cos\theta <$-0.2	3.28435±0.261512	0.287371-0.359213	13.7148±1.09202
-0.2$\leq \cos\theta <$0.1	2.78728±0.225118	0.215528-0.287371	11.6391±0.940046
0.1$\leq \cos\theta <$0.4	4.55579±0.241922	0.143685-0.215528	19.024±1.01022
0.4$\leq \cos\theta <$0.6	5.68846±0.313456	0.0957903-0.143685	23.7538±1.30893
0.6$\leq \cos\theta <$0.8	6.32305±0.323128	0.0478951-0.0957903	26.4037±1.34931
0.8$\leq \cos\theta <$0.9	6.09628±0.495257	0.0239476-0.0478951	25.4568±2.06809
0.9$\leq \cos\theta \leq$1.0	5.56222±0.491971	0-0.0239476	23.2267±2.05437

Table I.3: The differential cross-section off the free proton for incident beam energy E_γ =1175-1200 MeV.

$\cos(\theta^{\omega}_{c.m.})$	$d\sigma/d\cos(\theta^{\omega}_{c.m.})$ $[\mu b]$	$\lvert t-t_{min}\rvert$ $[GeV^2]$	$d\sigma/dt$ $[\mu b/GeV^2]$
-1.0$\leq \cos\theta <$-0.5	3.34118±0.170618	0.445743-0.594324	11.2436±0.574158
-0.5$\leq \cos\theta <$-0.2	2.97323±0.162402	0.356595-0.445743	10.0054±0.54651
-0.2$\leq \cos\theta <$0.1	3.59274±0.168507	0.267446-0.356595	12.0902±0.567054
0.1$\leq \cos\theta <$0.4	5.12846±0.16763	0.178297-0.267446	17.2581±0.564103
0.4$\leq \cos\theta <$0.6	5.18672±0.195929	0.118865-0.178297	17.4542±0.659333
0.6$\leq \cos\theta <$0.8	6.84631±0.222314	0.0594324-0.118865	23.039±0.748123
0.8$\leq \cos\theta <$0.9	8.12007±0.34459	0.0297162-0.0594324	27.3254±1.1596
0.9$\leq \cos\theta \leq$1.0	7.41862±0.333249	0-0.0297162	24.9649±1.12144

Table I.4: The differential cross-section off the free proton for incident beam energy E_γ =1200-1250 MeV.

$\cos(\theta^{\omega}_{c.m.})$	$d\sigma/d\cos(\theta^{\omega}_{c.m.})$ $[\mu b]$	$\lvert t-t_{min}\rvert$ $[GeV^2]$	$d\sigma/dt$ $[\mu b/GeV^2]$
-1.0$\leq \cos\theta <$-0.5	3.65666±0.184224	0.549287-0.732382	9.98566±0.503081
-0.5$\leq \cos\theta <$-0.2	3.67854±0.192775	0.439429-0.549287	10.0454±0.526433
-0.2$\leq \cos\theta <$0.1	3.9929±0.171085	0.329572-0.439429	10.9039±0.467201
0.1$\leq \cos\theta <$0.4	4.43645±0.170767	0.219715-0.329572	12.1151±0.466333
0.4$\leq \cos\theta <$0.6	5.93815±0.221202	0.146476-0.219715	16.216±0.604061
0.6$\leq \cos\theta <$0.8	7.18472±0.224467	0.0732382-0.146476	19.6201±0.612978
0.8$\leq \cos\theta <$0.9	8.66115±0.351721	0.0366191-0.0732382	23.652±0.960484
0.9$\leq \cos\theta \leq$1.0	10.5576±0.372063	0-0.0366191	28.8308±1.01603

Table I.5: The differential cross-section off the free proton for incident beam energy E_γ =1250-1300 MeV.

$\cos(\theta^{\omega}_{c.m.})$	$d\sigma/d\cos(\theta^{\omega}_{c.m.})$ $[\mu b]$	$\lvert t-t_{min}\rvert$ $[GeV^2]$	$d\sigma/dt$ $[\mu b/GeV^2]$
-1.0$\leq \cos\theta <$-0.5	3.72716±0.212776	0.645502-0.860669	8.66108±0.494443
-0.5$\leq \cos\theta <$-0.2	2.88006±0.204645	0.516401-0.645502	6.69261±0.475549
-0.2$\leq \cos\theta <$0.1	3.02779±0.177687	0.387301-0.516401	7.0359±0.412905
0.1$\leq \cos\theta <$0.4	3.85506±0.198726	0.258201-0.387301	8.95829±0.461794
0.4$\leq \cos\theta <$0.6	5.27889±0.28472	0.172134-0.258201	12.2669±0.661625
0.6$\leq \cos\theta <$0.8	6.44615±0.27131	0.0860669-0.172134	14.9794±0.630463
0.8$\leq \cos\theta <$0.9	8.93115±0.37033	0.0430334-0.0860669	20.754±0.860563
0.9$\leq \cos\theta \leq$1.0	10.865±0.412138	0-0.0430334	25.2478±0.957716

Table I.6: The differential cross-section off the free proton for incident beam energy E_γ =1300-1350 MeV.

$\cos(\theta^{\omega}_{c.m.})$	$d\sigma/d\cos(\theta^{\omega}_{c.m.})$ $[\mu b]$	$\lvert t-t_{min}\rvert$ $[GeV^2]$	$d\sigma/dt$ $[\mu b/GeV^2]$
-1.0$\leq \cos\theta <$-0.5	3.29301±0.228984	0.736561-0.982081	6.70619±0.466324
-0.5$\leq \cos\theta <$-0.2	2.29734±0.22141	0.589249-0.736561	4.67851±0.450899
-0.2$\leq \cos\theta <$0.1	2.6147±0.200806	0.441937-0.589249	5.32481±0.40894
0.1$\leq \cos\theta <$0.4	2.76771±0.215173	0.294624-0.441937	5.63642±0.438198
0.4$\leq \cos\theta <$0.6	4.93713±0.311594	0.196416-0.294624	10.0544±0.634558
0.6$\leq \cos\theta <$0.8	7.12333±0.378961	0.0982081-0.196416	14.5066±0.771751
0.8$\leq \cos\theta <$0.9	11.0595±0.552325	0.0491041-0.0982081	22.5226±1.1248
0.9$\leq \cos\theta \leq$1.0	13.3521±0.542957	0-0.0491041	27.1914±1.10573

Table I.7: The differential cross-section off the free proton for incident beam energy E_γ =1350-1400 MeV.

$\cos(\theta^{\omega}_{c.m.})$	$d\sigma/d\cos(\theta^{\omega}_{c.m.})$ $[\mu b]$	$\lvert t-t_{min}\rvert$ $[GeV^2]$	$d\sigma/dt$ $[\mu b/GeV^2]$
-1.0$\leq \cos\theta <$-0.5	2.24597±0.280435	0.81959-1.09279	4.11054±0.513248
-0.5$\leq \cos\theta <$-0.2	2.29918±0.25762	0.655672-0.81959	4.20792±0.471492
-0.2$\leq \cos\theta <$0.1	1.90688±0.248936	0.491754-0.655672	3.48994±0.455599
0.1$\leq \cos\theta <$0.4	2.6±0.239754	0.327836-0.491754	4.75848±0.438794
0.4$\leq \cos\theta <$0.6	4.4872±0.295317	0.218557-0.327836	8.2124±0.540484
0.6$\leq \cos\theta <$0.8	6.88071±0.36842	0.109279-0.218557	12.593±0.674276
0.8$\leq \cos\theta <$0.9	11.7284±1.31325	0.0546393-0.109279	21.4651±2.40349
0.9$\leq \cos\theta \leq$1.0	16.534±0.981698	0-0.0546393	30.2603±1.79669

Table I.8: The differential cross-section off the free proton for incident beam energy E_γ =1400-1450 MeV.

$\cos(\theta^{\omega}_{c.m.})$	$d\sigma/d\cos(\theta^{\omega}_{c.m.})$ $[\mu b]$	$\lvert t-t_{min}\rvert$ $[GeV^2]$	$d\sigma/dt$ $[\mu b/GeV^2]$
-1.0$\leq \cos\theta <$-0.5	2.022±0.293666	0.901073-1.20143	3.36599±0.48886
-0.5$\leq \cos\theta <$-0.2	2.60083±0.285765	0.720859-0.901073	4.32955±0.475708
-0.2$\leq \cos\theta <$0.1	2.19099±0.237048	0.540644-0.720859	3.6473±0.394609
0.1$\leq \cos\theta <$0.4	2.76976±0.233333	0.360429-0.540644	4.61077±0.388425
0.4$\leq \cos\theta <$0.6	3.47067±0.255256	0.240286-0.360429	5.77756±0.42492
0.6$\leq \cos\theta <$0.8	6.29869±0.329261	0.120143-0.240286	10.4853±0.548115
0.8$\leq \cos\theta <$0.9	9.05689±1.80971	0.0600716-0.120143	15.0768±3.01259
0.9$\leq \cos\theta \leq$1.0	23.2628±2.11148	0-0.0600716	38.7251±3.51494

Table I.9: The differential cross-section off the free proton for incident beam energy E_γ =1450-1500 MeV.

$\cos(\theta^{\omega}_{c.m.})$	$d\sigma/d\cos(\theta^{\omega}_{c.m.})$ $[\mu b]$	$\lvert t-t_{min}\rvert$ $[GeV^2]$	$d\sigma/dt$ $[\mu b/GeV^2]$
-1.0$\leq \cos\theta <$-0.5	2.06949±0.306222	0.980246-1.307	3.16679±0.468589
-0.5$\leq \cos\theta <$-0.2	1.12991±0.274153	0.784197-0.980246	1.72902±0.419516
-0.2$\leq \cos\theta <$0.1	2.21089±0.231619	0.588148-0.784197	3.38316±0.35443
0.1$\leq \cos\theta <$0.4	1.92274±0.194652	0.392099-0.588148	2.94223±0.297862
0.4$\leq \cos\theta <$0.6	3.93674±0.257057	0.261399-0.392099	6.02411±0.393356
0.6$\leq \cos\theta <$0.8	7.08631±0.308022	0.1307-0.261399	10.8437±0.471344
0.8$\leq \cos\theta <$0.9	12.4307±1.46408	0.0653498-0.1307	19.0218±2.24038
0.9$\leq \cos\theta \leq$1.0	-	0-0.0653498	-

Table I.10: The differential cross-section off the free proton for incident beam energy E_γ =1500-1550 MeV.

$\cos(\theta^{\omega}_{c.m.})$	$d\sigma/d\cos(\theta^{\omega}_{c.m.})$ $[\mu b]$	$\lvert t-t_{min}\rvert$ $[GeV^2]$	$d\sigma/dt$ $[\mu b/GeV^2]$
-1.0$\leq \cos\theta <$-0.5	2.59672±0.330995	1.05801-1.41068	3.68153±0.469272
-0.5$\leq \cos\theta <$-0.2	1.22518±0.308715	0.846405-1.05801	1.73701±0.437684
-0.2$\leq \cos\theta <$0.1	1.53892±0.237328	0.634804-0.846405	2.18182±0.336474
0.1$\leq \cos\theta <$0.4	2.27566±0.209201	0.423203-0.634804	3.22634±0.296597
0.4$\leq \cos\theta <$0.6	3.46667±0.256931	0.282135-0.423203	4.91491±0.364267
0.6$\leq \cos\theta <$0.8	8.0626±0.32182	0.141068-0.282135	11.4308±0.456264
0.8$\leq \cos\theta <$0.9	12.187±1.19518	0.0705338-0.141068	17.2782±1.69448
0.9$\leq \cos\theta \leq$1.0	-	0-0.0705338	-

Table I.11: The differential cross-section off the free proton for incident beam energy E_γ =1550-1600 MeV.

$\cos(\theta^{\omega}_{c.m.})$	$d\sigma/d\cos(\theta^{\omega}_{c.m.})$ $[\mu b]$	$\lvert t-t_{min}\rvert$ $[GeV^2]$	$d\sigma/dt$ $[\mu b/GeV^2]$
-1.0$\leq \cos\theta <$-0.5	2.38782±0.333027	1.13489-1.51319	3.15602±0.440167
-0.5$\leq \cos\theta <$-0.2	1.65931±0.283791	0.907912-1.13489	2.19313±0.375091
-0.2$\leq \cos\theta <$0.1	2.34295±0.25483	0.680934-0.907912	3.09671±0.336812
0.1$\leq \cos\theta <$0.4	2.56994±0.207149	0.453956-0.680934	3.39673±0.273792
0.4$\leq \cos\theta <$0.6	2.90695±0.24678	0.302637-0.453956	3.84216±0.326173
0.6$\leq \cos\theta <$0.8	6.86926±0.302231	0.151319-0.302637	9.0792±0.399463
0.8$\leq \cos\theta <$0.9	13.4319±1.18514	0.0756593-0.151319	17.7531±1.56642
0.9$\leq \cos\theta \leq$1.0	-	0-0.0756593	-

Table I.12: The differential cross-section off the free proton for incident beam energy E_γ =1600-1650 MeV.

$\cos(\theta^{\omega}_{c.m.})$	$d\sigma/d\cos(\theta^{\omega}_{c.m.})$ $[\mu b]$	$\lvert t-t_{min}\rvert$ $[GeV^2]$	$d\sigma/dt$ $[\mu b/GeV^2]$
-1.0$\leq \cos\theta <$-0.5	1.68287±0.326259	1.21004-1.61339	2.08613±0.40444
-0.5$\leq \cos\theta <$-0.2	1.54653±0.312451	0.968033-1.21004	1.91712±0.387323
-0.2$\leq \cos\theta <$0.1	1.86108±0.241366	0.726024-0.968033	2.30705±0.299204
0.1$\leq \cos\theta <$0.4	1.90275±0.184656	0.484016-0.726024	2.3587±0.228905
0.4$\leq \cos\theta <$0.6	3.33417±0.252353	0.322678-0.484016	4.13313±0.312824
0.6$\leq \cos\theta <$0.8	7.26153±0.31543	0.161339-0.322678	9.00159±0.391016
0.8$\leq \cos\theta <$0.9	12.3071±1.07326	0.0806694-0.161339	15.2562±1.33044
0.9$\leq \cos\theta \leq$1.0	-	0-0.0806694	-

Table I.13: The differential cross-section off the free proton for incident beam energy E_γ =1650-1700 MeV.

$\cos(\theta^{\omega}_{c.m.})$	$d\sigma/d\cos(\theta^{\omega}_{c.m.})$ $[\mu b]$	$\lvert t-t_{min}\rvert$ $[GeV^2]$	$d\sigma/dt$ $[\mu b/GeV^2]$
-1.0$\leq \cos\theta <$-0.5	1.16547±0.229069	1.32034-1.76045	1.32406±0.260238
-0.5$\leq \cos\theta <$-0.2	1.48502±0.222135	1.05627-1.32034	1.68709±0.252361
-0.2$\leq \cos\theta <$0.1	1.88757±0.20118	0.792205-1.05627	2.14441±0.228555
0.1$\leq \cos\theta <$0.4	1.86012±0.138615	0.528136-0.792205	2.11323±0.157476
0.4$\leq \cos\theta <$0.6	2.91505±0.174708	0.352091-0.528136	3.3117±0.198481
0.6$\leq \cos\theta <$0.8	7.64122±0.226531	0.176045-0.352091	8.68096±0.257355
0.8$\leq \cos\theta <$0.9	13.77±0.668578	0.0880227-0.176045	15.6437±0.759552
0.9$\leq \cos\theta \leq$1.0	-	0-0.0880227	-

Table I.14: The differential cross-section off the free proton for incident beam energy E_γ =1700-1800 MeV.

$\cos(\theta^{\omega}_{c.m.})$	$d\sigma/d\cos(\theta^{\omega}_{c.m.})$ $[\mu b]$	$\lvert t-t_{min}\rvert$ $[GeV^2]$	$d\sigma/dt$ $[\mu b/GeV^2]$
-1.0$\leq \cos\theta <$-0.5	1.46215±0.228272	1.46786-1.95714	1.49417±0.233271
-0.5$\leq \cos\theta <$-0.2	1.72686±0.216936	1.17429-1.46786	1.76467±0.221686
-0.2$\leq \cos\theta <$0.1	1.79722±0.196292	0.880714-1.17429	1.83658±0.20059
0.1$\leq \cos\theta <$0.4	1.83963±0.135827	0.587143-0.880714	1.87991±0.138801
0.4$\leq \cos\theta <$0.6	3.2496±0.168858	0.391429-0.587143	3.32076±0.172556
0.6$\leq \cos\theta <$0.8	8.03282±0.223992	0.195714-0.391429	8.20872±0.228897
0.8$\leq \cos\theta <$0.9	15.2603±0.56923	0.0978571-0.195714	15.5945±0.581695
0.9$\leq \cos\theta \leq$1.0	-	0-0.0978571	-

Table I.15: The differential cross-section off the free proton for incident beam energy E_γ =1800-1900 MeV.

$\cos(\theta^{\omega}_{c.m.})$	$d\sigma/d\cos(\theta^{\omega}_{c.m.})$ $[\mu b]$	$\lvert t-t_{min}\rvert$ $[GeV^2]$	$d\sigma/dt$ $[\mu b/GeV^2]$
-1.0$\leq \cos\theta <$-0.5	1.50241±0.233698	1.61538-2.15384	1.3951±0.217006
-0.5$\leq \cos\theta <$-0.2	1.31859±0.204122	1.29231-1.61538	1.22441±0.189542
-0.2$\leq \cos\theta <$0.1	1.59611±0.194135	0.96923-1.29231	1.4821±0.180268
0.1$\leq \cos\theta <$0.4	1.85439±0.137412	0.646153-0.96923	1.72194±0.127597
0.4$\leq \cos\theta <$0.6	2.90798±0.169039	0.430769-0.646153	2.70027±0.156965
0.6$\leq \cos\theta <$0.8	7.37941±0.230486	0.215384-0.430769	6.85232±0.214023
0.8$\leq \cos\theta <$0.9	15.7562±0.58192	0.107692-0.215384	14.6308±0.540355
0.9$\leq \cos\theta \leq$1.0	-	0-0.107692	-

Table I.16: The differential cross-section off the free proton for incident beam energy E_γ =1900-2000 MeV.

I.2. Inclusive differential cross-sections off LH_2

$\cos(\theta^{\omega}_{c.m.})$	$d\sigma/d\cos(\theta^{\omega}_{c.m.})$ $[\mu b]$	$\lvert t-t_{min}\rvert$ $[GeV^2]$	$d\sigma/dt$ $[\mu b/GeV^2]$
-1.0$\leq \cos\theta <$-0.5	1.65465±0.244867	0.219372-0.292496	11.1522±2.25024
-0.5$\leq \cos\theta <$-0.2	1.54382±0.265238	0.175497-0.219372	11.7852±2.44929
-0.2$\leq \cos\theta <$0.1	1.62612±0.240942	0.131623-0.175497	11.753±2.58903
0.1$\leq \cos\theta <$0.4	1.85938±0.237268	0.0877487-0.131623	12.7113±2.3174
0.4$\leq \cos\theta <$0.6	2.39253±0.387713	0.0584991-0.0877487	14.7897±3.66152
0.6$\leq \cos\theta <$0.8	2.98595±0.405049	0.0292496-0.0584991	21.1952±3.8491
0.8$\leq \cos\theta <$0.9	3.79839±0.669189	0.0146248-0.0292496	23.0677±5.50447
0.9$\leq \cos\theta \leq$1.0	3.47689±0.670162	0-0.0146248	23.4867±5.53265

Table I.17: The inclusive differential cross-section off the free proton for incident beam energy E_γ =1125-1150 MeV.

$\cos(\theta^{\omega}_{c.m.})$	$d\sigma/d\cos(\theta^{\omega}_{c.m.})$ $[\mu b]$	$\lvert t-t_{min}\rvert$ $[GeV^2]$	$d\sigma/dt$ $[\mu b/GeV^2]$
-1.0$\leq \cos\theta <$-0.5	1.97185±0.253615	0.297011-0.396014	9.95842±1.48403
-0.5$\leq \cos\theta <$-0.2	2.01287±0.220366	0.237609-0.297011	10.1656±2.07082
-0.2$\leq \cos\theta <$0.1	1.8481±0.222683	0.178207-0.237609	9.3335±1.56704
0.1$\leq \cos\theta <$0.4	2.50015±0.254002	0.118804-0.178207	11.8663±1.52203
0.4$\leq \cos\theta <$0.6	3.82166±0.367064	0.0792029-0.118804	19.3007±2.55943
0.6$\leq \cos\theta <$0.8	4.07414±0.424915	0.0396014-0.0792029	20.5757±2.40134
0.8$\leq \cos\theta <$0.9	3.90151±0.568335	0.0198007-0.0396014	19.7039±3.56694
0.9$\leq \cos\theta \leq$1.0	4.73852±0.575271	0-0.0198007	22.6452±4.36515

Table I.18: The inclusive differential cross-section off the free proton for incident beam energy E_γ =1150-1175 MeV.

$\cos(\theta^{\omega}_{c.m.})$	$d\sigma/d\cos(\theta^{\omega}_{c.m.})$ $[\mu b]$	$\lvert t-t_{min}\rvert$ $[GeV^2]$	$d\sigma/dt$ $[\mu b/GeV^2]$
-1.0$\leq \cos\theta <$-0.5	2.81417±0.299445	0.359213-0.478951	11.7514±1.73086
-0.5$\leq \cos\theta <$-0.2	3.50427±0.324969	0.287371-0.359213	14.6331±1.69067
-0.2$\leq \cos\theta <$0.1	2.31157±0.312763	0.215528-0.287371	9.65263±1.53078
0.1$\leq \cos\theta <$0.4	3.57544±0.297295	0.143685-0.215528	14.9303±1.48556
0.4$\leq \cos\theta <$0.6	4.47285±0.41971	0.0957903-0.143685	18.6777±2.3062
0.6$\leq \cos\theta <$0.8	5.97775±0.473341	0.0478951-0.0957903	24.9618±2.07447
0.8$\leq \cos\theta <$0.9	5.26409±0.718593	0.0239476-0.0478951	21.9817±3.387
0.9$\leq \cos\theta \leq$1.0	5.55466±0.808444	0-0.0239476	23.1951±3.387

Table I.19: The inclusive differential cross-section off the free proton for incident beam energy E_γ =1175-1200 MeV.

$\cos(\theta^{\omega}_{c.m.})$	$d\sigma/d\cos(\theta^{\omega}_{c.m.})$ $[\mu b]$	$\lvert t-t_{min}\rvert$ $[GeV^2]$	$d\sigma/dt$ $[\mu b/GeV^2]$
-1.0$\leq \cos\theta <$-0.5	3.35023±0.235981	0.445743-0.594324	11.8581±0.944708
-0.5$\leq \cos\theta <$-0.2	3.07233±0.21392	0.356595-0.445743	10.3389±0.774673
-0.2$\leq \cos\theta <$0.1	3.4897±0.19877	0.267446-0.356595	11.7434±0.84487
0.1$\leq \cos\theta <$0.4	4.28379±0.210792	0.178297-0.267446	14.4156±0.784479
0.4$\leq \cos\theta <$0.6	5.04952±0.304566	0.118865-0.178297	19.0545±1.19351
0.6$\leq \cos\theta <$0.8	6.14979±0.300864	0.0594324-0.118865	20.6951±1.16718
0.8$\leq \cos\theta <$0.9	7.48549±0.490853	0.0297162-0.0594324	25.1899±1.7666
0.9$\leq \cos\theta \leq$1.0	6.70989±0.458986	0-0.0297162	22.5799±1.7794

Table I.20: The inclusive differential cross-section off the free proton for incident beam energy E_γ =1200-1250 MeV.

$\cos(\theta^{\omega}_{c.m.})$	$d\sigma/d\cos(\theta^{\omega}_{c.m.})$ $[\mu b]$	$\lvert t-t_{min}\rvert$ $[GeV^2]$	$d\sigma/dt$ $[\mu b/GeV^2]$
-1.0$\leq \cos\theta <$-0.5	3.29345±0.270659	0.549287-0.732382	8.9938±0.728648
-0.5$\leq \cos\theta <$-0.2	2.95237±0.244723	0.439429-0.549287	8.06237±0.715864
-0.2$\leq \cos\theta <$0.1	3.31745±0.225999	0.329572-0.439429	9.05934±0.629635
0.1$\leq \cos\theta <$0.4	4.00858±0.221791	0.219715-0.329572	10.9467±0.613483
0.4$\leq \cos\theta <$0.6	5.3927±0.292269	0.146476-0.219715	14.7264±0.822062
0.6$\leq \cos\theta <$0.8	6.90463±0.326133	0.0732382-0.146476	18.8553±0.872741
0.8$\leq \cos\theta <$0.9	8.48366±0.507836	0.0366191-0.0732382	23.1673±1.41125
0.9$\leq \cos\theta \leq$1.0	10.7792±0.567656	0-0.0366191	29.436±1.5665

Table I.21: The inclusive differential cross-section off the free proton for incident beam energy E_γ =1250-1300 MeV.

$\cos(\theta^{\omega}_{c.m.})$	$d\sigma/d\cos(\theta^{\omega}_{c.m.})$ $[\mu b]$	$\lvert t-t_{min}\rvert$ $[GeV^2]$	$d\sigma/dt$ $[\mu b/GeV^2]$
-1.0$\leq \cos\theta <$-0.5	3.28399±0.301693	0.645502-0.860669	7.63125±0.74645
-0.5$\leq \cos\theta <$-0.2	2.1515±0.231202	0.516401-0.645502	4.99961±0.606812
-0.2$\leq \cos\theta <$0.1	2.61456±0.208568	0.387301-0.516401	6.07564±0.562183
0.1$\leq \cos\theta <$0.4	3.71601±0.210057	0.258201-0.387301	8.63515±0.565428
0.4$\leq \cos\theta <$0.6	5.40402±0.293796	0.172134-0.258201	12.5578±0.718529
0.6$\leq \cos\theta <$0.8	6.10832±0.303975	0.0860669-0.172134	14.1944±0.702686
0.8$\leq \cos\theta <$0.9	9.60075±0.497375	0.0430334-0.0860669	22.31±1.19444
0.9$\leq \cos\theta \leq$1.0	13.0227±0.550056	0-0.0430334	30.2619±1.30038

Table I.22: The inclusive differential cross-section off the free proton for incident beam energy E_γ =1300-1350 MeV.

$\cos(\theta^{\omega}_{c.m.})$	$d\sigma/d\cos(\theta^{\omega}_{c.m.})$ $[\mu b]$	$\lvert t-t_{min}\rvert$ $[GeV^2]$	$d\sigma/dt$ $[\mu b/GeV^2]$
-1.0$\leq \cos\theta <$-0.5	2.65773±0.319342	0.736561-0.982081	5.41244±0.698055
-0.5$\leq \cos\theta <$-0.2	2.02107±0.242933	0.589249-0.736561	4.11589±0.534614
-0.2$\leq \cos\theta <$0.1	2.30543±0.210726	0.441937-0.589249	4.69498±0.507705
0.1$\leq \cos\theta <$0.4	2.61465±0.217903	0.294624-0.441937	5.32471±0.465279
0.4$\leq \cos\theta <$0.6	4.51531±0.289427	0.196416-0.294624	9.1954±0.676547
0.6$\leq \cos\theta <$0.8	6.21536±0.321418	0.0982081-0.196416	12.6575±0.684377
0.8$\leq \cos\theta <$0.9	11.664±0.564587	0.0491041-0.0982081	23.7536±1.1626
0.9$\leq \cos\theta \leq$1.0	16.5075±0.606092	0-0.0491041	33.6174±1.24624

Table I.23: The inclusive differential cross-section off the free proton for incident beam energy E_γ =1350-1400 MeV.

$\cos(\theta^{\omega}_{c.m.})$	$d\sigma/d\cos(\theta^{\omega}_{c.m.})$ $[\mu b]$	$\lvert t-t_{min}\rvert$ $[GeV^2]$	$d\sigma/dt$ $[\mu b/GeV^2]$
-1.0$\leq \cos\theta <$-0.5	1.77715±0.302889	0.81959-1.09279	3.25252±0.67422
-0.5$\leq \cos\theta <$-0.2	1.57402±0.279209	0.655672-0.81959	2.88075±0.542065
-0.2$\leq \cos\theta <$0.1	2.03539±0.241776	0.491754-0.655672	3.72513±0.539278
0.1$\leq \cos\theta <$0.4	2.52916±0.226267	0.327836-0.491754	4.62882±0.496259
0.4$\leq \cos\theta <$0.6	4.8627±0.316301	0.218557-0.327836	8.89963±0.657942
0.6$\leq \cos\theta <$0.8	7.37107±0.36078	0.109279-0.218557	13.4904±0.720865
0.8$\leq \cos\theta <$0.9	10.7645±0.588305	0.0546393-0.109279	19.701±1.11718
0.9$\leq \cos\theta \leq$1.0	16.3154±0.633431	0-0.0546393	29.8602±1.1648

Table I.24: The inclusive differential cross-section off the free proton for incident beam energy E_γ =1400-1450 MeV.

$\cos(\theta^{\omega}_{c.m.})$	$d\sigma/d\cos(\theta^{\omega}_{c.m.})$ $[\mu b]$	$\lvert t-t_{min}\rvert$ $[GeV^2]$	$d\sigma/dt$ $[\mu b/GeV^2]$
-1.0$\leq \cos\theta <$-0.5	1.64556±0.362735	0.901073-1.20143	2.73934±0.651208
-0.5$\leq \cos\theta <$-0.2	2.15318±0.274174	0.720859-0.901073	3.58435±0.523299
-0.2$\leq \cos\theta <$0.1	1.87378±0.247069	0.540644-0.720859	3.11925±0.448867
0.1$\leq \cos\theta <$0.4	2.76318±0.236272	0.360429-0.540644	4.59982±0.43527
0.4$\leq \cos\theta <$0.6	3.33969±0.29482	0.240286-0.360429	5.55952±0.514416
0.6$\leq \cos\theta <$0.8	6.22759±0.332903	0.120143-0.240286	10.367±0.607934
0.8$\leq \cos\theta <$0.9	11.0407±0.571527	0.0600716-0.120143	18.3792±1.04597
0.9$\leq \cos\theta \leq$1.0	20.8718±0.689093	0-0.0600716	34.745±1.18389

Table I.25: The inclusive differential cross-section off the free proton for incident beam energy E_γ =1450-1500 MeV.

$\cos(\theta^{\omega}_{c.m.})$	$d\sigma/d\cos(\theta^{\omega}_{c.m.})$ $[\mu b]$	$\lvert t-t_{min}\rvert$ $[GeV^2]$	$d\sigma/dt$ $[\mu b/GeV^2]$
-1.0$\leq \cos\theta <$-0.5	0.973719±0.301578	0.980246-1.307	1.49001±0.761724
-0.5$\leq \cos\theta <$-0.2	1.1845±0.278461	0.784197-0.980246	1.81255±0.522073
-0.2$\leq \cos\theta <$0.1	1.88218±0.225405	0.588148-0.784197	2.88016±0.399945
0.1$\leq \cos\theta <$0.4	2.06372±0.206824	0.392099-0.588148	3.15796±0.360655
0.4$\leq \cos\theta <$0.6	3.22716±0.265225	0.261399-0.392099	4.93829±0.471574
0.6$\leq \cos\theta <$0.8	7.14619±0.355311	0.1307-0.261399	10.9353±0.544103
0.8$\leq \cos\theta <$0.9	13.1365±0.603796	0.0653498-0.1307	20.1019±1.00828
0.9$\leq \cos\theta \leq$1.0	21.6879±0.710695	0-0.0653498	33.1874±1.10485

Table I.26: The inclusive differential cross-section off the free proton for incident beam energy E_γ =1500-1550 MeV.

$\cos(\theta^{\omega}_{c.m.})$	$d\sigma/d\cos(\theta^{\omega}_{c.m.})$ $[\mu b]$	$\lvert t-t_{min}\rvert$ $[GeV^2]$	$d\sigma/dt$ $[\mu b/GeV^2]$
-1.0$\leq \cos\theta <$-0.5	1.84975±0.363592	1.05801-1.41068	1.91691±0.499376
-0.5$\leq \cos\theta <$-0.2	0.863887±0.290019	0.846405-1.05801	1.45819±0.541928
-0.2$\leq \cos\theta <$0.1	1.32963±0.242014	0.634804-0.846405	2.36689±0.426271
0.1$\leq \cos\theta <$0.4	2.095±0.206242	0.423203-0.634804	2.99579±0.360168
0.4$\leq \cos\theta <$0.6	3.35992±0.272943	0.282135-0.423203	4.66903±0.398413
0.6$\leq \cos\theta <$0.8	7.81787±0.359051	0.141068-0.282135	10.6697±0.489112
0.8$\leq \cos\theta <$0.9	13.1954±0.606902	0.0705338-0.141068	18.8336±0.899398
0.9$\leq \cos\theta \leq$1.0	24.2359±0.73742	0-0.0705338	32.2639±1.02483

Table I.27: The inclusive differential cross-section off the free proton for incident beam energy E_γ =1550-1600 MeV.

$\cos(\theta^{\omega}_{c.m.})$	$d\sigma/d\cos(\theta^{\omega}_{c.m.})$ $[\mu b]$	$\lvert t-t_{min}\rvert$ $[GeV^2]$	$d\sigma/dt$ $[\mu b/GeV^2]$
-1.0$\leq \cos\theta <$-0.5	2.01395±0.420014	1.13489-1.51319	2.66186±0.608383
-0.5$\leq \cos\theta <$-0.2	1.27919±0.252545	0.907912-1.13489	1.42616±0.494231
-0.2$\leq \cos\theta <$0.1	1.99003±0.244883	0.680934-0.907912	2.55571±0.340909
0.1$\leq \cos\theta <$0.4	2.32089±0.203608	0.453956-0.680934	2.84239±0.29946
0.4$\leq \cos\theta <$0.6	3.34425±0.293116	0.302637-0.453956	4.62377±0.416282
0.6$\leq \cos\theta <$0.8	7.09207±0.335258	0.151319-0.302637	9.3737±0.462618
0.8$\leq \cos\theta <$0.9	14.0042±0.644528	0.0756593-0.151319	18.5096±0.835716
0.9$\leq \cos\theta \leq$1.0	25.7016±0.763255	0-0.0756593	33.9702±1.0589

Table I.28: The inclusive differential cross-section off the free proton for incident beam energy E_γ =1600-1650 MeV.

$\cos(\theta^{\omega}_{c.m.})$	$d\sigma/d\cos(\theta^{\omega}_{c.m.})$ $[\mu b]$	$\lvert t-t_{min}\rvert$ $[GeV^2]$	$d\sigma/dt$ $[\mu b/GeV^2]$
-1.0$\leq \cos\theta <$-0.5	1.34398±0.35379	1.21004-1.61339	1.66603±0.679921
-0.5$\leq \cos\theta <$-0.2	1.10645±0.28516	0.968033-1.21004	1.37158±0.42419
-0.2$\leq \cos\theta <$0.1	1.59889±0.21849	0.726024-0.968033	1.98204±0.320742
0.1$\leq \cos\theta <$0.4	2.08335±0.204998	0.484016-0.726024	2.58258±0.250913
0.4$\leq \cos\theta <$0.6	3.55511±0.2903	0.322678-0.484016	4.40701±0.360583
0.6$\leq \cos\theta <$0.8	6.49954±0.330686	0.161339-0.322678	8.05701±0.436014
0.8$\leq \cos\theta <$0.9	13.5057±0.603063	0.0806694-0.161339	16.742±0.790403
0.9$\leq \cos\theta \leq$1.0	26.6705±0.785844	0-0.0806694	33.0616±0.999361

Table I.29: The inclusive differential cross-section off the free proton for incident beam energy E_γ =1650-1700 MeV.

$\cos(\theta^{\omega}_{c.m.})$	$d\sigma/d\cos(\theta^{\omega}_{c.m.})$ $[\mu b]$	$\lvert t-t_{min}\rvert$ $[GeV^2]$	$d\sigma/dt$ $[\mu b/GeV^2]$
-1.0$\leq \cos\theta <$-0.5	1.99755±0.297308	1.32034-1.76045	2.26935±0.351175
-0.5$\leq \cos\theta <$-0.2	1.2982±0.21277	1.05627-1.32034	1.47485±0.263359
-0.2$\leq \cos\theta <$0.1	1.3975±0.162968	0.792205-1.05627	1.58765±0.231919
0.1$\leq \cos\theta <$0.4	1.78705±0.138795	0.528136-0.792205	2.03021±0.181715
0.4$\leq \cos\theta <$0.6	3.24025±0.190804	0.352091-0.528136	3.68115±0.232867
0.6$\leq \cos\theta <$0.8	8.20369±0.254147	0.176045-0.352091	9.31997±0.312793
0.8$\leq \cos\theta <$0.9	14.981±0.473299	0.0880227-0.176045	17.0195±0.566108
0.9$\leq \cos\theta \leq$1.0	30.6064±0.634303	0-0.0880227	34.7709±0.741506

Table I.30: The inclusive differential cross-section off the free proton for incident beam energy E_γ =1700-1800 MeV.

$\cos(\theta^{\omega}_{c.m.})$	$d\sigma/d\cos(\theta^{\omega}_{c.m.})$ $[\mu b]$	$\lvert t-t_{min}\rvert$ $[GeV^2]$	$d\sigma/dt$ $[\mu b/GeV^2]$
-1.0$\leq \cos\theta <$-0.5	1.13956±0.2725	1.46786-1.95714	1.16451±0.330295
-0.5$\leq \cos\theta <$-0.2	1.06539±0.190081	1.17429-1.46786	1.08872±0.227456
-0.2$\leq \cos\theta <$0.1	1.6419±0.186453	0.880714-1.17429	1.67786±0.19157
0.1$\leq \cos\theta <$0.4	1.84433±0.140795	0.587143-0.880714	1.88471±0.153298
0.4$\leq \cos\theta <$0.6	3.29803±0.185735	0.391429-0.587143	3.37025±0.196185
0.6$\leq \cos\theta <$0.8	7.9936±0.252312	0.195714-0.391429	8.16864±0.279267
0.8$\leq \cos\theta <$0.9	14.6772±0.47905	0.0978571-0.195714	14.9986±0.507277
0.9$\leq \cos\theta \leq$1.0	36.5631±0.696078	0-0.0978571	37.3637±0.727486

Table I.31: The inclusive differential cross-section off the free proton for incident beam energy E_γ =1800-1900 MeV.

$\cos(\theta^{\omega}_{c.m.})$	$d\sigma/d\cos(\theta^{\omega}_{c.m.})$ $[\mu b]$	$\lvert t-t_{min}\rvert$ $[GeV^2]$	$d\sigma/dt$ $[\mu b/GeV^2]$
-1.0$\leq \cos\theta <$-0.5	1.34003±0.311851	1.61538-2.15384	1.24432±0.274297
-0.5$\leq \cos\theta <$-0.2	1.16322±0.194793	1.29231-1.61538	1.08014±0.193286
-0.2$\leq \cos\theta <$0.1	1.2571±0.159563	0.96923-1.29231	1.16731±0.167058
0.1$\leq \cos\theta <$0.4	1.71789±0.140231	0.646153-0.96923	1.59519±0.142421
0.4$\leq \cos\theta <$0.6	2.96482±0.196143	0.430769-0.646153	2.75305±0.198805
0.6$\leq \cos\theta <$0.8	6.9488±0.250789	0.215384-0.430769	6.45247±0.255954
0.8$\leq \cos\theta <$0.9	17.408±0.542007	0.107692-0.215384	16.1646±0.520859
0.9$\leq \cos\theta \leq$1.0	39.1293±0.743975	0-0.107692	36.3344±0.741029

Table I.32: The inclusive differential cross-section off the free proton for incident beam energy E_γ =1900-2000 MeV.

J. Differential Cross-sections off LD_2

Here, the differential cross-sections for ω mesons produced off the bound proton, off the bound neutron and the quasi-free inclusive differential cross-section are listed in tables.

J.1. Exclusive differential cross-sections off the bound proton

$\cos(\theta^{\omega}_{c.m.})$	$d\sigma/d\cos(\theta^{\omega}_{c.m.})$ $[\mu b]$	$\lvert t-t_{min}\rvert$ $[GeV^2]$	$d\sigma/dt$ $[\mu b/GeV^2]$
-1.0$\leq \cos\theta <$-0.5	1.21867±0.155604	0.32902-0.438693	5.55591±0.709398
-0.5$\leq \cos\theta <$-0.2	0.993755±0.152452	0.263216-0.32902	4.53052±0.695028
-0.2$\leq \cos\theta <$0.1	1.53316±0.162755	0.197412-0.263216	6.98967±0.741999
0.1$\leq \cos\theta <$0.4	2.30638±0.159214	0.131608-0.197412	10.5148±0.725856
0.4$\leq \cos\theta <$0.6	2.58548±0.216408	0.0877387-0.131608	11.7872±0.986603
0.6$\leq \cos\theta <$0.8	3.04043±0.216497	0.0438693-0.0877387	13.8613±0.987008
0.8$\leq \cos\theta <$0.9	3.64894±0.329291	0.0219347-0.0438693	16.6355±1.50124
0.9$\leq \cos\theta \leq$1.0	4.7915±0.391389	0-0.0219347	21.8444±1.78434

Table J.1: The differential cross-section off the bound proton for incident beam energy E_γ =1158-1208 MeV.

$\cos(\theta^{\omega}_{c.m.})$	$d\sigma/d\cos(\theta^{\omega}_{c.m.})$ $[\mu b]$	$\lvert t-t_{min}\rvert$ $[GeV^2]$	$d\sigma/dt$ $[\mu b/GeV^2]$
-1.0$\leq \cos\theta <$-0.5	1.8848±0.299047	0.421934-0.562579	6.70057±1.06313
-0.5$\leq \cos\theta <$-0.2	1.24753±0.298005	0.337547-0.421934	4.43504±1.05942
-0.2$\leq \cos\theta <$0.1	1.69536±0.281688	0.253161-0.337547	6.0271±1.00142
0.1$\leq \cos\theta <$0.4	2.59386±0.288839	0.168774-0.253161	9.22132±1.02684
0.4$\leq \cos\theta <$0.6	2.96905±0.354681	0.112516-0.168774	10.5551±1.26091
0.6$\leq \cos\theta <$0.8	4.27138±0.37642	0.0562579-0.112516	15.185±1.33819
0.8$\leq \cos\theta <$0.9	2.99735±0.509266	0.028129-0.0562579	10.6557±1.81047
0.9$\leq \cos\theta \leq$1.0	6.14213±0.61953	0-0.028129	21.8356±2.20246

Table J.2: The differential cross-section off the bound proton for incident beam energy E_γ =1208-1233 MeV.

$\cos(\theta^{\omega}_{c.m.})$	$d\sigma/d\cos(\theta^{\omega}_{c.m.})$ $[\mu b]$	$\lvert t-t_{min}\rvert$ $[GeV^2]$	$d\sigma/dt$ $[\mu b/GeV^2]$
-1.0$\leq \cos\theta <$-0.5	1.72525±0.260149	0.475834-0.634445	5.43861±0.820083
-0.5$\leq \cos\theta <$-0.2	1.19022±0.278988	0.380667-0.475834	3.752±0.879471
-0.2$\leq \cos\theta <$0.1	2.59186±0.257057	0.2855-0.380667	8.17048±0.810336
0.1$\leq \cos\theta <$0.4	2.6455±0.263911	0.190334-0.2855	8.33957±0.831943
0.4$\leq \cos\theta <$0.6	3.39044±0.352342	0.126889-0.190334	10.6879±1.11071
0.6$\leq \cos\theta <$0.8	4.2249±0.359354	0.0634445-0.126889	13.3184±1.13281
0.8$\leq \cos\theta <$0.9	7.04888±0.539255	0.0317223-0.0634445	22.2206±1.69993
0.9$\leq \cos\theta \leq$1.0	7.7401±0.621885	0-0.0317223	24.3996±1.96041

Table J.3: The differential cross-section off the bound proton for incident beam energy E_γ =1233-1258 MeV.

$\cos(\theta^{\omega}_{c.m.})$	$d\sigma/d\cos(\theta^{\omega}_{c.m.})$ $[\mu b]$	$\lvert t-t_{min}\rvert$ $[GeV^2]$	$d\sigma/dt$ $[\mu b/GeV^2]$
-1.0$\leq \cos\theta <$-0.5	1.64144±0.219908	0.553404-0.737871	4.44912±0.596061
-0.5$\leq \cos\theta <$-0.2	1.02825±0.199392	0.442723-0.553404	2.78707±0.540452
-0.2$\leq \cos\theta <$0.1	2.27721±0.187401	0.332042-0.442723	6.17238±0.50795
0.1$\leq \cos\theta <$0.4	2.4001±0.195958	0.221361-0.332042	6.50547±0.531144
0.4$\leq \cos\theta <$0.6	3.41363±0.244916	0.147574-0.221361	9.25264±0.663845
0.6$\leq \cos\theta <$0.8	4.97174±0.274193	0.0737871-0.147574	13.4759±0.7432
0.8$\leq \cos\theta <$0.9	6.29601±0.418602	0.0368936-0.0737871	17.0653±1.13462
0.9$\leq \cos\theta \leq$1.0	7.25111±0.464348	0-0.0368936	19.6541±1.25862

Table J.4: The differential cross-section off the bound proton for incident beam energy E_γ =1258-1308 MeV.

$\cos(\theta^{\omega}_{c.m.})$	$d\sigma/d\cos(\theta^{\omega}_{c.m.})$ $[\mu b]$	$\lvert t-t_{min}\rvert$ $[GeV^2]$	$d\sigma/dt$ $[\mu b/GeV^2]$
-1.0$\leq \cos\theta <$-0.5	2.23602±0.257406	0.647902-0.863869	5.17675±0.595937
-0.5$\leq \cos\theta <$-0.2	1.63552±0.235072	0.518322-0.647902	3.7865±0.54423
-0.2$\leq \cos\theta <$0.1	2.20957±0.218377	0.388741-0.518322	5.11552±0.505579
0.1$\leq \cos\theta <$0.4	2.91808±0.203146	0.259161-0.388741	6.75584±0.470316
0.4$\leq \cos\theta <$0.6	3.99122±0.285828	0.172774-0.259161	9.24033±0.661739
0.6$\leq \cos\theta <$0.8	5.59037±0.340268	0.0863869-0.172774	12.9426±0.787776
0.8$\leq \cos\theta <$0.9	6.42689±0.455711	0.0431935-0.0863869	14.8793±1.05505
0.9$\leq \cos\theta \leq$1.0	9.27908±0.544988	0-0.0431935	21.4826±1.26174

Table J.5: The differential cross-section off the bound proton for incident beam energy E_γ =1308-1358 MeV.

$\cos(\theta^{\omega}_{c.m.})$	$d\sigma/d\cos(\theta^{\omega}_{c.m.})$ $[\mu b]$	$\lvert t-t_{min}\rvert$ $[GeV^2]$	$d\sigma/dt$ $[\mu b/GeV^2]$
-1.0$\leq \cos\theta <$-0.5	1.5272±0.291799	0.737372-0.983163	3.10671±0.593592
-0.5$\leq \cos\theta <$-0.2	1.03701±0.282083	0.589898-0.737372	2.10954±0.573827
-0.2$\leq \cos\theta <$0.1	1.67402±0.224294	0.442423-0.589898	3.40538±0.45627
0.1$\leq \cos\theta <$0.4	2.51635±0.216157	0.294949-0.442423	5.11889±0.439717
0.4$\leq \cos\theta <$0.6	3.9447±0.289881	0.196633-0.294949	8.02451±0.589691
0.6$\leq \cos\theta <$0.8	4.9495±0.33525	0.0983163-0.196633	10.0685±0.681982
0.8$\leq \cos\theta <$0.9	8.46759±0.547787	0.0491582-0.0983163	17.2252±1.11434
0.9$\leq \cos\theta \leq$1.0	10.321±0.592507	0-0.0491582	20.9955±1.20531

Table J.6: The differential cross-section off the bound proton for incident beam energy E_γ =1358-1408 MeV.

$\cos(\theta^{\omega}_{c.m.})$	$d\sigma/d\cos(\theta^{\omega}_{c.m.})$ $[\mu b]$	$\lvert t-t_{min}\rvert$ $[GeV^2]$	$d\sigma/dt$ $[\mu b/GeV^2]$
-1.0$\leq \cos\theta <$-0.5	1.92476±0.254138	0.862067-1.14942	3.34909±0.442201
-0.5$\leq \cos\theta <$-0.2	1.53961±0.253807	0.689654-0.862067	2.67893±0.441625
-0.2$\leq \cos\theta <$0.1	1.75546±0.179216	0.51724-0.689654	3.05451±0.311836
0.1$\leq \cos\theta <$0.4	2.03865±0.150532	0.344827-0.51724	3.54726±0.261926
0.4$\leq \cos\theta <$0.6	3.28255±0.212143	0.229885-0.344827	5.71165±0.369129
0.6$\leq \cos\theta <$0.8	4.67595±0.249275	0.114942-0.229885	8.13617±0.433739
0.8$\leq \cos\theta <$0.9	7.41125±0.521613	0.0574712-0.114942	12.8956±0.907608
0.9$\leq \cos\theta \leq$1.0	12.0104±0.535134	0-0.0574712	20.8981±0.931135

Table J.7: The differential cross-section off the bound proton for incident beam energy E_γ =1408-1508 MeV.

$\cos(\theta^{\omega}_{c.m.})$	$d\sigma/d\cos(\theta^{\omega}_{c.m.})$ $[\mu b]$	$\lvert t-t_{min}\rvert$ $[GeV^2]$	$d\sigma/dt$ $[\mu b/GeV^2]$
-1.0$\leq \cos\theta <$-0.5	1.85533±0.273013	1.02209-1.36279	2.72285±0.400669
-0.5$\leq \cos\theta <$-0.2	1.31174±0.256879	0.817672-1.02209	1.92508±0.376991
-0.2$\leq \cos\theta <$0.1	1.78444±0.191644	0.613254-0.817672	2.61881±0.281253
0.1$\leq \cos\theta <$0.4	2.13721±0.159454	0.408836-0.613254	3.13653±0.234012
0.4$\leq \cos\theta <$0.6	2.92656±0.190944	0.272557-0.408836	4.29496±0.280226
0.6$\leq \cos\theta <$0.8	5.66519±0.228798	0.136279-0.272557	8.31413±0.33578
0.8$\leq \cos\theta <$0.9	9.36011±0.632471	0.0681393-0.136279	13.7367±0.928202
0.9$\leq \cos\theta \leq$ 1.0	-	0-0.0681393	-

Table J.8: The differential cross-section off the bound proton for incident beam energy E_γ =1508-1608 MeV.

$\cos(\theta^{\omega}_{c.m.})$	$d\sigma/d\cos(\theta^{\omega}_{c.m.})$ $[\mu b]$	$\lvert t-t_{min}\rvert$ $[GeV^2]$	$d\sigma/dt$ $[\mu b/GeV^2]$
-1.0$\leq \cos\theta <$-0.5	1.7383±0.352002	1.17711-1.56948	2.21513±0.44856
-0.5$\leq \cos\theta <$-0.2	1.89628±0.313844	0.941686-1.17711	2.41645±0.399935
-0.2$\leq \cos\theta <$0.1	1.68446±0.242135	0.706265-0.941686	2.14652±0.308555
0.1$\leq \cos\theta <$0.4	1.95067±0.173469	0.470843-0.706265	2.48576±0.221053
0.4$\leq \cos\theta <$0.6	3.01749±0.208542	0.313895-0.470843	3.84522±0.265747
0.6$\leq \cos\theta <$0.8	5.41459±0.250698	0.156948-0.313895	6.89987±0.319467
0.8$\leq \cos\theta <$0.9	10.1976±0.683316	0.0784738-0.156948	12.9949±0.870756
0.9$\leq \cos\theta \leq$1.0	-	0-0.0784738	-

Table J.9: The differential cross-section off the bound proton for incident beam energy E_γ =1608-1708 MeV.

$\cos(\theta^{\omega}_{c.m.})$	$d\sigma/d\cos(\theta^{\omega}_{c.m.})$ $[\mu b]$	$\lvert t-t_{min}\rvert$ $[GeV^2]$	$d\sigma/dt$ $[\mu b/GeV^2]$
-1.0$\leq \cos\theta <$-0.5	1.57282±0.369209	1.32547-1.7673	1.77992±0.417823
-0.5$\leq \cos\theta <$-0.2	1.08189±0.320665	1.06038-1.32547	1.22434±0.362887
-0.2$\leq \cos\theta <$0.1	0.776013±0.222867	0.795284-1.06038	0.878192±0.252212
0.1$\leq \cos\theta <$0.4	1.59423±0.176891	0.530189-0.795284	1.80414±0.200182
0.4$\leq \cos\theta <$0.6	2.64874±0.218709	0.35346-0.530189	2.9975±0.247507
0.6$\leq \cos\theta <$0.8	6.30621±0.260715	0.17673-0.35346	7.13656±0.295044
0.8$\leq \cos\theta <$0.9	11.7393±0.73391	0.0883649-0.17673	13.285±0.830545
0.9$\leq \cos\theta \leq$1.0	-	0-0.0883649	-

Table J.10: The differential cross-section off the bound proton for incident beam energy E_γ =1708-1808 MeV.

$\cos(\theta^{\omega}_{c.m.})$	$d\sigma/d\cos(\theta^{\omega}_{c.m.})$ $[\mu b]$	$\lvert t-t_{min}\rvert$ $[GeV^2]$	$d\sigma/dt$ $[\mu b/GeV^2]$
-1.0$\leq \cos\theta <$-0.5	1.3808±0.385012	1.47385-1.96513	1.4053±0.391843
-0.5$\leq \cos\theta <$-0.2	1.34472±0.335462	1.17908-1.47385	1.36858±0.341414
-0.2$\leq \cos\theta <$0.1	1.24391±0.233247	0.88431-1.17908	1.26598±0.237386
0.1$\leq \cos\theta <$0.4	1.86085±0.173988	0.58954-0.88431	1.89387±0.177075
0.4$\leq \cos\theta <$0.6	2.67117±0.213306	0.393026-0.58954	2.71857±0.217091
0.6$\leq \cos\theta <$0.8	6.71658±0.269952	0.196513-0.393026	6.83575±0.274742
0.8$\leq \cos\theta <$0.9	11.4977±0.655211	0.0982566-0.196513	11.7017±0.666837
0.9$\leq \cos\theta \leq$1.0	-	0-0.0982566	-

Table J.11: The differential cross-section off the bound proton for incident beam energy E_γ =1808-1908 MeV.

$\cos(\theta^{\omega}_{c.m.})$	$d\sigma/d\cos(\theta^{\omega}_{c.m.})$ $[\mu b]$	$\lvert t-t_{min}\rvert$ $[GeV^2]$	$d\sigma/dt$ $[\mu b/GeV^2]$
-1.0$\leq \cos\theta <$-0.5	1.79586±0.38188	1.62185-2.16247	1.66094±0.353189
-0.5$\leq \cos\theta <$-0.2	1.06079±0.316308	1.29748-1.62185	0.981093±0.292544
-0.2$\leq \cos\theta <$0.1	1.54422±0.258632	0.97311-1.29748	1.4282±0.239201
0.1$\leq \cos\theta <$0.4	1.42836±0.182154	0.64874-0.97311	1.32105±0.168469
0.4$\leq \cos\theta <$0.6	2.6216±0.220578	0.432493-0.64874	2.42464±0.204006
0.6$\leq \cos\theta <$0.8	6.99831±0.283049	0.216247-0.432493	6.47252±0.261783
0.8$\leq \cos\theta <$0.9	13.0578±0.652645	0.108123-0.216247	12.0768±0.603612
0.9$\leq \cos\theta \leq$1.0	-	0-0.108123	-

Table J.12: The differential cross-section off the bound proton for incident beam energy E_γ =1908-2008 MeV.

J.2. Exclusive differential cross-sections off the bound neutron

$\cos(\theta^{\omega}_{c.m.})$	$d\sigma/d\cos(\theta^{\omega}_{c.m.})$ $[\mu b]$	$\lvert t-t_{min}\rvert$ $[GeV^2]$	$d\sigma/dt$ $[\mu b/GeV^2]$
-1.0$\leq \cos\theta <$-0.5	1.37191±0.478806	0.330516-0.440687	6.22623±2.173
-0.5$\leq \cos\theta <$-0.2	1.71157±0.637041	0.264412-0.330516	7.76773±2.89112
-0.2$\leq \cos\theta <$0.1	1.38438±0.623418	0.198309-0.264412	6.28282±2.8293
0.1$\leq \cos\theta <$0.4	3.03911±0.666563	0.132206-0.198309	13.7926±3.02511
0.4$\leq \cos\theta <$0.6	3.2784±0.92125	0.0881375-0.132206	14.8786±4.18097
0.6$\leq \cos\theta <$0.8	4.21473±1.09745	0.0440687-0.0881375	19.128±4.98063
0.8$\leq \cos\theta <$0.9	4.57179±1.31485	0.0220344-0.0440687	20.7485±5.96727
0.9$\leq \cos\theta \leq$1.0	5.44688±2.14257	0-0.0220344	24.7199±9.72376

Table J.13: The differential cross-section off the bound neutron for incident beam energy E_γ =1158-1208 MeV.

$\cos(\theta^{\omega}_{c.m.})$	$d\sigma/d\cos(\theta^{\omega}_{c.m.})$ $[\mu b]$	$\lvert t-t_{min}\rvert$ $[GeV^2]$	$d\sigma/dt$ $[\mu b/GeV^2]$
-1.0$\leq \cos\theta <$-0.5	1.78205±0.796108	0.423326-0.564434	6.31446±2.82091
-0.5$\leq \cos\theta <$-0.2	1.7512±1.05363	0.338661-0.423326	6.20515±3.7334
-0.2$\leq \cos\theta <$0.1	3.07095±0.925031	0.253996-0.338661	10.8815±3.27773
0.1$\leq \cos\theta <$0.4	2.9103±1.07319	0.16933-0.253996	10.3123±3.80271
0.4$\leq \cos\theta <$0.6	4.16673±1.34966	0.112887-0.16933	14.7643±4.78234
0.6$\leq \cos\theta <$0.8	6.6872±1.89512	0.0564434-0.112887	23.6952±6.71511
0.8$\leq \cos\theta <$0.9	6.57292±2.26916	0.0282217-0.0564434	23.2903±8.04047
0.9$\leq \cos\theta \leq$1.0	7.96776±3.59519	0-0.0282217	28.2327±12.7391

Table J.14: The differential cross-section off the bound neutron for incident beam energy E_γ =1208-1233 MeV.

$\cos(\theta^{\omega}_{c.m.})$	$d\sigma/d\cos(\theta^{\omega}_{c.m.})$ $[\mu b]$	$\lvert t-t_{min}\rvert$ $[GeV^2]$	$d\sigma/dt$ $[\mu b/GeV^2]$
-1.0$\leq \cos\theta <$-0.5	2.54154±0.883865	0.477206-0.636274	7.98882±2.77825
-0.5$\leq \cos\theta <$-0.2	3.08688±0.89286	0.381765-0.477206	9.70298±2.80653
-0.2$\leq \cos\theta <$0.1	2.9621±0.902063	0.286323-0.381765	9.31076±2.83545
0.1$\leq \cos\theta <$0.4	2.20736±1.02904	0.190882-0.286323	6.93839±3.23458
0.4$\leq \cos\theta <$0.6	4.43824±1.38936	0.127255-0.190882	13.9507±4.36717
0.6$\leq \cos\theta <$0.8	5.5502±1.79172	0.0636274-0.127255	17.4459±5.63191
0.8$\leq \cos\theta <$0.9	10.9234±3.1636	0.0318137-0.0636274	34.3355±9.94414
0.9$\leq \cos\theta \leq$1.0	12.4147±3.18831	0-0.0318137	39.0231±10.0218

Table J.15: The differential cross-section off the bound neutron for incident beam energy E_γ =1233-1258 MeV.

$\cos(\theta^{\omega}_{c.m.})$	$d\sigma/d\cos(\theta^{\omega}_{c.m.})$ $[\mu b]$	$\lvert t-t_{min}\rvert$ $[GeV^2]$	$d\sigma/dt$ $[\mu b/GeV^2]$
-1.0$\leq \cos\theta <$-0.5	3.56644±0.648922	0.554778-0.739704	9.64288±1.75454
-0.5$\leq \cos\theta <$-0.2	2.56059±0.653351	0.443823-0.554778	6.92328±1.76652
-0.2$\leq \cos\theta <$0.1	2.70975±0.637704	0.332867-0.443823	7.32658±1.72421
0.1$\leq \cos\theta <$0.4	4.58358±0.687474	0.221911-0.332867	12.393±1.85878
0.4$\leq \cos\theta <$0.6	2.91407±0.820786	0.147941-0.221911	7.87901±2.21923
0.6$\leq \cos\theta <$0.8	5.6302±1.32597	0.0739704-0.147941	15.2228±3.58514
0.8$\leq \cos\theta <$0.9	6.55031±2.12217	0.0369852-0.0739704	17.7106±5.73789
0.9$\leq \cos\theta \leq$1.0	10.58±2.76176	0-0.0369852	28.606±7.4672

Table J.16: The differential cross-section off the bound neutron for incident beam energy E_γ =1258-1308 MeV.

$\cos(\theta^{\omega}_{c.m.})$	$d\sigma/d\cos(\theta^{\omega}_{c.m.})$ $[\mu b]$	$\lvert t-t_{min}\rvert$ $[GeV^2]$	$d\sigma/dt$ $[\mu b/GeV^2]$
-1.0$\leq \cos\theta <$-0.5	1.33608±0.738157	0.649312-0.86575	3.08653±1.70524
-0.5$\leq \cos\theta <$-0.2	4.33779±0.738857	0.51945-0.649312	10.0209±1.70686
-0.2$\leq \cos\theta <$0.1	3.01786±0.64589	0.389587-0.51945	6.97167±1.49209
0.1$\leq \cos\theta <$0.4	2.96183±0.686326	0.259725-0.389587	6.84223±1.58551
0.4$\leq \cos\theta <$0.6	4.77661±0.942227	0.17315-0.259725	11.0346±2.17667
0.6$\leq \cos\theta <$0.8	6.03308±1.13359	0.086575-0.17315	13.9372±2.61875
0.8$\leq \cos\theta <$0.9	9.26871±2.07469	0.0432875-0.086575	21.412±4.79282
0.9$\leq \cos\theta \leq$1.0	11.6255±2.97309	0-0.0432875	26.8565±6.86824

Table J.17: The differential cross-section off the bound neutron for incident beam energy E_γ =1308-1358 MeV.

$\cos(\theta^{\omega}_{c.m.})$	$d\sigma/d\cos(\theta^{\omega}_{c.m.})$ $[\mu b]$	$\lvert t-t_{min}\rvert$ $[GeV^2]$	$d\sigma/dt$ $[\mu b/GeV^2]$
-1.0$\leq \cos\theta <$-0.5	3.00684±0.858604	0.738837-0.985117	6.10454±1.74315
-0.5$\leq \cos\theta <$-0.2	1.99981±0.786933	0.59107-0.738837	4.06005±1.59764
-0.2$\leq \cos\theta <$0.1	3.05451±0.656123	0.443302-0.59107	6.20132±1.33207
0.1$\leq \cos\theta <$0.4	2.96364±0.539376	0.295535-0.443302	6.01683±1.09505
0.4$\leq \cos\theta <$0.6	4.26924±0.73268	0.197023-0.295535	8.66748±1.4875
0.6$\leq \cos\theta <$0.8	8.78712±1.11688	0.0985117-0.197023	17.8398±2.26751
0.8$\leq \cos\theta <$0.9	9.5939±2.46144	0.0492558-0.0985117	19.4777±4.99726
0.9$\leq \cos\theta \leq$1.0	11.5308±3.13086	0-0.0492558	23.41±6.35632

Table J.18: The differential cross-section off the bound neutron for incident beam energy E_γ =1358-1408 MeV.

$\cos(\theta^{\omega}_{c.m.})$	$d\sigma/d\cos(\theta^{\omega}_{c.m.})$ $[\mu b]$	$\lvert t-t_{min}\rvert$ $[GeV^2]$	$d\sigma/dt$ $[\mu b/GeV^2]$
-1.0$\leq \cos\theta <$-0.5	1.22414±0.676416	0.863631-1.15151	2.12615±1.17484
-0.5$\leq \cos\theta <$-0.2	1.1594±0.582506	0.690905-0.863631	2.01371±1.01173
-0.2$\leq \cos\theta <$0.1	1.88954±0.413895	0.518178-0.690905	3.28185±0.718875
0.1$\leq \cos\theta <$0.4	2.13425±0.362897	0.345452-0.518178	3.70688±0.630299
0.4$\leq \cos\theta <$0.6	5.30213±0.514034	0.230302-0.345452	9.20902±0.892802
0.6$\leq \cos\theta <$0.8	8.975±0.729411	0.115151-0.230302	15.5883±1.26688
0.8$\leq \cos\theta <$0.9	17.6618±1.64957	0.0575754-0.115151	30.676±2.86506
0.9$\leq \cos\theta \leq$1.0	25.4391±3.0845	0-0.0575754	44.184±5.35732

Table J.19: The differential cross-section off the bound neutron for incident beam energy E_γ =1408-1508 MeV.

$\cos(\theta^{\omega}_{c.m.})$	$d\sigma/d\cos(\theta^{\omega}_{c.m.})$ $[\mu b]$	$\lvert t-t_{min}\rvert$ $[GeV^2]$	$d\sigma/dt$ $[\mu b/GeV^2]$
-1.0$\leq \cos\theta <$-0.5	1.42671±0.622907	1.0238-1.36507	2.09031±0.912637
-0.5$\leq \cos\theta <$-0.2	1.1883±0.476797	0.819043-1.0238	1.74101±0.698567
-0.2$\leq \cos\theta <$0.1	2.11199±0.372811	0.614282-0.819043	3.09433±0.546215
0.1$\leq \cos\theta <$0.4	3.05323±0.326316	0.409521-0.614282	4.47336±0.478094
0.4$\leq \cos\theta <$0.6	3.57112±0.41492	0.273014-0.409521	5.23214±0.60791
0.6$\leq \cos\theta <$0.8	7.75426±0.593428	0.136507-0.273014	11.361±0.869446
0.8$\leq \cos\theta <$0.9	16.9307±1.48529	0.0682535-0.136507	24.8056±2.17614
0.9$\leq \cos\theta \leq$1.0	-	0-0.0682535	-

Table J.20: The differential cross-section off the bound neutron for incident beam energy E_γ =1508-1608 MeV.

$\cos(\theta^{\omega}_{c.m.})$	$d\sigma/d\cos(\theta^{\omega}_{c.m.})$ $[\mu b]$	$\lvert t-t_{min}\rvert$ $[GeV^2]$	$d\sigma/dt$ $[\mu b/GeV^2]$
-1.0$\leq \cos\theta <$-0.5	1.61622±0.697428	1.17898-1.57198	2.05629±0.887327
-0.5$\leq \cos\theta <$-0.2	2.2912±0.548642	0.943186-1.17898	2.91506±0.698029
-0.2$\leq \cos\theta <$0.1	0.818819±0.367018	0.707389-0.943186	1.04177±0.466951
0.1$\leq \cos\theta <$0.4	2.09684±0.303052	0.471593-0.707389	2.66778±0.385568
0.4$\leq \cos\theta <$0.6	3.70857±0.418106	0.314395-0.471593	4.71835±0.53195
0.6$\leq \cos\theta <$0.8	6.70281±0.573722	0.157198-0.314395	8.52788±0.729937
0.8$\leq \cos\theta <$0.9	15.3885±1.40865	0.0785988-0.157198	19.5785±1.7922
0.9$\leq \cos\theta \leq$1.0	-	0-0.0785988	-

Table J.21: The differential cross-section off the bound neutron for incident beam energy E_γ =1608-1708 MeV.

$\cos(\theta^{\omega}_{c.m.})$	$d\sigma/d\cos(\theta^{\omega}_{c.m.})$ $[\mu b]$	$\lvert t-t_{min}\rvert$ $[GeV^2]$	$d\sigma/dt$ $[\mu b/GeV^2]$
-1.0$\leq \cos\theta <$-0.5	0.841833±0.697313	1.32751-1.77002	0.951215±0.787917
-0.5$\leq \cos\theta <$-0.2	1.15042±0.487618	1.06201-1.32751	1.2999±0.550976
-0.2$\leq \cos\theta <$0.1	0.998191±0.370754	0.796507-1.06201	1.12789±0.418927
0.1$\leq \cos\theta <$0.4	1.42226±0.310693	0.531005-0.796507	1.60706±0.351062
0.4$\leq \cos\theta <$0.6	3.2362±0.42803	0.354003-0.531005	3.65669±0.483645
0.6$\leq \cos\theta <$0.8	8.34268±0.578441	0.177002-0.354003	9.42667±0.6536
0.8$\leq \cos\theta <$0.9	14.4309±1.46529	0.0885008-0.177002	16.306±1.65568
0.9$\leq \cos\theta \leq$1.0	-	0-0.0885008	-

Table J.22: The differential cross-section off the bound neutron for incident beam energy E_γ =1708-1808 MeV.

$\cos(\theta^{\omega}_{c.m.})$	$d\sigma/d\cos(\theta^{\omega}_{c.m.})$ $[\mu b]$	$\lvert t-t_{min}\rvert$ $[GeV^2]$	$d\sigma/dt$ $[\mu b/GeV^2]$
-1.0$\leq \cos\theta <$-0.5	2.17748±0.665925	1.47606-1.96808	2.2128±0.676726
-0.5$\leq \cos\theta <$-0.2	2.00997±0.510366	1.18085-1.47606	2.04257±0.518644
-0.2$\leq \cos\theta <$0.1	0.63995±0.321394	0.885635-1.18085	0.65033±0.326607
0.1$\leq \cos\theta <$0.4	1.11328±0.306932	0.590423-0.885635	1.13134±0.31191
0.4$\leq \cos\theta <$0.6	3.2571±0.440744	0.393616-0.590423	3.30993±0.447893
0.6$\leq \cos\theta <$0.8	7.94819±0.590128	0.196808-0.393616	8.07711±0.5997
0.8$\leq \cos\theta <$0.9	15.7837±1.45901	0.0984039-0.196808	16.0397±1.48268
0.9$\leq \cos\theta \leq$1.0	-	0-0.0984039	-

Table J.23: The differential cross-section off the bound neutron for incident beam energy E_γ =1808-1908 MeV.

$\cos(\theta^{\omega}_{c.m.})$	$d\sigma/d\cos(\theta^{\omega}_{c.m.})$ $[\mu b]$	$\lvert t-t_{min}\rvert$ $[GeV^2]$	$d\sigma/dt$ $[\mu b/GeV^2]$
-1.0$\leq \cos\theta <$-0.5	1.38767±0.635577	1.62423-2.16565	1.28153±0.586963
-0.5$\leq \cos\theta <$-0.2	0.581385±0.493646	1.29939-1.62423	0.536916±0.455888
-0.2$\leq \cos\theta <$0.1	0.762979±0.382404	0.974541-1.29939	0.70462±0.353155
0.1$\leq \cos\theta <$0.4	1.2608±0.310174	0.649694-0.974541	1.16436±0.286449
0.4$\leq \cos\theta <$0.6	3.42751±0.433945	0.433129-0.649694	3.16535±0.400753
0.6$\leq \cos\theta <$0.8	8.44001±0.608027	0.216565-0.433129	7.79445±0.56152
0.8$\leq \cos\theta <$0.9	17.2278±1.63994	0.108282-0.216565	15.9101±1.5145
0.9$\leq \cos\theta \leq$1.0	-	0-0.108282	-

Table J.24: The differential cross-section off the bound neutron for incident beam energy E_γ =1908-2008 MeV.

J.3. Inclusive differential cross-sections off LD_2

$\cos(\theta^{\omega}_{c.m.})$	$d\sigma/d\cos(\theta^{\omega}_{c.m.})$ $[\mu b]$	$\lvert t-t_{min}\rvert$ $[GeV^2]$	$d\sigma/dt$ $[\mu b/GeV^2]$
-1.0$\leq \cos\theta <$-0.5	2.69113±0.268513	0.330516-0.440687	12.4148±1.58791
-0.5$\leq \cos\theta <$-0.2	1.81992±0.317195	0.264412-0.330516	9.82039±1.4764
-0.2$\leq \cos\theta <$0.1	1.89873±0.303583	0.198309-0.264412	10.5486±1.43603
0.1$\leq \cos\theta <$0.4	2.94903±0.310323	0.132206-0.198309	16.4406±1.36019
0.4$\leq \cos\theta <$0.6	3.93479±0.343992	0.0881375-0.132206	19.5272±1.70381
0.6$\leq \cos\theta <$0.8	5.82039±0.364475	0.0440687-0.0881375	27.0279±1.91212
0.8$\leq \cos\theta <$0.9	8.41807±0.550022	0.0220344-0.0440687	34.6789±2.94339
0.9$\leq \cos\theta \leq$1.0	7.94793±0.578699	0-0.0220344	40.216±3.26244

Table J.25: The inclusive differential cross-section off the LD_2 target for incident beam energy E_γ =1158-1208 MeV.

$\cos(\theta^{\omega}_{c.m.})$	$d\sigma/d\cos(\theta^{\omega}_{c.m.})$ $[\mu b]$	$\lvert t-t_{min}\rvert$ $[GeV^2]$	$d\sigma/dt$ $[\mu b/GeV^2]$
-1.0$\leq \cos\theta <$-0.5	3.37164±0.490295	0.433405-0.577874	11.0799±1.91103
-0.5$\leq \cos\theta <$-0.2	3.50822±0.439059	0.346724-0.433405	12.9496±2.09756
-0.2$\leq \cos\theta <$0.1	2.75608±0.444475	0.260043-0.346724	10.9893±1.94596
0.1$\leq \cos\theta <$0.4	4.24256±0.478431	0.173362-0.260043	16.7927±1.7926
0.4$\leq \cos\theta <$0.6	5.30991±0.608107	0.115575-0.173362	18.3108±2.27696
0.6$\leq \cos\theta <$0.8	8.43546±0.643086	0.0577874-0.115575	30.4442±2.50943
0.8$\leq \cos\theta <$0.9	8.72663±0.954919	0.0288937-0.0577874	30.6714±3.71426
0.9$\leq \cos\theta \leq$1.0	13.5068±1.10332	0-0.0288937	46.5892±3.82426

Table J.26: The inclusive differential cross-section off the LD_2 target for incident beam energy E_γ =1208-1233 MeV.

$\cos(\theta^{\omega}_{c.m.})$	$d\sigma/d\cos(\theta^{\omega}_{c.m.})$ $[\mu b]$	$\lvert t-t_{min}\rvert$ $[GeV^2]$	$d\sigma/dt$ $[\mu b/GeV^2]$
-1.0$\leq \cos\theta <$-0.5	4.93815±0.453277	0.486589-0.648785	15.985±1.74532
-0.5$\leq \cos\theta <$-0.2	3.84367±0.485489	0.389271-0.486589	11.7842±1.53874
-0.2$\leq \cos\theta <$0.1	3.58512±0.44777	0.291953-0.389271	12.6713±1.60026
0.1$\leq \cos\theta <$0.4	4.39242±0.458055	0.194635-0.291953	14.6935±1.50643
0.4$\leq \cos\theta <$0.6	6.80329±0.552845	0.129757-0.194635	21.4079±1.63585
0.6$\leq \cos\theta <$0.8	8.91105±0.591927	0.0648785-0.129757	28.0657±1.95857
0.8$\leq \cos\theta <$0.9	11.3705±0.886234	0.0324392-0.0648785	37.2176±2.99313
0.9$\leq \cos\theta \leq$1.0	18.1795±1.04532	0-0.0324392	58.7461±3.29246

Table J.27: The inclusive differential cross-section off the LD_2 target for incident beam energy E_γ =1233-1258 MeV.

$\cos(\theta^{\omega}_{c.m.})$	$d\sigma/d\cos(\theta^{\omega}_{c.m.})$ $[\mu b]$	$\lvert t-t_{min}\rvert$ $[GeV^2]$	$d\sigma/dt$ $[\mu b/GeV^2]$
-1.0$\leq \cos\theta <$-0.5	5.95502±0.423991	0.559121-0.745495	15.9223±1.15389
-0.5$\leq \cos\theta <$-0.2	2.30203±0.497342	0.447297-0.559121	7.82541±0.945354
-0.2$\leq \cos\theta <$0.1	4.33117±0.372523	0.335473-0.447297	13.1519±0.939957
0.1$\leq \cos\theta <$0.4	4.56319±0.336652	0.223649-0.335473	13.6066±0.846078
0.4$\leq \cos\theta <$0.6	5.78023±0.39496	0.149099-0.223649	16.5427±1.04333
0.6$\leq \cos\theta <$0.8	10.3499±0.476744	0.0745495-0.149099	29.0505±1.27355
0.8$\leq \cos\theta <$0.9	14.7155±0.746313	0.0372748-0.0745495	39.5929±2.0118
0.9$\leq \cos\theta \leq$1.0	19.8281±0.817342	0-0.0372748	53.5836±2.193

Table J.28: The inclusive differential cross-section off the LD_2 target for incident beam energy E_γ =1258-1308 MeV.

$\cos(\theta^{\omega}_{c.m.})$	$d\sigma/d\cos(\theta^{\omega}_{c.m.})$ $[\mu b]$	$\lvert t-t_{min}\rvert$ $[GeV^2]$	$d\sigma/dt$ $[\mu b/GeV^2]$
-1.0$\leq \cos\theta <$-0.5	4.48685±0.372535	0.649312-0.86575	11.0514±1.08023
-0.5$\leq \cos\theta <$-0.2	3.89965±0.365299	0.51945-0.649312	10.2613±0.966803
-0.2$\leq \cos\theta <$0.1	3.78657±0.333004	0.389587-0.51945	8.8944±0.841971
0.1$\leq \cos\theta <$0.4	4.79966±0.318309	0.259725-0.389587	11.4978±0.848076
0.4$\leq \cos\theta <$0.6	6.7196±0.416031	0.17315-0.259725	17.0787±1.08637
0.6$\leq \cos\theta <$0.8	10.2397±0.468678	0.086575-0.17315	24.4836±1.18488
0.8$\leq \cos\theta <$0.9	15.0352±0.738707	0.0432875-0.086575	35.5039±1.63786
0.9$\leq \cos\theta \leq$1.0	24.505±0.800579	0-0.0432875	57.5167±1.8854

Table J.29: The inclusive differential cross-section off the LD_2 target for incident beam energy E_γ =1308-1358 MeV.

$\cos(\theta^{\omega}_{c.m.})$	$d\sigma/d\cos(\theta^{\omega}_{c.m.})$ $[\mu b]$	$\lvert t-t_{min}\rvert$ $[GeV^2]$	$d\sigma/dt$ $[\mu b/GeV^2]$
-1.0$\leq \cos\theta <$-0.5	3.13172±0.386018	0.738837-0.985117	6.77481±0.886839
-0.5$\leq \cos\theta <$-0.2	2.47445±0.361708	0.59107-0.738837	5.62408±0.944082
-0.2$\leq \cos\theta <$0.1	3.86368±0.312795	0.443302-0.59107	7.77404±0.725673
0.1$\leq \cos\theta <$0.4	4.27683±0.327587	0.295535-0.443302	8.72011±0.706192
0.4$\leq \cos\theta <$0.6	6.58181±0.403837	0.197023-0.295535	14.012±0.796365
0.6$\leq \cos\theta <$0.8	11.1208±0.467343	0.0985117-0.197023	23.3385±0.935232
0.8$\leq \cos\theta <$0.9	18.6036±0.753812	0.0492558-0.0985117	36.7213±1.59606
0.9$\leq \cos\theta \leq$1.0	25.842±0.816945	0-0.0492558	54.0281±1.71049

Table J.30: The inclusive differential cross-section off the LD_2 target for incident beam energy E_γ =1358-1408 MeV.

$\cos(\theta^{\omega}_{c.m.})$	$d\sigma/d\cos(\theta^{\omega}_{c.m.})$ $[\mu b]$	$\lvert t-t_{min}\rvert$ $[GeV^2]$	$d\sigma/dt$ $[\mu b/GeV^2]$
-1.0$\leq \cos\theta <$-0.5	3.47239±0.341455	0.863631-1.15151	6.58032±0.672022
-0.5$\leq \cos\theta <$-0.2	2.78723±0.281606	0.690905-0.863631	5.06311±0.540123
-0.2$\leq \cos\theta <$0.1	3.09661±0.243381	0.518178-0.690905	5.49537±0.479567
0.1$\leq \cos\theta <$0.4	4.49752±0.23187	0.345452-0.518178	7.4541±0.422104
0.4$\leq \cos\theta <$0.6	6.90084±0.314497	0.230302-0.345452	12.7029±0.523745
0.6$\leq \cos\theta <$0.8	11.9287±0.336696	0.115151-0.230302	20.9616±0.600023
0.8$\leq \cos\theta <$0.9	20.4036±0.583057	0.0575754-0.115151	35.6502±1.02152
0.9$\leq \cos\theta \leq$1.0	36.0355±0.673291	0-0.0575754	62.9087±1.14902

Table J.31: The inclusive differential cross-section off the LD_2 target for incident beam energy E_γ =1408-1508 MeV.

$\cos(\theta^{\omega}_{c.m.})$	$d\sigma/d\cos(\theta^{\omega}_{c.m.})$ $[\mu b]$	$\lvert t-t_{min}\rvert$ $[GeV^2]$	$d\sigma/dt$ $[\mu b/GeV^2]$
-1.0$\leq \cos\theta <$-0.5	2.59253±0.358492	1.0238-1.36507	4.06215±0.566911
-0.5$\leq \cos\theta <$-0.2	2.16764±0.271256	0.819043-1.0238	3.41789±0.462957
-0.2$\leq \cos\theta <$0.1	2.83424±0.247735	0.614282-0.819043	4.14271±0.372724
0.1$\leq \cos\theta <$0.4	4.05465±0.223257	0.409521-0.614282	6.17594±0.330426
0.4$\leq \cos\theta <$0.6	6.15489±0.281199	0.273014-0.409521	9.17056±0.424443
0.6$\leq \cos\theta <$0.8	12.3437±0.329571	0.136507-0.273014	18.2483±0.500847
0.8$\leq \cos\theta <$0.9	23.4171±0.575687	0.0682535-0.136507	34.2678±0.858404
0.9$\leq \cos\theta \leq$1.0	45.0426±0.699177	0-0.0682535	65.6721±1.03585

Table J.32: The inclusive differential cross-section off the LD_2 target for incident beam energy E_γ =1508-1608 MeV.

$\cos(\theta^{\omega}_{c.m.})$	$d\sigma/d\cos(\theta^{\omega}_{c.m.})$ $[\mu b]$	$\lvert t-t_{min}\rvert$ $[GeV^2]$	$d\sigma/dt$ $[\mu b/GeV^2]$
-1.0$\leq \cos\theta <$-0.5	2.70967±0.409991	1.17898-1.57198	3.66107±0.655237
-0.5$\leq \cos\theta <$-0.2	2.36374±0.325471	0.943186-1.17898	3.24269±0.48516
-0.2$\leq \cos\theta <$0.1	2.75903±0.264538	0.707389-0.943186	3.5445±0.344965
0.1$\leq \cos\theta <$0.4	4.16739±0.233998	0.471593-0.707389	5.18662±0.319406
0.4$\leq \cos\theta <$0.6	6.05912±0.310778	0.314395-0.471593	7.818±0.406554
0.6$\leq \cos\theta <$0.8	12.946±0.36199	0.157198-0.314395	16.3844±0.478425
0.8$\leq \cos\theta <$0.9	27.2284±0.672964	0.0785988-0.157198	34.296±0.879894
0.9$\leq \cos\theta \leq$1.0	50.9339±0.826175	0-0.0785988	64.8778±1.05252

Table J.33: The inclusive differential cross-section off the LD_2 target for incident beam energy E_γ =1608-1708 MeV.

$\cos(\theta^{\omega}_{c.m.})$	$d\sigma/d\cos(\theta^{\omega}_{c.m.})$ $[\mu b]$	$\lvert t-t_{min}\rvert$ $[GeV^2]$	$d\sigma/dt$ $[\mu b/GeV^2]$
-1.0$\leq \cos\theta <$-0.5	4.27017±0.489001	1.32751-1.77002	4.76867±0.59882
-0.5$\leq \cos\theta <$-0.2	1.58568±0.325864	1.06201-1.32751	1.87668±0.417713
-0.2$\leq \cos\theta <$0.1	1.62627±0.265471	0.796507-1.06201	1.79884±0.308358
0.1$\leq \cos\theta <$0.4	3.1077±0.240134	0.531005-0.796507	3.44906±0.278739
0.4$\leq \cos\theta <$0.6	4.90924±0.295435	0.354003-0.531005	5.69631±0.380424
0.6$\leq \cos\theta <$0.8	12.42±0.390296	0.177002-0.354003	14.1862±0.450923
0.8$\leq \cos\theta <$0.9	29.1266±0.74136	0.0885008-0.177002	32.551±0.88274
0.9$\leq \cos\theta \leq$1.0	57.6385±0.935573	0-0.0885008	65.0174±1.05765

Table J.34: The inclusive differential cross-section off the LD_2 target for incident beam energy E_γ =1708-1808 MeV.

$\cos(\theta^{\omega}_{c.m.})$	$d\sigma/d\cos(\theta^{\omega}_{c.m.})$ $[\mu b]$	$\lvert t-t_{min}\rvert$ $[GeV^2]$	$d\sigma/dt$ $[\mu b/GeV^2]$
-1.0$\leq \cos\theta <$-0.5	1.88645±0.50004	1.47606-1.96808	1.88104±0.535028
-0.5$\leq \cos\theta <$-0.2	2.16195±0.338053	1.18085-1.47606	2.20586±0.420785
-0.2$\leq \cos\theta <$0.1	1.81869±0.247293	0.885635-1.18085	1.98153±0.260226
0.1$\leq \cos\theta <$0.4	2.94592±0.241945	0.590423-0.885635	2.92748±0.258926
0.4$\leq \cos\theta <$0.6	6.1315±0.310312	0.393616-0.590423	6.00665±0.327709
0.6$\leq \cos\theta <$0.8	14.2224±0.399622	0.196808-0.393616	14.2072±0.424874
0.8$\leq \cos\theta <$0.9	28.0426±0.779501	0.0984039-0.196808	28.5109±0.806784
0.9$\leq \cos\theta \leq$1.0	65.0816±1.05123	0-0.0984039	65.262±1.08708

Table J.35: The inclusive differential cross-section off the LD_2 target for incident beam energy E_γ =1808-1908 MeV.

$\cos(\theta^{\omega}_{c.m.})$	$d\sigma/d\cos(\theta^{\omega}_{c.m.})$ $[\mu b]$	$\lvert t-t_{min}\rvert$ $[GeV^2]$	$d\sigma/dt$ $[\mu b/GeV^2]$
-1.0$\leq \cos\theta <$-0.5	3.1284±0.451509	1.62423-2.16565	2.87608±0.452533
-0.5$\leq \cos\theta <$-0.2	1.63533±0.352923	1.29939-1.62423	1.46549±0.385311
-0.2$\leq \cos\theta <$0.1	2.29393±0.290879	0.974541-1.29939	2.07957±0.269433
0.1$\leq \cos\theta <$0.4	2.76332±0.239089	0.649694-0.974541	2.5102±0.219029
0.4$\leq \cos\theta <$0.6	5.67839±0.315965	0.433129-0.649694	5.1526±0.302983
0.6$\leq \cos\theta <$0.8	14.9814±0.427252	0.216565-0.433129	13.8593±0.402231
0.8$\leq \cos\theta <$0.9	30.5238±0.819814	0.108282-0.216565	27.7624±0.766434
0.9$\leq \cos\theta \leq$1.0	75.474±1.16401	0-0.108282	69.2139±1.0824

Table J.36: The inclusive differential cross-section off the LD_2 target for incident beam energy E_γ =1908-2008 MeV.

K. Total Cross-sections

E_γ^{beam} [MeV]	$\sigma_p^{free} \pm \sigma_{stat.}^{err} \pm \sigma_{syst.}^{err}$ [μb]	$\sigma_{incl} \pm \sigma_{stat.}^{err} \pm \sigma_{syst.}^{err}$ [μb]
1125-1150	4.915±0.157±0.860	4.437±0.122±0.400
1150-1175	6.549±0.174±1.148	5.191±0.287±0.471
1175-1200	8.165±0.200±1.059	7.344±0.332±0.606
1200-1250	9.257±0.154±1.216	8.884±0.239±0.757
1250-1300	10.019±0.152±1.301	9.087±0.208±0.753
1300-1350	8.973±0.169±0.936	8.581±0.222±0.785
1350-1400	8.632±0.193±0.923	8.291±0.225±0.784
1400-1450	8.286±0.250±0.961	7.910±0.257±0.828
1450-1500	8.816±0.352±0.983	8.268±0.250±0.824
1500-1550	8.074±0.433+0.936-0.933	7.953±0.254±0.828
1550-1600	8.528±0.406+0.957-0.923	8.077±0.259±0.775
1600-1650	7.306±0.293+0.896-0.768	8.810±0.254±0.812
1650-1700	8.039±0.402+0.896-0.768	8.560±0.245±0.804
1700-1800	8.323±0.283+1.262-0.949	9.176±0.184±0.940
1800-1900	8.936±0.261+1.340-0.998	9.776±0.180±0.976
1900-2000	8.838±0.282+1.435-1.131	9.901±0.184±1.166

Table K.1: The total cross-sections for ω-photoproduction off the LH_2 target. The systematic errors listed are from the analysis. In addition, there is a ≈10 % systematic error which affects the overall normalization.

E_γ^{beam} [MeV]	$\sigma_p^{bound} \pm \sigma_{stat.}^{err} \pm \sigma_{syst.}^{err}$ [μb]	$\sigma_n^{bound} \pm \sigma_{stat.}^{err} \pm \sigma_{syst.}^{err}$ [μb]	$\sigma_{incl} \pm \sigma_{stat.}^{err} \pm \sigma_{syst.}^{err}$ [μb]
1158-1208	3.974±0.080±0.659	5.011±0.519±1.589	7.444±0.283±0.765
1208-1233	4.895±0.216±0.698	6.837±0.851±1.657	10.209±0.475±1.037
1233-1258	5.982±0.338±0.851	8.146±0.871±1.826	12.629±0.432±1.279
1258-1308	5.544±0.155±0.826	7.783±0.861±1.159	13.234±0.307±1.460
1308-1358	6.633±0.178±0.774	8.004±0.633±1.163	13.968±0.341±1.472
1358-1408	6.037±0.197±0.729	8.685±0.856±1.758	13.220±0.323±1.453
1408-1508	6.158±0.159±0.754	9.375±1.062±1.406	14.654±0.242±1.638
1508-1608	6.652±0.248+0.822-0.811	8.674±0.461+1.309-1.297	15.235±0.234±1.695
1608-1708	6.939±0.296+0.948-0.852	8.372±0.689+1.355-1.258	16.357±0.264±1.835
1708-1808	6.716±0.293+1.073-0.837	7.828±0.600+1.423-1.188	15.834±0.265±1.808
1808-1908	7.055±0.270+1.155-0.914	8.355±0.612+1.807-1.302	16.845±0.276±2.014
1908-2008	7.672±0.289+1.212-0.938	8.406±0.671+2.450-1.260	18.451±0.283±2.059

Table K.2: The total cross-sections for ω-photoproduction off the LD_2 target. The systematic errors listed are from the analysis. In addition, there is a ≈10 % systematic error which affects the overall normalization.

List of Figures

List of Tables

Bibliography

[1] W.-T. Chiang *et al.*, Nucl. Phys. A **700** 429 (2002)

[2] V. Shklyar *et al.*, Phys. Lett. **B650** 172 (2007)

[3] V. Heiny *et al.*, Eur. Phys. J. **A6** 83 (1999)

[4] J. Weiß *et al.*, Eur. Phys. J. **A16** 275 (2003)

[5] I. Jaegle *et al.*, Phys. Rev. Lett. **100**:252002 (2008)

[6] I.Jaegle *et al.*, Eur. Phys. J. A **47**:11 (2011)

[7] F. Klein, arXiv:0807.0594v1 [hep-ex] 3 Jul 2008

[8] V. Metag, Pramana-journal of physics, Vol. 75, No. 2, August(2010)

[9] D. Trnka, *Investigation of in-medium modifications of the ω meson in photonuclear reactions*, PhD thesis, Universität Gießen (2006)

[10] P. Mühlich *et al.*,Nucl. Phys. A **773**, 156 (2006)

[11] M. Kaskulov *et al.*, Eur. Phys. J. **A31**, 245 (2007)

[12] M. Kotulla *et al.*, Phys. Rev. Lett. 100, 192302 (2008)

[13] G. Penner, U. Mosel, Phys. Rev. C **66**, 055212 (2002)

[14] F.-J. Klein *et al.*, πN Newsl. **14**, 141 (1998)

[15] Aachen-Berlin-Bonn-Hamburg-Heidelberg-Mnchen Collaboration, Phys. Rev. **175**, 1669 (1668)

[16] H. R. Crouch *et al.*, Phys. Rev. **155**, 1476 (1967)

[17] G. Penner, *Vector Meson Production and Nucleon Resonance Analysis in a Coupled-Channel Approach*, PhD thesis, Universität Gießen (2002)

[18] J. Barth *et al.*, Eur. Phys. J. **A18** (2003) 117

[19] M. Williams *et al.*, Phys. Rev. C **C80**, 065209 (2009)

[20] E. Hourany, Nucl. Phys. A **755** (2005) 447c-450c

[21] PDG - Particle Data Group: Particle Physics Booklet, C. Amsler *et al.*, Physics Letters B 667,1 (2008)

[22] M. Lacombe *et al.*, Phys. Lett. B101, 139 (1981)

[23] V. Sklyar *et al.*, Phys. Rev. C **71**, 055206 (2005)

[24] The Bonn Electron Stretcher Accelerator ELSA: Past and Future, W. Hillert, Eur. Phys. J. A 28, 139 (2006)

[25] R. Burgwinkel, *Aufbau, Test und Eichung des hochauflsenden Tagging-Systems TOPAS II am Bonner SAPHIR-Detektor*, PhD thesis, Universität Bonn (1996)

[26] B. Kopf, *Untersuchung der photoinduzierten Reaktionen* $\gamma p \to p\pi^0\pi^0$ *und* $\gamma p \to p\pi^0\eta$ *an einen Flüssig-Wasserstoff-Target*, PhD thesis, Universität Dresden (2002)

[27] E. Aker *et al.*, NIM A321 69 (1992)

[28] A. Fösel, *Entwicklung und Bau des Innendetektors fr das Crystal Barrel Experiment an ELSA/Bonn*, PhD thesis, Universität Erlangen (2000)

[29] A. R. Gabler *et al.*, NIM A346 168 (1994)

[30] R. Novotny *et al.*, *The* BaF_2 *photon spectromete TAPS*, IEEE transactions on nuclear science 38 387 (1991)

[31] S. Jansen, *Entwicklung eines neuen CPV-Systems fr TAPS*, Dipl. thesis, Universität Gießen (1998)

[32] Techniques for Nuclear and Particle Physics Experiments, Second Revised Edition, W. R. Leo, Springer-Verlag (1994)

[33] http://hpfr02.physik.uni-freiburg.de/projects/compass/electronics/s-link-catch.html

[34] C. Schmidt, *Entwicklung eines neuen Datenakquisitionssystems fr das CB-ELSA-Experiment*, PhD thesis, Universität Bonn (2004)

[35] R. Castelijns, *Photoproduction of strange mesons and hyperons on the proton*, PhD thesis, KVI, Groningen (2006)

[36] I. Horn, *The decay of the γp system into the $p\pi^0\eta$ final state*, PhD thesis, Universität Bonn (2004)

[37] C. J. Y. Powrie *et al.*, Phys. Rev. C**64** (2001) 034602

[38] D. Elsner, *Untersuchung kleiner Partialwellenbeitrge in der Nhe dominierender Resonanzzustnde des Protons mit linear polarisierten Photonen*, PhD thesis, Universität Bonn (2007)

[39] J. Junkersfeld, *Kalibration des Crystal-Barrel-ELSA Detektors mit Hilfe der Reaktion $\gamma p \to \pi^0 p$*, Dipl. thesis, Universität Bonn (2000)

[40] F. M. Marqués *et al.*, NIM A365, 392 (1995)

[41] I. Jaelge, *$\pi^0\pi^0$, η and η' photoproduction off deuterium or The search for missing resonances*, PhD thesis, Universität Basel (2009)

[42] M. Kotulla, *Experiment zür Bestimmung des magnetischen Moments der $\Delta^+(1232)$ Resonanz*, PhD thesis, Universität Gießen (2002)

[43] V. Sugat, *Strangeness Production on the Deuterium Target*, PhD thesis, KVI, Groningen (2007)

[44] R. Brun *et al.*, GEANT, users guide and reference manual, CERN, DD/US/86 (1983)

[45] The GEANT-CALOR interface users guide, C. Zeitnitz and T.A. Gabriel (2001)

[46] Y.-S. Tsai, Pair Production and Bremsstrahlung of Charged Leptons, Rev. Mod. Phys. 46 815 (1974)

[47] K. Fournet-Ponse, Die Photonenmarkierungsanlage für das Crystal-Barrel/TAPS-Experiment an ELSA, PhD thesis, Universität Bonn (2009)

[48] V. Shklyar, Private communication, Gießen (2011)

[49] J. Junkersfeld, Eur. Phys. J. A **31** (2007) 365

[50] I. Jaelge, Private communication, Basel (2008)

[51] I. Jaegle *et al.*, Eur. Phys. J. A **47**, (2011) 89.

Acknowledgements

First of all I would like to thank my supervisor Prof. Volker Metag for including me in his group and for the immense support that I have felt from him all through my work. The organized weekly group meetings were a great opportunity for discussions and guidance and for that I thank all members of the group. In particular I would like to thank Dr. Mariana Nanova, Dr. David Trnka and Dr. Martin Kotulla which helped me a great deal with my analysis.

I would also like to thank Dr. Rainer Novotny who was the person that made me go to Gießen in the first place, since he told me about the position during an experiment we performed, together with Werner Döring, in Mainz during my diploma work. His enthusiasm in answering any question that one might have was one of the things that really attracted me to wanting joining this group and he was a wonderful supervisor to me during the beginning of my PhD when my work consisted of investigation of crystals for the electromagnetic calorimeter for the PANDA-collaboration.

Huge thanks go to Dr. Igal Jaegle, formerly at the University of Basel, for his great reception of me during several stays in Basel, where he patiently explained his analysis which were of great help to me. On top of that, he always promptly answered any question that I emailed to him.

A special thank you to Karoly Makonyi, my office mate since I first arrived in Gießen, who is always eager to help in any way possible and has now become a dear friend of mine.

I would like to thank Vitaly Shklyar for providing me with his cross-section calculations.

I would like to thank the members of the CBELSA-Collaboration, especially the people who collected the data I analysed.

Thank you Andrew Wilson and Volker Crede at the Florida State University for the

exchanging of ideas about the analysis of the LH_2 data.

A special thank you to Künkel Bäckerei for making the best Cafe Latte ever, which always gave me a good start of the day.

Last, but not least, I would like to thank my family; my parents for being so encouraging, my husband for his tremendous support and my daughters, who definitely did not increase the speed of my work, but brought so much joy to my life.

Erklärung

Hiermit versichere ich, dass ich die vorliegende Arbeit selbständig verfasst habe. Es wurden außer den in dieser Arbeit genannten Quellen und Hilfsmittel keine Weiteren verwendet.

Diese Arbeit und die in ihr gezeigten Ergebnisse wurden bisher keiner anderen Prüfungsbehörde vorgelegt und auch noch nicht veröffentlicht.

Frida Dietz

Gießen, Feb 2013.